Sascha Patrick Quanz

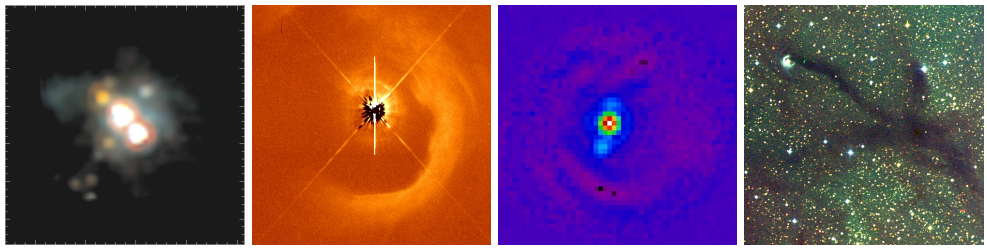

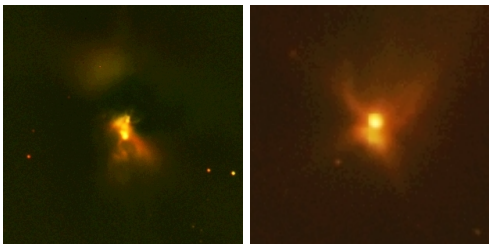

Circumstellar disks and envelopes around young low-mass stars

Dissertation

submitted to the
Combined Faculties for the Natural Sciences and for Mathematics
of the Ruperto-Carola University of Heidelberg (Germany)
for the degree of

Doctor of Natural Sciences

presented by

Diplom-Physicist

Sascha Patrick Quanz

born in Eschwege (Germany)

Oral examination: July 4, 2007

Circumstellar disks and envelopes around young low-mass stars

Referees: **Prof. Dr. Thomas Henning**

Prof. Dr. Ralf S. Klessen

Abstract:

In this PhD thesis astronomical observations of the immediate surroundings of young low-mass stars are presented and interpreted. Particular emphasis is put on FU Orionis stars (FUors). These objects are surrounded by an active accretion disk and a circumstellar envelope, both consisting of gas, dust and ice components. During the FUor-phase the envelope is dispersed and partly accreted onto the disk. Using data from the HUBBLE SPACE TELESCOPE, the SPITZER SPACE TELESCOPE, and the VERY LARGE TELESCOPE INTERFEROMETER, accretion disks and envelopes are investigated, and physical parameters, possible dust compositions, and ice properties are derived. Evidence for dust coagulation and grain growth within the disks is found, indicating dust processing in the early phases of accretion disk evolution. Furthermore, evidence for FUors in a young stellar cluster is presented, suggesting that most young, low-mass stars possibly undergo this phase of enhanced accretion, regardless of their immediate stellar environment. Based on spectroscopic diagnostics, an evolutionary sequence for FUors is found, which fits into the general paradigm of low-mass star formation. Finally, a deep near-infrared survey in the Taurus star-forming region reveals numerous new candidates for young low-mass stars and Brown Dwarfs surrounded by circumstellar disks. Based on photometric measurements and theoretical models, the least massive objects discerned by the survey are found to have masses in the range of several Jupiter masses. This makes them excellent candidates for being among the least massive free-floating objects with circum-sub-stellar disks known today.

Zusammenfassung:

In der vorliegende Dissertation werden astronomische Beobachtungen der unmittelbaren Umgebung junger, massearmer Sterne dargestellt und interpretiert. Ein Schwerpunkt liegt dabei auf FU Orionis Objekten (FUors). Diese Objekte sind von einer aktiven Akkretionsscheibe und einer zirkumstellaren Hülle umgeben, die aus Gas-, Staub- und Eiskomponenten aufgebaut sind. Im Laufe der FUor-Phase wird die Hülle teilweise auf die Scheibe akkretiert und der Rest durch Stern- oder Scheibenwinde auseinander getrieben. Mit Daten des HUBBLE SPACE TELESCOPE, des SPITZER SPACE TELESCOPE und des VERY LARGE TELESCOPE INTERFEROMETER werden Akkretionsscheiben und Hüllen untersucht und physikalische Größen, mögliche Staubzusammensetzungen und Eiseigenschaften abgeleitet. Es ergeben sich deutliche Hinweise, dass Staubteilchen bereits in diesen frühen Phasen der Scheibenentwicklung koagulieren und wachsen. Des weiteren wird gezeigt, dass FUors auch in jungen Sternhaufen existieren. Somit scheinen junge, massearme Sterne diese Evolutionsphase unabhängig von ihrer unmittelbaren Umgebung zu durchlaufen. Basierend auf Spektren wird eine Entwicklungssequenz für FUors abgeleitet, welche sich direkt in die allgemeine Evolution junger Sterne einfügt. Letztlich werden neue Kandidaten für junge Sterne und Braune Zwerge in der Sternentstehungsregion Taurus vorgestellt, welche möglicherweise von zirkumstellaren Scheiben umgeben sind. Die Objekte wurden im Rahmen einer Durchmusterung bei nah-infraroten Wellenlängen entdeckt. Photometrische Messungen und theoretische Modelle deuten darauf hin, dass einige dieser Objekte Massen in der Größenordnung von nur wenigen Jupitermassen besitzen. Somit sind sie exzellente Kandidaten, um zu den bisher masseärmsten, ungebundenen Objekten zu gehören, welche zusätzlich von einer Scheibe umgeben sind.

Meinen Eltern, Ingrid und Lothar,
meinem Bruder, Florian,
und
Silke Maria Zoller
gewidmet

Contents

1. Introduction

The birth of low-mass stars in a nutshell

IN THIS PHD THESIS astronomical observations of the immediate circumstellar surroundings of young, low-mass stars are presented and interpreted. Emphasis is put on circumstellar disks and envelopes surrounding the young objects. How these disks and envelopes form, which evolutionary phase they define in the life of a young star, and how star, disk, and envelope can be observationally probed will shortly be described in this introduction.

1.1 The evolution of young low-mass stars

In recent years our understanding of the formation of stars and planets was revolutionized. Already Kant (1755) and Laplace (1795) developed first ideas about the origin of our Solar System that were at least qualitatively not too far away from today's paradigm. However, the progress in astronomical observing techniques and computer based theoretical modeling allows us nowadays to address questions related to star and planet formation also quantitatively. Recently published textbooks like, for instance, Stahler & Palla (2005) and Schulz (2005) provide comprehensive overviews explaining the current understanding of the star formation process so that we can restrict ourselves in this introduction only to the most important aspects.

Most stars are born in the interstellar medium in large complexes known as molecular clouds. Within these clouds new stars form out of the collapse of so-called cloud cores which are very cold (10 - 20 K) and consist of high density gas and dust (10^5 - 10^6 cm^{-3}). Many stars and their possibly associated planetary systems can form from a single cloud core by fragmentation. Though many - possibly most - stars evolve in cluster environments and/or are members of binary or multiple systems, we will describe here, for the sake of simplicity, how isolated low-mass stars are believed to form. The general principle of this process is mainly also true for more complex environments but feedback processes and stellar interactions do certainly alter and influence the individual stages. It should also be mentioned that the term "low-mass objects" includes objects with masses ranging from roughly 0.1 $M_\odot$ - 2.0 $M_\odot$. It seems, however, that at least also for intermediate mass objects (2.0 $M_\odot$ - 8.0 $M_\odot$), the so-called Herbig Ae/Be stars (HAeBes; Herbig, 1960), and for Brown Dwarfs with masses below the hydrogen burning limit, the formation process is quite similar (e.g., van Boekel et al., 2006; Luhman et al., 2007b). For the most

massive stars the formation process is still heavily debated in the literature (e.g., Beuther et al., 2007), but most recent results support the idea that, indeed, circumstellar disks as described below, play a key role also in the high-mass regime (Cesaroni et al., 2007).

The process of low-mass star formation can schematically be divided into four phases, covering the evolution from a collapsing cloud to a fully grown star, possibly with a developed planetary system. These phases can observationally be distinguished by their spectral energy distribution (SED), and sources in the respective phases are identified as Class 0 through III in the Lada and Andre classification scheme (Lada & Wilking, 1984; Adams et al., 1987; Andre et al., 1993). In Figure 1.1 we show sketches of sources in each of the four phases, and the corresponding SEDs. In the first phase (observationally Class 0), the density at the core of a collapsing molecular cloud fragment increases rapidly as material falls in more or less spherically. Due to rotation and conservation of angular momentum, a flattened structure builds up around the forming star, which will become the circumstellar disk as it flattens further. The central object itself is in this phase called a proto-star and derives its luminosity largely from accretion shocks. This object is not yet burning hydrogen in its center. Class 0 sources can be observed at far-infrared and millimeter wavelengths only as they are too deeply embedded in material for photons of shorter wavelengths to escape. In the second phase (Class I), the central object has become much more compact and the angular momentum of the cloud material inhibits further spherical infall. Accretion onto the forming star proceeds through the disk while the outer disk regions are continuously supplied with fresh material from the surrounding envelope. Typically, as these sources are still surrounded by a dusty envelope they show a deep absorption band at a wavelength of 10μm caused by silicate dust particles. In the direction perpendicular to the disk, part of the accreting material ($\sim$10 - 30 %) may be ejected from the system in a bipolar outflow (Konigl & Pudritz, 2000; Tomisaka, 1998; Shu et al., 1999). Class I sources are very bright in the infrared, and the main energy source for this radiation is the release of gravitational energy by accreting material in the disk. Hence, such accreting disks are called active disks. The third phase (Class II) begins when the supply of fresh material in the outer regions of the disk comes to a halt. The forming star has essentially reached its final mass, but will yet become significantly smaller and hotter while it derives its luminosity from Kelvin-Helmholtz contraction. The regions above and below the disk do no longer contain much obscuring dust, and the star is optically visible. The disk is still very bright and dominates the SED at infrared and millimeter wavelengths. However, in this phase the main energy source in the disk is absorption of stellar radiation and the disk is said to be passive. The disk of Class II objects is still massive (typically up to a few percent of the mass of the central object) but will disperse on a time scale of several million years. It is during this phase that planets are believed to form out of the disk material. One diagnostics to test how the dust within the disks evolves is to analyze the above-mentioned 10μm silicate feature. Seen in absorption in still more deeply embedded objects, the feature is now seen mostly in emission as the upper layers of the disk are heated by the radiation of the central source. The shape and strength of the silicate emission can now be used to analyze the dust composition providing evidence for grain growth and chemical processing of the dust in some objects compared to others. Low-mass stars in this stage are normally referred to as Classical TTauri Stars (CTTS). There is some evidence that sometime between the typical Class I and II period there might be the so-called ”FU-Orionis phase” of young low-mass stars. This phenomenon is named after the prototype object FU Orionis and is introduced in

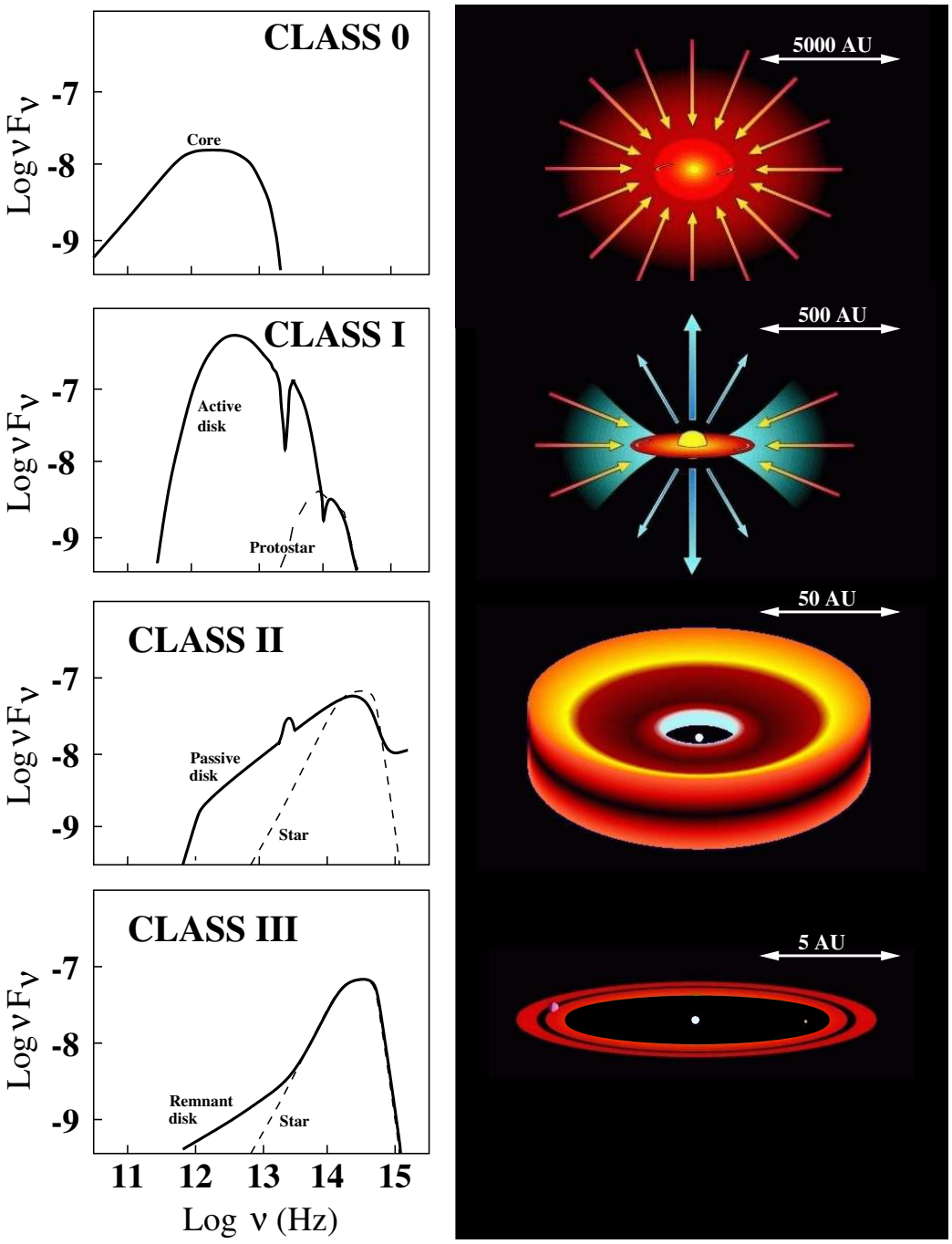

Figure 1.1 Highly simplified sketch showing the typical evolutionary stages of a young low-mass stars. (Original figures by Antonella Natta, Mark McCaughrean, Carsten Dominik, and Vincent Icke.)

more detail in the following section. In the fourth and final phase (Class III) there is only a gas-poor remnant disk left. Accretion of material onto the central object is very limited as most matter was already accreted, has been dispersed by stellar radiation pressure or was used for building up (gaseous) planets. As no longer strong accretion signatures are observable these objects are called Weak-line TTauri Stars (WTTS). Still, terrestrial plan-

ets may continue to assemble through the merging of larger bodies, so-called planetesimals, made of refractory material. Later on, it is also possible that the disk is replenished with smaller dust particles via the destructive collision of larger bodies. Those disks are then called Debris Disks. The SEDs of Class III objects show only at longer infrared wavelengths signs of remaining dusty material. The optical and near-infrared emission is mostly photospheric.

1.2 The FU Orionis phenomenon

As in some of the following chapters the focus will be on so-called FU Orionis objects it seems worthwhile to provide a short introduction to this group of objects and give an up-to-date overview. Named after the prototype object FU Orionis, this small, but quite remarkable class of low-mass Young Stellar Objects (YSOs) is normally referred to as FU Ori objects (FUors). For the first members of this class an outburst in optical light of up to 4-6 magnitudes over short time scales (months to years), followed by a decrease in luminosity over several years or decades, was observed (Herbig, 1977). Other objects were included in the class as they shared common specific spectroscopic features, e.g., double-peaked line profiles, a spectral type varying with wavelength and often CO bandhead absorption features in the near-infrared. Since for one object (V1057 Cyg) the pre-outburst spectrum is known resembling that of a classical TTauri star (Welin, 1976), it is commonly assumed that FUors should be low-mass YSOs. Most observational data can be explained by the presence of an accretion disk surrounding the young stars (Figure 1.2)[1]. A dramatic temporal increase in the accretion rate (of up to 10^{-5} - $10^{-4}\mathrm{M}_{\odot}/\mathrm{yr}$), where the disk outshines the star by several orders of magnitude, can account for the observed outbursts in luminosity. Several scenarios, possibly triggering such an increased accretion rate, have thus far been proposed and are summarized below. Apart from revealing the mechanisms leading to the observed outbursts, it is important to investigate whether all TTauri stars undergo such epochs of enhanced accretion or whether FUors are a special class of YSOs. Most observations of classical TTauri stars show that the derived accretion rates of 10^{-10} - $10^{-7}\mathrm{M}_{\odot}/\mathrm{yr}$ (e.g., Gullbring et al., 1998) are not sufficient to build up a low-mass star over time scales of a few Myr. Even if a significant fraction of the matter is accreted in the very early phases of a YSO, FUor-phases might provide an elegant solution to speed up the accretion process. In terms of the evolutionary state of FUors, it is commonly assumed that they are younger than classical TTauri stars. In the above-mentioned classification scheme they should be placed somewhere between Class I and Class II. Support for this assumption comes from observations showing remnant dusty envelopes around some objects (see Figure 1.2). Others are even more deeply embedded sources hardly detectable at optical wavelengths. Based on the estimated star formation rate in the solar neighborhood and on the outburst statistics of known FUors in the last 60 years, it seems possible that all young low-mass stars undergo even *several* outbursts before entering the more quiescent TTauri phase (Figure 1.3). For a detailed overview concerning the FU Ori phenomenon the reader is referred to Hartmann & Kenyon (1996).

[1]Herbig et al. (2003) found that some spectral properties are well explained in the context of rapidly rotating late-type stars with strong stellar winds. However, most recent observational results, partly presented in this thesis, clearly support the accretion disk model.

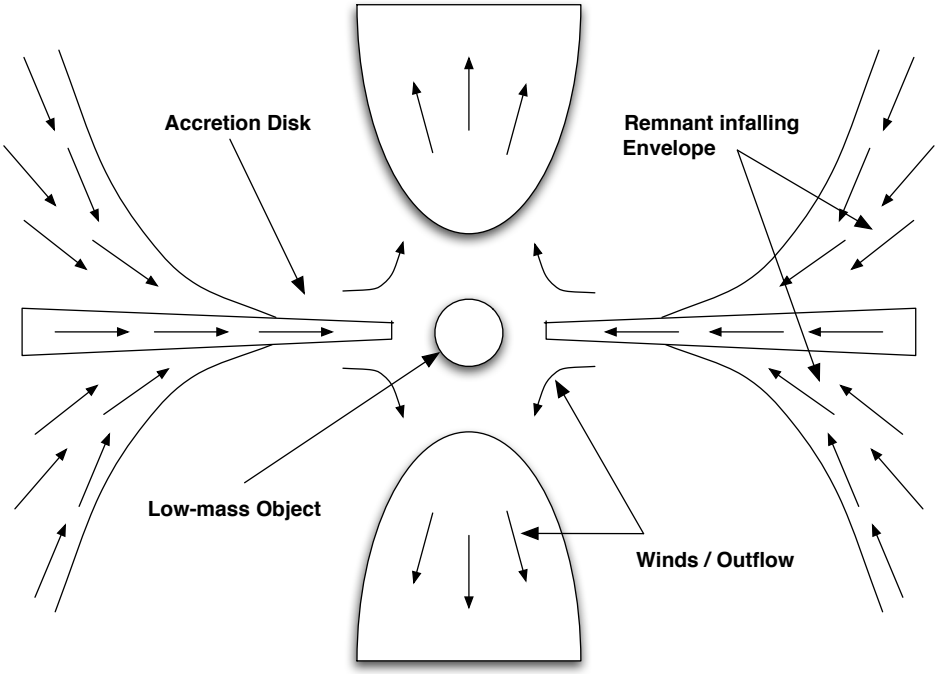

Figure 1.2 Schematic picture of FU Ori objects. The outburst is caused by an increase of the disk accretion rate from 10^{-10} - $10^{-7}\mathrm{M}_{\odot}/\mathrm{yr}$ of up to 10^{-5} - $10^{-4}\mathrm{M}_{\odot}/\mathrm{yr}$. Taking into account the typical duration of a single outburst event of roughly 100 years, $10^{-2}\mathrm{M}_{\odot}$ might be added to the central object during this period. Mass is fed continuously to the disk via a remnant dust envelope providing an elegant explanation for a possible outburst mechanism (see following sections) and enabling re-occurring outbursts. Roughly 10 - 30 % of the accreted material should be ejected from the disk via strong disk winds. However, as summarized in Table 1.1, not all FUors show signs of winds and/or molecular outflows. Picture adapted from Hartmann & Kenyon (1996).

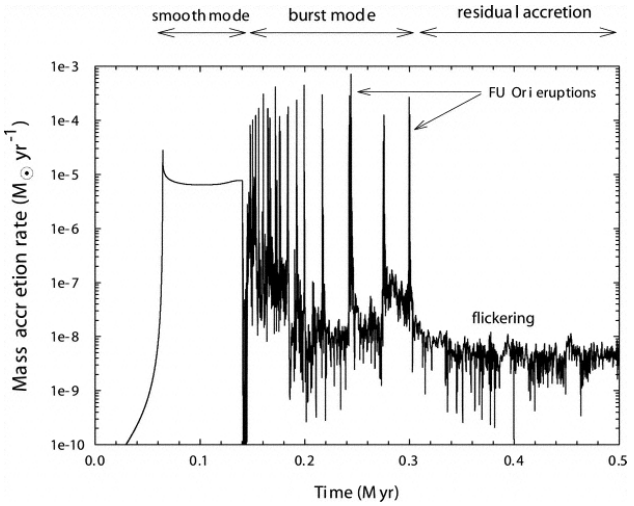

Figure 1.3 Simulations showing the evolution of the accretion rate of a young low-mass object over time (Vorobyov & Basu, 2006). Before the star enters the CTTS-phase with rather low accretion rates several FUor-outbursts can occur.

1.2.1 Basic observational properties

As already mentioned the first FUors were originally identified by their outbursts in optical light (Herbig, 1966, 1977; Kolotilov & Petrov, 1983, 1985). The optical light curves of three of the best studied objects, FU Ori, V1515 Cyg, and V1057 Cyg, showed an increase in brightness of 4 magnitudes or more. While FU Ori and V1057 Cyg exhibit short rise times to maximum light (less than one year) V1515 Cyg took more than a decade to reach maximum brightness. Also, the decay time scales vary significantly: FU Ori will probably need more than 100 years to reach its pre-outburst luminosity while V1057 Cyg shows a ten times more rapid fading curve. This already shows that it is difficult to assign clear-cut properties to this group of young objects. The situation became even worse in recent years when objects were included to the FUor group without having shown any outburst but sharing only spectroscopic properties with the initial group members. In the following some of the most important observational properties of FUors are summarized (partly taken from Hartmann & Kenyon, 1996). Once again it should be stressed that not all FUors show *all* of these features, and for some objects not all properties were observationally tested. However, typically the following features characterize a FUor:

- An outburst in optical and/or near-infrared wavelengths of several magnitudes over short time scales (months to several years) followed by a longer fading phase (several decades) possibly to pre-outburst luminosity.
- NIR spectra showing strong CO band head absorption features at 2.3 μm indicative of very high temperatures related to high accretion rates (Calvet et al., 1991).
- An SED showing large IR emission excesses with the object being sometimes heavily extincted. This suggests the presence of a surrounding circumstellar envelope of dusty material.
- Water vapor bands, characteristic of K-M giant/supergiant atmospheres (effective temperatures $\sim$3000 K), in the 1-2 μm and 5-8 μm region.
- Contrary to the NIR spectra, optical spectra indicating spectral types of late F to G (effective temperatures $\sim$7000-6000 K) including lower surface gravities than classical TTauri stars.
- Broad and strongly blue shifted absorption lines typically observed in the Balmer lines, especially in Hα. The emission component in the P Cygni Hα profile is often completely missing.
- At high spectral resolution FUors appear to be rapidly rotating showing double-peaked absorption line profiles. However, there is evidence for differential rotation, with the velocity widths being smaller for lines in the IR than for optical lines. This strongly supports the accretion disk model where these features are produced by the rotation of the disk.
- Unlike classical TTauri stars, there is no evidence of hot excess continuum in the near UV in the spectra of some FUors. Possibly, the commonly assumed magnetospheric accretion columns of TTauri stars, where at their base the nearly free-falling gas collides with the stellar surface creating the hot UV emission, do not exist for FUors. The dynamic pressure of the accretion disk might be sufficient to crush

the stellar magnetic fields back up against the outer stellar layers (Shu et al., 1994; Hartmann & Kenyon, 1996).

- FUors are clearly young systems, showing strong Li I absorption at 0.67 μm.
- In the direct surroundings often reflection nebulae are present (see, e.g., Goodrich, 1987).

Many of these peculiar features, differentiating FUors from other YSOs, can directly be explained by the presence of a heavily accreting circumstellar disk surrounding the young star, e.g., the IR excess emission, the changing spectral type with wavelength, the rotation signatures and double-peaked line profiles. Due to the high accretion rates the disk can possibly dominate the observed emission at *all* wavelengths. Finally, an accretion disk can also explain the heavy outbursts in luminosity as will be discussed in the next section.

1.2.2 Outburst mechanisms

Different ideas have been put forward to explain the outburst in optical and NIR emission of FUors. All ideas identify a mechanism helping to increase the accretion rate of the circumstellar disk. The most common explanations include (a) interactions of binary or multiple systems where tidal forces disturb the circumstellar disk (Bonnell & Bastien, 1992; Clarke & Syer, 1996; Reipurth & Aspin, 2004), (b) planet-disk interactions, where thermal instabilities in the disk are caused by the presence of a massive planet (Lodato & Clarke, 2004), (c) thermal instabilities in the disk alone (Bell & Lin, 1994; Bell et al., 1995) or (d), more recently, gravitational instabilities (Vorobyov & Basu, 2006; Boley et al., 2006). Although some FUors appear to be in binary or even multiple systems (e.g., FU Ori, Z CMa, L1551 IRS 5; AR 6A+B and RNO1B+C are even FUor-binaries) it is not yet clear whether the observed separations are small enough to account for an outburst caused by the objects' interaction. Also, not all FUors seem to have a close companion (e.g., V1057 Cyg, Herbig et al., 2003). In addition, the model requiring a massive planet orbiting within the accretion disk seems also questionable from an evolutionary point of view: If FUors are indeed very young objects then there might not yet have been enough time for one a more planets to form. Thus, possible outburst mechanisms are still debated and it is not clear whether there is only one mechanism responsible for the observed outbursts. It might well be that for different objects different trigger events caused the observed increase in luminosity.

1.2.3 The current sample of FUors and FUor candidates

As mentioned above it is not directly evident how many FUors have been found as some objects show some typical properties of FUors but lack the observational evidence of other characteristics. Especially the comparatively short outburst time limits the probability to observe an object during its phase of increasing luminosity. Despite these problems, Table 1.1 lists the current sample of objects that are either observationally well constrained FUors or at least FUor candidates. In addition, an overview concerning the observational evidences for the FUor status of each object is provided and a reference for the discovery of the object is given.

Object Name	RA (J2000)	DEC (J2000)	Distance[a] [pc]	Outburst[a]	CO band head absorption	Binary / Multiple	Outflow / Jet / HH	Ref.
RNO 1B	00h36m46.3s	63d28′54.1″	850	1978?	yes	yes	?	(12)
RNO 1C	00h36m46.9s	63d28′58.6″	850	?	yes	yes	?	(13)
PP 13S*	04h10m40.8s	38d07′55.0″	300	<1900	yes	?	yes	(5)
L1551 IRS 5	04h31m34.1s	18d08′04.9″	140	?	yes	yes	yes	(4)
LDN 1415 IRS	04h41m36.2s	54d19′24.1″	170	1996-2006	?	no	yes	(17)
V883 Ori	05h38m18.1s	-07d02′26.0″	460	?	yes	no	no	(7)
Reipurth 50	05h40m27.7s	-07d27′28.0″	460	1960-1970	flat	no	yes	(7)
FU Ori	05h45m22.4s	09d04′12.3″	450	1937	yes	yes	no	(3)
V1647 Ori	05h46m13.1s	-00d06′04.8″	400	2004	emission	?	yes?	(16),(21)
CB 34 V (V1184 Tau)	05h47m03.8s	21d00′36.0″	1500	<1994	?	?	?	(2)
AR 6A	06h40m59.3s	09d35′52.0″	800	?	yes	yes	?	(14)
AR 6B	06h40m59.3s	09d35′49.2″	800	?	yes	yes	?	(14)
Z CMa	07h03m43.2s	-11d33′06.2″	930-1150	?	yes	yes	yes	(11)
BBW 76	07h50m35.4s	-33d06′24.8″	1700	<1930	yes	no	no	(1),(20)
V346 Nor	16h32m32.1s	-44d55′31.5″	700	∼1984	yes	no	yes	(10)
OO Ser	18h29m49.1s	01d16′19.0″	311	1994-1995	?	?	?	(15)
HBC 687 (Parsamian 21)	19h29m00.7s	09d38′39.0″	400-1800	?	?	?	yes	(6)
V1515 Cyg	20h23m48.0s	42d12′25.9″	1000-1050	1950s	yes	no	yes	(3)
V1057 Cyg	20h58m53.7s	44d15′28.5″	600-700	1970	yes	no	yes	(3)
Braid nebula	21h00m25.2s	52d30′15.5″	800	1999	yes	?	yes	(19)
V1331 Cyg	21h01m09.2s	50d21′44.7″	550-700	?	emission	no	yes	(8)
V1735 Cyg	21h47m20.7s	47d32′03.7″	900	1952-1965	yes	no	yes	(9)
V733 Cep	22h53m33.3s	62d32′23.1″	800	1953-1984	yes	?	yes	(18)

Table 1.1 Current list of FUors and FUor candidates. The '?'-symbol denotes lacking observations. [a]References for these values are partly given in Ábrahám et al. (2004). (1)Eisloeffel et al. (1990), (2)Yun et al. (1997), (3)Herbig (1977), (4)Carr et al. (1987), (5)Sandell & Aspin (1998), (6)Staude & Neckel (1992), (7)Strom & Strom (1993), (8)Welin (1976), (9)Elias (1978), (10)Graham & Frogel (1985), (11)Hartmann et al. (1989), (12)Staude & Neckel (1991), (13)Kenyon et al. (1993), (14)Aspin & Reipurth (2003), (15)Hodapp et al. (1996), (16)sub-millimeter source detected by Mitchell et al. (2001), (17)Stecklum et al. (2007), (18)Reipurth et al. (2007), (19)Movsessian et al. (2006), (20)Reipurth (1985), (21)outburst history summarized by Briceño et al. (2004)

1.3 Outline of this thesis

After this short introduction it is time to go *in medias res*. In the following chapters, astronomical observations of young low-mass objects are discussed and interpreted. Special emphasis is put on the dust and ice components of the circumstellar material contained in disks and envelopes. In a broader context, these components will eventually form rocky planets or the cores of gaseous planets. In this respect, these observations investigate not only the initial conditions and early phases of star formation, but tell us also something about the physical environment in which planets are about to form.

As already mentioned above, in several chapters of this thesis FU Orionis objects will play an important role. In chapter 2 and 3 two individual young objects (V1331 Cyg and FU Ori) are discussed in this context in detail. While chapter 2 is based on optical imaging data helping to constrain and analyze the general dust morphology and origin of the young star, chapter 3 deals with high-resolution interferometric observations in the mid-infrared enabling us to resolve the active accretion disk around FU Ori. An analytical disk model is used to explain the presented observations and for the first time a possible dust composition for the disk is derived. In chapter 4 mid-infrared imaging and spectroscopic observations of the RNO 1 region are presented. It shows that the two known FUors in this region are possibly members of a small young cluster. One source, a suspected but yet undetected deeply embedded YSO, is imaged for the first time and shown to be responsible for a large scale outflow in this region. The first systematic and comprehensive study of the spectral properties of FUors in the mid-infrared is presented in chapter 5. Two distinct groups of objects are defined, and the dust and ice composition of the circumstellar disks and envelopes are analyzed. The results strongly support the idea that the FUor-phase is the link between the Class I and Class II sources. In chapter 6 the results from a near-infrared imaging survey for new young objects in the Taurus star forming region are presented. Among other results, new candidates for young low-mass stars and Brown Dwarfs surrounded by circumstellar disks are presented and discussed. Some of these objects are excellent candidates for being among the least massive free-floating objects known today. Finally, chapter 7 summarizes the most important findings and provides an outlook for on-going and possible future studies in the context of this thesis.

2. Dust rings and filaments around V1331 Cygni

The dusty environment of an isolated young star

Parts of this chapter were published in the Astrophysical Journal.
(Quanz, S. P., Henning, Th., Apai, D., 2007, ApJ 656, 287)

IN THIS CHAPTER we characterize the small- and large-scale environment of the young star V1331 Cygni with high-resolution HUBBLE SPACE TELESCOPE/WFPC2 and Digitized Sky Survey images. In addition to a previously known outer dust ring ($\approx 30''$ in diameter), the HST/WFPC2 scattered light image reveals an inner dust ring for the first time. This ring has a maximum radius of $\approx 6.5''$ and is possibly related to a molecular envelope. Large-scale optical images show that V1331 Cyg is located at the tip of a long dust filament linking it to the dark cloud LDN 981. We discuss the origin of the observed dust morphology and analyze the object's relation to its parent dark cloud LDN 981. Finally, based on recent results from the literature, we investigate the properties of V1331 Cyg and conclude that in its current state the object does not show sufficient evidence to be characterized as an FU Ori object.

2.1 Introduction

As briefly described in the first chapter, stars form from collapsing molecular cloud cores. Different mechanisms can trigger this process: turbulence may lead to overdensities in molecular cloud cores, or external triggers, such as supernovae shock waves or nearby violent stellar winds, may initiate the collapse of such cores. After the initial collapse and the formation of a central object, low- and intermediate-mass stars (several tenths to a few solar masses) continue to accrete matter via a circumstellar disk. The disk is replenished with matter from a remaining envelope in the early stages. This phase might coincide with the FUor phenomenon observed for a small group of young, low-mass objects (see chapter 1 and Hartmann & Kenyon, 1996, for a review.).

In this chapter we focus on the young star V1331 Cyg. Due to the similarity of its spectrum to that of the well-known FUor V1057 Cyg prior to its outburst, V1331 Cyg was classified as a pre-outburst FUor candidate by Welin (1976) and also Herbig (1989). Further support for this classification came from the ring-like reflection nebula surrounding V1331 Cyg (Kuhi, 1964) that appeared very similar to those found around other FUors

(Goodrich, 1987). Due to a lack of photospheric absorption lines the spectral type of V1331 Cyg was mostly derived from photometric measurements and covers a range from G0 (Kolotilov & Petrov, 1983), through F0-F2 (Mundt et al., 1981) and F0-A8 (Chavarria, 1981) to B0.5 (Cohen & Kuhi, 1979). Also the distance towards V1331 Cyg is uncertain and literature estimates range from 694 pc (Chavarria, 1981) to 550 pc (Shevchenko et al., 1991). We adopt the conservative distance of 550 pc which is in agreement with most recent publications (e.g., McMuldroch et al., 1993; Mundt & Eislöffel, 1998; Henning et al., 1998). Strong P Cygni absorption in many of its lines suggested the presence of circumstellar matter surrounding the object (Chavarria, 1981; Mundt, 1984). A compact circumstellar disk was suggested by Weintraub et al. (1991) based on submillimeter continuum observations. McMuldroch et al. (1993) found additional evidence for the existence of a massive 0.5 $M_{\odot}$ disk surrounded by a flattened gaseous envelope from CO synthesis maps. Furthermore, these authors identified a bipolar outflow and a radially expanding gaseous ring containing more than 0.07 $M_{\odot}$. They suggested that this ring was a swept-up gaseous torus from an energetic mass ejection stage that was probably linked to one or several FUor outburst(s) $\sim 4 \times 10^3$ years ago.

In the following we present and discuss high-resolution images of the dusty circumstellar environment of V1331 Cyg. The possible origin of the observed dust structure, the object's relation to its parent molecular cloud and possible external triggers for the star formation process are discussed. We also investigate the FUor-like nature of V1331 Cyg.

2.2 Data reduction

V1331 Cyg (RA: $21^h01^m09.21^s$, DEC: +50° 21′ 44.8″, J2000) was observed with WFPC2 onboard the HST in August 2000. Two exposures with 230 seconds each were taken in the F606W filter with the WF3 camera. We performed simple image processing and cosmic ray removal. The center of the star was saturated leading to overflowing columns along the y-axis of the detector (roughly NNE to SSW in Fig. 2.1). A simulated WFPC2 Point Spread Function (PSF) was created using the TinyTim software package (Krist, 1993, version 6.3)[1]. This PSF was subtracted from the original image in order to reveal faint circumstellar structures. The accurate scaling of the reference PSF was not straightforward due to the saturation of the original image. We minimized the residuals in the center of the star and along the diffraction spikes, which simultaneously allowed an accurate positioning of the PSF. For analyzing the large scale environment we additionally downloaded Digitized Sky Survey 2 (DSS2) data from the ESO Online Digitized Sky Survey homepage[2].

2.3 Results

2.3.1 Small-scale morphology (HST/WFPC2)

Fig. 2.1 shows the resulting image for the F606W exposures with the PSF being subtracted. The high resolution of the WF3 camera ($1.22\,\lambda/D \approx 0.064''$ with a pixel scale of $\sim 0.1''$/pixel) reveals the structure of the dusty circumstellar environment in great detail:

[1] http://www.stsci.edu/software/tinytim/

[2] http://archive.eso.org/dss/dss

In addition to the large dust ring already mentioned by Kuhi (1964) we find for the first time direct evidence for an additional ring-like dust structure close to the central star. In the following we refer to the former ring as the ”outer ring”, call the latter one ”inner ring” and refer to a faint arc in the south-west (roughly 23″ from the central star) as the ”SW-Arc”.

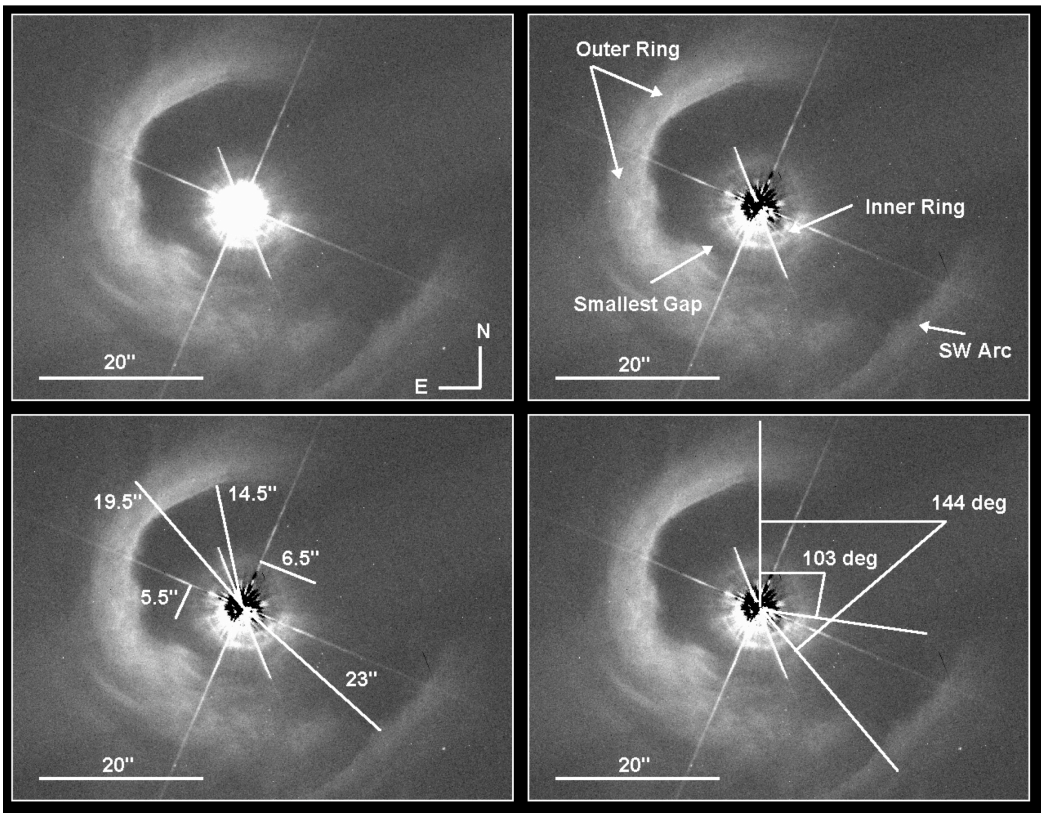

Figure 2.1 Cleaned original image (upper left) and PSF-subtracted image (upper right) of V1331 Cyg in the WFPC2 F606W filter. The dusty environment is resolved and the outer and inner dust ring are clearly visible. Selected radii of the dust rings and opening angles for the dust free regions are shown in the lower left and lower right panel, respectively. North is up, and east is to the left in all images.

For the outer ring we computed a mean surface brightness of 21.12 mag/arcsec^2 in the Vega magnitude system (Gonzaga, 2002). The inner edge of its north-eastern part is well-defined, while it becomes more fuzzy as the ring continues southwards (Fig. 2.1). In the north-east the distance between the inner edge of the outer dust ring and the central star is $\approx 14.5''$, while the outer radius of the ring is $\approx 19.5''$. From north-west to south-west the outer ring is intersected over an angular range of $\approx 144^\circ$ (not taking into account the SW-Arc) and no scattered light is visible.

The newly resolved inner ring is separated from the outer ring by a well-defined gap with a smallest projected distance of $\approx 2.6''$ south-east of the central object. The inner dust ring extends almost exactly half a circle around V1331 Cyg from the north-east to the south-west and scattered light can be traced very close to the center. The inner ring is mostly visible in regions where the inner edge of the outer ring appears rather fuzzy. The outer radius of the inner ring is $\approx 5.5''$ measured along the diffraction spike in south-east

direction and $\approx 6.5''$ measured along the diffraction spike in south-west direction (lower left panel of Fig. 2.1).

Assuming a distance of 550 pc the radius of the inner dust ring corresponds to $\approx$ 3,000 AU and $\approx$ 3,600 AU in the south-east and south-west direction, respectively, the inner radius of the outer dust ring is roughly 8,000 AU, and the distance between the central object and the faint SW-Arc is $\approx$ 13,000 AU.

2.3.2 Large-scale morphology (DSS)

Fig. 2.2 shows an R-band image from the DSS2 data archive. The image is $40' \times 40'$ in size and centered on V1331 Cyg. The object is located at the eastern tip of a $\approx 8'$ long dark filament (F1 in Fig. 2.2). The filament links V1331 Cyg to the dark cloud Lynds 981 (LDN 981, RA: $20^h00^m15^s$, DEC: +50° 17.3′, J2000; Lynds, 1962). The cloud consists of a roughly elliptical core with five elongated dark filaments stretching radially outwards to which in the following we refer to as F1-F5. The semi-major and semi-minor axes of the core are $\approx 240''$ and $\approx 160''$, respectively. The lengths and widths of the filaments are summarized in Table 2.1. The outer dust ring of V1331 Cyg is clearly visible in the DSS2 image and the dark filament F1 seems to intersect the outer dust ring in the north-west. Furthermore, a fainter filament (F1s) seems to run southwards from the object.

Filament	Length	Width
LDN 981-F1	$\sim 490''$ (1.31 pc)	$\sim 40''$ (0.11 pc)
LDN 981-F2	$\sim 180''$ (0.48 pc)	$\sim 72''$ (0.19 pc)
LDN 981-F3	$\sim 110''$ (0.29 pc)	$\sim 63''$ (0.17 pc)
LDN 981-F4	$\sim 220''$ (0.53 pc)	$\sim 63''$ (0.17 pc)
LDN 981-F5	$\sim 220''$ (0.53 pc)	$\sim 90''$ (0.24 pc)

Table 2.1 Apparent and physical sizes of the five filaments related to LDN 981 shown in Fig. 2.2. The size of the roughly elliptical core of the dark cloud is $\sim 240''$ (0.64 pc) along the semimajor axis and $\sim 160''$ (0.43 pc) along the semiminor axis. We assume a distance of 550 pc.

2.4 Discussion

2.4.1 Possible origin for the dust rings

The direct vicinity of V1331 Cyg is certainly shaped by the star and hence provides information on recent stellar activity. The observed morphology is defined by a prominent, symmetrical pair of rings seen in scattered light. To explain the apparent morphology of the previously known outer dust ring it was suggested that we are looking into a cone-shaped wind-blown cavity with its axis parallel to the star's (and disk's) rotation axis (Mundt & Eislöffel, 1998). The unresolved circumstellar disk should thus have an almost pole-on orientation. This picture is supported by the observations of a bipolar molecular outflow whose relative strength implies that V1331 Cyg is viewed nearly pole-on (McMuldroch et al., 1993). Furthermore, from observed P-Cygni profiles in Hα and Na I

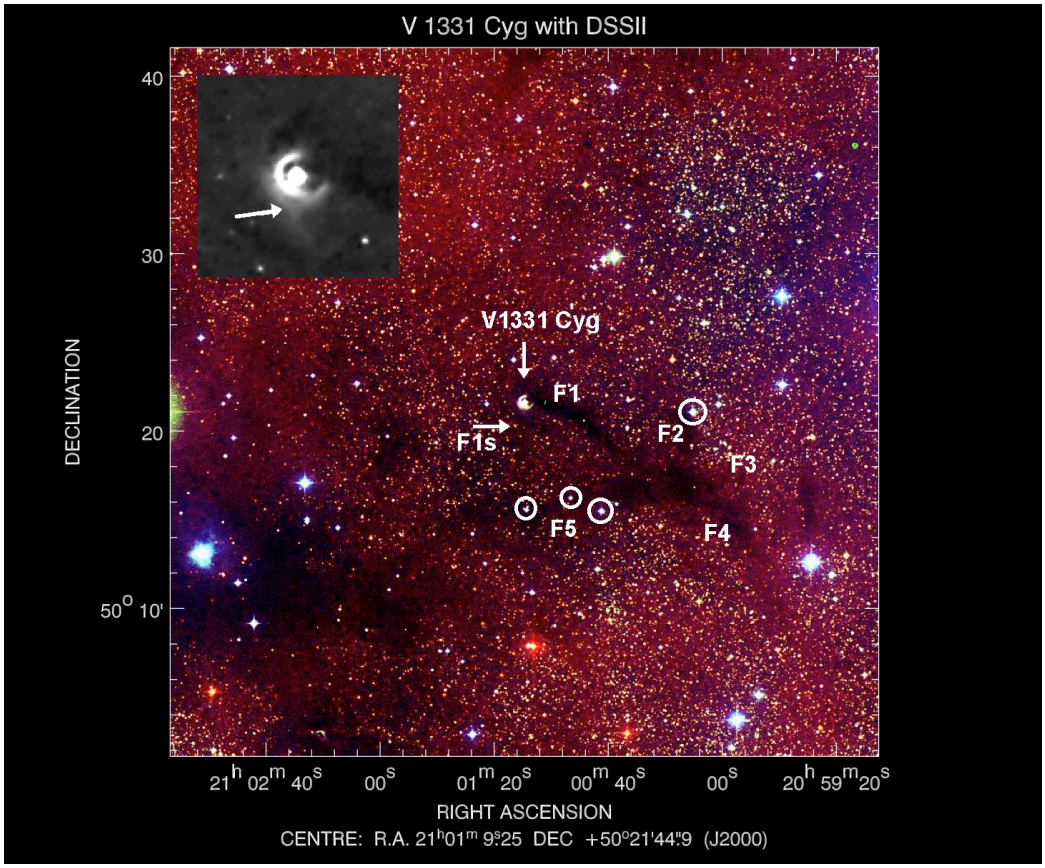

Figure 2.2 True color image 40'x40' in size from the three DSS2 filters. V1331 Cyg is located in the center of the image. The bright outer ring of V1331 Cyg is clearly visible and also its apparent connection to a dark filament (F1) stretching in and intersecting the dust ring in the north west. This filament is part of the "hand-like" dark cloud LDN 981 which has its center south west of V1331 Cyg. Also visible is an additional fainter and more wiggled filament stretching southwards from V1331 Cyg. A weak signal of scattered light (indicated by the arrow) can be seen along the edge of this filament in the close-up inset image taken with the blue filter of DSS2. Finally, we indicated some stars from the Hα survey by Feigelson & Kriss (1983). These objects were not classified as pre-main-sequence stars, although their position relative to LDN 981 might suggest that they recently evolved from the filaments.

Mundt (1984) and Mundt & Eislöffel (1998) derived corresponding wind velocities that showed that the outflow is oriented relatively close to the line of sight.

The existence of strong winds creating the observed cavity was also proposed to explain an expanding torus of molecular gas (McMuldroch et al., 1993). This torus lies outside the outer dust ring following its outer edge closely from the north-east to the south-west. McMuldroch et al. (1993) computed a momentum between $1.5\,M_{\odot}kms^{-1}$ and $11.9\,M_{\odot}kms^{-1}$ for the gas torus and concluded that the current mass loss rate of $10^{-6}\,M_{\odot}yr^{-1}$ and wind velocities ($\approx 370\,kms^{-1}$) (Mundt, 1984) are not sufficient to sweep up the torus within its assumed lifetime of $\sim 4 \times 10^3$ yr. They speculate that the torus was created in a more vigorous stage of V1331 Cyg, possibly during an FUor event. Since such an outburst is attributed to an increase in the mass accretion rate of the circum-

stellar disk which in turn leads to an increase of the system's mass loss rate (e.g., due to disk winds[3]) such an event might explain the ejection of the torus and the creation of the well-shaped wind-blown cavity we observe in our scattered light image today.

For the inner dust ring we believe that the scattered light HST image reveals the dusty counterpart to a molecular structure surrounding the inner star-disk system. The dimensions of the newly discovered inner ring are very similar to those of a flattened CO envelope found by McMuldroch et al. (1993). The assumed circumstellar disk seems to be more compact (source size less than 2000 AU) as it was unresolved in 1.3 mm dust continuum observations (McMuldroch et al., 1993; Henning et al., 1998). Fig. 2.3 shows a simplified sketch of the circumstellar environment of V1331 Cyg being in agreement with most observational data.

2.4.2 V1331 Cyg and LDN 981

Fig. 2.2 shows that the dark filament LDN 981-F1 is responsible for the observed break in the outer dust ring. Either the dust filament lies in the foreground and by chance in the line-of-sight toward V1331 Cyg, or V1331 Cyg itself recently emerged from the filament.

The most direct evidence for the filament being directly associated with V1331 Cyg is the fact that V1331 Cyg illuminates part of the filament running southwards (see, Figure 2.2 inset). The direct association is further supported by the identical line-of-sight velocity of the LDN complex and the envelope of V1331 Cyg: Park et al. (2004) measured the ^{13}CO velocity component of LDN 981-1 and LDN 981-2 (RA: $21^h00^m13.2^s$, DEC:

[3]Typical values are $\dot{\mathrm{M}}_{\mathrm{wind}}/\dot{\mathrm{M}}_{\mathrm{acc}} = 0.1$ (e.g., Konigl & Pudritz, 2000)

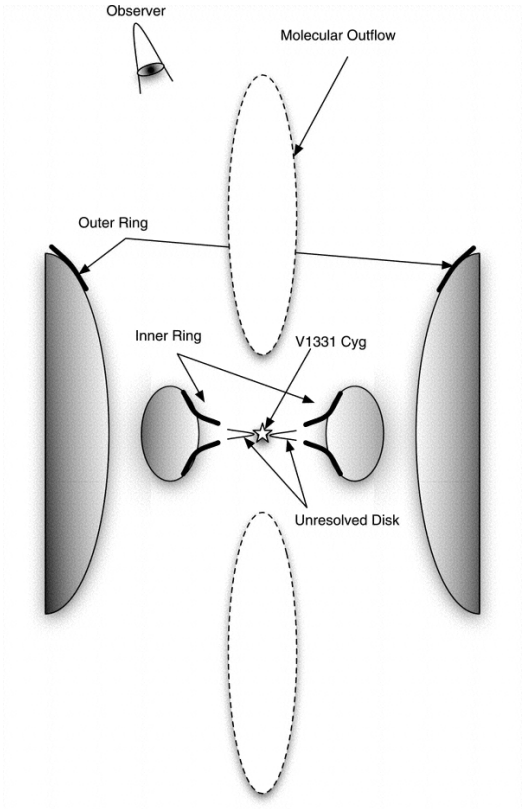

Figure 2.3 Simplified sketch of the immediate surroundings of V1331 Cyg explaining the observed ring-like structures.

+50° 20′ 06.0″ and RA: $21^h00^m15.0^s$, DEC: +50° 16′ 56.0″, J2000) to be v_{LSR} = 0.1 kms^{-1} and v_{LSR} =0.5 kms^{-1} with Δv = 1.12 kms^{-1} and Δ v = 1.73 kms^{-1}, respectively. Levreault (1988b) derived a CO velocity in the direction of V1331 Cyg of v_{LSR} = -0.7 kms^{-1}. Based on these observations V1331 Cyg has to lie close to the edge of the two filaments (F1 and F1s), most likely at their intersection. If so, V1331 Cyg has probably evolved from the filaments and is in the process of dispersing the filaments through its winds.

2.4.3 Isolated or triggered star formation?

Although V1331 Cyg is well established as a young star and the relation to LDN 981 is convincing it seems as if no additional star formation is going on within LDN 981 (Alves et al., 1998). In an earlier Hα survey Feigelson & Kriss (1983) found no evidence for additional pre-main-sequence stars in an area of 20′×20′ ($\approx$ 3.2×3.2 pc) centered on V1331 Cyg. In Fig. 2.2 we marked some objects from that survey that appear to be related to LDN 981. However, they did not show strong Hα emission and were thus not classified as pre-main-sequence stars. According to the VizieR database (Ochsenbein et al., 2000) these objects were also not detected in UV surveys and do not show a very prominent NIR-excess emission in the 2MASS database which would have been indicative of a young age.

Apart from having no additional young stars nearby, molecular line observations suggest that the parent cloud LDN 981 itself is stable and without on-going star formation, too: From CS(3-2) and DCO spectral line profiles Lee et al. (2004) found no evidence for infall signatures. However, as these authors pointed only towards the center of the filament LDN 981-F2 (see, Figure 2.2, RA: $21^h00^m13.1^s$, DEC: +50° 20′ 05.9″, J2000) with a beam of 43″ (FWHM) these results might not be applicable to the whole dark cloud (see also section 4.4).

The region closest to LDN 981, where evidence for recent star formation is found, is LDN 988. Recently, Herbig & Dahm (2006) analyzed the young stellar cluster associated with the Be star LkHα324 (RA: $21^h03^m54.2^s$, DEC: +50° 15′ 09″, J2000) for which they assume a distance of 600 pc and which lies east of V1331 Cyg at a projected distance of $\approx$ 30′ (4.8 pc). Although the stars do not form a group following a single well-defined pre-main-sequence model, theoretical isochrones suggest a median age of 0.8 Myr for the population.

It is worth to investigate, whether there is any evidence for a casual link between the star formation process in LDN 981 and LDN 988. Especially, since there is data suggesting that LDN 981 might be in a gravitationally stable configuration, it is not clear why and how V1331 Cyg should have formed at all. In this respect we identify and analyze three possibilities: (1) a propagating density wave triggered the star formation in LDN 988 and continued to travel in the direction of V1331 Cyg; (2) a nearby supernova (SN) explosion triggered simultaneously the formation of V1331 Cyg and the stellar cluster in LDN 988 via shock waves; and (3) a high proper motion early-type O- or B-star passed by and its winds initiated the star formation process. The possibility of spontaneous star formation in the filaments is discussed in section 4.4.

In the first case, assuming a local speed of sound of 0.3 kms^{-1} within the molecular cloud, any subsonic pressure wave would need at least 15 Myr to reach from LDN 988 to LDN 981, an order of magnitude longer than the estimated age of the cluster. Thus, shock waves would need to travel roughly two orders of magnitudes faster than the value above in order to create a casual link between the two regions and this seems highly unlikely.

To identify a possible SN explosion as an external star-formation trigger, we searched the available SN-remnant catalogs (e.g., catalog version 2001 of Green, 1996) in a radius of 3° around V1331 Cyg. We found only one candidate, G089.0+04.7 (HB21), with a projected distance of $\sim 2.58°$. However, Byun et al. (2006) estimated the distance of G089.0+04.7 to be 1.7 kpc and derived an age for the remnant of 1.5×10^4 yr scaled to this distance. This supernova remnant is hence too young and also too distant to have triggered the formation of V1331 Cyg.

Finally, we searched for early-type O- and B-stars in the vicinity of V1331 Cyg that could have triggered its formation via stellar winds. Based on the Hipparcos proper motion catalog (Perryman et al., 1997), we identified 6 objects within a radius of 3° with spectral types between B1 and B8. We plotted the projected trajectories, the six stars have travelled during the last 1 Myr, and found only one candidate (HIC 103530) that passed by V1331 Cyg as close as $\approx 0.4°$ (≈ 3.8 pc at the distance of V1331 Cyg). From the Hipparcos parallax (2.58 ± 0.65 mas) we derived a maximum distance to HIC 103530 of ≈ 518 pc which is at the lower limit of the distance estimates for V1331 Cyg. However, given the spectral type of HIC 103530 (B5Vn) and its minimum separation of 3.8 pc from its position relative to V1331 Cyg it seems unlikely that the star was triggering the formation of V1331 Cyg.

In summary, all observations suggest that V1331 Cyg formed in isolation.

2.4.4 Star formation in filaments

Large dust filaments are common structures in star-forming regions. Within these filaments sometimes denser fragments can be found possibly arising from collapsing globules that eventually will form new stars (see, e.g. Schneider & Elmegreen, 1979; Apai et al., 2005). Analyzing the spatial distribution of young stars in the Taurus molecular cloud Hartmann (2002) found that most of these young objects are aligned along three filaments following the distribution of denser gas and dust. The mean separation between the stars along the filaments was found to be about 0.25 pc, consistent with a roughly uniform density along the filaments. This value is well in agreement with the estimated Jeans length λ_J in the densest gaseous filaments[4] (Hartmann, 2002).

A direct comparison between these examples and the dark cloud LDN 981 is difficult as we lack appropriate data to determine whether we find any denser globules within the dark filaments. Furthermore, the spatial extension of the filaments, e.g., in Taurus, is much larger (partly more than 12 pc) and numerous stars have already formed. However, two important points can be noted: First, based on the estimates for the typical Jeans length λ_J in Taurus, one might expect additional stars to form also within the filaments of LDN 981. And second, while the three major filaments in Taurus lie more or less parallel to each other with young stars almost spaced equally along the filaments, LDN 981 shows filaments reaching radially outwards from an elliptical center with one young star at the tip of one filament. This difference in the morphological structure of the observed filaments might suggest a different origin for the filaments. Recently, Burkert & Hartmann (2004) presented 2D simulations of collapsing, self-gravitating gaseous "sheets" with different initial geometries. Collapsing elliptical sheets tend to produce filaments with major mass concentrations at the ends, but with additional sub-fragments spaced along the filament (similar to Taurus). The filamentary structure of LDN 981, on the other hand, has

[4]Typically, the Jean's length is given by $\lambda_J = 0.19\,\mathrm{pc}\,(\frac{T}{10\,\mathrm{K}})^{1/2}(\frac{n_{H_2}}{10^4\mathrm{cm}^{-3}})^{1/2}$.

resemblance to results from simulations of a collapsing ”ghost”-sheet with highly irregular boundaries (see, Figure 12 of Burkert & Hartmann, 2004). In this case, stars form first at the ends of the filaments and, in addition, the first stars are thought to form at the end of the thinnest and longest filaments, which is exactly what we observe in LDN 981. Thus, even if this model is still very limited and simple it might explain the differences in the observed filamentary structures and also the formation of V1331 Cyg at the end of the very elongated filament LDN 981-F1. One problem arises, though: Burkert & Hartmann (2004) modeled *collapsing* gaseous sheets and there seem to be indications that infall is not present in LDN 981 (Lee et al., 2004). However, this result is based on a single pointing with moderate spatial resolution towards the center of LDN 981-F2 which might not be representative for the whole cloud (see, also section 4.3). The theoretical model predicts stronger infall signatures along the edges of the filaments as well as along the thinner and longer filaments. A more sensitive and spatially larger search for these signatures within the filaments in LDN 981 may hence be worthwhile.

It seems as if LDN 981's picture as a collapsing cloud core might be able to explain both the filamentary structure and the formation of V1331 Cyg at the tip of the most elongated filament. To test this hypothesis, future studies of the whole dark cloud should address the issue of additional denser globules within the filaments of LDN 981 and further (sub-)millimeter observations can be used to better constrain the dynamics of the filaments.

2.4.5 V1331 Cyg - an FU Ori object?

V1331 Cygni was among a group of ten young stars initially defined as pre-outburst FUors by Welin (1976). And as described in section 2.4.1, the circumstellar environment of V1331 Cyg bears indeed evidence of a more active evolutionary phase some thousand years ago, which possibly puts V1331 Cyg in between two consecutive outbursts Based on recent observational results from the literature we shortly investigate whether V1331 Cyg fulfills the criteria of an FUor even in its *present* stage.

FUors share in general several common features summarized in Hartmann & Kenyon (1996). For the first members of the group a rapid outburst in optical and NIR luminosity of several magnitudes was observed. The outburst is followed by a decrease in luminosity which can last between serveral tens to hundreds of years. However, the photometric behavior of V1331 Cyg over the last 40 years shows no evidence for a significant increase or decrease in NIR flux (Ábrahám et al., 2004).

Apart from the outburst which might be difficult to observe, the best criterion to identify an FUor is its spectroscopic behavior. While modest resolution optical spectra reveal spectral types of late F to G supergiants most infrared features are best fitted with K-M giant-supergiant atmospheres. Although no clear spectral type could thus far be derived for V1331 Cyg most authors agree on a spectral type earlier than F2 (Cohen & Kuhi, 1979; Mundt et al., 1981; Chavarria, 1981). Only one author found a spectral type of G0 (Kolotilov & Petrov, 1983).

Furthermore FUors show strong CO bandhead absorption at 2.3μm while V1331 Cyg shows unambiguously varying CO bandhead emission (Biscaya et al., 1997).

Thus, V1331 Cyg can currently not be classified as an FUor object and seems to be in a more quiescent evolutionary phase.

2.5 Summary and conclusions

The main results of this chapter can be summarized as follows:

- We presented high-resolution scattered light images of the dusty environment of V1331 Cyg. Two circumstellar dust rings, well separated by a gap, are detected with the inner ring being resolved for the first time. This dust ring is probably related to a known flattened CO structure several thousand AU in size.
- The outer ring-like dust structure likely represents the remnants of the molecular core V1331 Cyg formed from. As V1331 Cyg is surrounded by a circumstellar disk seen close to pole-on stellar and/or disk winds and outflows might have created a cavity towards the line of sight of the observer.
- The large scale structure suggests that V1331 Cyg is physically related to the dark cloud LDN 981 and lies at the edge in between two dark filaments where it recently emerged from. The distance estimates for V1331 Cyg and LDN 981 are in good agreement.
- V1331 Cyg is likely to be the only young star in LDN 981 and did presumably form in isolation.
- Based on recent results of 2D simulations of collapsing irregular gaseous sheets that appear very similar to the morphology observes for LDN 981, we suggest that LDN 981 is undergoing a gravitational collapse and may potentially form additional stars along the filaments in the future.
- We did not find any evidence for a possible external trigger for the formation of V1331 Cyg, such as propagating shock waves from a nearby supernova remnant or high proper-motion early-type stars in the vicinity.
- Finally, observational results from the last decades show that V1331 Cyg does not fulfill the criteria for an FUor in its current status. However, more vigorous events such as FUor outbursts might have occurred in the past and helped creating the dust morphology we observe today.

3. The accretion disk around FU Orionis

The VLTI/MIDI perspective

Parts of this chapter were published in the Astrophysical Journal.
(Quanz, S. P., Henning, Th., Bouwman, J., Ratzka, Th., Leinert, Ch., 2006, ApJ 648, 472)

THE FOLLOWING CHAPTER deals with the first mid-infrared interferometric measurements of FU Orionis. We clearly resolve structures that are best explained with an optically thick accretion disk. A simple accretion disk model fits the observed SED and visibilities reasonably well and does not require the presence of any additional structure such as a dusty envelope. The inclination and also the position angle of the disk can be constrained from the multibaseline interferometric observations. Our disk model is in general agreement with most published near-infrared interferometric measurements. From the shape and strength of the 8-13 μm spectrum, the dust composition of the accretion disk is derived for the first time. We conclude that most dust particles are amorphous and already much larger than those typically observed in the ISM. Although the high accretion rate of the system provides both high temperatures out to large radii and an effective transport mechanism to distribute crystalline grains, we do not see any evidence for crystalline silicates in either the total spectrum or the correlated flux spectra from the inner disk regions. Possible reasons for this non-detection are mentioned. All results are discussed in context with other high spatial resolution observations of FU Ori and other FU Ori objects.

3.1 Introduction

As the general observational properties of FUors were already given in chapter 1, we concentrate on most recent results for individual objects in the following. Based on near-infrared (NIR) and/or mid-infrared (MIR) interferometry as a technique to study the inner few AU of the accretion disks, new insights to some of the best studied FUors were provided recently. Millan-Gabet et al. (2006) found that accretion disks alone can not reproduce the SED and observed low K-band visibilities for V1057 Cyg, V1515 Cyg and Z CMa-SE simultaneously. They concluded that additional uncorrelated flux may arise due to scattering by large dusty envelopes. Ábrahám et al. (2006) presented the first VLTI/MIDI observations of V1647 Ori whose eruptive behavior suggests that it is either an FUor or an EX Lupi (EXor) type object. In this case it was possible to fit both, the SED

and the observed MIR visibility with a simple disk model with moderate disk flaring. For FU Ori itself it was Malbet et al. (2005) who analyzed a wealth of NIR interferometric data. They showed that the NIR visibilities and the SED could be fitted with two models: One consisting simply of an optically thick and geometrically thin accretion disk and a second one consisting of an accretion disk and an embedded "hot spot". From their error statistics these authors concluded that the latter model was more likely.

In summary it becomes clear that up to now no coherent picture can be derived from the interferometric observations of FUors. And although the group of objects studied so far is comparatively small it appears rather inhomogeneous.

In this chapter the first MIR interferometric measurements of FU Orionis are presented. The data are thus complementary to the NIR observations of Malbet et al. (2005). In section 3.1 the observations and the data reduction process are briefly described. In section 3.2 the findings derived from the N-band acquisition images are discussed. The 8-13 μm spectrum of FU Ori is analyzed in section 3.3. Section 3.4 and 3.5 discuss the results from the interferometric measurements, i.e. the visibilities and the correlated flux spectra, respectively. A simple analytical disk model and its fit to the SED and the visibilities is presented in section 3.6. Finally, a summary, conclusions and some future prospects are mentioned in section 3.7.

3.2 Observations and data reduction

The observations were carried out between 2004 October 31 and November 4 with the Mid-Infrared Interferometric Instrument (MIDI) at ESO's Very Large Telescope Interferometer (VLTI) on Paranal/Chile. Together with the Keck Interferometer Nuller that recently started to produce first scientific results (Mennesson et al., 2005), MIDI is currently worldwide the only instrument able to conduct spectrally resolved interferometric observations in the mid-infrared (Leinert et al., 2004). For the observations MIDI was used in high-sens mode using the NaCl prism as dispersive element yielding a spectral resolution of 30. The maximum projected baseline was 86.25 m and the minimum projected baseline 44.56 m leading to an angular resolution at 10 μm of 0.″029 and 0.″056, respectively. For an assumed distance of 450 pc these values correspond to 13.1 AU and 25.2 AU. A journal of the observations including projected baselines, position angles and calibrator stars is given in Table 3.1. For completeness we also mention the observations from December 2004 although they are disregarded in the following sections. These observations had almost exactly the same baseline and position angle as the October observations but showed in general a lower level of total and correlated flux due to rather poor observing conditions in terms of seeing and transparency. The calibrator stars for the data reduction were chosen by analyzing all calibrator stars observed over the whole night. We selected those showing a good agreement in their transfer functions, i.e. their instrumental visibilities after the assumed sizes were taken into account. The data reduction was carried out with the software package MIA+EWS-1.3. This software consists of two independent reduction programs (MIA and EWS) which were both applied for comparison. The software, further information and manuals can be downloaded from the Internet[1]. A general description of the basic data reduction steps is also given in Leinert et al. (2004) and we refer the reader to this paper. As the results derived with MIA and EWS agreed quite

[1] http://www.strw.leidenuniv.nl/∼nevec/MIDI/index.html

Date	Object	Projected Baseline	Position Angle	Comment
31.10.2004	FU Ori	44.56 m (UT2-UT3)	46.54°	-
	HD37160			Calibrator [a]
02.11.2004	FU Ori	86.25 m (UT2-UT4)	84.24°	-
	HD 31421			Calibrator
	HD 37160			Calibrator
	HD 50778			Calibrator
04.11.2004	FU Ori	56.74 m (UT3-UT4)	106.64°	-
	HD 25604			Calibrator
	HD 20644			Calibrator
	HD 37160			Calibrator
	HD 50778			Calibrator
29.12.2004	FU Ori	44.80 m (UT2-UT3)	46.61°	-
	HD 37160			Calibrator
	HD 94510			Calibrator [a]

Table 3.1 Journal of MIDI observations of FU Orionis and the calibrators used for the data reduction. [a] Observed twice that night

well (overall differences in the correlated flux $\leq 8\%$), only plots resulting from the MIA package are presented in the following.

3.3 The MIDI acquisition image

FU Ori was found to be a binary system by Wang et al. (2004). Reipurth & Aspin (2004) confirmed the detected companion and concluded that it was a young star of spectral type K showing clear NIR excess. In the same paper it was also stated that it was very unlikely that the binary component (FU Ori S) triggered the outburst of FU Ori observed in the late 1930s. Knowing about the existence of the fainter companion the integration time of

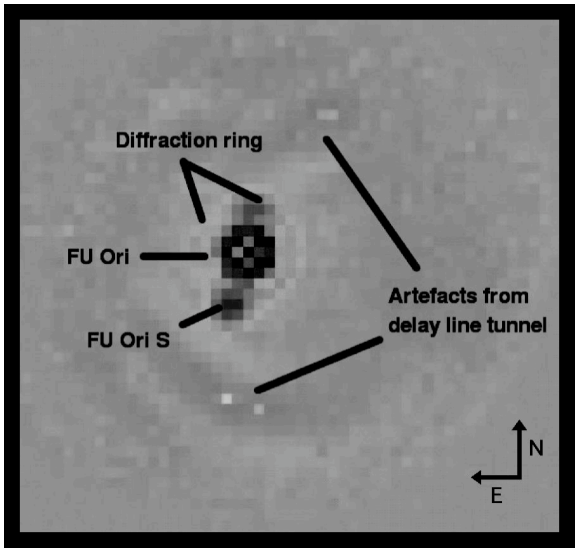

Figure 3.1 FU Ori and FU Ori S as seen in the MIDI acquisition images at 8.7 μm. The image was taken with UT3 on the 31st of October 2004 using the AO-system MACAO.

some MIDI acquisition images was increased in order to derive N-band photometry for both components. In three images FU Ori S was clearly visible (Figure 3.1) and aperture photometry could be applied to the observations. The results are summarized in Table 3.2. Interestingly, FU Ori S shows a relatively higher N-band excess than FU Ori itself. This can be explained in terms of differences in the geometry of an assumed circumstellar disks (e.g., larger flaring angle or smaller disk inclination). We furthermore derive a separation between the components of $0.''48 \pm 0.''01$ and a position angle of $162.5^\circ \pm 4.1^\circ$ (measured from north eastward) which is in good agreement with the results from Wang et al. (2004) and Reipurth & Aspin (2004). Our errors are standard deviations based on Gaussian fitting of 3 independent images. For an assumed distance of 450 pc the separation corresponds to 217.8 ± 4.5 AU.

	J [mag]	H [mag]	K' [mag]	L' [mag]	N [mag]
FU Ori	6.30±0.03	5.64±0.05	5.25±0.02	4.18±0.04	2.75±0.19
FU Ori S	10.75±0.23	9.92±0.21	9.15±0.15	8.09±0.16	5.28±0.11

Table 3.2 Photometric values for the FU Ori system. J to L' are taken from Reipurth & Aspin (2004), N-band values are derived from MIDI 8.7 μm acquisition images. The errors for the N-band fluxes are standard deviations based on measurements of three acquisition images. Two were taken on 31.10.2004 and one on 02.11.2004.

3.4 The total uncorrelated mid-infrared spectrum

3.4.1 Comparison to SPITZER observations

Figure 3.2 shows the MIR spectrum of FU Ori. The spectrum obtained with MIDI is the average over the first three observing nights using both Unit Telescopes (UTs). For comparison SPITZER IRS data are plotted additionally. Those data were available from the SPITZER Data Archive. For the data reduction we used the *droopres* intermediate data product processed through the SSC pipeline S12.0.2. The SMART reduction package developed by the IRS Instrument Team at Cornell (Higdon et al., 2004) was used to extract the spectrum. Within the error bars the spectra agree quite well. A broad and weak silicate emission feature is present between 8-13 μm. However, the averaged MIDI spectrum appears to be a little flatter than the more roundish SPITZER spectrum.

3.4.2 Possible dust composition

In contrast to other YSOs the observed silicate emission feature of FU Ori is rather weak (see also Hanner et al., 1998). Such a broad and flat MIR dust spectrum can be explained by grains that already underwent some coagulation process (Bouwman et al., 2001). To test this hypothesis we derived a possible dust composition by fitting a dust model to the normalized and continuum subtracted SPITZER spectrum from 6-13 μm.

This analysis method is similar to approaches that were successfully applied in previous studies for determining the dust composition of observed dust emission features of other YSOs (e.g., Bouwman et al., 2001). In the model we assume that the observed emission can be computed from the sum of the emission of individual dust species. The species

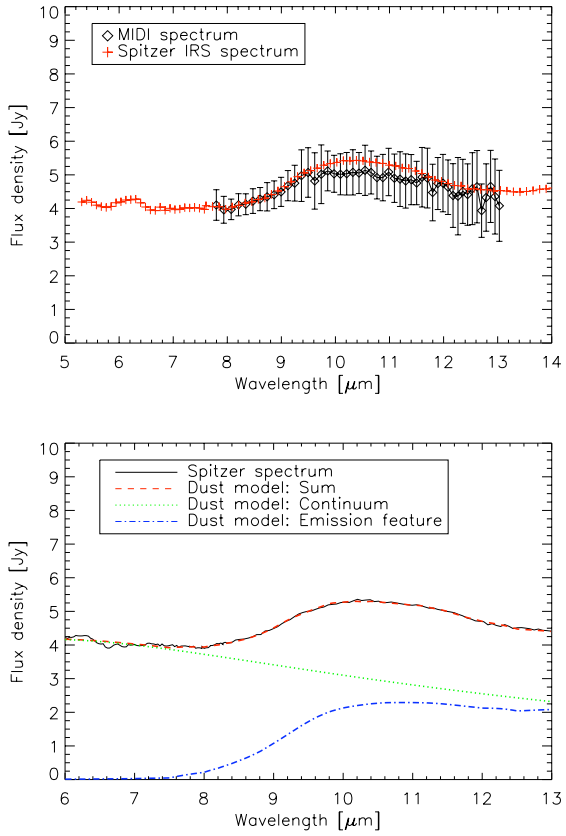

Figure 3.2 *Top:* MIR spectrum of FU Ori from 5.3-14 μm. Data from the MIDI observations (black diamonds) range from 8-13 μm. They agree within the error bars with SPITZER IRS data (red crosses). The errors for SPITZER are smaller than the symbols and are not shown. The larger MIDI errors arise from averaging six independently calibrated measurements (3 nights and 2 telescopes each night). The observed silicate feature is rather flat and broad. *Bottom:* MIR spectrum of FU Ori and the resulting dust model fit. The SPITZER spectrum (black solid line) can be fitted quite well with the dust composition given in Table 3.4. The green dotted line shows the contribution of the underlying continuum, the blue dash-dotted line shows the silicate emission and the red dashed line shows the sum of both, i.e., the total flux, which is hardly distinguishable from the observed spectrum.

we used are summarized in Table 3.3 together with references for their optical properties. We furthermore took into account different grain sizes. For each of the dust species the opacities were calculated for 0.1, 1.5, and 6.0 μm sized particles. To estimate the possible contribution of Polycyclic Aromatic Hydrocarbons (PAHs) to the emission we used a template spectrum based on profiles that were derived from observations (Peeters et al., 2002; van Diedenhoven et al., 2004). Finally, in order to reproduce the observed spectrum we fitted the following emission model to the SPITZER data using a least square minimization

$$F_\nu - B_\nu(T_{\rm cont})C_0 = B_\nu(T_{\rm dust})\left(\sum_{i=1}^{3}\sum_{j=1}^{5} C_{i,j}\kappa_\nu^{i,j}\right) + C_{\rm PAH} I_\nu^{\rm PAH} \quad . \tag{3.1}$$

Here, F_ν is the observed flux and $B_\nu(T_{\rm cont})$ and $B_\nu(T_{\rm dust})$ denote the Planck function at the temperature of the underlying continuum and of the silicate grains, respectively. $\kappa_\nu^{i,j}$ is the mass absorption coefficient for the silicate species j with the grain size i, $I_\nu^{\rm PAH}$ is the template emission spectrum for the PAHs, and C_0, $C_{i,j}$, and $C_{\rm PAH}$ are the weighting factors for the continuum, the silicate emission and the PAH contribution, respectively. A more detailed description of the dust model and plots showing the different dust opacities is given in Bouwman et al. 2007 (in preparation).

The model results are shown in Figure 3.2 (bottom) and Table 3.4 summarizes the corresponding dust composition. As for the underlying continuum we fitted a temperature of 880 K, we believe that this optically thick emission most likely arises from the inner

Species	Chemical Formula	Shape	Ref.
Amorphous olivine	$MgFeSiO_4$	Homogeneous	(1)
Amorphous pyroxene	$MgFeSi_2O_6$	Homogeneous	(1)
Crystalline forsterite	Mg_2SiO_4	Inhomogeneous	(2)
Crystalline enstatite	$MgSiO_3$	Inhomogeneous	(3)
Amorphous silica	SiO_2	Inhomogeneous	(4)

Table 3.3 Dust species used in the dust model. Apart from the name, the chemical formula, the shape and also the reference to laboratory measurements for the optical properties are given. Mie-theory was used to calculated the opacities for the homogeneous spheres whereas for the inhomogeneous spheres we used the distribution of hollow spheres given by Min et al. (2005) to simulate grains that are not perfectly symmetric. *References:* (1) Dorschner et al. (1995), (2) Servoin & Piriou (1973), (3) Jaeger et al. (1998), (4) Spitzer & Kleinman (1960).

parts of the disk close to the star. The outer and thus cooler regions of the disk would then be responsible for the weak silicate emission for which we fitted a temperature of 230 K to the optically thin emission layer. The results strongly support the idea that most particles are amorphous and much larger in size than those in the ISM. PAHs, silica particles and crystalline silicates do not seem to be present at all. Although the derived fractions of different dust species do depend on the model applied to the data (e.g., in terms of the precise grain sizes considered and also in terms of particle structures) the main conclusions remain unaltered: (1) we do not find evidence for crystalline silicates and (2) the grains are considerably larger than those found in the ISM. For a more detailed discussion about the influence of different model parameters we refer to Voshchinnikov et al. (2006) and van Boekel et al. (2004).

	0.1 μm	1.5 μm	6.0 μm	Total
Amorphous olivine	0.17	< 0.01	0.18	0.35
Amorphous pyroxene	< 0.01	0.07	0.57	0.64
Crystalline silicates [a]	< 0.01	< 0.01	< 0.01	< 0.01

Table 3.4 Possible dust composition for the observed 10 μm silicate feature as derived with our dust model. The mass fraction of three grain sizes for different dust species is given. [a] forsterite and enstatite

As the disk is much brighter in the optical and NIR than the central star (see section 3.7), stellar radiation is probably not able to produce the observed weak emission feature in an optically thin disk surface layer. However, it was shown that the silicate feature of FU Ori can be reproduced taking into account self-irradiation of the disk (Lachaume, 2004). In this case the hot inner parts of the accretion disk serve as flux source and illuminate the disk surface layer under a certain angle.

3.5 The visibilities

In Figure 3.3 and Table 3.5 the visibilities measured for FU Ori at three different baselines are shown. The errors are computed as standard deviations resulting from the use of different calibrators for each night (see Table 3.1). In most of the following plots the position of the atmospheric ozone band is indicated as this part of the spectrum suffers from imperfect corrections during the data reduction process. Here, small "dips" and "bumps" in otherwise flat spectra are remnants from the data reduction.

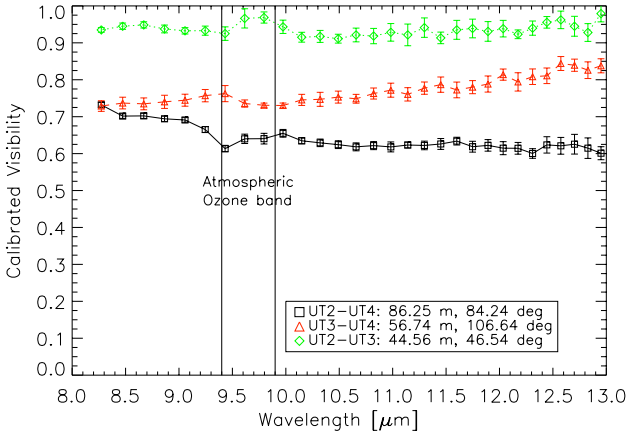

Figure 3.3 Calibrated Visibilities of FU Ori for three different baselines.

3.5.1 Qualitative assessment

The calibrated visibility of the shortest baseline (UT2-UT3) remains almost constant at ≈ 0.95 over the whole wavelength range and the source is only marginally resolved. As expected, for the longest baseline (UT2-UT4) the lowest visibility is observed ranging from ≈ 0.73 at 8.3 μm to ≈ 0.6 at 13 μm. For the intermediate baseline (UT3-UT4) the visibility shows a slight increase from ≈ 0.73 at 8.3 μm to ≈ 0.85 at 13 μm. The fact that the object is clearly resolved with two baselines in the MIR supports the argument of Malbet et al. (2005) that we are observing an extended circumstellar structure, i.e. a disk, and not only the stellar photosphere (Herbig et al., 2003).

For the two baselines UT2-UT3 and UT2-UT4 the observations are consistent with expectations from thermal disk emission: Despite the decreasing resolution for longer wavelengths the visibilities indicate larger sizes for the emitting regions (see also subsection 3.5.3). The observed increase in visibility for the UT3-UT4 baseline implies that for this baseline, however, the object appears smaller at 13 μm than at 8 μm. This is difficult to imagine in the context of a circumstellar disk as emitting source, and certainly a second observation for this baseline configuration seems eligible. Theoretically it is possible that the photometric measurements carried out directly after the interferometric observations are corrupted due to technical problems or different weather conditions. This in turn might then lead to a change in the visibility function. However, the calibrators observed at this night did not show any sign of poor photometric measurements and their transfer function was very stable over the whole night. In addition, also other YSOs with circumstellar disks showed an increasing visibility for certain baselines when observed

Wavelength [μm]	V [UT2-UT3 [a]]	V [UT2-UT4 [b]]	V [UT3-UT4 [c]]
12.95	0.98±0.02	0.60±0.02	0.84±0.02
12.83	0.93±0.02	0.61±0.03	0.83±0.02
12.70	0.94±0.03	0.63±0.03	0.84±0.02
12.57	0.96±0.02	0.62±0.02	0.84±0.02
12.44	0.96±0.02	0.62±0.02	0.81±0.02
12.31	0.94±0.02	0.60±0.01	0.81±0.02
12.17	0.92±0.01	0.61±0.02	0.79±0.02
12.03	0.94±0.02	0.61±0.02	0.81±0.02
11.89	0.93±0.03	0.62±0.02	0.79±0.02
11.75	0.94±0.03	0.62±0.01	0.78±0.02
11.60	0.94±0.03	0.63±0.01	0.77±0.02
11.45	0.91±0.02	0.63±0.01	0.79±0.02
11.30	0.94±0.03	0.62±0.01	0.78±0.02
11.14	0.92±0.03	0.62±0.01	0.76±0.02
10.98	0.93±0.02	0.62±0.01	0.77±0.02
10.82	0.92±0.02	0.62±0.01	0.76±0.01
10.66	0.92±0.02	0.62±0.01	0.75±0.01
10.49	0.91±0.01	0.62±0.01	0.75±0.02
10.32	0.92±0.02	0.63±0.01	0.75±0.02
10.15	0.92±0.01	0.63±0.01	0.75±0.02
9.97	0.94±0.02	0.65±0.01	0.73±0.01
9.80	0.97±0.02	0.64±0.01	0.73±0.01
9.62	0.97±0.03	0.64±0.01	0.74±0.01
9.43	0.93±0.02	0.61±0.01	0.76±0.02
9.25	0.93±0.01	0.67±0.01	0.76±0.02
9.06	0.93±0.01	0.69±0.01	0.74±0.02
8.86	0.94±0.01	0.69±0.01	0.74±0.02
8.67	0.95±0.01	0.70±0.01	0.73±0.02
8.47	0.95±0.01	0.70±0.01	0.74±0.02
8.27	0.94±0.01	0.73±0.01	0.73±0.01

Table 3.5 Calibrated visibilities for FU Ori observed with three different baselines. The errors are standard deviations resulting from calibrations with different calibrator stars for each night. [a] Projected Baseline: 44.56 m, Position Angle: 46.54°; [b] Projected Baseline: 86.25 m, Position Angle: 84.24°; [c] Projected Baseline: 56.74 m, Position Angle: 106.64°

with MIDI. Thus, since we do not find any evidence for excluding this dataset due to bad quality we decided to keep it in our analyses.

3.5.2 Comparison to MIR visibilities of HAeBe stars

As thus far no MIDI visibilities for TTauri stars have been published we are limited to a comparison between FU Ori and circumstellar disks around Herbig Ae/Be stars

(HAeBes). These stars as well as models applied to them normally show a prominent drop in the visibility between 8 and 10 μm from where the curve remains almost constant (Leinert et al., 2004). Qualitatively, this drop results from the intensity distribution of the passive disks around the HAeBes: At the short wavelength end the hot inner rims of the disks provide an overproportional contribution to the flux and are at the same time confined to a small spatial region leading to a high visibility. Most of the rest of the MIR emission originates from a large area of the hot, illuminated surface layer of the flared circumstellar disk. The visibilities for FU Ori show hardly any wavelength dependence and are very flat from 8-13 μm regardless of baseline. Thus, its seems as if the flux distribution of FU Ori is smoother and the visibilities show no sign of a significant contribution from a hot inner rim. However, as FU Ori is surrounded by a heavily active accretion disk where the disk alone produces the majority of the observed flux at almost all wavelengths (see section 3.7) differences in the intensity distribution and thus in the visibility can be expected.

Apart from differences in the shape of the visibility curves most HAeBes are much better resolved, i.e., show lower visibilities, than FU Ori (Leinert et al., 2004). This, however, can (at least partly) be explained by the distance to these objects which is in general less than 200 pc. FU Ori on the other hand has an assumed distance of 450 pc, and if it was closer to the Earth we would observe lower visibilities also for this object.

3.5.3 Geometry of the emitting regions

To derive a simple model for the geometry of the emitting regions we assume a Gaussian brightness distribution for each baseline. This is a reasonable first approximation for objects showing high visibilities. The FWHM, and hence the physical size of this Gaussian in arcsec, can be computed by

$$\Theta = \sqrt{\frac{ln(V(f))}{-3.56 \cdot f^2}} \tag{3.2}$$

where $V(f)$ is the measured visibility for a certain spatial frequency $f = \frac{B}{\lambda}$ (in arcsec^{-1}) derived from the projected baseline B and the wavelength λ. Equation 3.2 results from a simple Fourier transformation of the assumed brightness distribution. We computed the FWHM for all three baselines at three different wavelengths (9.0, 11.0, and 12.5 μm). For this we averaged for each baseline 5 visibility points from Table 3.5 centered on the specified wavelengths. Table 3.6 gives the resulting sizes of the emitting regions in AU for an assumed distance to FU Ori of 450 pc. The results are visualized in Figure 3.4 where the FWHM are shown in their orientation on the sky. As expected for thermal disk emission the FWHM increases with wavelength for a given baseline. The only exception is the 12.5 μm size for the UT3-UT4 baseline which is surprisingly a little smaller than that seen at 11.0 μm.

Apart from size estimations for each individual baseline our measurements based on different position angles allow to constrain the geometry of the disk. We fitted the derived FWHM with an ellipse for each of the considered wavelengths in order to derive a simple model for the spatial orientation of an assumed disk-like structure. The resulting best fit ellipses are overplotted in Figure 3.4 and their parameters are summarized in the lower half of Table 3.6. As one would expect from a disk-like structure showing a decrease in temperature with radius the semimajor axes of the ellipses increase with wavelength.

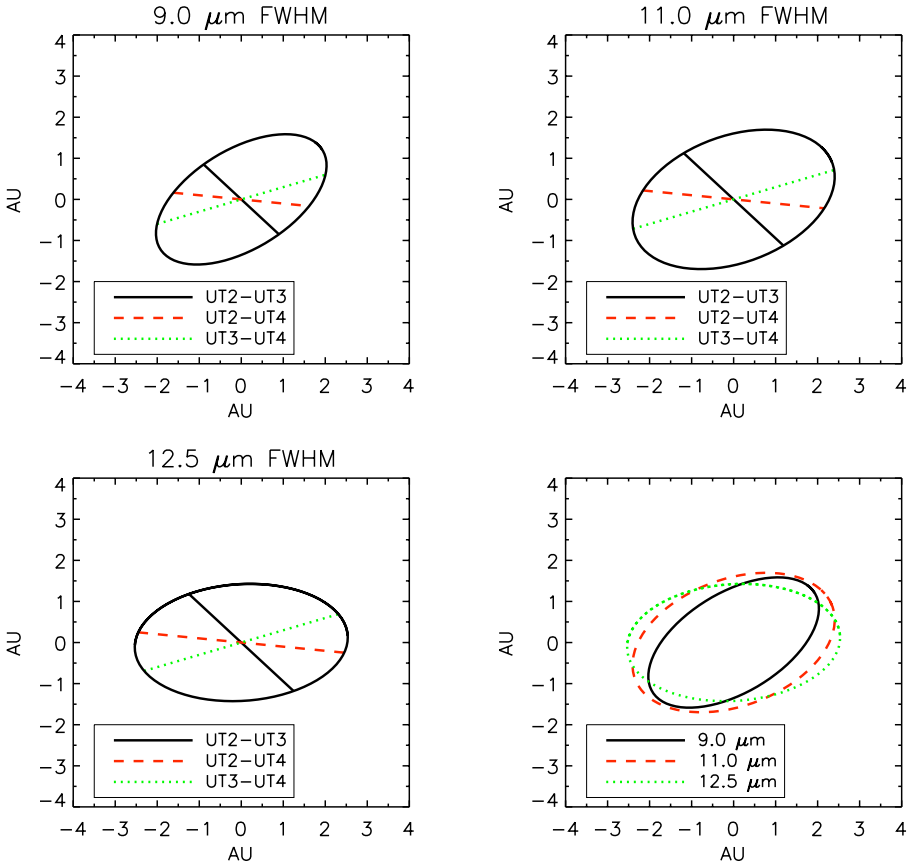

Figure 3.4 Sizes and orientation of the emitting regions on the sky for different wavelengths (9.0 μm (upper left), 11.0 μm (upper right) and 12.5 μm (lower left)). The sizes correspond to FWHM of assumed Gaussian brightness distributions and are given in Table 3.6. The resulting best fit ellipses for each wavelength are overplotted and combined in a fourth plot (lower right). The center of the plots corresponds to the position of FU Ori. North is up and east is to the left.

However, due to the increasing visibility of the UT3-UT4 baseline the semiminor axis and also the total area of the ellipse are slightly smaller at 12.5 μm than at 11.0 μm. An inclination angle for an assumed circular disk can be derived by computing the $arccos$ of the ratio of the semiminor and semimajor axis. The resulting angles agree very well ($55.4^\circ \pm 2.4^\circ$) and are also in good agreement to what was found for FU Ori disk models based on NIR observations (Malbet et al., 2005). By combining the derived inclination angle with rotational velocity measurements in the optical spectral region, it is possible to estimate the central mass. Based on Kenyon et al. (1988) we derive $M/M_\odot \approx 0.36$ for FU Ori which is reasonably consistent with typical values for low-mass pre-main sequence stars. In addition to the inclination the fitted ellipses provide also information on the position angle of the disk. The position angles (measured from north eastwards) for the semimajor axes at different wavelengths show a larger scatter ($109.1^\circ \pm 11.6^\circ$) than the inclinations and differ significantly from the NIR findings of Malbet et al. (2005) (see also section 3.7). It seems as if the position angle becomes smaller for longer wavelengths, although one has to keep in mind that, again, at least for the UT3-UT4 baseline the in-

creasing visibility is the main reason for the observed rotation. At this point we leave it to future investigations to derive a 3-D disk model based on a more complex dust distribution possibly able to confirm the apparent changes in the position angle for different wavelength regimes.

	9.0 μm	11.0 μm	12.5 μm
UT2-UT3 (44.56 m)	$2.47^{+0.40}_{-0.46}$	$3.27^{+0.67}_{-0.82}$	$3.43^{+0.81}_{-1.02}$
UT2-UT4 (86.25 m)	$3.25^{+0.24}_{-0.25}$	$4.34^{+0.07}_{-0.08}$	$4.93^{+0.17}_{-0.17}$
UT3-UT4 (56.74 m)	$4.19^{+0.28}_{-0.30}$	$5.00^{+0.35}_{-0.37}$	$4.83^{+0.43}_{-0.46}$
Semimajor axis a [AU]	2.28	2.51	2.54
Semiminor axis b [AU]	1.21	1.54	1.42
Ellipse area [AU^2]	8.67	12.14	11.33
Position angle θ [a]	122.2°	111.1°	93.9°
Inclination i [b]	58.0°	52.2°	56.0°

Table 3.6 *Upper half:* Derived FWHM (in AU) of Gaussian brightness distributions for the three baselines and three wavelengths using equation 3.2. The distance to FU Ori is assumed to be 450 pc. *Lower half:* Parameters of best ellipses fitted to the data for the three considered wavelengths. [a]Position of a measured from north eastward; [b]Assuming an underlying circular disk.

3.6 The correlated mid-infrared spectra

3.6.1 The origin of the correlated flux

The correlated flux is directly linked to the total flux, i.e., the flux from a single UT telescope, via the visibility:

$$F_{\rm corr}(\lambda) = V(\lambda) \cdot F_{\rm total}(\lambda) \tag{3.3}$$

Figure 3.5 depicts the results for the correlated flux for the three different baselines. The total spectrum is plotted for comparison. Taking into account the spatial resolution of the three baselines it is possible to estimate the origin of the correlated 8-13 μm flux. Our UT2-UT3 baseline has a spatial resolution of $\approx$ 25 AU at the distance of FU Ori, and if we assume an average visibility of 0.95 one knows that 95% of the 8-13 μm flux must come from within this 25 AU. Similarly, for the UT2-UT4 baseline 65% of the flux is emitted from the inner 13 AU. For the UT3-UT4 baseline 75% of the 8-13 μm flux comes from the inner 20 AU.

3.6.2 Lacking crystalline silicates?

The spatially resolved MIR spectra of the MIDI instrument make it possible to study the radial dependence of the dust composition in the protoplanetary disk (van Boekel et al., 2004). In section 3.4 we showed that the spatially unresolved (total) spectrum of FU Ori can be fitted with mainly large amorphous dust grains. The shape of the spatially resolved

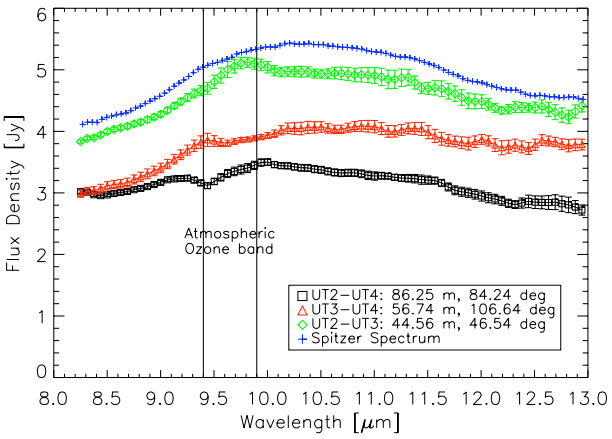

Figure 3.5 Observed correlated flux for the three different baselines and position angles.

(correlated) flux spectra contains information about the dust composition of the inner parts of the disk.

To compare the shape of the correlated spectra to the total spectrum we first subtracted the continuum for which we fitted a straight line between the flux at 8.25 and 12.95 μm. Then we normalized all continuum subtracted correlated flux spectra and the total SPITZER spectrum by

$$F_{\mathrm{norm}} = \frac{F_{\mathrm{sub}}}{F_{\mathrm{mean,sub}}} \tag{3.4}$$

where F_{sub} and $F_{\mathrm{mean,sub}}$ denote the continuum subtracted spectra and their mean value, respectively. By applying this formula all correlated spectra conserve their shape and can be compared to the total spectrum as illustrated in Figure 3.6. To identify those parts of the spectra that differ significantly, we furthermore computed the deviation from the total SPITZER spectrum for each wavelength in units of the data error:

$$\sigma_{\mathrm{dev}} = \frac{F_{\mathrm{norm,corr}} - F_{\mathrm{norm,total}}}{\sigma_{\mathrm{corr}}} \tag{3.5}$$

$F_{\mathrm{norm,corr}}$ and $F_{\mathrm{norm,total}}$ are the normalized correlated spectra and the normalized total spectrum and σ_{corr} denotes the standard deviation of the correlated spectra (MIDI errors) at a given wavelength. We applied the same normalization factors to the errors as we did to the spectra. Figure 3.6 shows that no clear deviations from the total unresolved spectrum are observed for any of the correlated spectra. This means that with the given spatial resolution and sensitivity no significant chemical difference in the dust composition is observed and the spectra of the inner parts of the disk look very similar to the total unresolved disk spectrum.

This finding is somewhat surprising. As seen in section 3.4 the silicate dust grains apparently already underwent noticeable coagulation. Thus, the disk does not consist of purely ISM dust anymore and must already have a significant age. In addition it is known that apart from grain growth also thermal annealing takes place within protoplanetary disks and transform the amorphous silicates into crystalline silicates (see, Henning et al., 2006; van den Ancker et al., 2000). However, neither the total spectrum nor the correlated spectra indicate the presence of crystalline silicates. This is even more surprising considering the high temperatures in the disk interior due to viscous heating of this actively accreting star (section 3.7). Annealing processes transforming ISM amorphous dust into

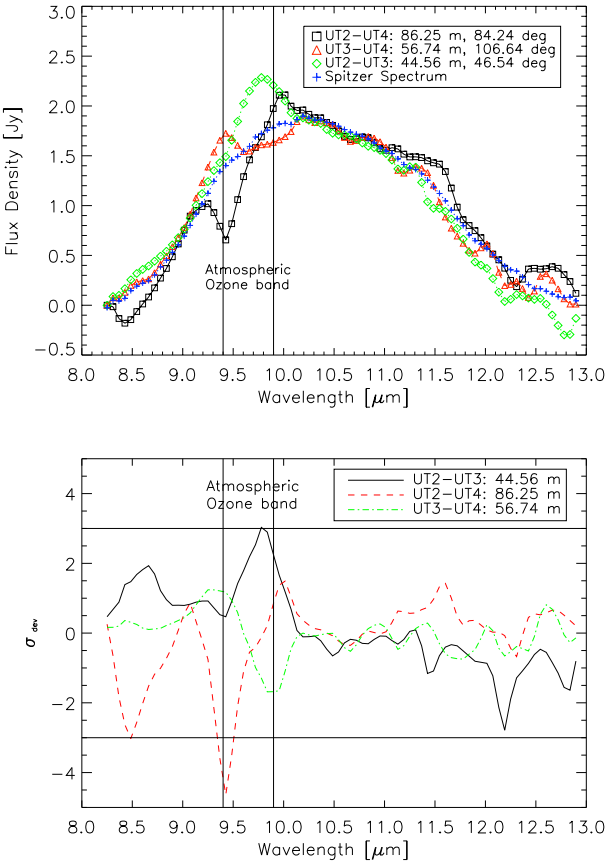

Figure 3.6 *Top:* Continuum subtracted and normalized correlated spectra for the three different baselines and the normalized total spectrum. For clarity the errorbars have not been overplotted. They equal those of Figure 3.5. *Bottom:* Variations of the normalized correlated spectra with respect to the normalized total SPITZER spectrum in error units. Most variations are clearly below the 3σ threshold, indicating that the shape of the correlated spectra equals that of the total spectrum.

crystalline dust set in in disk regions where $T \geq 800$K (e.g., Gail, 2001). In addition to that, high accretion rates directly relate to a faster vertical and horizontal mixing within the protoplanetary disk (Gail, 2004). This effect also eases the detection of crystalline silicates within the accretion disk surrounding FU Ori. But why don't we find any evidence for their existence?

A possible explanation might be that they simply cannot be detected as the related feature is rather weak and dominated by the underlying continuum. This hypothesis can be checked by analyzing the longer wavelength regime of the SPITZER spectrum as depicted in Figure 3.7. As at longer wavelengths the temperature of the continuum is decreasing the contrast between the continuum and possible emission features due to the presence of crystalline silicate particles increases. Hence, spectral signatures of these particles should be more easily detectable. Figure 3.7, however, shows that also between 14 and 34 μm the spectrum of FU Ori does not bear any clear signs of crystalline silicates. Normally crystalline forsterite particles have emission bands at 16.4, 23.9, 27.7 and 33.8 μm and enstatite grains show features at 18.8, 21.5, and 24.5 μm (Molster & Kemper, 2005). If one argued that possibly around 27.7-27.8 μm a weak forsterite feature was present one should keep in mind that the features at 23.9 and 33.8 μm are normally stronger (Min et al., 2005) but are not seen at all. Thus, also in the longer wavelength MIR spectrum of FU Ori no crystalline silicates are present. This suggests that apparently the non-detection is at least not only due to contrast problems between the emission features and the underlying continuum.

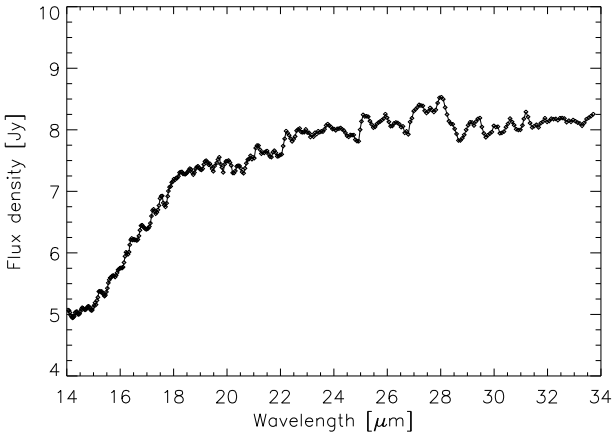

Figure 3.7 SPITZER spectrum from 14-34 μm. The spectrum was smoothed by a factor of three. Similar to the shorter wavelength spectrum in Figure 3.2 this spectrum appears rather smooth without any striking features. The "jumps" in the spectrum indicate where the order of the spectrograph is changing, leading to variations in the detected flux (approximately at 19.6, 22.1, 25.0, and 26.7 μm).

What else can prevent us from detecting crystalline silicates? In case FU Ori underwent its first of possible multiple outbursts and phases of enhanced accretion, it is possible that not enough time has yet elapsed for the crystalline silicate particles to reach the disk surface where they can be detected by means of MIR spectroscopy. This hypothesis is, however, questionable as the large sizes of the amorphous silicates indicate that, at least for dust coagulation, enough time has passed. Recently, Dullemond et al. (2006) found that, assuming the crystallization by thermal annealing happens at the very early phases of disk evolution, the level of crystallinity is linked to the properties of the molecular cloud core from which the disk formed. It was found that rapidly rotating cores produce rather massive disks with a high accretion rate but a low level of crystallinity. As we observe these properties for FU Ori, the proposed model, although yet very simple and with limited predictive power, might provide an interesting way to explain at least partly the lack of crystalline silicates in the FU Ori accretion disk. Finally, another possibility might be that the vertical and radial mixing within the disk does not work as efficient as expected. In consequence, not enough crystalline dust grains reach the disk surface at radii, where the contrast between the emission feature and the dust continuum allows their detection. As will be presented in chapter 6, also other FUors with silicate emission do not show any evidence for crystalline grains. This makes this finding quite interesting and requires further investigations.

3.6.3 Comparison to TTauri stars and HAeBe Stars

The results from the correlated flux allow a comparison to disks around other YSOs that have also been observed with VLTI/MIDI. Crystalline silicates seem to be commonly present in protoplanetary disks, and for three intermediate-mass HAeBes stars van Boekel et al. (2004) found that the degree of crystallization within the disk depends on the distance from the central star. The inner parts of the disks are more crystalline than the outer disk regions. This can be explained by assuming that in the inner disk regions, where the disk has higher temperatures, dust processing and annealing occurs and that over time crystalline particles are transported outwards. Not only for intermediate mass stars but also for the TTauri star RY Tau the same radial dependence of the crystallinity was observed (Schegerer et al., 2007, in preparation). Thus, crystalline silicates should in general

be more easily detectable in the correlated spectra of protoplanetary disks. For reasons mentioned in the previous section it seems thus surprising that the disk around FU Orionis does not seem to contain any detectable amount of crystalline dust.

As described in the introduction, FUors are believed to be low-mass or TTauri-like stars in a state of enhanced accretion. From sub-millimeter and millimeter observations Weintraub et al. (1991) concluded that FUors are possibly in an evolutionary younger stage than classical TTauri stars. Their younger age is also supported by theoretical models where the protostellar disk is continuously replenished by a dusty envelope (see chapter 1). Hence, it is puzzling that apparently in the disk surrounding FU Ori the amorphous grains have already grown considerably. This means that the disk can not be in its native dust composition and might either have a significant age or grain growth sets in very early during the evolution of the disk. Furthermore, from the SPITZER "Formation and Evolution of Planetary Systems (FEPS)" legacy program it is known that apparently the amount of crystalline silicates in TTauri disks is not correlated with the average size of amorphous dust particles (Bouwman et al. 2007, in preparation). Crystalline dust particles are created in the *early* phases of disk evolution where the accretion rate and the disk temperature are thought to be higher. If the FUor-phase is indeed common to most/all TTauri stars, then the non-detection of crystalline particles is even more puzzling.

3.7 A simple disk model

3.7.1 The SED

The work presented in this chapter is more intended to show the observational results rather than to create a sophisticated disk model possibly able to match the observed SED and visibilities with highest accuracy. Thus, instead of applying a complex radiative transfer model, we decided to use a simple analytical disk model in a first step. In this model the effective temperature and also the surface density are prescribed by the following broken power law distributions

$$T(r) = T_{1\mathrm{AU}}\Big(\frac{r}{1\mathrm{AU}}\Big)^{-q} \tag{3.6}$$

$$\Sigma(r) = \Sigma_0\Big(\frac{r}{r_0}\Big)^{-p} \tag{3.7}$$

For equation 3.6 the temperature at 1 AU ($T_{1\mathrm{AU}}$) and the exponent q are free parameters. For the surface density (equation 3.7) the total disk mass M_{D} and the exponent p are free parameters. As the integrated surface density must equal the total mass of the disk the radial dependence of the surface density $\Sigma(r)$ can be computed. The shape of the total SED (and also the observed visibilities) require a double power-law to fit the data. At a radius of 3 AU the temperature and surface density distribution change. However, we made sure that for both parameters the transition was smooth and continuous. Figure 3.8 shows the SED and the resulting fit from the simple disk model. The model parameters are summarized in Table 3.7. Based on the value for the visual extinction A_{V}, we interpolated the extinction for the other wavelengths following the findings of Mathis (1990). The disk inclination i was derived from the ellipses fitted to the FWHM of assumed Gaussian brightness distributions (see subsection 3.5.3). For the position angle θ we used two values: One was already derived in subsection 3.5.3, and for the second one we fitted

Parameter	Variable	Value
Inner disk radius	$R_{\rm in}$	5.5 $R_\odot$
Outer disk radius	$R_{\rm out}$	100 AU
Disk inclination [a]	i	55.4°
Disk position angle [b]	θ	109.1° [a] / 93.4° [c]
Extinction	A_V	2.6
Temperature at 1 AU	$T_{1AU,1}$	670 K
Power law index for temperature	$q1$	-0.75
Power law index for surface density	$p1$	-0.9
Disk mass	$M_{D,1}$	0.03 $M_\odot$
Temperature at 1 AU	$T_{1AU,2}$	550 K
Power law index for temperature	$q2$	-0.53
Power law index for surface density	$p2$	-1.4
Disk mass	$M_{D,2}$	0.01 $M_\odot$

Table 3.7 Parameters of the simple disk model used to fit the SED. The upper part of the table gives the parameters for the inner 3 AU. Farther out in the disk the temperature and surface density follow distributions defined by the parameters in the lower part of the table. [a] As derived in subsection 3.5.3 ; [b] Only required for visibility computation ; [c] Resulting from χ^2-fit

the disk model to the observed visibilities with θ being the only free parameter (see also subsection 3.7.2).

It is evident that this simple approach is not able to reproduce all features of the SED (e.g., the weak silicate emission feature). For the moment, however, we restrict ourselves to this simple approach and, as mentioned above, a detailed modeling is left for further investigations. It is striking that rather high disk temperatures are required to fit the SED. The temperature dependence from the radius is shown in Figure 3.8. In the inner 0.35 AU no dust can withstand the high temperatures >1500 K even on the disk surface, and only the gaseous disk component can survive. It is interesting to note that the power law index of $q1 = 0.75$ of the inner disk region equals exactly the one derived in analytical disk models for (1) geometrically flat, optically thick *passive* disks (e.g., Adams et al., 1987) and for (2) flat, steady state, optically thick *accretion* disks (e.g., Pringle, 1981). Thus, from the temperature distribution alone one can not distinguish between the two different cases (see also Kenyon & Hartmann, 1987). However, in the context of FU Ori the passive disk model, where the disk is merely re-processing radiation from the central star, is unlikely and only an accretion disk model matches most observations (Hartmann & Kenyon, 1996). A nice example is the recently detected magnetic field in the innermost regions of the disk surrounding FU Ori which can only be explained in the picture of a heavily accreting disk (Donati et al., 2005). As in classical accretion disk models the disk temperature is directly related to the mass accretion rate $\dot{M}$, it is possible to derive the $\dot{M}$ required to produce the observed high temperatures. Bell et al. (1997) analyzed the effective disk temperature and also the midplane temperature of an accretion disk as a function of the mass accretion rate. They show in their Figure 1 that one needs $\dot{M} \geq 10^{-5}\,M_\odot$/yr to reach the effective temperature we find in our model. Such high values for $\dot{M}$ were also found by Hartmann & Kenyon (1996) and Lachaume et al. (2003).

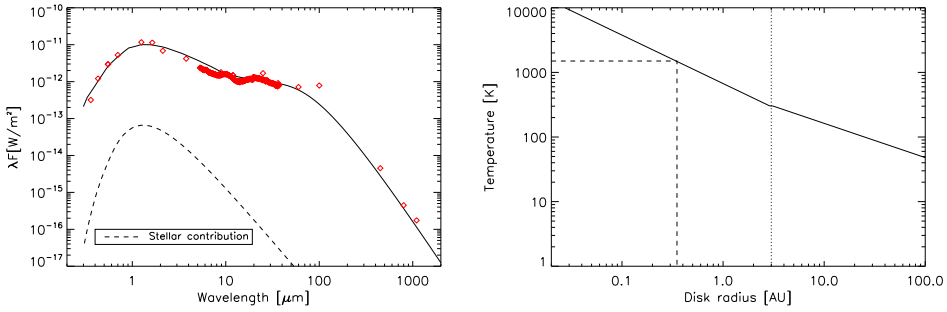

Figure 3.8 *Left:* SED fit of a geometrically thin, optically thick accretion disk model. The disk parameters are shown in Table 3.7. The contribution of the central star (in this case we assume $T_{\rm eff}$ = 3700 K, $R_{\rm star}$ = 2.5 $R_\odot$) can be neglected. Although simple, the disk model agrees reasonably well with the observed fluxes for most wavelength regimes. The data points were taken from Clarke et al. (2005) (U,B,V,R), Przygodda et al. (2003) (8.9 μm, 11.9 μm), Reipurth & Aspin (2004) (J, H, K, L), Weintraub et al. (1991) (450 μm, 850 μm, 1.3mm), SPITZER IRS data archive (MIR Spectrum) and IRAS data archive (12 μm, 25 μm, 60 μm, 100 μm). *Right:* Disk temperature distribution of the simple analytical model. The dotted line at 3 AU indicates where the slope of the temperature distribution changes. The dashed lines show that within the inner 0.35 AU the temperature is above the dust sublimation temperature of 1500 K.

Due to the high accretion rate the midplane temperature of the disk in the inner ≈10 AU is even much higher than the effective disk temperature (Bell et al., 1997). Concerning the temperature law farther out than 3 AU the value we adopt here for $q2$ is in good agreement to what can be found in the literature for isothermal flared disks (Kenyon & Hartmann, 1987). In their model the index value diverges from the flat solution where q = 0.75 at a certain point in the inner disk and approaches q = 0.5 for radii much larger than the stellar radius. At intermediate radii the temperature index might be approximated by values in between these most extreme cases depending on the actual flaring of the disk.

In summary, the temperature distribution indicates that in the innermost disk regions the disk luminosity is accretion dominated whereas farther out it is irradiation dominated. This is expected for an active accretion disk since the luminosity released by accretion is a much steeper function of distance to the star than that by absorption of radiation from the central star and the hot innermost disk regions (roughly one finds: $L_{\rm acc} \propto r^{-4}$, whereas $L_{\rm abs} \propto r^{-2}$).

3.7.2 Model visibilities

Mid-infrared results

For this simple disk model it is straightforward to compute the visibilities as a function of projected baseline and wavelength. Assuming that each part of the disk surface is emitting as a blackbody with an effective temperature $T(r)$ the corresponding total flux and visibility for an axisymmetric face-on disk is given by:

$$F_\lambda = \frac{2\pi}{d^2} \int_{r_{min}}^{r_{max}} r B_\lambda(T(r)) dr \tag{3.8}$$

$$V_\lambda(B_P) = \frac{2\pi}{F_\lambda d^2} \int_{r_{min}}^{r_{max}} r B_\lambda(T(r)) J_0 \left[\frac{2\pi}{\lambda} B_P \frac{r}{d} \right] dr \tag{3.9}$$

with F_λ being the flux, B_λ the Planck function, J_0 the zeroth-order Bessel function of the first kind, B_P the projected baseline and d the distance to the object (see also equations (2), (3), and following in Malbet et al., 2005).

Taking into account the inclination of the disk and the position angle as given in Table 3.7 we computed the corresponding visibilities for the three different baselines. The results for two different position angles are shown in Figure 3.9. In the upper panel the disk inclination and the position angle are derived from the ellipses fitting described in subsection 3.5.3. In the lower panel the position angle was fitted to the observed visibilities with a least squares fit. While the ellipse fitting yielded a position angle of $109.1° \pm 11.6°$ a least square analysis leads to a value of $93.4° \pm 6.8°$. From the plots in Figure 3.9 one realizes that changing the position angle mostly affects the visibility of the shortest baseline while the curves for the other baselines change only marginally.

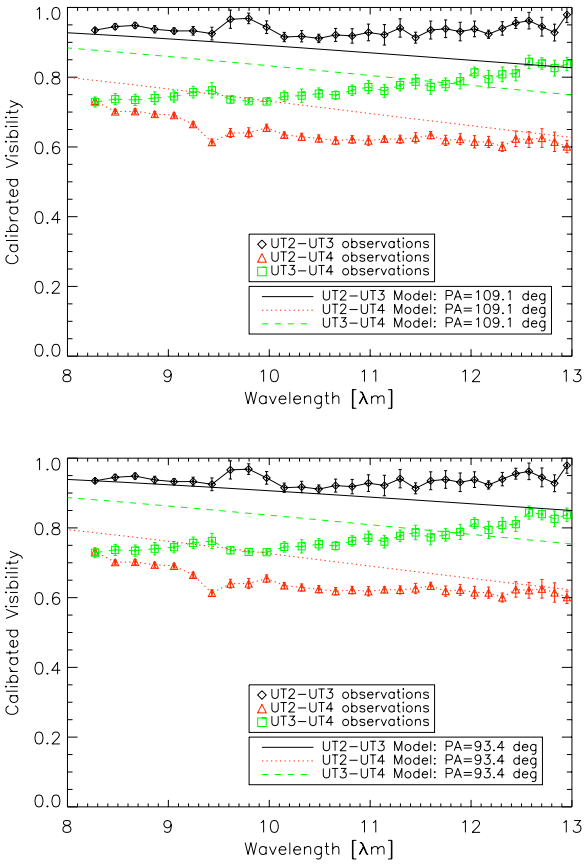

Figure 3.9 MIR visibilities derived from the simple disk model in comparison to the observations. The baselines and projection angles correspond to those given in Table 3.1. The disk position angle was assumed to be 109.1° (top) and 93.4° (bottom). Changing the position angle has the biggest impact on the visibilities of the shortest baseline. Apparently, both models do show the right trend but they can not account for increasing visibilities.

Fitting the UT3-UT4 baseline proofs quite a challenge as the observed visibility is increasing over the 8-13 μm wavelength interval while all other modeled visibilities are decreasing. Especially for this baseline better fits are expected from more sophisticated disk models. However, given the simplicity of the current models the fits seem in reasonable agreement with the observations. It is obvious that interferometric measurements can

put additional constraints on the structure and geometry of circumstellar disks that cannot be derived from SED fitting alone.

Interestingly, Malbet et al. (2005) were able to fit their NIR visibilities of FU Ori with two models: (1) a similar disk model as presented here and (2) a disk with an embedded "hot spot". They concluded that the latter model was more likely based on statistical arguments. The major differences between their models and ours is that (1) they fit the SED with single power laws for the temperature neglecting the flux longward of 20 μm and (2) their best fits yield disk position angles of $47^\circ\,^{+7^\circ}_{-11^\circ}$ and $8^\circ\,^{+21^\circ}_{-21^\circ}$. The inclination angles ($55^\circ\,^{+5^\circ}_{-7^\circ}$ and $48^\circ\,^{+9^\circ}_{-10^\circ}$, respectively), are in good agreement with our value. In Figure 3.10 we compare both of their models to our observations and find that both models do not fit the MIDI visibilities as good as the model presented here. Even more we find that our MIR interferometric measurements rule out their first model of a simple accretion disk. This model predicts a higher visibility for the UT3-UT4 baseline than for the UT2-UT3 baseline which is not observed. The model with an embedded "hot spot" in the accretion disk shows the right trend for the visibilities, but the values for the UT3-UT4 and UT2-UT4 baseline are higher than for our models which already give slightly too high values compared to the observations. The main reason for the higher visibilities resulting from the model applied by Malbet et al. (2005) is the single power law approach which provides less MIR flux compared to our models.

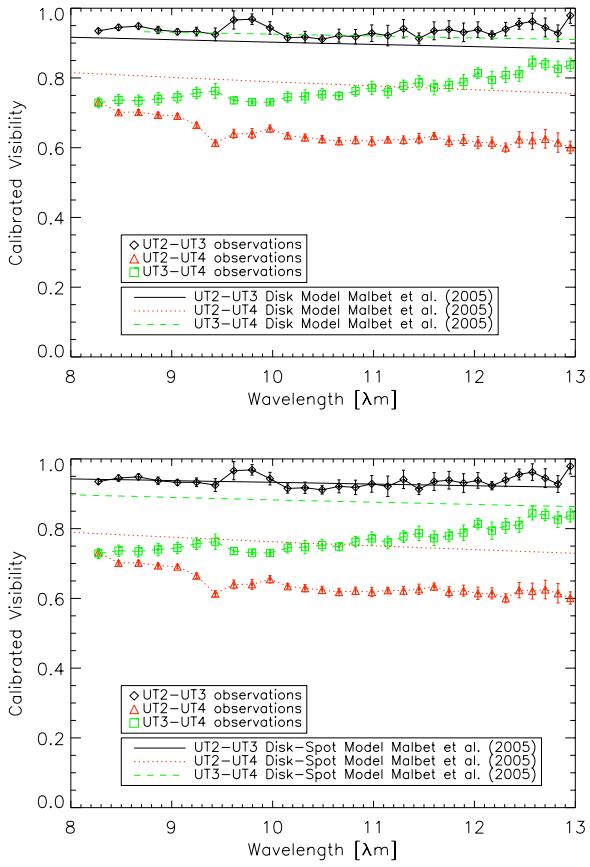

Figure 3.10 MIR visibilities derived from models for FU Ori presented in Malbet et al. (2005) in comparison to the observations. *Top:* Model consisting of a simple accretion disk. This model can be ruled out by our observations as it predicts higher visibilities for the UT3-UT4 baseline than for the UT2-UT3 baseline which is not observed. *Bottom:* Model consisting of an accretion disk and an embedded "hot spot". This model shows the right trend but does not fit the observations as good as the models presented in this chapter.

Near-infrared results

We also compared our models to the measured NIR visibilities from Malbet et al. (2005), restricting ourselves to those observations where the object was clearly resolved. The results are given in Table 3.8. Except for the observations done with north-west baseline of the Palomar Testbed Interferometer (PTI/NW) both of our models agree with the NIR visibilities within the error bars.

Interferometer	Filter	Baseline [m]	Pos. Angle [deg]	V^2 (observed)	V^2 (model)[a]
PTI/NW	H	85.6	14.1	0.79±0.05	0.92 / 0.94
PTI/NS	K	102.7	63.6	0.72±0.08	0.78 / 0.80
PTI/NS	H	103.7	61.8	0.83±0.04	0.80 / 0.82
PTI/SW	K	82.5	-55.6	0.82±0.08	0.85 / 0.87
PTI/NW	K	84.2	14.0	0.79±0.05	0.91 / 0.93
VLTI[b]	K	89.6	54.2	0.87±0.05	0.83 / 0.85

Table 3.8 Comparison of observed NIR square visibilities from Malbet et al. (2005) to our disk model with two different position angles. The observations were carried out with different baselines at the Palomar Testbed Interferometer (PTI) and the Very Large Telescope Interferometer (VLTI). [a]For two different position angles: 109.1° / 93.4°. [b]VINCI data.

Concerning the predicted ”hot spot” in the accretion disk (Malbet et al., 2005) our observations do not yield new insights into its nature as they do not have the required spatial resolution to confirm its existence. Also the calibrated phase of our observations do not contain any information on which basis we could speculate about this possible second companion.

3.8 Conclusions and future prospects

We presented the first multi-baseline MIR interferometric observations of FU Orionis with MIDI/VLTI. The findings can be summarized as follows:

- FU Orionis was clearly resolved in the MIR with two VLTI baselines and marginally resolved with a third baseline indicating the presence of warm dusty material surrounding FU Ori out to several tens of AU.
- The inclination and the position angle of the accretion disk can be inferred from multi-baseline measurements with MIDI/VLTI. Thus, the instrument provides means for deriving disk parameters that are otherwise only poorly constrained from models and SED fits.
- The correlated flux indicates that 95% of the 8-13 μm flux comes from within the inner 25AU of the disk for the shortest of our baselines while 65% of this flux arise from the inner 13AU for our longest baseline.
- The shapes and strengths of the total 8-13 μm spectrum and the (spatially resolved) correlated spectra indicate that most dust particles within the accretion disk are

amorphous and already significantly larger than typical particles in the ISM. If FU Ori is indeed younger than a classical TTauri star then this indicates that grain growth takes already place in the early phases of accretion disk evolution.

- No spectra, neither the total nor the spatially resolved correlated spectra, bear significant traces of crystalline silicates. Given the high accretion rate and disk temperature of the system, this is unexpected. From studies of TTauri stars it is known that crystalline grains should be produced when the accretion rates are higher. Thus, the results presented here require further investigations.

- The SED and the observed MIR visibilities can be fitted reasonably well with a simple analytical disk model prescribing a broken power law for the effective temperature distribution of the protoplanetary disk. Within the innermost 3AU the temperature decreases with $T \propto r^{-0.75}$, farther out the temperature goes with $T \propto r^{-0.53}$. The derived power law index for the inner regions is equal to what is derived theoretically for flat, steady state, optically thick accretion disks (Pringle, 1981). For the outer disk region the derived value is in good agreement to what can be found for isothermal flared disks (Kenyon & Hartmann, 1987).

- From the acquisition image, N-band aperture photometry could be derived for the companion FU Ori S. This young K-type star seems to have more relative MIR excess than FU Ori itself hinting at a circumstellar disk with larger flaring angle or smaller disk inclination.

Putting these results into context with other high spatial resolution studies of FU Ori and other FUors we conclude that:

- Most of the published NIR visibilities of FU Ori (Malbet et al., 2005) do agree with our newly derived disk models.

- Our interferometric observations rule out one out of two disk models for FU Ori presented by Malbet et al. (2005). Due to the lack of sufficient spatial resolution the presence of the proposed second very close companion can neither be confirmed nor disproved with the current set of MIDI data.

- In contrast to NIR interferometric observations of other FUors (Millan-Gabet et al., 2006) our data do not clearly require the introduction of an extended dusty structure providing additional uncorrelated flux.

- For the inner 3AU we require a significantly different disk model (e.g., $\Sigma \propto r^{-0.9}$, $T \propto r^{-0.75}$) to fit our visibilities and SED in comparison to what was found for the outbursting star V1647 Ori ($\Sigma \propto r^{-1.5}$, $T \propto r^{-0.53}$) (Ábrahám et al., 2006).

Although the present results provide important new insights into the FU Ori system new questions arose as well. Future investigations will include a more thorough and detailed modeling of the observations with numerical radiative transfer disk models. These models will not only need to consider the high accretion rates but also such effects as self-irradiation of the disk. It will be interesting to see whether these models are able to confirm the apparent rotation of the disk's position angle with wavelength and whether they can reproduce the increasing visibility curve for the UT3-UT4 baseline. Also, these disk models will have to match the observed NIR and MIR visibilities simultaneously

with higher accuracy than the current simple models. From the observational side, re-measuring the UT3-UT4 baseline might be eligible and any other new baseline configuration will certainly help to constrain the disk geometry (especially the position angle) even better. Concerning the dust structure the lack of crystalline silicates needs to be analyzed in greater detail. Is it just a contrast effect that we do not see any crystalline features in the spectra or are they simply not there? Eventually we will have to face the problem that currently all FUors that have been observed with high spatial resolution techniques draw a rather inhomogeneous picture of the group. Apparently, some are still surrounded by nearby dense envelopes while for others the circumstellar disks suffice to explain the observations. However, even those disk-systems (i.e., FU Ori and V1647 Ori) seem to be different in terms of physical properties as different temperature and surface density profiles are derived.

Without any doubt interferometric observations of circumstellar disks in the NIR and MIR provide an unprecedented means for deriving geometrical disk properties and put new constraints on the physical (and chemical) processes taking place within protoplanetary disks. And as more and more interferometric data of circumstellar disks are published our view on the cradle of planetary systems will be, once more, refined.

4. The environment of the FU Orionis stars RNO 1B/1C

Deeply embedded objects and shocked molecular hydrogen

Parts of this chapter were published in the Astrophysical Journal.
(Quanz, S. P., Henning, Th., Bouwman, J., Linz, H., Lahuis, F., 2007, ApJ 658, 487)

IN THIS CHAPTER observations of the dark cloud L1287 with SPITZER IRAC and IRSare presented. The mid-infrared (MIR) IRAC images show deeply embedded infrared sources in the vicinity of the FU Orionis objects RNO 1B and RNO 1C suggesting their association with a small young stellar cluster. We resolve for the first time the MIR point source associated with IRAS 00338+6312 which is a deeply embedded intermediate-mass protostar driving a known molecular outflow. The IRAC colors of all the objects are consistent with those of young stars ranging from deeply embedded Class 0/I sources to Class II objects, some of which appear to be locally reddened. The two IRS spectra show strong absorption bands due to ices and dust particles, confirming that the circumstellar environment around RNO 1B/1C has a high optical depth. Additional hydrogen emission lines from pure rotational transitions are superposed on the spectra. Given the outflow direction, we attribute these emission lines to shocked gas in the molecular outflow powered by IRAS 00338+6312. The derived shock temperatures are in agreement with predictions for high-velocity C-type shocks.

4.1 Introduction

The dark cloud L1287 contains the Galactic nebulae GN 00.34.0 (associated with the young F-type star RNO 1) and GN 00.33.9. The latter one harbors the point source IRAS 00338+6312 (d = 800 pc; Persi et al., 1988). Two young stars, RNO 1B and RNO 1C,[1] lie slightly to the south west of the catalog position of the point source. These objects exhibit properties of FU Orionis objects: (1) Staude & Neckel (1991) found that RNO 1B brightened by at least 3 mag over a period of 12 years and that it shows a variable and blueshifted P Cygni profile in Hα and additional broad and double-peaked absorption lines in its optical spectrum, and (2) Kenyon et al. (1993) obtained near-infrared spectroscopic data for

[1] We use the same nomenclature as Staude & Neckel (1991)

both objects and found the FUor-typical strong 2.3 μm CO absorption bands. As the error ellipse of the IRAS source includes both objects, it was debated whether there is yet another deeply embedded source close to the FUor objects or whether IRAS (the INFRARED ASTRONOMICAL SATELLITE) just measured the integrated flux from these two objects. From high-resolution, near-infrared polarimetric maps, Weintraub & Kastner (1993) concluded that an additional embedded object should be present close to the location of the IRAS source. This idea was supported by the discovery of a 3.6 cm continuum peak (Anglada et al., 1994) and an H_2O maser (Fiebig, 1995), both nearly coincident with the IRAS position. A bipolar outflow in the region was found by Snell et al. (1990) and later confirmed by Yang et al. (1991). As the positions of the IRAS source and the FUors line up along the outflow axis, it has long been uncertain which source is driving the outflow. From interferometric observations in CS, Yang et al. (1995) suggested that the IRAS source was the most likely candidate. Recently, Xu et al. (2006) mapped the outflow in CO and came to the same conclusion. However, McMuldroch et al. (1995) presented (sub-)millimeter observations favoring RNO 1C as the outflow's driving source.

In this chapter, we present mid-infrared (MIR) imaging and spectroscopic data taken with the INFRARED ARRAY CAMERA (IRAC) and INFRARED SPECTROGRAPH (IRS) on board the SPITZER SPACE TELESCOPE. The MIR point source associated with the IRAS source is resolved, and we find additional, partly deeply embedded, objects. The two IRS spectra probe the composition of the dense circumstellar environment in the vicinity of RNO 1B/1C and bear additional traces of shocked H_2 gas.

4.2 Observations and data reduction

All data were part of Guaranteed Time Observation program 124 by R. Gehrz and are publicly available from the SPITZER archive. An overview of the observational setup and the data sets is provided in Table 4.1. The IRAC images were obtained in sub-array mode, leading to an effective field-of-view of $\sim 40''$ centered on the position given in Table 4.1. The spectra taken with the IRS cover the wavelength range 5-37 μm. Overplotting the IRS spectral slits on the Two Micron All Sky Survey (2MASS) Ks-filter image reveals that RNO 1B and RNO 1C apparently were not centered within the slits (Figure 4.1). The short-wavelength, low-resolution spectrum (5.2-14.5 μm, R $\sim$ 64-128) and the short-wavelength, high-resolution spectrum (9.9-19.6 μm, R $\sim$ 600) close to RNO 1B seem mainly to probe flux coming from between the two objects. The spectrum close to RNO 1C presumably also contains less flux than expected as a result of the slight mispointing. The long-wavelength, high-resolution part of each spectrum (18.7-37.2 μm, R $\sim$ 600) includes flux from both components and additional flux from the IRAS source, as all three objects lie within the slit of the spectrograph.

The IRAC images were reduced with the MOPEX package provided by the SPITZER Science Center. Interpolation, outlier detection, and co-addition of the images were carried out for each filter individually. The astrometry was refined by comparing the positions of detected sources with known 2MASS objects. The photometry was carried out with the `DAOPHOT` package provided within the `IRAF`[2] environment. As there were only a limited number of sources available within the small field covered by the camera, we measured the point-spread function (PSF) of RNO 1C and used it as a reference in order to perform

[2] See http://iraf.noao.edu/

Instrument	RA (J2000)[a]	DEC (J2000)[a]	AOR Key	Filter [μm] or Module	Ramp duration / # of Cycles	Frame Time / # of Frames / Dither Positions	Date
IRAC	00:36:45.8	+63:28:56	5027072	3.6, 4.5, 5.8, 8.0	-	0.4 s / 1 / 4	2003-12-20
IRS	00:36:46.34[b]	+63:28:53.76[b]	6586624	Low Resolution	6 s / 3	-	2004-01-07
	00:36:46.89[c]	+63:28:58.44[c]					
IRS	00:36:46.34[b]	+63:28:53.76[b]	6586624	High Resolution	6 s / 5	-	2004-01-07
	00:36:46.89[c]	+63:28:58.44[c]					

Table 4.1 Journal of SPITZER observations of the RNO 1 region. [a]Average slit position (low resolution spectrograph) in case of spectroscopic observations. [b]close to RNO 1B. [c]close to RNO 1C.

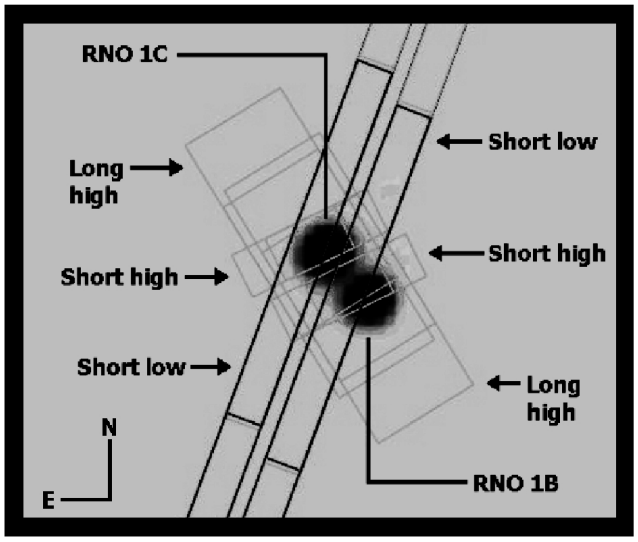

Figure 4.1 Slits of the different modules of the SPITZER IRS overplotted on the inverted 2MASS Ks-filter image. The two FUors RNO 1B and RNO 1C are not centered in the slits. North is up, and east is to the left.

PSF photometry for all the other sources. Following the IRAC Data Handbook (section 5.1.1), we converted the pixel values from MJy sr^{-1} to DN s^{-1} and computed the corresponding magnitudes as $m = -2.5\,log(x) + \Delta_{ZP}$, with x denoting the flux measured in DN s^{-1} and Δ_{ZP} being the zero point for each filter.[3] For the initial PSF fit, we used a PSF size of 2 pixels and applied aperture corrections as described in the Data Handbook to obtain the final magnitudes.

Our final IRS spectra are based on the intermediate `droopres` (for the low-resolution data) and `rsc` (for the high-resolution data) products processed through the S13.2.0 version of the SPITZER data pipeline. Partially derived from the `SMART` software package (Higdon et al., 2004), these intermediate data products were further processed using spectral extraction tools developed by the "Formation and Evolution of Planetary Systems" (FEPS) SPITZER Legacy Science team (see, Explanatory Supplement version 3.0 within the FEPS data deliveries.[4])

For the short low-resolution observations, the spectra where extracted using a 6.0 pixel fixed-width aperture in the spatial dimension resulting in a 39.96 arcsec^2 extraction aperture on the sky. The background was subtracted using associated pairs of imaged spectra from the two nodded positions along the slit. This process also subtracts stray-light contamination from the peak-up apertures and adjusts pixels with anomalous dark current relative to the reference dark frames. Pixels flagged by the SPITZER data pipeline as being "bad" were replaced with a value interpolated from an 8 pixel perimeter surrounding the errant pixel. The high-resolution spectra were extracted with the full aperture size (53.11 arcsec^2 for the Short-High and 247.53 arcsec^2 for the Long-High module). The sky contribution was estimated by fitting a continuum to the data. Both, the low- and high-resolution spectra, were calibrated using a spectral response function derived from IRS spectra appropriate for the two nod positions in the slit at which we extracted the spectra, and Cohen or MARCS stellar models for a suite of calibrators provided by the SPITZER Science Center. The multiple orders in our spectra match to within 10%. These small flux

[3] Zero points taken from Hartmann et al. (2005): 19.66 (3.6 μm), 18.94 (4.5 μm), 16.88 (5.8 μm), and 17.39 (8 μm).

[4] See http://ssc.spitzer.caltech.edu/legacy/fepshistory.html

offsets are likely related to small pointing offsets. We computed correction factors for possible flux loss due to telescope mispointing based on the PSF of the IRS instrument. However, accurate results can only be obtained if the flux is dominated by one source. The offsets also result in low-level fringing at wavelengths longer than 20 μm in the low-resolution spectra and at all wavelengths in the high-resolution spectra. We removed these fringes using the `IRSFRINGE` package (developed by F. L.). The relative errors between spectral points within one order are dominated by the noise on each individual point and not by the calibration. Based on our experience with SPITZER IRS data, we estimate a relative flux calibration error across a spectral order of $\approx 5\%$ and an absolute calibration error between orders or modules of $\approx 10\%$. These values, however, are based on point-source observations with accurate telescope pointing. The data presented here are more complicated, as at least part of the emission is moderately extended, multiple sources contribute to the observed fluxes, each contribution is wavelength dependent, and the telescope slits were not centered on the main objects. Thus, an accurate flux calibration between the different modules is difficult; apparent offsets are discussed further in section 4.3.2.

4.3 Results

4.3.1 IRAC photometry

Within the limited field-of-view of the IRAC subarray mode, we identified eight sources that were detected in at least three of the four IRAC bands. Figure 4.2 provides a comparison between the RNO 1B/1C region as seen in the 2MASS Ks filter and the 5.8 μm IRAC filter. For the first time, the MIR point source related to IRAS 00338+6312 is detected in the IRAC band. Additional, fainter objects are also present, some of which have not yet been detected before. Figure 4.3 shows a color composite image of the RNO 1B/1C complex based on three IRAC filters. Table 4.2 lists all objects that were identified in at least three IRAC bands and summarizes the derived fluxes. The errors are based on the results from the PSF-photometry. Since we used the PSF of RNO 1C as reference, the corresponding errors are relatively small compared with the other objects'.

IRAS 00338+6312 and RNO 1G[5] were not detected in the shortest IRAC band, at 3.6 μm. The 2MASS image in Figure 4.2 shows that at least the IRAS source is deeply embedded in a dense, dusty environment, explaining the non-detection at this wavelength. Figure 4.4 shows two color-color plots based on the four IRAC bands for all objects listed in Table 4.2. Following Hartmann et al. (2005), who analyzed a large sample of pre-main-sequence stars in the Taurus star-forming region, we use these plots to classify the different objects. The colors of the reddest objects (IRAS 00338+6312 and RNO 1G) are consistent with those of very young protostars. The colors of the newly discovered objects RNO1 IRAC 1 and RNO1 IRAC 3 are consistent with Class 0/I systems, although it still has to be confirmed that these are indeed nearby objects and not highly reddened background sources. While the colors of the FUor object RNO 1C fit in the region of Class II objects from Hartmann et al. (2005) in both plots (Figure 4.4), RNO 1B fits into this regime only in one color-color diagram. In the right panel of Figure 4.4 RNO 1B is too red for a Class II source in the [4.5]-[5.8] color, but not red enough in the [3.6]-[4.5]

[5]The object we call RNO 1G appears to be identical to the embedded young stellar object from Weintraub & Kastner (1993).

No.	Object name	RA (J2000)[a]	DEC (J2000)	3.6 μm [mag]	4.5 μm [mag]	5.8 μm [mag]	8.0 μm [mag]
1	RNO 1B	00:36:46.05	+63:28:53.29	7.16±0.13	6.67±0.06	5.76±0.12	5.01±0.09
2	RNO 1C	00:36:46.65	+63:28:57.90	6.56±0.01	6.04±0.01	5.58±0.01	4.61±0.02
3	RNO 1F	00:36:45.74	+63:29:04.09	10.28±0.09	9.46±0.08	8.58±0.05	8.20±0.03
4	RNO 1G[a]	00:36:47.14	+63:28:49.95	-	10.33±0.06	8.74±0.04	8.05±0.07
5	IRAS 00338+6312	00:36:47.34	+63:29:01.61	-	9.05±0.07	7.19±0.05	6.72±0.03
6	RNO1 IRAC 1	00:36:48.44	+63:28:39.98	13.72±0.15	11.82±0.14	10.93±0.20	9.65±0.04
7	RNO1 IRAC 2	00:36:47.90	+63:28:36.30	12.00±0.08	10.86±0.10	10.86±0.16	9.82±0.14
8	RNO1 IRAC 3	00:36:47.85	+63:28:41.23	13.07±0.10	11.78±0.08	10.74± 0.10	9.74±0.05

Table 4.2 Apparent brightness at different wavelengths for objects that were detected in at least three IRAC bands. The coordinates are measured in the 3.6 μm image. Only the positions of the IRAS source and RNO 1G were measured in the 4.5 μm exposure. [a]Embedded YSO from Weintraub & Kastner (1993).

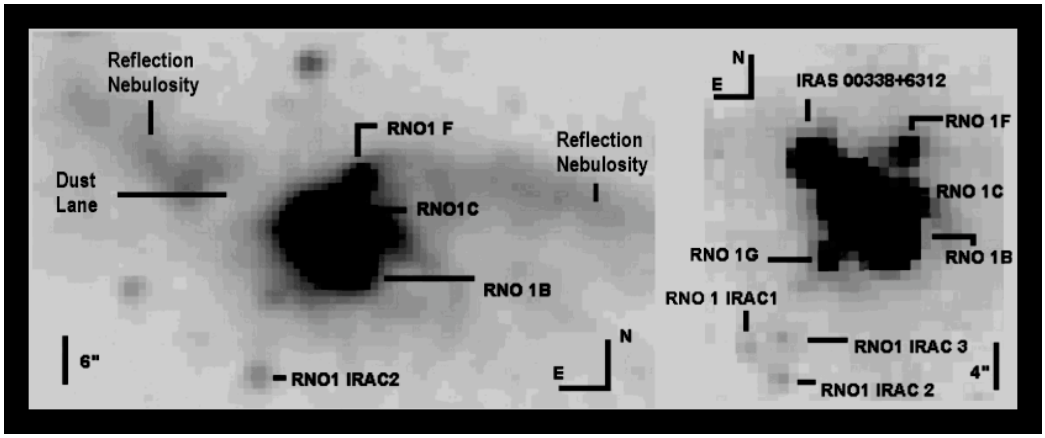

Figure 4.2 RNO 1B/1C region in the 2MASS Ks filter (left) and the 5.8 μm IRAC filter (right). The images are inverted and the contrast also set to make also fainter objects visible. The IRAC image contains more sources, and in particular, the IRAS source clearly shows up at 5.8 μm, whereas it seems hidden behind a dust lane in the 2MASS image. The magnitudes of the individual sources are listed in Table 4.2.

color to be a Class 0/I object. Finally, RNO1 IRAC 2 and RNO 1F, which both show up in the 2MASS Ks-band image, can also be interpreted as Class II objects. However, the colors of RNO1 IRAC 2, and partly also those of RNO 1F, may have been altered by local extinction effects.

4.3.2 IRS spectroscopy

In Figure 4.5 we show the SPITZER IRS spectra without any extinction correction. As pointed out above, the spectral slits of the short wavelength modules were apparently not directly centered on the objects RNO 1B and RNO 1C, and thus the measured fluxes cannot be attributed to these objects with very high accuracy. Also, there seems to be an offset in the flux in the high-resolution regime compared with the low-resolution part of the spectrum. To see to what extent this effect is caused by different aperture sizes, we plot the spectra in intensities (i.e., flux density per solid angle) rather than in janskys per wavelength. This shows, however, that even after this correction significant offsets remain: around 13 μm, the difference between the low-resolution spectrum and the short-wavelength, high-resolution spectrum amounts to factors of ≈ 1.25 and ≈ 1.08 for RNO 1B and RNO 1C, respectively, with the high-resolution part showing higher intensities. At least for the RNO 1B spectrum, this offset is larger than normally expected from the calibration accuracy. We thus believe that part of this offset can be attributed to the different orientations of the spectral slits on the sky probing different regions of the extended emission. The offset between the short- and long-wavelength ranges of the high-resolution data corresponds to factors of ≈ 1.5 and ≈ 2.0 at 20 μm for RNO 1B and RNO 1C, respectively. Also, here the short high-resolution spectrum shows higher intensities. This can be explained by the approximately 5 times smaller aperture in the Short-High module. Although this aperture is probing significantly smaller regions on the sky, these regions do presumably contribute in total to flux in the wavelength regime above mentioned . The large aperture of the Long-High module, on the other hand, is certainly also probing regions without any significant flux (see also Figure 4.1).

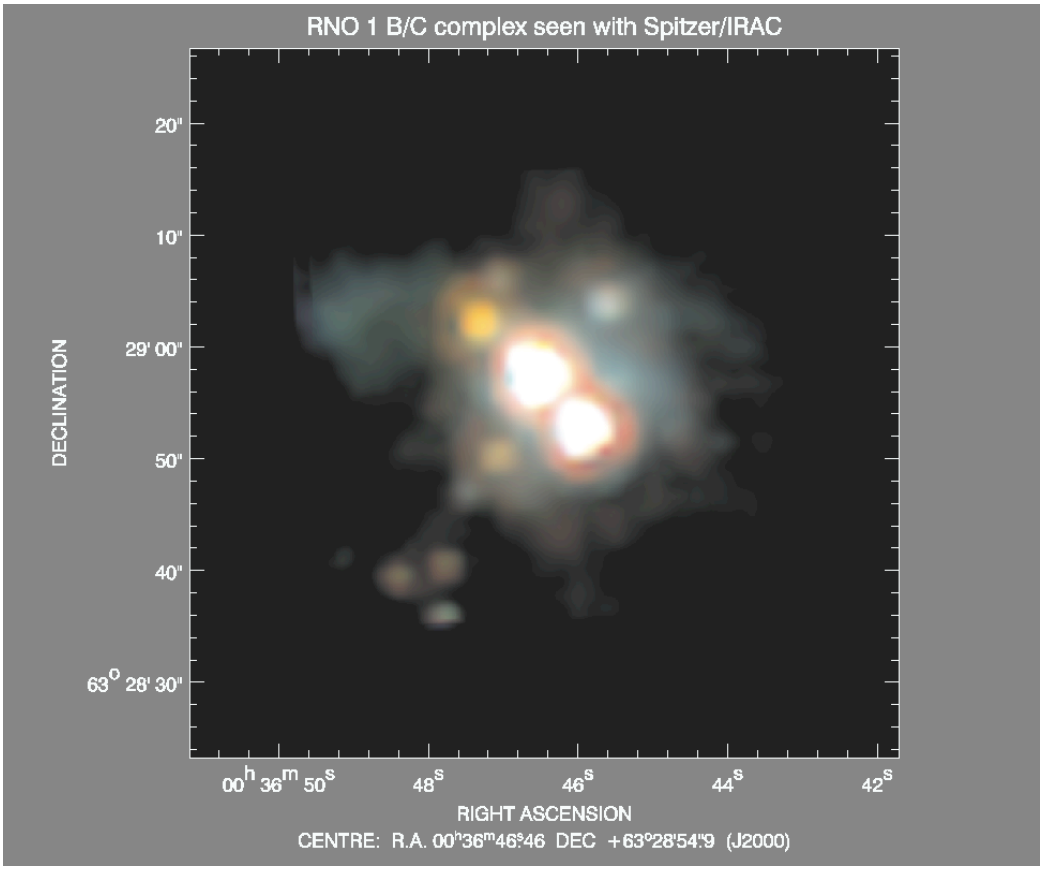

Figure 4.3 Color composite of the RNO 1B/1C region based on the three IRAC bands at 3.6, 4.5, and 8.0 μm. The image is centered on RNO 1C. We applied a logarithmic color stretch to enhance the fainter sources. The extended emission east of the IRAS source, which is predominantly seen in the 4.5 μm filter (green) is possibly related to H_2 emission within the bipolar outflow of this object.

Ices and silicates

At 6 μm, both spectra show clear water ice absorption bands. At slightly longer wavelength ($\sim$ 6.85 μm), additional absorption, possibly arising from NH_4^+ (Schutte & Khanna, 2003) or CH_3OH ice (van Dishoeck, 2004), is present. The 10 μm silicate band is also seen in absorption in both spectra (stronger close to RNO 1C), although the shape of the feature differs from the absorption feature caused by typical silicate grains in the interstellar medium (ISM). To analyze the differences in more detail, we fitted a continuum to the 10 μm region of the spectra and computed the optical depth (Figure 4.6). In both cases the peak of the absorption is slightly shifted toward shorter wavelengths, indicating a non–ISM-like dust composition. Additional absorption (RNO 1C) or possibly additional dust emission on top of the absorption feature (RNO 1B) is seen at longer wavelengths. At 15.2 μm, CO_2 ice creates a strong absorption band, and at $\sim$ 18 μm additional silicate absorption seems to be present. All these features indicate the existence of a dense dusty and icy environment in which the two FUors are embedded. A further analysis of these features will be presented in chapter 6.

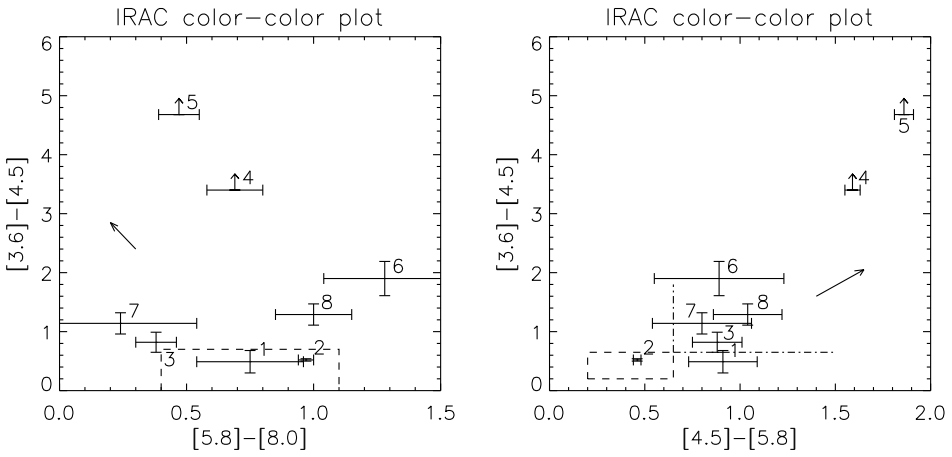

Figure 4.4 IRAC color-color plots for the objects listed in Table 4.2. The dashed boxes indicate the regions corresponding to Class II objects from Hartmann et al. (2005). The dash-dotted region in the right panel defines the position of Class 0/I sources in Hartmann et al. (2005). In the left panel, the Class 0/I objects from Hartmann et al. (2005) have the same [5.8]-[8.0] colors as the Class II objects but redder [3.6]-[4.5] colors. Thus, they lie "above" the dashed box. The reddening vectors correspond to $A_V = 30$ mag and are based on a Vega-like spectrum and the reddening law given by Mathis (1990).

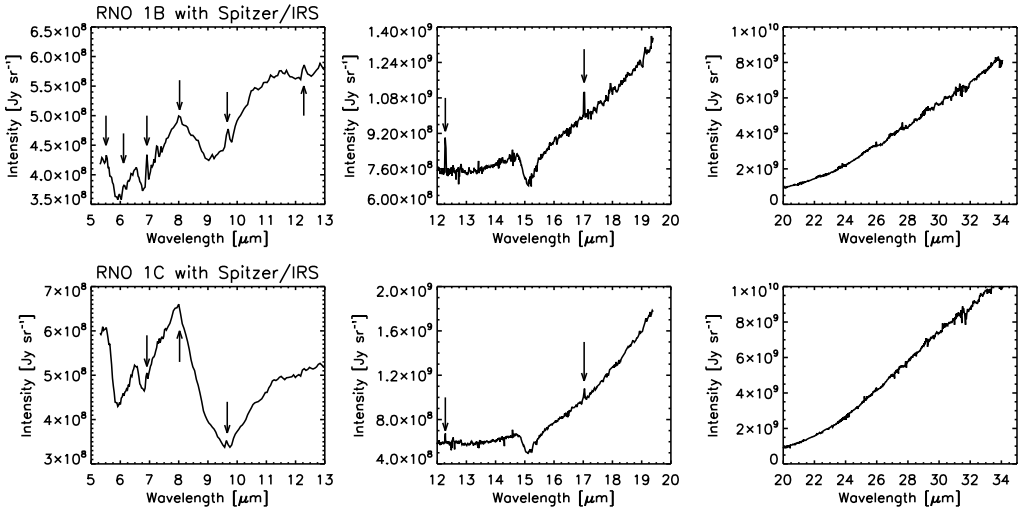

Figure 4.5 SPITZER IRS spectra close to RNO 1B (top) and RNO 1C (bottom). The leftmost column shows the low-resolution data while the other two columns present the high-resolution spectra. The positions of the H_2 emission lines are indicated by arrows.

Pure rotational H_2 emission

In addition to the ice and silicate features, H_2 emission lines from purely rotational quadrupole transitions are present in both spectra (Figure 4.5). While in the spectrum close to RNO 1B all transitions from S(1) to S(7) can be identified, the spectrum close to

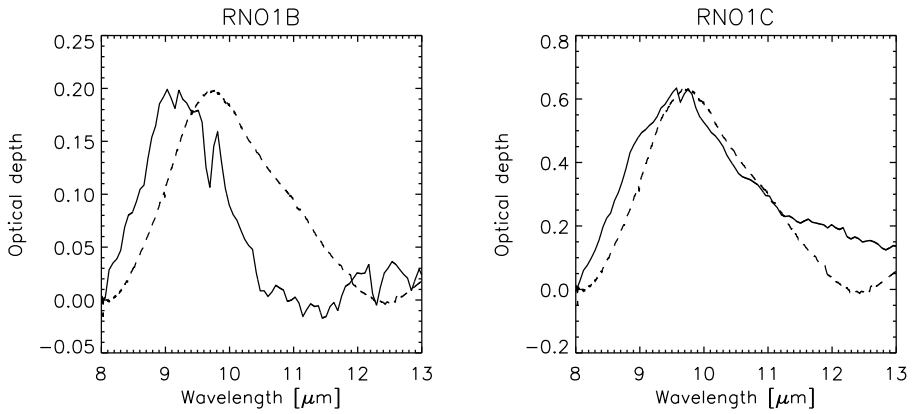

Figure 4.6 Comparison of the optical depth of the 10 μm absorption feature with a typical ISM absorption feature. The solid lines show the optical depth observed toward the RNO complex, while the dashed lines represent the (scaled) optical depth toward the Galactic center (Kemper et al., 2004). The absorption in the RNO region cannot be solely caused by pure ISM silicate grains, as both absorption features seem to be slightly shifted toward shorter wavelengths. Furthermore, while the spectrum close to RNO 1C shows additional absorption longward of 11 μm (possibly blended with H_2O ice at 13 μm), the feature close to RNO 1B is too narrow, and an additional emission feature might contribute longward of $\sim$10.5 μm.

RNO 1C shows only the lines from S(1) to S(5). This can be accounted for with the higher continuum flux close to the S(6) and S(7) lines in the latter spectrum and with apparently lower excitation temperatures (see below). The lowest transition, S(0), near 28.22 μm, is not detected in either spectrum. This is a consequence of the strongly rising continuum at longer wavelengths. Here the spectral slit contained flux from both RNO objects and also from the deeply embedded IRAS source, so that the continuum emission and the related flux errors completely dominate a possible weak emission line. A detailed analysis is provided in Appendix D.

Keeping in mind the molecular outflow that is powered by IRAS 00338+6312 and directly oriented in the direction of RNO 1C and RNO 1B (see, e.g., Xu et al., 2006), the detection of H_2 emission lines in both spectra hints at shock-induced emission related to the outflow. The spectra consequently bear information about the circumstellar material close to RNO 1B/1C and the outflow coming from the IRAS source. Since we observe H_2 lines even in the 10 μm silicate absorption bands, the outflow appears to lie in front of the dusty environment, as otherwise the high extinction ($A_V = 9.2$ mag and $A_V \approx 12.0$ mag for RNO 1B and RNO 1C, respectively; Staude & Neckel, 1991) would have prevented a detection. The measurement of the relative strengths of multiple H_2 lines allows an analysis of the physical conditions of the shocked material. For this we assume local thermal equilibrium (LTE) and optically thin line emission which is supported by the low Einstein coefficients of the involved quadrupole transitions (Table 4.3). Following Parmar et al. (1991) the column density of an upper energy level $N_u(J)$ is then given by

$$N_u(J) = \frac{4\pi}{e^{-\tau}} \frac{I(J)}{A_{ul}\,\Delta E_{ul}}\ \mathrm{cm}^{-2} \tag{4.1}$$

where $I(J)$ denotes the observed line intensity in erg s^{-1} cm^{-2} sr^{-1}, ΔE_{ul} is the energy difference between the two states involved in the transition, A_{ul} is the Einstein coefficient

for the transition and τ is the optical depth at the observed wavelength. In Figure 4.7 we show Gaussian fits to the observed emission lines in the spectrum close to RNO 1B, and Figure 4.8 presents corresponding fits to the lines detected close RNO 1C.

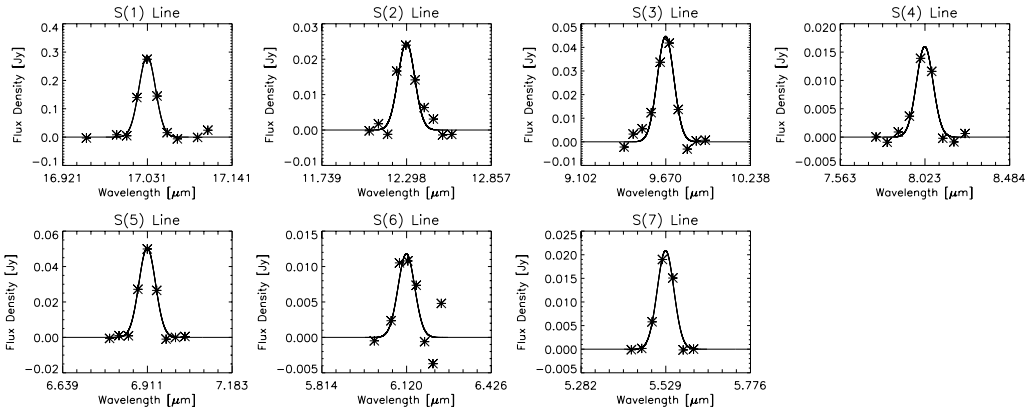

Figure 4.7 Gaussian fits to the H_2 lines in the spectrum close to RNO 1B after continuum subtraction. The line at 12.28 μm shown here was measured in the low-resolution spectrum. Table 4.3, however, contains the flux of this line measured in both the low- and high-resolution parts of the spectrum. The line at 6.11 μm is blended with the ice feature in this region.

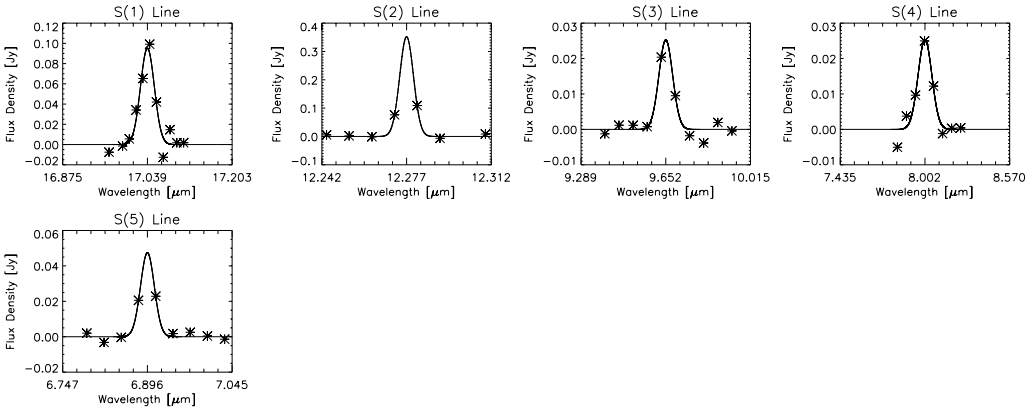

Figure 4.8 Same as Figure 4.7 but for the spectrum close to RNO 1C. Here, the 12.28 μm line was only detected in the high-resolution spectrum.

Before fitting the emission lines, we subtracted the underlying continuum, which was fitted with a second-degree polynomial. The integrated line fluxes and column densities that were finally derived are listed in Table 4.3. We corrected the line fluxes for extinction effects using the results of Mathis (1990) and assuming $A_V = 3.55$ mag. This value represents the extinction found by Staude & Neckel (1991) toward the nearby star RNO 1 and should be a better estimate of the line-of-sight extinction than the extinction values mentioned above toward RNO 1B and RNO 1C. In any case, the influence of the extinction on the derived shock temperatures and column densities (see below) is negligible. The 1-σ errors in the line flux, the line intensity and the column density (Table 4.3) were derived by generating 500 spectra and adding Gaussian noise to each measured flux point

based on the initial individual 1-σ uncertainty. From these spectra we computed the mean values and related errors of the listed parameters. Especially, at the short-wavelength end, this shows that not all lines were detected at the 3-σ confidence level. However, since most lines were convincingly measured, we decided to keep the tentative detections in our analyses.

Since we assume LTE, the rotational energy levels will be populated following Boltzmann statistics with a unique temperature for several lines. The involved temperatures $T_{\rm rot}$ of the shocked material can be derived from a so-called "rotational diagram". By using the results from equation. 4.1, plotting the logarithm of $N_u(J)/(g_s g_J)$ against E_J/k (i.e. the formal temperature corresponding to the absolute upper energy level of the respective rotational transition), and fitting a straight line to the data, one finds that the slope of the line is proportional to $-1/T_{\rm rot}$. Here g_s denotes the spin degeneracy of each energy level (1 for even J, 3 for odd J) and $g_J = 2J + 1$ is the rotational degeneracy. These numbers assume that the ortho-to-para ratio of the involved hydrogen is close to its LTE value of 3 at $T_{\rm rot}$. A deviation from this LTE assumption (i.e., ortho-to-para < 3) would result in a downward displacement of the data points with an odd J-number (ortho-H_2) relative to the points with even J (para-H_2) and thus create a "zig-zag" pattern in the rotational plot (see, e.g., Neufeld et al., 2006; Wilgenbus et al., 2000).

In Figures 4.9, 4.10, and 4.11, we show rotational plots for the measured lines near RNO 1B and RNO 1C. In all the plots, the error bars for the data points denote the 1-σ uncertainty in the measured column density.

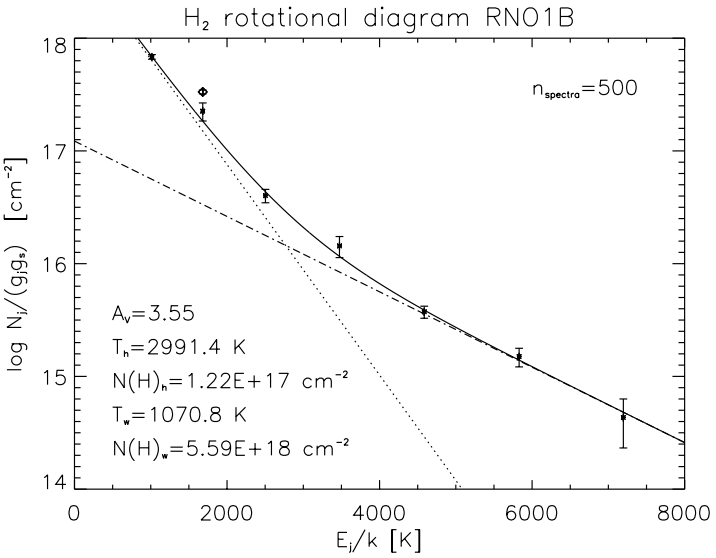

Figure 4.9 Rotational diagram of the H_2 lines shown in Figure 4.7. The data are well constrained by the superposition of a hot and a warm component, providing upper and lower limits for the temperature range of the shocked gas. The diamond at $\approx$1682 K corresponds to the 12.28 μm line measured in the high-resolution module. The observed line flux, and hence the derived column density, is slightly higher than that in the low-resolution spectrum. For the fit, however, the low-resolution data point was used, as all other higher energy data points were also obtained with the low-resolution spectrograph and uncertainties related to the different apertures and their orientations for the high- and low-resolution modules are thus minimized.

Transition	Wavelength [μm]	Energy [a] E$_J$/k [K]	A-Coeff.[b] [s^{-1}]	Beam Size[c] [arcsec^2]	Line Flux[d] [W cm^{-2}]	Line Intensity[d] [erg cm^{-2} s^{-1} sr^{-1}]	Column Density[d,e] [cm^{-2}]
				H_2 lines close to RNO 1B			
S(1) J=3-1	17.0348	1015.08	4.76(-10)	53.11	7.91(-21)±3.8(-22)	6.34(-5)±3.0(-6)	1.44(19)±6.8(17)
S(2) J=4-2	12.2786	1681.63	2.75(-9)	53.11	1.33(-20)±5.2(-22)	1.06(-4)±4.1(-6)	3.00(18)±1.2(17)
				39.96	6.75(-21)±1.2(-21)	7.18(-5)±1.3(-5)	2.03(18)±3.7(17)
S(3) J=5-3	9.6649	2503.73	9.83(-9)	39.96	2.00(-20)±2.7(-21)	2.13(-4)±2.9(-5)	1.33(18)±1.8(17)
S(4) J=6-4	8.0251	3474.48	2.64(-8)	39.96	9.12(-21)±1.9(-21)	9.71(-5)±2.1(-5)	1.87(17)±4.0(16)
S(5) J=7-5	6.9095	4585.94	5.88(-8)	39.96	2.13(-20)±2.6(-21)	2.26(-4)±2.8(-5)	1.68(17)±2.1(16)
S(6) J=8-6	6.1086	5829.66	1.14(-7)	39.96	7.04(-21)±1.3(-21)	7.50(-5)±1.4(-5)	2.54(16)±4.8(15)
S(7) J=9-7	5.5112	7196.20	2.00(-7)	39.96	1.32(-20)±6.1(-21)	1.41(-4)±6.5(-5)	2.46(16)±1.1(16)
				H_2 lines close to RNO 1C			
S(1) J=3-1	17.0348	1015.08	4.76(-10)	53.11	3.26(-21)±2.7(-22)	2.61(-5)±2.1(-6)	5.92(18)±4.8(17)
S(2) J=4-2	12.2786	1681.63	2.75(-9)	53.11	5.17(-21)±7.7(-22)	4.14(-5)±6.2(-6)	1.17(18)±1.7(17)
S(3) J=5-3	9.6649	2503.73	9.83(-9)	39.96	7.52(-21)±2.0(-21)	8.00(-5)±2.1(-5)	4.98(17)±1.3(17)
S(4) J=6-4	8.0251	3474.48	2.64(-8)	39.96	1.34(-20)±4.1(-21)	1.43(-4)±4.4(-5)	2.74(17)±8.5(16)
S(5) J=7-5	6.9095	4585.94	5.88(-8)	39.96	1.10(-20)±3.3(-21)	1.17(-4)±3.5(-5)	8.69(16)±2.6(16)

Table 4.3 Properties of the observed Hydrogen emission lines close to RNO 1B and RNO 1C. The numbers in parentheses denote powers of 10. The 12.28 μm emission line close to RNO 1B was measured in the low- and high-resolution part of the spectrograph. See text for discussion about the apparent flux difference between the two measurements. [a]Energy level of the upper state following Jennings et al. (1987). [b]Wolniewicz et al. (1998). [c]Corresponds to the instrument aperture size in case of the Short-High module (53.11 arcsec^2; see the SPITZER Observer's Manual). For all other transitions (i.e., Short-Low module) the number denotes the extracted beam size during the data reduction process (39.96 arcsec^2). [d]Corrected for extinction using A_V = 3.55 mag. [e]Upper energy state.

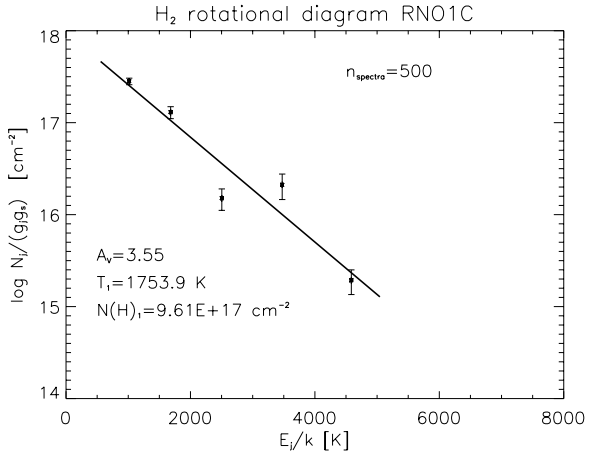

Figure 4.10 Rotational diagram of the H_2 lines shown in Figure 4.7. The apparent zig-zag pattern is indicative of an ortho-to-para ratio smaller than 3.

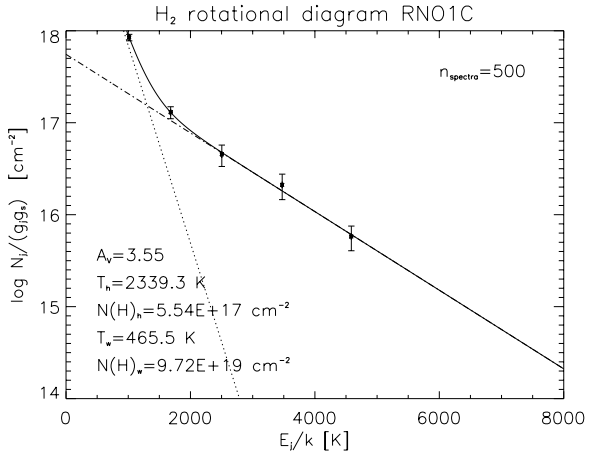

Figure 4.11 Same as Figure 4.10, but for an assumed ortho-to-para ratio of 1. A two component fit similar to that in Figure 4.9 is now possible.

The rotational diagram for RNO 1B in Figure 4.9 shows a clear curvature in the data points. This departure from a single straight line is indicative of several temperature components in the shocked material. We thus fitted the data with two superposed temperature regimes (hot and warm) that represent the minimum and maximum of the involved temperatures rather than any distinct intermediate value. The dash-dotted line fits the high-energy regime and represents the hot component, with a temperature of 2991 ± 596 K. The dotted line corresponds to a temperature of 1071 ± 121 K, designating the warm component. The uncertainties in the temperatures denote the 1-σ confidence level of the fits. As the derived temperature is extremely sensitive to the slope of the fitted straight line, the corresponding errors are rather large.

In addition to the temperatures, one can also derive the total H_2 column density of the observed shock within the given aperture. From the y-intersects of the fits, we estimate the hot component to have $N_{1B}^{\rm hot}(H_2) \approx 1.2 \times 10^{17} {\rm cm}^{-2}$, and for the warm component we find $N_{1B}^{\rm hot}(H_2) \approx 5.6 \times 10^{18} {\rm cm}^{-2}$.

For the column densities derived from the spectrum close to RNO 1C, we plotted the two rotational diagrams shown in Figures 4.10 and 4.11. First, we fitted the data with a single temperature component of 1754 ± 321 K. However, the shocked material is apparently not in LTE, as the data points with odd and even J-numbers are difficult to fit simultaneously with a straight line or a curve. As mentioned above, this displacement is

indicative of a departure from the LTE ortho-to-para ratio of 3. Figure 4.11 shows the same data, assuming an ortho-to-para ratio of 1. Now a two-component fit, similar to that in Figure 4.9, is possible. For the hot component we derive a temperature of 2339 ± 468 K, while the warm component is significantly colder with 466 ± 264 K. The total H_2 column densities amount to $N_{1C}^{hot}(H_2) \approx 5.5 \times 10^{17} cm^{-2}$ and $N_{1C}^{hot}(H_2) \approx 9.7 \times 10^{19} cm^{-2}$, respectively.

Table 4.4 summarizes the temperatures and total column densities of the different components for both spectra.

Component	T [K]	$\log_{10}$ N(H_2) [cm^{-2}]
	RNO 1B	
Hot[a]	2991±596	17.09±0.36
Warm[a]	1071±121	18.75±0.09
	RNO 1C	
Hot[b]	2339±468	17.74±0.31
Warm[b]	466±264	19.99±1.17
Single[a]	1754±321	17.98±0.31

Table 4.4 Upper and lower limits on the temperatures and the total H_2 column densities of the observed shocked components. For the data derived close to RNO 1C, the results from the two component fit and the single component fit with different ortho-to-para ratios are given. [a]ortho-to-para ratio of 3. [b]ortho-to-para ratio of 1.

4.4 Discussion

The IRAC images reveal for the first time the embedded MIR point source associated with IRAS 00338+6312. However, Weintraub & Kastner (1993) already concluded from polarimetric observations that an additional source should be present close to the position of the IRAS point source. Furthermore, many authors analyzing the bipolar outflow related to this region have concluded that a deeply embedded object was most likely the driving source (Yang et al., 1995; Xu et al., 2006; Weintraub & Kastner, 1993) instead of one of the RNO objects (McMuldroch et al., 1995). Previous ground-based MIR observations (Polomski et al., 2005) may not have been sensitive enough to detect IRAS 00338+6312.

The observed properties of IRAS 00338+6312 convincingly classify the object as a young protostar and support the idea that it is indeed driving the molecular outflow. From their CO measurements, Xu et al. (2006) derive a total mass for this bipolar outflow of 1.4 $M_\odot$, indicating that IRAS 00338+6312 is an intermediate-mass protostar. The detection of the IRAS source also solves the problem that, up to now, the spectral energy distributions of RNO 1B and RNO 1C were unusually steep longward of 25 μm for FUors (Weintraub & Kastner, 1993). The images presented here have sufficient sensitivity and spatial resolution to show that the newly revealed source associated with IRAS 00338+6312 is most probably responsible for this flux excess.

In addition to the IRAS object, Weintraub & Kastner (1993) suspected another embedded source, which we identify with RNO 1G. Furthermore, the detection of RNO 1F

(Weintraub et al., 1996), which was initially assumed to be a density enhancement rather than an independent self-luminous source (Weintraub & Kastner, 1993), is confirmed with our IRAC images. Only RNO 1D, which was thought to be located between RNO 1B and RNO 1C (Staude & Neckel, 1991), does not show up in our images. This source was, however, also not detected by Weintraub & Kastner (1993) and only tentatively seen in the data of Weintraub et al. (1996).

It is not clear whether all the detected objects are physically confined to the RNO 1B/1C region. In particular, the membership of the newly discovered objects RNO1 IRAC 1, RNO1 IRAC 2, and RNO1 IRAC 3 needs to be confirmed. However, the IRAC observations suggest that RNO 1B and RNO 1C belong to a small cluster of (partly very) young objects. To our knowledge, although some FUors are known or suspected to be in binary or multiple systems (e.g., Reipurth & Aspin, 2004), the existence of FUors in a cluster-like environment is, so far, a unique finding. Only the FUor candidate V1184 Tau (CB34) also belongs to a small cluster (Khanzadyan et al., 2002) but its classification as FUor is far less certain than for the RNO objects (Yun et al., 1997). In any case, the still deeply embedded protostars in the close vicinity of RNO 1B/1C place strong constraints on the age of the objects if one assumes coeval evolution.

The magnitudes we derive for the two FUor objects at 3.6 μm can be compared with previous ground-based measurements at 3.8 μm by Kenyon et al. (1993) and Polomski et al. (2005). However, one certainly has to keep in mind not only that the IRAC filter is different in terms of central wavelength but also that the spectral width differs from that of the ground based instruments. While Kenyon et al. (1993) found $L_{3.8\,\mu\mathrm{m}} = 6.36$ mag and $L_{3.8\,\mu\mathrm{m}} = 6.5$ mag for RNO 1B and RNO 1C, respectively, Polomski et al. (2005) observed RNO 1C to be slightly brighter than RNO 1B ($L_{3.8\,\mu\mathrm{m}} = 6.27$ mag vs. $L_{3.8\,\mu\mathrm{m}} = 6.42$ mag). Also in our measurements RNO 1C seems to be the brighter component. However, both objects appear to be fainter in our observations compared with those of Polomski et al. (2005). Apart from the differences in the filter properties, intrinsic variations in the luminosity of the FUors or changing local extinction effects can account for the apparent variability in these objects.

The detection of H_2 rotational line emission can in general be attributed to collisional excitation from C- or J-type shocks (e.g., Draine & McKee, 1993; Moro-Martín et al., 2001). C-type shocks are magnetic and less violent toward molecules as compared with the mostly hydrodynamic J-type shocks, which can dissociate H_2 molecules even at lower shock velocities. From our rotational diagrams, we derived shock temperatures that are similar to those found in the outflow from Cepheus A by Froebrich et al. (2002). Those authors could fit a two component C-shock model to their data and derived shock velocities between 25 and 30 km s^{-1} for a cold and a hot component, respectively. By comparing our results directly with theoretical shock models, we find that the C-shock model 1 from Timmermann (1998) can explain both, the hot and warm components, in the spectrum close to RNO 1B. Considering our derived temperatures as an upper and a lower limit for the shocked material, shock velocities between 15 and 30 km s^{-1} are required. However, model 1 of Timmermann (1998) predicts on ortho-to-para ratio of ~ 2 at the low-velocity/low-temperature limit, which is not directly evident from our observations. More recent models by Wilgenbus et al. (2000) predict lower shock temperatures in C-type shocks for the same shock velocities, in comparison with Timmermann (1998). Following their models, our hot component in Figure 4.9 requires velocities exceeding 40 km s^{-1}. Slightly slower velocities (≈ 35 km s^{-1}) are already needed to explain the hot

component in the shock close to RNO 1C (Figure 4.11). The warm component in this diagram represents shock velocities between 15 and 20 $\mathrm{km\,s^{-1}}$. Although it is clear that some uncertainties between the observations and theory still remain, C-type shocks seem to provide a solid explanation for the observed shock temperatures.

The measurement of an ortho-to-para ratio smaller than 3 in Figure 4.11 implies that despite the high temperatures, the gas has not yet reached equilibrium between the ortho and para states. Thus, the observed ratio is the legacy of the temperature history of the gas (see, e.g., Neufeld et al., 1998, 2006), and transient heating by a recently passing shock wave has caused higher temperatures. As the corresponding region on the sky lies closer to the IRAS source than the region probed in Figure 4.9, the observations suggest that we are seeing the signatures of at least two shock waves: The first shock wave is probed close to RNO 1B (Figure 4.9), where we observe several temperature components that have apparently reached their equilibrium state. A more recent shock wave is seen close to RNO 1C (Figure 4.11), where the ratio of the line column densities also hints at high shock velocities and temperatures but the gas is not yet in thermal equilibrium.

4.5 Conclusions and future prospects

Our conclusions can be summarized as follows:

- We detected and resolved the MIR point source associated with IRAS 00338+6312, which appears to be an embedded intermediate-mass protostar driving the known molecular outflow in the RNO 1B/1C region.

- The detection of additional (partly previously unknown) point sources suggests that the FU Orionis objects RNO 1B/1C belong to a young, small stellar cluster. To our knowledge, these are the only well-studied and confirmed FUors that apparently belong to a cluster-like environment.

- All but two objects were detected in all four IRAC bands, and their colors are consistent with those of Class 0/I-II objects. The two objects that were not detected at 3.6 μm (including IRAS 00338+6312) are still very deeply embedded protostars.

- Having apparently extremely young objects in the direct vicinity of the FUors confirms the suspected young age for these types of objects, although their MIR colors are consistent with Class II objects.

- The two MIR spectra of the region bear clear signs of a dense, icy and dusty circumstellar environment, as solid state features are seen in absorption.

- The spectra show also H_2 emission lines from purely rotational transitions. We presume that these lines arise from shocked material within the molecular outflow. The derived shock temperatures and velocities are in agreement with C-type shock models.

- The observations of the H_2 lines suggest that the outflow lies in front of RNO 1B/1C, as otherwise the high optical depth toward these objects would have prevented the detection.

- While in one spectrum the gas probed by the H_2 line emission seems to be in LTE, the other spectrum shows a deviation from the expected LTE ortho-to-para H_2 ratio. This indicates the presence of at least two shock waves, the most recent one being responsible for the non-LTE line ratios.

The results presented here advantageously combine space-based MIR imaging and spectroscopy. While the images give insight into the photometric properties of several young embedded objects and also FU Orionis type stars, the spectra provide information on the dusty and icy circumstellar environment of the young cluster as well as on shocked gas within a molecular outflow. In this context the existence of FUors in a cluster-like environment needs to be pointed out. It is still a matter of debate whether all young low-mass stars undergo a FUor phase or whether these objects form a special sub-group of YSOs (e.g., Hartmann & Kenyon, 1996). Our results suggest that the FUor phenomenon occurs also in young (small) stellar clusters, thus making it perhaps more common than so far expected. In addition, the co-existence of FUors and very young protostars in the same environment strengthens the idea that the FUor-phase of YSOs is linked to the early stages of the star formation process.

Possible future investigations of the RNO 1B/1C region should address whether the observed objects do indeed belong to the same region and whether all of them are young stars. Furthermore, a detailed study of the shocked material, including high-resolution narrow-band imaging and spectroscopic mapping (e.g., with the SPITZER IRS) will provide deeper insights into its extension, physical conditions, and relation to the molecular outflow. A more complete analysis of the ice and dust features in the observed spectra is presented in the following chapter.

5. Evolution of dust and ice features around FUors

Mid-infrared spectroscopy of envelopes and active accretion disks

---

Parts of this chapter were submitted to the Astrophysical Journal.
(Quanz, S. P., Henning, Th., Bouwman, J., van Boekel, R., Juhàsz, A., Linz., H., Pontoppidan, K. M., and Lahuis, F., 2007, to be submitted)

AFTER HAVING discussed some mid-infrared spectra of FUors already in the previous chapters, we present in the following spectroscopy data for a sample of 14 FUors and 2 TTauri stars observed with the SPITZER SPACE TELESCOPE or with the INFRARED SPACE OBSERVATORY (ISO). Based on the appearance of the 10 μm silicate feature we define 2 categories of FUors. Objects showing the silicate feature in absorption (Category 1) are still embedded in a dusty and icy envelope. The shape of the 10 μm silicate absorption bands is compared to typical dust compositions of the interstellar medium and found to be in general agreement. Only one object appears to be too rich in amorphous pyroxene dust, but a superposed emission feature can explain the observed shape. We derive optical depths and extinction values from the silicate band and additional ice bands at 6.0, 6.8 and 15.2 μm. In particular the analysis of the CO_2 ice band at 15.2 μm allows us to search for evidence for ice processing and constrains whether the absorbing material is physically linked to the central object or in the foreground. For objects showing the silicate feature in emission (Category 2), we argue that the emission comes from the surface layer of accretion disks. Analyzing the dust composition reveals that significant grain growth has already taken place within the accretion disks, but no clear indications for crystallization are present. We discuss how these observational results can be explained in the picture of a young, and highly active accretion disk. Finally, a framework is proposed as to how the two categories of FUors can be understood in a general paradigm of the evolution of young, low-mass stars. As only one object (Parsamian 21) shows PAH emission normally seen toward evolved Post-AGB stars, we question its status as a FUor and discuss other possible classifications.

5.1 Introduction

By means of mid-infrared (MIR) spectroscopy gaseous and solid state features have been observed and analyzed in a variety of astronomical environments. While ground-based

observations are restricted to certain atmospheric windows (e.g., the N-band around 10 μm), spectrographs onboard space-borne telescopes, such as ISO and SPITZER, enable us to study a broad wavelengths range from the near-infrared (NIR) to well beyond 30 μm. Those instruments fostered and revolutionized our understanding in numerous astronomical fields of research. In particular the star-formation community benefitted from studies based on data from the space telescopes. The composition of dust grains and their evolution (e.g., grain growth and crystallization) in protoplanetary disks was analyzed to great extend in young, intermediate mass Herbig Ae/Be stars (HAeBes) (e.g., Bouwman et al., 2001; Meeus et al., 2001; Acke & van den Ancker, 2004; van Boekel et al., 2005), but also in the young, less massive TTauri stars (e.g., Forrest et al., 2004; Kessler-Silacci et al., 2006; Sargent et al., 2006). In addition, the ice and dust features of younger and more deeply embedded objects were studied (e.g., Watson et al., 2004) and the ice inventory of molecular clouds was investigated (e.g., Knez et al., 2005; Bergin et al., 2005).

While Lorenzetti et al. (2000) presented far-infrared spectroscopy data for 6 FUors observed with ISO-LWS, a dedicated MIR study of a larger sample of FUors is still missing. Larsson et al. (2000) showed the ISO-SWS spectra for 6 FUors for comparison, but no analysis was carried out. Hanner et al. (1998) discussed ground-based 8-13μm spectra for four FUors (FU Ori, V1515 Cyg, V1057 Cyg, V1735 Cyg) and fitted a simple dust model to the data to check whether silicate particles from the interstellar medium (ISM) can reproduce the observed features. Schütz et al. (2005) published additional ground-based data for another four objects in the same wavelength regime. As three objects (Z CMa, V346 Nor, V883 Ori) showed the 10μm feature in absorption they inferred the optical depth from fitting an ISM dust model to the spectra. The fourth object (Bran 76, alias BBW 76) was not analyzed in greater detail. Polomski et al. (2005) presented data on RNO 1B, Z CMa, and Parsamian 21 and derived dust temperatures and optical depths. To our knowledge, the first MIR spectra of FUors observed with SPITZER were presented in Green et al. (2006). The main focus of this publication was an accurate SED modeling of FU Ori, V1515 Cyg, and V1057 Cyg. Spectral solid state features were not analyzed in greater detail. The spectrum of V346 Nor was presented for comparison. In chapter 3, the first detailed dust composition modeling for the FU Ori spectrum was presented and evidence for grain growth in the accretion disk was found. The SPITZER spectra of RNO 1B/1C were also shown in the previous chapter. However, the dust composition was not yet analyzed in detail.

In this chapter we compile MIR spectra for 14 FU Orionis objects observed with ISO and/or SPITZER. This is the largest sample studied so far, and part of these data have not been published before. For objects where the spectra show a sufficient signal-to-noise ratio, the dust and ice composition of the circumstellar material is investigated.

5.2 Observations and data reduction

The mid-infrared spectra we present in this chapter are compiled from the archives of the ISO[1] and the SPITZER[2] satellite. With the Short Wavelength Spectrograph (SWS) onboard ISO seven objects classified as FUors were observed between April 1996 and October 1997. For one object (OO Ser) data were taken at five different epochs documenting

[1]The ISO archive can be accessed via http://www.iso.vilspa.esa.es/ida/

[2]http://ssc.spitzer.caltech.edu/archanaly/archive.html

a decay in luminosity over a few months. Table 5.1 summarizes the ISO-observations with object names, coordinates, ISO-SWS observing mode and scan speed, integration time on target, possible pointing offsets (see below), and the date of the observation. For the data reduction Highly Processed Data Products (HPDP) or SWS Auto Analysis Results (AAR) were downloaded from the ISO archive for speed 1 and 2 or speed 3 and 4 observations, respectively. With the OSIA software package (version 4.0)[3] the following reduction steps were carried out: For each object the spectra from the ISO-SWS up- and down-scan were flat-fielded and rebinned. After sigma clipping, the speed 3 and speed 4 spectra were de-fringed. This procedure was not required for the speed 1 and speed 2 data as the HPDP are already de-fringed. Finally, the spectra from the up- and down-scan were combined and rebinned to a spectral resolution of 100. In case the resulting spectrum showed signs of a pointing offset (e.g., aperture jumps) a correction based on the measured beam profiles along the different axes was applied to the raw data and the data reduction was repeated. The applied offsets are listed in Table 5.1.

The SPITZER observations are summarized in Table 5.2. Two objects (HL Tau and XZ Tau) are not classified as FUors but were part of a small SPITZER/IRS map including L1551 IRS 5, and data for all three objects could be downloaded simultaneously. Interestingly, XZ Tau is a binary system that recently was found to show EXor-type variations (Coffey et al., 2004), i.e., another type of short term eruptions of young stars. Thus, a comparison to the FUor data presented here is reasonable. In addition, the data of HL Tau enables us to compare the FUor spectra to that of a well-studied TTauri star with a highly inclined accretion disk seen almost edge-on (Close et al., 1997). Part of the SPITZER spectrum of HL Tau was already published in Bergin et al. (2005). The object V1647 Ori was observed three times within a period of roughly 5 months to monitor its brightness as it underwent an eruption beginning of 2004. However, to our knowledge, thus far no spectrum was published.

The data reduction process of the SPITZER data and their spectral resolution is described in detail in chapter 4. In particular, for the objects RNO 1B and RNO 1C apparent flux density offsets between the low-resolution (SL) and the short wavelength high-resolution (SH) part of the spectra, as well as between the short and long wavelengths part of the high-resolution (LH) spectra, are discussed in the chapter mentioned above. For the other objects presented here, the discrepancies in the flux densities between the SL and the SH part of the spectrum were $< 10\%$ and we matched the longer wavelength part to the shorter regime by multiplying a scalar factor. Only Bran 76 (also known as BBW 76) showed a larger offset of $\approx 15\%$ as already mentioned by Green et al. (2006). For Parsamian 21 (HBC 687) we do not show the SH spectrum between 14 and 20 μm as the slit of the spectrograph was not centered on the source and significant flux loss occurred for which we could not correct. An additional correction between the SH and the LH module of the spectrum was required for XZ Tau, HL Tau and L1551 IRS 5 where the flux densities of the LH part had to be scaled down by 10 - 15%. This offset can be explained by the larger aperture of this module which possibly probed additional large scale emission from the surroundings of these objects.

[3] http://sws.ster.kuleuven.ac.be/osia/

Object	RA (J2000)	DEC (J2000)	AOT / Speed	Time on target [sec]	Offset [″] y / z	Date
OO Ser	18h29m49.05s	+01d16′19.2″	SWS01 / 1	1062	- / -	1996-04-14
	18h29m49.08s	+01d16′19.8″	SWS01 / 1	1140	4 / 3	1996-10-24
	18h29m49.05s	+01d16′19.2″	SWS01 / 2	1140	- / -	1997-03-08
	18h29m49.05s	+01d16′19.2″	SWS01 / 3	3454	- / -	1997-04-12
	18h29m49.09s	+01d16′19.8″	SWS01 / 3	3454	- / -	1997-09-22
RNO 1B	00h36m46.24s	+63d28′54.3″	SWS01 / 2	1912	- / -	1996-08-27
V346 Nor	16h32m32.05s	-44d55′28.9″	SWS01 / 2	1912	- / -	1996-08-31
Z CMa	07h03m43.17s	-11d33′06.6″	SWS01/ 2	3454	3 / 3	1997-11-07
V1735 Cyg	21h47m20.60s	+47d32′04.9″	SWS01 / 2	1912	4 / 4	1996-08-06
Reipurth 50	05h40m17.89s	-07d27′29.3″	SWS01 / 3	3454	5 / 5	1997-10-13
L1551 IRS 5	04h31m34.06s	+18d08′04.8″	SWS01 / 4	6538	- / -	1997-09-06

Table 5.1 Journal of ISO-SWS observations. The coordinates denote the pointing position of the telescope saved in the header of the data files. The speed of the observations, the time spent on the target and possible pointing offsets in the telescope's y and z axis are given as well. The offsets were corrected during the data reduction.

Object	RA (J2000)	DEC (J2000)	AOR	Integration time [sec]	Date
Bran 76 (BBW 76)	07h50m35.52s	-33d06′24.12″	3571200	12 (SL, LL)	2004-04-14
FU Ori	05h45m22.39s	+09d04′12.5″	3569920	12 (SL, SH, LH)	2004-03-04
L1551 IRS 5	04h31m34.08s	+18d08′04.92″	3531776	6 (SL, SH, LH)	2004-03-04
Parsamian 21 (HBC 687)	19h29m00.72s	+09d38′47.11″	5039872	36 (SL)	2004-04-18
				48 (SH, LH)	
RNO 1B	00h36m46.34s	+63d28′53.76″	6586624	36 (SL)	2004-01-07
				60 (SH, LH)	
RNO 1C	00h36m46.89s	+63d28′58.44″	6586624	36 (SL)	2004-01-07
				60 (SH, LH)	
V1057 Cyg	20h58m53.76s	+44d15′28.44″	3570176	12 (SL, SH, LH)	2003-12-15
V1515 Cyg	20h23m48.00s	+42d12′25.56″	3570432	12 (SL, SH, LH)	2004-05-11
V1647 Ori[a]	05h46m13.13s	+00d06′05.21″	12261120	12 (SL)	2004-10-20
				24 (SH, LH)	
	05h46m13.15s	-00d06′04.41″	11569920	48 (SL)	2005-03-11
				484 (SH), 240 (LH)	
	05h46m13.14s	+00d06′04.69″	12644096	12 (SL, LL)	2005-03-24
V1735 Cyg	21h47m20.6s	+47d32′00.7″	3570944	12 (SL, SH, LH)	2003-12-17
V346 Nor	16h32m32.1s	-44d55′28.6″	3570688	12 (SL, SH, LH)	2004-02-27
HL Tau	04h31m38.4s	+18d13′57.9″	3531776	6 (SL, SH, LH)	2004-03-04
XZ Tau AB	04h31m40.1s	+18d13′57.4″	3531776	6 (SL, SH, LH)	2004-03-04

Table 5.2 Journal of SPITZER-IRS observations. The coordinates denote the average slit position of the low-resolution spectrograph computed by the onboard software. The AOR of the observations, the time spent on the target for the different modules and the observation date are given as well. [a]The object was observed at three different epochs.

5.3 Results

5.3.1 General overview

Figures 5.1-5.8 show the complete sample of spectra. For Bran 76 and the third observation of V1647 Ori only low-resolution SPITZER data were available. To increase the signal to noise, all SPITZER LH data and the SH data of V1735 Cyg were smoothed by a factor of three. Most of the yet remaining spikes in these spectra are not real but rather flux jumps between the different orders of the spectrographs. As mentioned in the introduction of this chapter, parts of the data shown here were already published: Green et al. (2006) presented the SPITZER data for FU Ori, V1515 Cyg, V1057 Cyg, Bran 76, and V346 Nor and used disk-envelope models to explain the SEDs. The spectrum of HL Tau was shown by Bergin et al. (2005). Schütz et al. (2005) used the ISO data for Z CMa and V346 Nor to compare with their ground-based data. Finally, Larsson et al. (2000) showed the ISO/SWS SEDs of the outbursting object OO Ser and used the ISO/SWS data for RNO1B, Z CMa, V1057 Cyg, and V1735 Cyg for comparison. Unfortunately, for most objects the quality of the ISO/SWS data is significantly worse than that of the SPITZER observations. Even after the data have been rebinned to a spectral resolution of 100, artefacts remain in the spectra. In Figure 5.9 we show data for four objects that were observed with both SPITZER and ISO. Especially for the objects with lower flux levels the noise in the SWS data is significant. The reason for this is the short integration time for most objects which is reflected in the speed parameter in Table 5.1. In consequence, the ISO data are mainly used for qualitative statements rather then for quantitative analyses

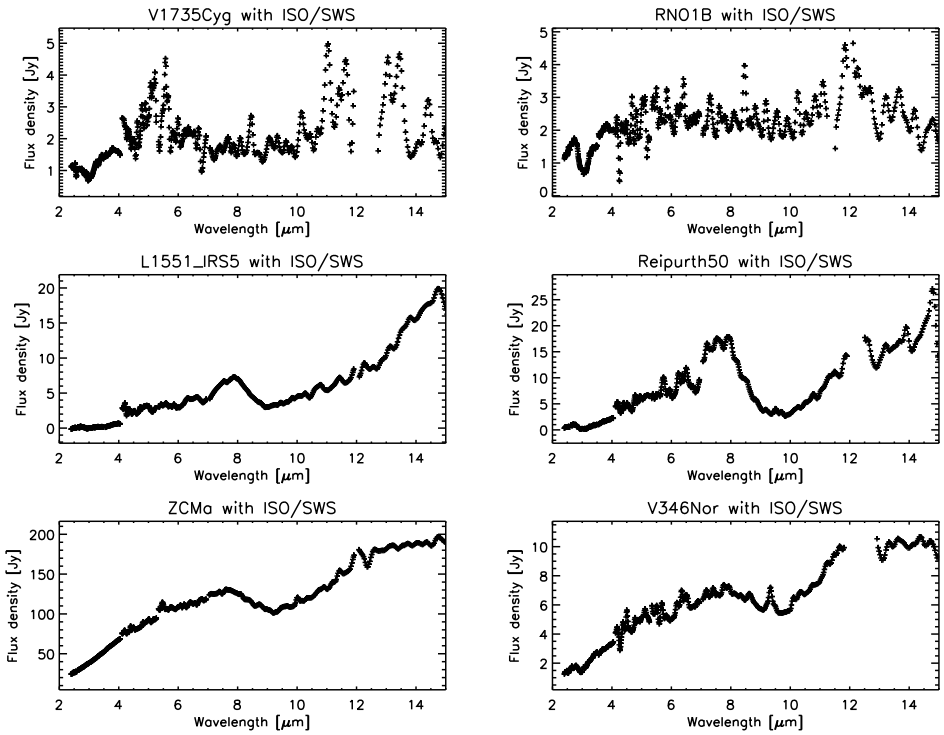

Figure 5.1 ISO-SWS spectra in the 2-15 μm range for 6 of our targets. The poor signal-to-noise ratio in the data shows most extremely in the plots on top.

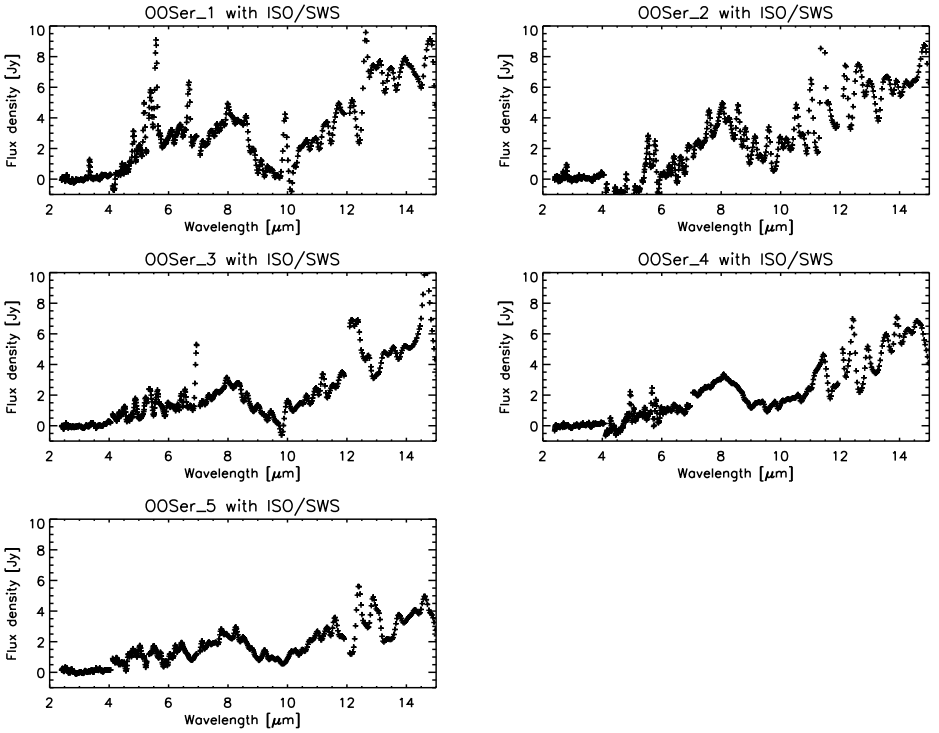

Figure 5.2 Same as Figure 5.1 but for the object OO Ser which was observed at 5 different epochs.

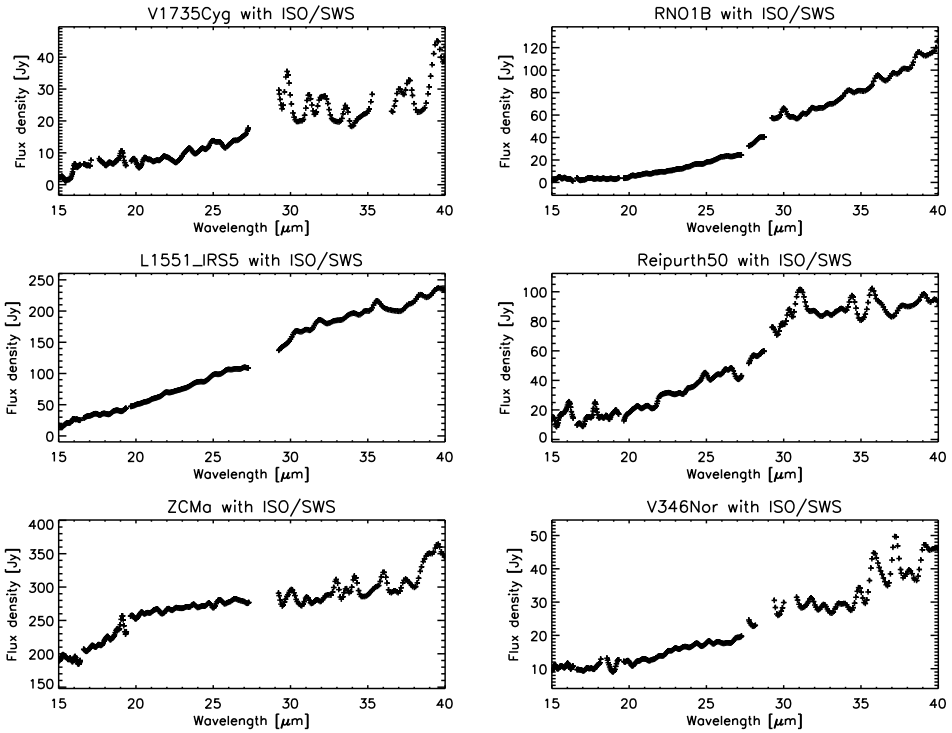

Figure 5.3 Same as Figure 5.1 but between 15 and 40 μm.

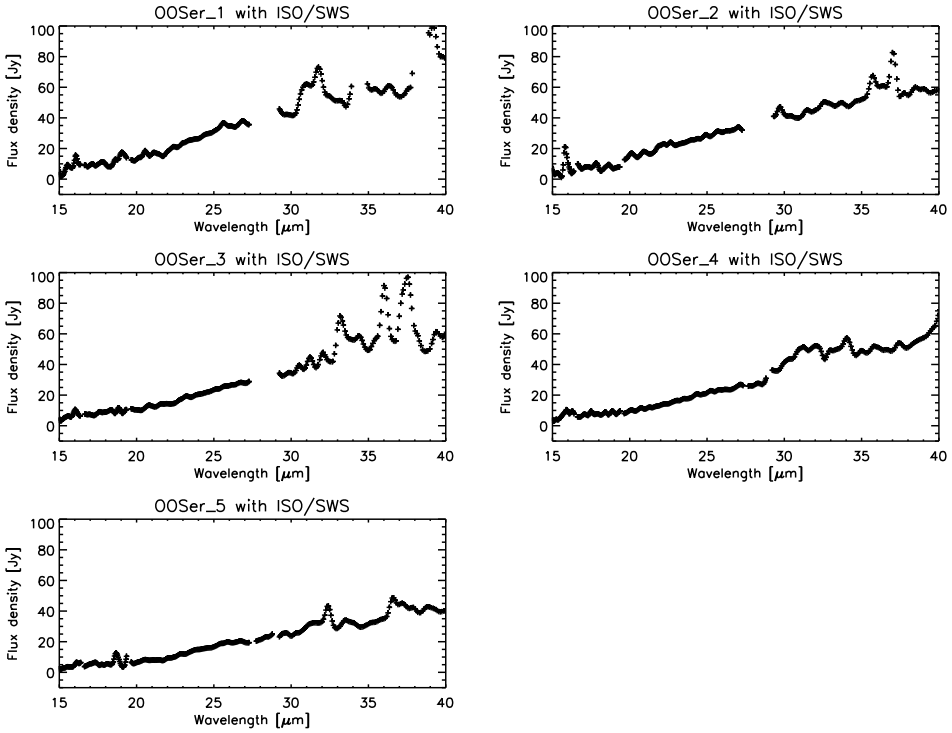

Figure 5.4 Same as Figure 5.2 but between 15 and 40 μm.

throughout the rest of the chapter. Only the ISO data for Z CMa (with a high flux level) and Reipurth 50 (published for the first time) will be examined, at least in part, in more detail in one of the consecutive sections.

From Figures 5.1-5.8 it becomes clear that for all objects the flux densities increase toward longer wavelengths indicative of warm dusty material surrounding all objects. However, Figures 5.1, 5.2, 5.5, and 5.6 show that there are striking differences within the group of FUors: While some objects show a silicate emission feature in the 10 μm region, other objects show deep absorption profiles. Since other spectral features do further support such a differentiation we will in the following distinguish the objects via the behavior of their 10 μm feature and discuss the two categories separately in the following subsections. A complete overview of the most prominent spectral features between 3 and 16 μm is given in Table 5.3.

5.3.2 Objects with 10 μm emission

Qualitative analysis of the 10 μm region

In Figure 5.10 we compiled all objects showing signs of silicate emission in the 10 μm band. To subtract the underlying continuum we fitted a polynomial of first order to the flux at 8 and 13 μm. As we are thus far only interested in a qualitative comparison among the various objects, the exact shape of the continuum is not important. For comparison we overplot the silicate emission feature of typical interstellar medium (ISM) dust grains, scaled to the observed spectra (red, dashed lines in Figure 5.10; Kemper et al., 2004). We note that the spectrum of each object is shown twice: While the first plot shows the

Object	Instrument	H_2O (ice) 3.08μm	H_2CO(?)/HCOOH(?)/ H_2O (ice) 5.85 / 6.0 μm	H_2O (gas) 5.8 / 6.8μm	CH_3OH(?)/ NH_4^+(?) 6.85μm	Silicates 10.0μm	CO_2 (ice) 15.2μm	PAH[a]
OO Ser	ISO-SWS	-	-	-	-	abs	abs	-
V346 Nor	ISO-SWS	abs	abs	-	-	abs	-	-
	SPITZER IRS	-	abs	-	abs	abs	abs	-
Z CMa	ISO-SWS	-	-	-	-	abs	-	-
Reipurth 50	ISO-SWS	abs	abs	-	abs	abs	-	-
L1551 IRS 5	ISO-SWS	abs	abs	-	abs	abs	abs	-
	SPITZER IRS	-	abs	-	abs	abs	abs	-
RNO 1B	ISO-SWS	abs	-	-	-	flat	-	-
RNO 1B	SPITZER IRS	-	abs	-	abs	abs	abs	-
RNO 1C	SPITZER IRS	-	abs	-	abs	abs	abs	-
V1735 Cyg	ISO-SWS	abs	abs?	-	-	flat	-	-
	SPITZER IRS	-	-	-	-	abs	abs?	-
Parsamian 21	SPITZER IRS	-	-	-	-	em	-	em
Bran 76 (BBW 76)	SPITZER IRS	-	-	abs	-	em	-	-
V1057 Cyg	SPITZER IRS	-	-	abs	-	em	abs (gas)	-
V1515 Cyg	SPITZER IRS	-	-	abs	-	em	-	-
V1647 Ori	SPITZER IRS	-	abs	-	abs	em	abs	-
FU Ori	SPITZER IRS	-	-	abs	-	em	-	-
V883 Ori[b]	ESO Timmi2	-	-	-	-	abs	-	-
XZ Tau AB	SPITZER IRS	-	-	-	-	em	-	-
HL Tau	SPITZER IRS	-	abs	-	abs	abs	abs	-

Table 5.3 Overview of prominent spectroscopic features (mostly ices and dust) seen in the spectra presented in Figures 5.1, 5.2, 5.5, 5.6, 5.7, 5.8. A "?"-symbol behind an ice species in the header indicates a possible but unknown contribution to the observed profile. In the main table "abs" denotes an absorption feature, "em" an emission feature. For objects where ISO and SPITZER data are available, the SPITZER data is of higher quality and thus more reliable. [a] Any significant emission at 6.2 or 7.7 μm (C-H modes), 8.6, 11.3 or 12.7 μm (C-C modes) or at 8.2 μm (origin not clear yet). [b]Observations from Schütz et al. (2005).

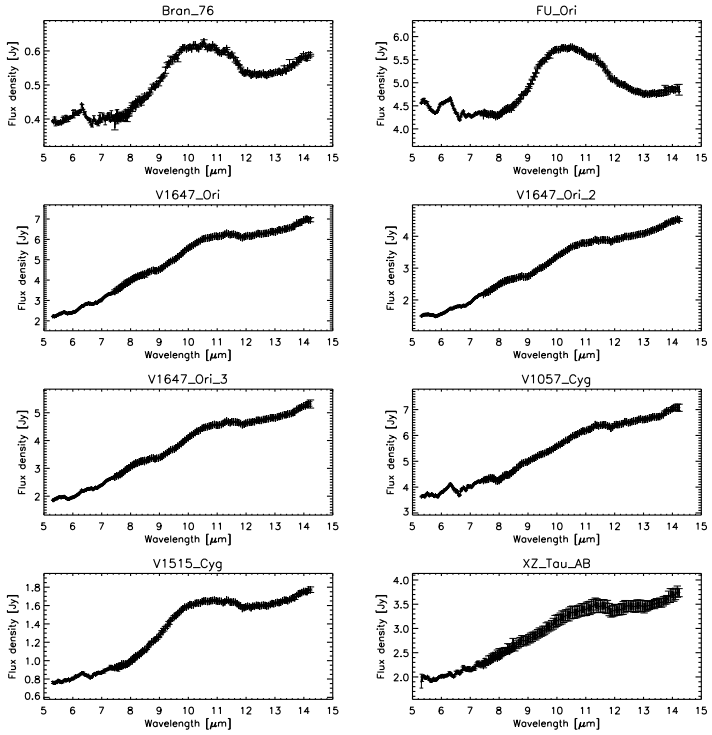

Figure 5.5 SPITZER low-resolution spectra between 5 and 14 μm.

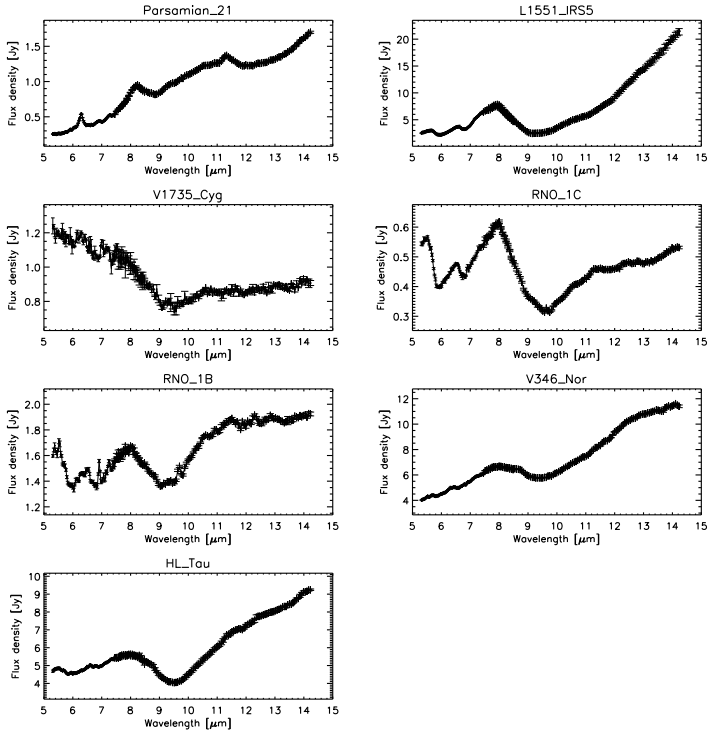

Figure 5.6 Same as Figure 5.5.

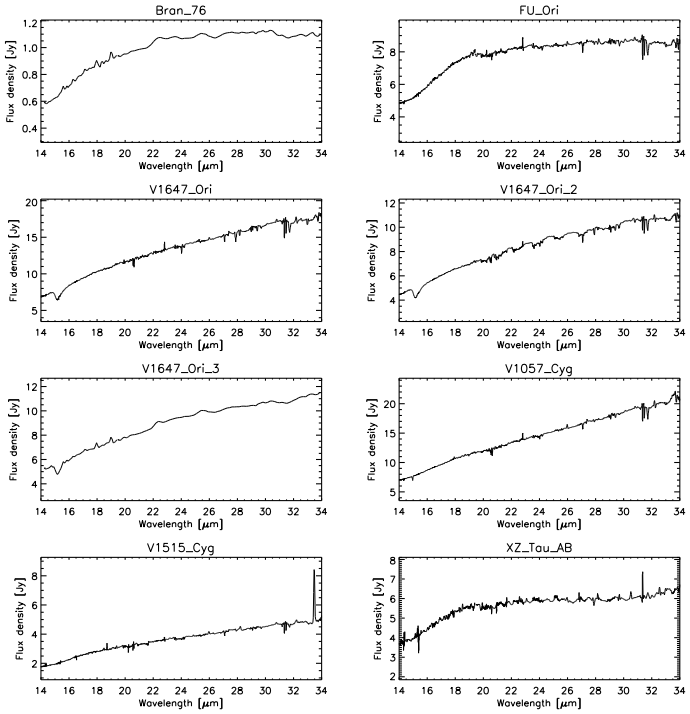

Figure 5.7 Same objects as in Figure 5.5, but now showing the high-resolution part of the spectrum between 14 and 34 μm.

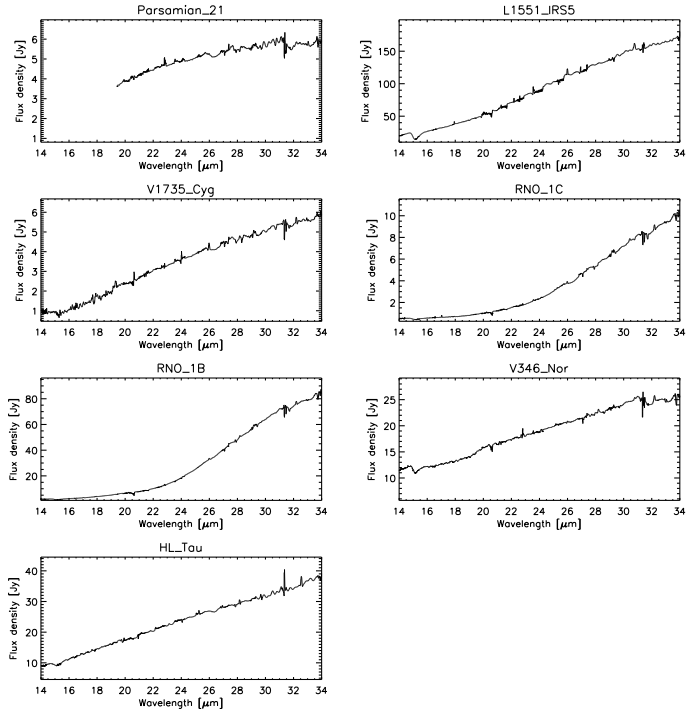

Figure 5.8 Same objects as in Figure 5.6, but now showing the high-resolution part of the spectrum between 14 and 34 μm.

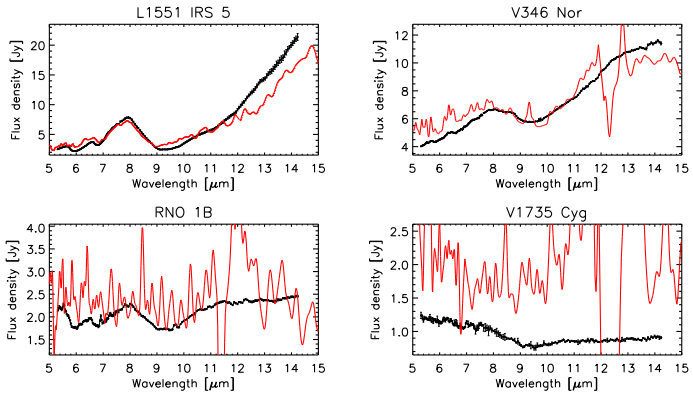

Figure 5.9 Comparison between ISO/SWS and SPITZER/IRS data for objects observed with both satellites. The ISO data (red, solid lines) are significantly more noisy. In our sample only data for objects with high flux levels are suitable for quantitative analyses.

observed spectrum of the source, the second one shows the dereddened spectrum. For the dereddening we compiled optical extinction values from the literature (see caption of Figure 5.10) and used the extinction law described in Mathis (1990) to derive corresponding extinction values for the MIR. It is assumed that all of the extinction is caused by material in the line of sight toward the objects and that no self-shadowing effect (e.g., by an inclined accretion disk with a certain flaring angle) is present. The continuum was fitted for the dereddened spectra separately. It shows that for most objects the interstellar extinction is not negligible and that it can have substantial influence on the shape of the silicate feature (see, e.g., V1057 Cyg and V1647 Ori). For a fair comparison it thus seems reasonable to evaluate the dereddened and not the observed spectra.

At first glance, when comparing the spectra, it is noteworthy that all emission features differ from the typical shape of the typical ISM dust feature. Green et al. (2006) claimed that the emission peak for the first four objects in Figure 5.10 was close to 9.5 μm and that the dust features appeared to be pristine. We find that all features peak longward of 9.7 μm (the typical peak position for ISM type dust; Kemper et al., 2004) and that they show additional flux excess compared to the ISM feature at even longer wavelengths. This indicates that dust grain processing has already set in. Furthermore, it should be noted that the spectrum of Parsamian 21 looks significantly different compared to the others. The most prominent characteristic are strong emission bands around 8.2 μm and probably also around 11.3 μm from polycyclic aromatic hydrocarbons (PAHs). Polomski et al. (2005) already suspected the existence of PAH emission in the spectrum of this source based on ground-based observations, but a firm confirmation was thus far lacking. We discuss the spectrum of Parsamian 21 in more detail below.

For a better comparison of the emission features, we plotted in Figure 5.11 the normalized fluxes of the objects between 8 and 13 μm. The normalization was done via

$$F_{\rm norm}(\lambda) = 1 + \frac{F_{\rm obs}(\lambda) - F_{\rm cont}(\lambda)}{< F_{\rm cont} >} \tag{5.1}$$

where $F_{\rm obs}(\lambda)$ is the observed flux, $F_{\rm cont}(\lambda)$ is the continuum flux and $< F_{\rm cont} >$ denotes the mean value of the underlying continuum in the considered wavelength regime. This normalization ensures that the shape of the emission feature is preserved. From Figure 5.11 it becomes clear that the emission features of Bran 76, FU Ori, and V1515 Cyg

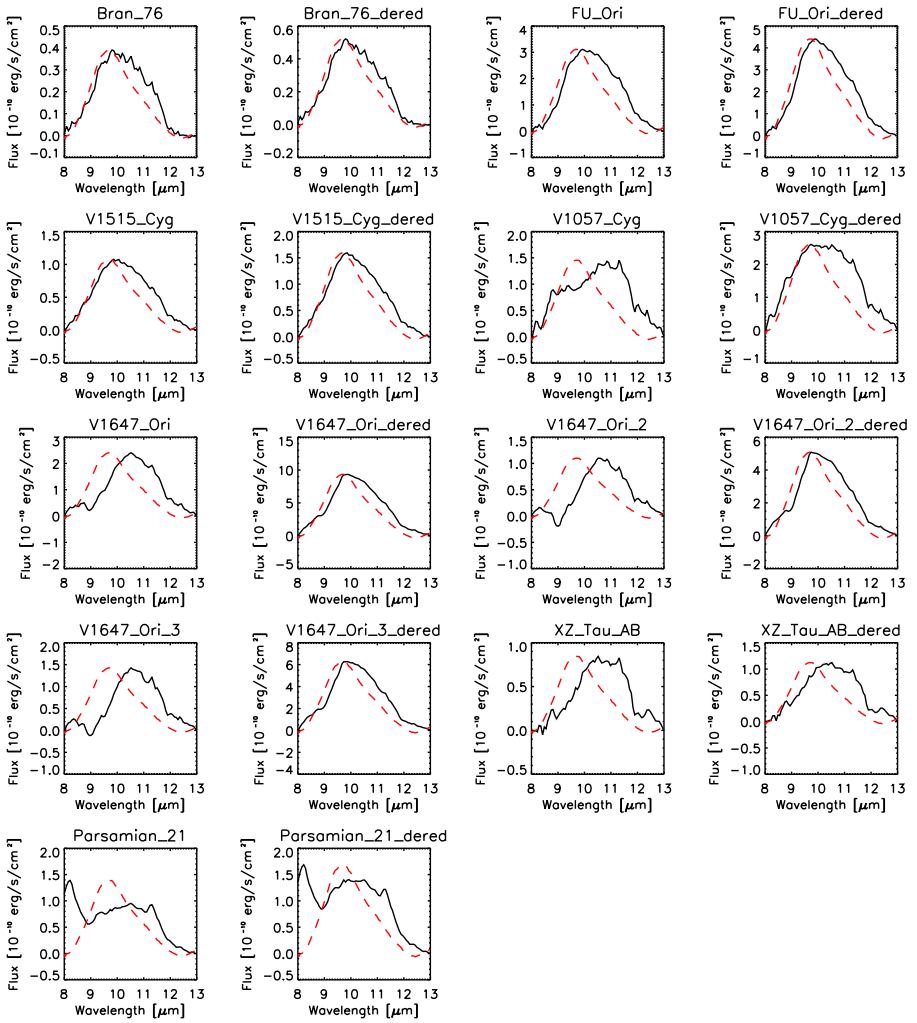

Figure 5.10 Continuum subtracted silicate emission profiles (black, solid lines). Each spectrum is shown twice, i.e., with and without being corrected for interstellar extinction as explained in the text. The assumed values for A_V are: 2.2 mag (Bran 76; Reipurth et al., 2002), 2.4 mag (FU Ori; Skinner et al., 2006), 3.2 mag (V1515 Cyg; Herbig, 1977), 3.2 mag (V1057 Cyg; Herbig, 1977), 11.0 mag (V1647 Ori; Muzerolle et al., 2005), 11.0 mag (XZ Tau; White & Ghez, 2001), 4.0 mag (Parsamian 21; Staude & Neckel, 1992). We used the extinction law from Mathis (1990) with R_V=3.1. For comparison the red, dashed line shows the typical ISM silicate feature observed toward the galactic center from Kemper et al. (2004). As mentioned in the text V1647 Ori was observed at three different epochs.

are quite similar in terms of shape and strength. The features of V1057 Cyg and XZ Tau are far less pronounced and much broader[4]. The emission profiles of V1647 Ori and Parsamian 21 are slightly stronger than those of the other objects and, as mentioned above, the latter object is the only one showing strong PAH emission bands. The three epochs of data for V1647 Ori allow us to study the variability of this object in the 10 μm region

[4]In contrast to our analysis Green et al. (2006) found the feature of V1057 Cyg to be comparable in shape (and thus in dust composition) to those of Bran 76, FU Ori, and V1515 Cyg.

over a period of approximately five months. Figure 5.11 shows that between October 2004 (epoch 1) and mid of March 2005 (epoch 2) the flux level decreased significantly. At the third epoch (end of March 2005) the flux appears to have slightly increased again (see also Figure 5.5). The overall shape of the feature during the six months period did, however, not change. To put these results in a broader context with other young objects

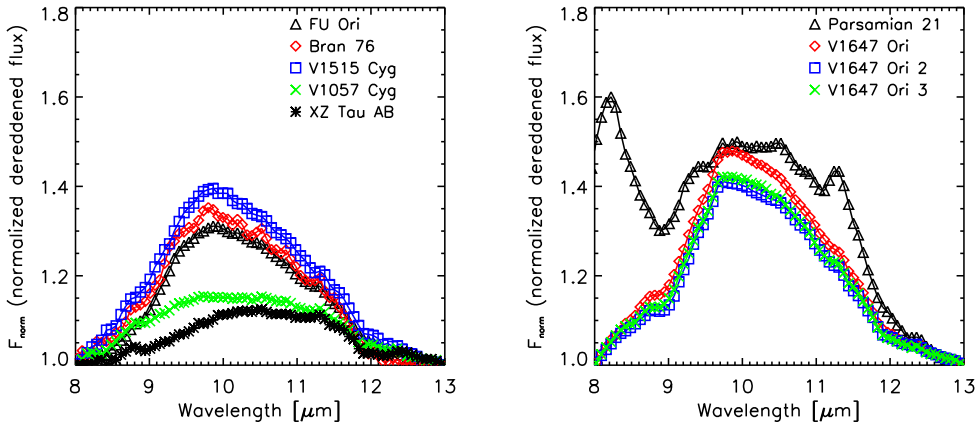

Figure 5.11 Dereddened and normalized 10 μm dust emission features of the objects shown in Figure 5.10. For a better comparison the dereddened spectra are shown.

and to get a first idea on the dust grain properties, we plot in Figure 5.12 the flux ratio at 9.8 and 11.3 μm against the computed peak over the continuum in the normalized spectra. This figure also shows the region typically occupied by young TTauri stars and the slightly more massive Herbig Ae/Be stars (see, e.g., Przygodda et al., 2003; van Boekel et al., 2003, 2005). We find that the objects presented here tend to have in general a relatively weak peak over continuum emission and a flux ratio between 0.8 and 1.0. While the strength of the peak over the continuum is interpreted as a tracer for grain sizes (with higher peak values denoting smaller grains), the flux ratio is a more general tracer for grain processing, i.e., grain growth as well as crystallization. This is explained by the fact that

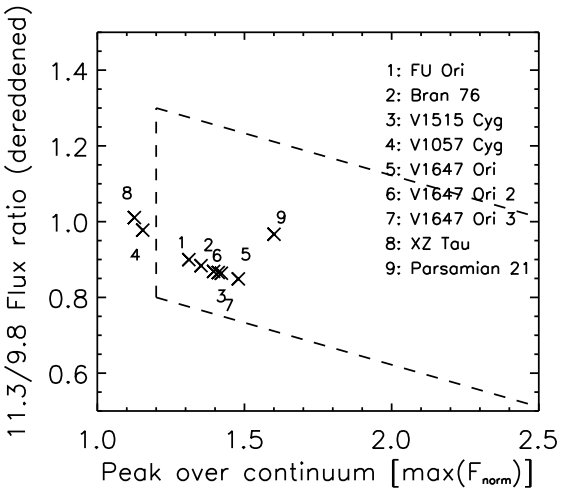

Figure 5.12 The flux ratio between 11.3 and 9.8 μm plotted against the normalized peak over the continuum. The dashed line indicates the region where typically TTauri stars (Przygodda et al., 2003) and Herbig Ae/Be stars (van Boekel et al., 2003, 2005) are located.

not only the growing of grains leads to a broader and flatter silicate feature between 9.8 and 12.0 μm (Bouwman et al., 2001), but also the crystallization process introduces distinct emission peaks of forsterite and enstatite longward of 10 μm (see, e.g., van Boekel et al., 2005). Taking these considerations into account, we find that our sample shows clear evidence for grain growth and dust processing. For a more quantitative analysis of the dust composition we fitted a dust model to the data as explained in the following subsection.

Dust composition

In Figure 5.13 we fitted an analytical dust model to the spectrum of FU Ori between 7 and 17 μm. To equally weight the short- and high-resolution part of the spectrum, we rebinned the data to a spectral resolution of 100, still sufficient to disentangle contributions from different dust species. Instead of fitting a two component model to the data, with one temperature for the underlying continuum and one temperature for the emission layer, as we did in chapter 3, we use a new model described in Juhász et al. 2007 (to be submitted). In this model the temperatures for the disk midplane, the disk surface layer and an inner disk rim are fitted by powerlaw distributions instead of single black body temperatures. In this respect, the model represents more realistically the temperature distribution in a protoplanetary disk. The input parameter for the model were taken from the simple accretion disk model in chapter 3. The dust model was based on opacities for six dust species (amorphous olivine and pyroxene, crystalline forsterite and enstatite, silica, and amorphous carbon) in three grain sizes (0.1, 1.5, and 6.0 μm). References for the optical properties of the grains are given in Juhász et al. 2007 (to be submitted) and chapter 3 (Table 3.3). In contrast to chapter 3, this time we included also carbon grains in the fit. However, as shown in Figure 5.13 and summarized in Table 5.4, the best fit ($\chi^2 = 45.3$) does not require any carbon grains. The derived mass fractions agree with the results based on the more simple two component dust model used in chapter 3 (see Table 3.4). The large fraction of big, amorphous grains can be explained with the need for a high-temperature continuum. Most of the large amorphous olivine and pyroxene grains produce the underlying continuum emission. The smaller grains are responsible for the observed emission feature. Still, we emphasize that also in the disk surface layer large grains are present: Comparing the derived composition to that of the interstellar medium (van Boekel et al., 2005), we find a significantly higher fraction of 1.5 μm grains in the dust of FU Ori. Furthermore, the model does predict a negligible amount of crystalline grains (< 0.01), no silica dust and, as mentioned above, no carbon grains. Certainly, the values for the derived mass fractions should not be taken literally, as, for instance, the temperature structure in the disk and the dust opacities are not perfectly known. However, the models presented here and in chapter 3 agree on two very important aspects: (1) there is clear evidence for dust coagulation in the spectra of FUors, and (2) there is hardly any contribution from crystalline grains detectable in the data. This lack of crystalline grains was already noticed and discussed in chapter 3, but we will reinvestigate this issue below.

The PAH features of Parsamian 21

As its features are significantly different than those of the other FUors, we plot in Figure 5.14 the dereddened spectrum of Parsamian 21 and analyze it in more detail. The

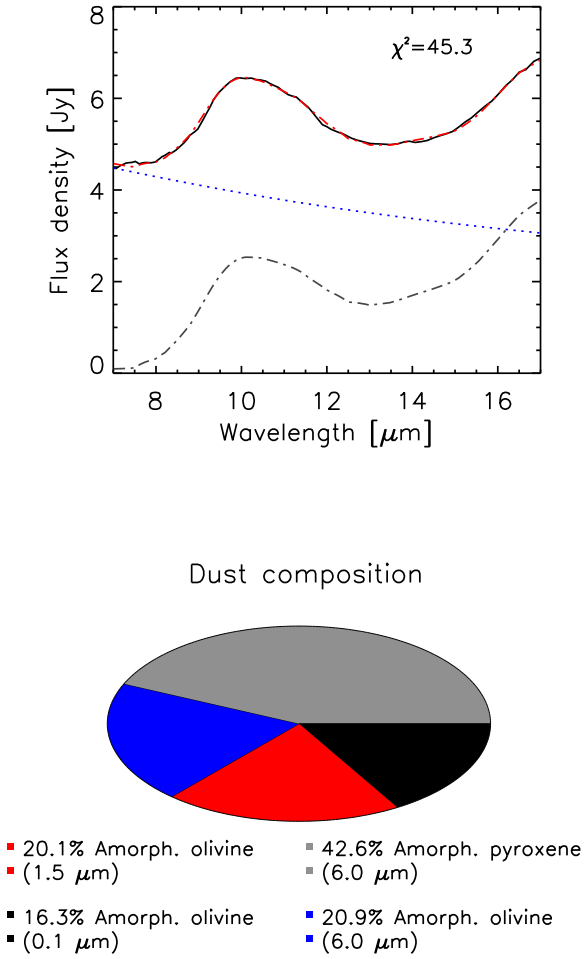

Figure 5.13 Results from a dust model fit to the 7-17 μm region of the spectrum of FU Ori. *Top:* Fitting results using the dust model described in the text. The observed spectrum is shown in the black, solid line, the blue, dotted line illustrates the contribution from the fitted continuum, and the grey, dash-dotted line denotes the computed emission feature. The sum of the fitted components is shown in the red, dash-dotted line, matching the observed spectrum. *Bottom:* Mass fractions of the fitted dust species for the model shown above. The spectrum is fitted solely with amorphous grains, part of which have grown significantly.

Species	0.1 μm	1.5 μm	6.0 μm	Total
Amorphous olivine	0.16	0.20	0.21	0.57
Amorphous pyroxene	0.0	0.0	0.43	0.43
Crystalline forsterite	$<$0.01	0.0	0.0	$<$0.01
Crystalline enstatite	0.0	0.0	0.0	0.0
Silica	0.0	0.0	0.0	0.0
Amorphous carbon	0.0	0.0	0.0	0.0

Table 5.4 Mass fractions of dust species with different grain sizes derived from the dust model fit.

vertical lines illustrate, where typically PAH emission bands are located. While prominent PAH emission is present at 6.3, 8.2 and (possibly) 11.3 μm, no bands are seen at 7.7, 8.6 and 12.7 μm. In addition, the spectrum bears signs of underlying silicate emission and it is difficult to disentangle the 11.3 μm emission band in its possible contributions from crystalline forsterite and PAHs. PAHs are commonly seen in the spectra of HAeBe stars (e.g., Meeus et al., 2001; Acke & van den Ancker, 2004; Sloan et al., 2005) and, more recently, PAH emission was also detected in TTauri spectra (Geers et al., 2006).

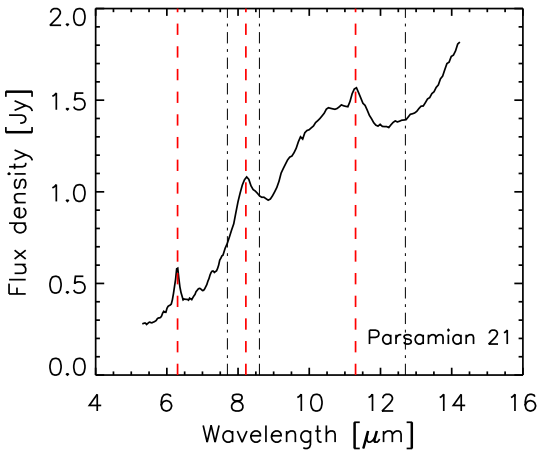

Figure 5.14 Dereddened SPITZER MIR spectrum of Parsamian 21 (assuming $A_V = 4.0$ mag) illustrating the strong PAH emission features not seen in any other FUor. Note also the steeply rising continuum and the underlying silicate dust emission. The vertical lines indicate the positions of typical PAH emission bands: strong emission is detected at 6.3, 8.2 and 11.3 μm (red, dashed lines), no emission is seen at 7.7, 8.6 and 12.7 μm.

However, the spectrum of Parsamian 21 differs significantly from the spectra of other young objects: it shows a broad and strong feature at 8.2 μm which is not detected in any other young source. Only HD 135344 shows also a peculiar PAH spectrum in the 7-9 μm range, probably caused by a blend of two peaks at 8.0 and 8.2 μm, respectively (Sloan et al., 2005). The spectrum of Parsamian 21 fits best to the objects defining group C′ in Peeters et al. (2002). However, only two objects belong to this group in that paper and both are Post-AGB stars (CRL 2688, IRAS 13416-6243). Like Parsamian 21 they show no PAH complex at 7.7 μm and no 8.6 μm but the peculiar broad band at 8.2 μm. However, in contrast to Parsamian 21, their feature at 11.2 μm is extremely weak. While most PAH emission bands are well characterized by their C-H or C-C modes, the identification of the 8.6 μm band yet remains unknown (Peeters et al., 2002). In section 5.4.3 we will critically review the findings presented here and discuss their implications with respect to the FUor status of Parsamian 21.

5.3.3 Objects with 10 μm absorption

Analysis of the 10 μm region

In Figure 5.15 we plot the optical depth in the 10 μm region for the objects showing the silicate band in absorption. To derive the optical depth, we fitted the continuum with a polynomial of first order to the observed spectra between 8 and 13 μm, assuming that no absorption due to silicates is present at these wavelengths. We then computed the optical depth τ using

$$F_{\rm obs}(\lambda) = F_{\rm cont}(\lambda) \cdot e^{-\tau} \tag{5.2}$$

where $F_{\rm obs}(\lambda)$ is the observed flux and $F_{\rm cont}(\lambda)$ the assumed continuum. To derive the wavelength position and value of the maximum optical depth, we did the following: As some spectra are quite noisy (e.g., V1735 Cyg, RNO 1B, Z CMa, and Reipurth 50) we fitted the data between 8.8 and 10.2 μm, i.e., the region with the greatest optical depth, with a polynomial of second order (shown as red, dash-dotted lines in Figure 5.15). The wavelength position of the maximum optical depth (vertical, red, dash-dotted lines in Figure 5.15) and the corresponding value are then derived from the fit. From the spectra with

a high signal to noise ratio and strong absorption profiles (e.g., the SPITZER spectra of L1551 IRS 5 and HL Tau) it becomes clear that the fit matches the shape of the absorption feature quite well and that this approach seems reasonable. The black, dotted horizontal line in Figure 5.15 shows the assumed continuum level. In Table 5.5 we summarize the derived maximum optical depth for each object $\tau_{\rm silicate}$ and the corresponding wavelength. We give also values for the extinction in the silicate band $A_{\rm silicate}$ and estimates for the corresponding extinction in the optical A_V. $A_{\rm silicate}$ was derived via

$$A_{\rm silicate} = -2.5 \log_{10} \left(e^{-\tau_{\rm silicate}} \right) \quad . \tag{5.3}$$

The errors for $\tau_{\rm silicate}$ and $A_{\rm silicate}$ are based on the 1-σ uncertainties in the spectra and the resulting fluctuations of the polynomial fit. A_V and its error are derived from averaging over the extinction models of Mathis (1990) and Weingartner & Draine (2001) and assuming two different values of R_V for each model ($R_V = 3.1$ and 5.0 for Mathis (1990) and $R_V = 3.0$ and 5.5 for Weingartner & Draine (2001)). As already noted by Cohen & Kuhi (1979) one has to be careful when deriving a value for the optical extinction based on the silicate feature, as uncertainties in the underlying continuum and unknown dust compositions influence the results. Hence, for comparison, Table 5.5 gives also values for A_V found in the literature. Unfortunately, it is not always clear how these values were derived, and for some objects additional assumptions had to be made without knowing how appropriate they really are.

For V346 Nor and RNO 1C the values for A_V agree quite well. Also for Z CMa, Reipurth 50 and L1551 IRS 5 the values are in general agreement. Due to the high extinction toward the latter two objects, a good estimate of A_V is difficult. We would like to point out, however, that a value of $A_V \gtrsim 150$ mag for L1551 IRS 5 as mentioned in Stocke et al. (1988) and quoted, for instance, by White et al. (2000) and Fridlund et al. (2002) appears to be an overestimate. In contrast to what Stocke et al. (1988) note, we do see a near-infrared (NIR) counterpart to the L1551 IRS 5 system with $K_S \approx 9.7$ mag in yet unpublished NIR data taken with the OMEGA2000 camera at the Calar Alto Observatory

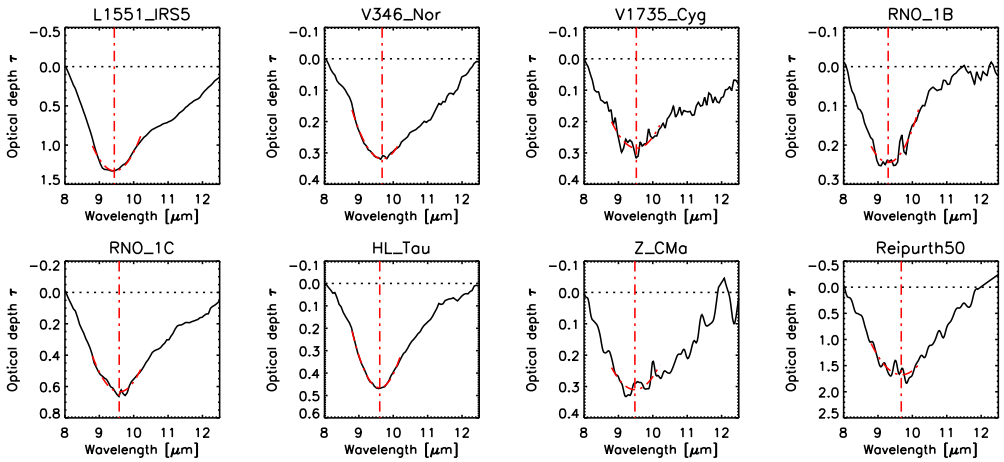

Figure 5.15 Observed optical depths of the 10 μm silicate absorption feature (black, solid line). The dotted line shows the assumed continuum. The vertical red, dash-dotted lines indicate the position of the maximum optical depth of the second order polynomial fitted to the data between 8.8 and 10.2 (also plotted in red, dash-dotted lines).

(Spain). The above mentioned value for A_V would translate into $A_K \approx 15$ mag, and thus the intrinsic K_S-band magnitude of L1551 IRS 5 would be ≈ -5 mag at a distance of 140 pc. For young low-mass objects this appears to be definitely too luminous. For V1735 Cyg and HL Tau our derived values for A_V are lower than those found in the literature. However, for V1735 Cyg no errors are given and it is unclear what assumptions lead to the extinction value for HL Tau given by Close et al. (1997). Finally, RNO 1B also shows a discrepancy between our value for A_V and that given by Staude & Neckel (1991). In this case, however, the silicate absorption feature bears evidence for additional superposed emission as will be described in the next paragraph. Thus, we attribute, at least part of, the missing optical depth to an underlying silicate emission feature.

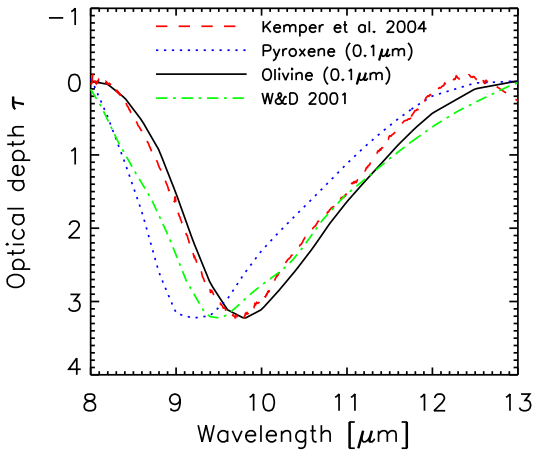

Figure 5.16 Optical depths for different dust grain populations on an arbitrary scale. The black, solid line shows the profile for 0.1 μm sized amorphous olivine grains (Dorschner et al., 1995), the red, dashed line shows the ISM feature toward the galactic plane from Kemper et al. (2004), the green, dash-dotted line is the profile based on Weingartner & Draine (2001) and Draine (2003), and the blue, dotted line is for 0.1 μm sized amorphous pyroxene grains (Dorschner et al., 1995).

To measure not only the depth of the absorption profile, but to get also an idea of the dust composition responsible for the observed absorption, we analyzed the shape of the silicate feature. In Figure 5.16 we show the optical depths computed or measured for different dust grain compositions. Depending on the composition the wavelengths of the maximum optical depth changes. The most extreme cases are amorphous olivine grains with a size of 0.1 μm peaking at a wavelength slightly longward of 9.7 μm, and amorphous pyroxene grains with the same size peaking around 9.2 μm wavelength. As mentioned above, in Table 5.5 we already give the wavelengths of the maximum optical depths observed toward our sources and it shows that there is indeed a broad range of values, indicating different dust compositions. In Figure 5.17 we plot again the observed optical depth of our objects as shown in Figure 5.15, but now we overplot one or two of the absorption profiles presented in Figure 5.16, scaled to the maximum observed optical depth. Whether this scaling is appropriate is difficult to determine but it shows that most observed features agree reasonably well with one or two of the reference profiles. Three objects (L1551 IRS 5, V346 Nor and V1735 Cyg) show additional absorption longward of 11 μm when compared to the dust features, but at least part of this absorption can be attributed to H_2O libration bands (e.g., Pontoppidan et al., 2005). V1735 Cyg, RNO 1C and Z CMa seem to agree best with the dust model computed by Draine (2003) based on the particle size distribution from Weingartner & Draine (2001). V346 Nor requires short-

Object	$\tau_{\rm silicate}$	$\lambda_{\rm silicate}$ [μm]	$A_{\rm silicate}$ [mag]	A_V [mag]	A_V [mag]
L1551 IRS 5	1.33±0.03	9.44	1.44±0.03	21.83± 4.70	19[a], 30[b], $\gtrsim$150[c]
V346 Nor	0.32±0.01	9.68	0.35±0.01	4.98± 0.86	6.2[d]
V1735 Cyg	0.29±0.03	9.52	0.31±0.03	4.60± 0.91	10.0[e,f]
RNO 1B	0.24±0.01	9.30	0.27±0.01	4.15± 1.03	9.2[g]
RNO 1C	0.63±0.01	9.58	0.69±0.01	10.11± 1.87	$\gtrsim$12[g]
HL Tau	0.47±0.01	9.61	0.51±0.01	7.38± 1.32	$\approx$24.0[h,i]
Z CMa	0.31±0.06	9.48	0.34±0.20	5.05± 1.04	2.8±0.1[j]
Reipurth 50	1.68±0.34	9.68	1.82±0.20	26.18± 4.34	$\approx$50[k]

Table 5.5 Optical depths and extinction values as derived from the spectra shown in Figure 5.15. [a] Snell & Schloerb (1985), [b] Smith et al. (1987), [c] Stocke et al. (1988), based on the apparent absence of a K-band source (K>15), [d] Graham & Frogel (1985), assuming E(B-V)=2.0, [e] Sato et al. (1992), [f] Levreault (1988a), [g] Staude & Neckel (1991), based on optical data and assuming spectral type, [h] Bergin et al. (2005), [i] Close et al. (1997), based on large H-K=2.14 value, [j] Cohen & Kuhi (1979), based on optical data and assuming spectral type, [k] Casali (1991), based on NIR colors, assumed intrinsic color temperatures and strength of additional ice absorption features.

ward of 10 μm a mixture of the same model and the dust composition observed toward the galactic center (Kemper et al., 2004). Longward of 10 μm the former model alone fits better. For Reipurth 50 a combination of both models explains the data well over the whole wavelength regime with the Draine (2003) model fitting the short and the Kemper et al. (2004) model fitting the long wavelength part. L1551 IRS 5 is best fitted with a mixture of small, amorphous pyroxene grains and the model from Draine (2003). The profile of HL Tau agrees extremely well with the galactic center dust profile from Kemper et al. (2004), but seems to require just a little bit more amorphous pyroxene to account for a small shift toward shorter wavelengths. Finally, the absorption profile of RNO 1B

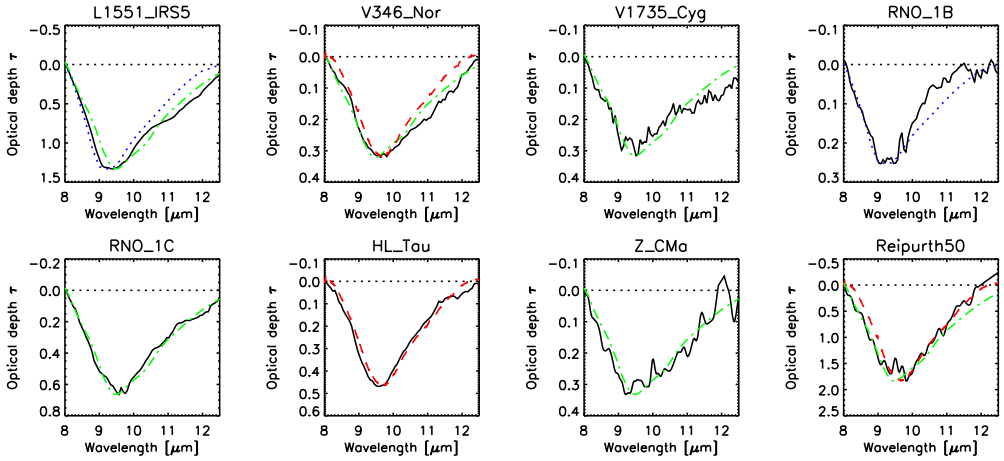

Figure 5.17 Same observed spectra as in Figure 5.15 (black, solid lines), but now overplotted with reference spectra with different dust compositions (same color and line style code as in Figure 5.16).

is special in two ways: First, the short wavelength range is best fitted solely with small, amorphous pyroxene grains. And secondly, between 10 and 11.5 μm the profile shows a significantly lower optical depth than any of the reference profiles. In combination with our findings for the visual extinction (see above) this suggests that RNO 1B shows silicate emission superposed on the absorption feature. Interestingly, the apparent lack of optical depth longward of 10 μm indicates that at these wavelengths the contribution of the emission is relatively larger compared to the other wavelengths in the silicate band. This in turn means that the emission profile does not have the typical shape of the ISM dust feature but a broader and more evolved profile like the other FUors emission profiles shown in Figure 5.10.

The 15.2 μm CO_2 ice feature

The shape of the bending mode profile of CO_2 ice around 15.2 μm does not only allow a detailed analysis of the involved ice inventory, but it enables to derive information about potential ice processing due to heating effects (e.g., Pontoppidan et al., 2005). In Figure 5.18 we present two reference cases which we will use in the following as a benchmark for comparison with the FUor spectra. The first object in Figure 5.18 (CK2) is a highly extincted background star behind the Serpens dark cloud (Knez et al., 2005), and the second object (HH46) is an embedded low-mass protostar (Boogert et al., 2004). While the spectrum of CK2 probes mainly the ice composition of the intervening dark

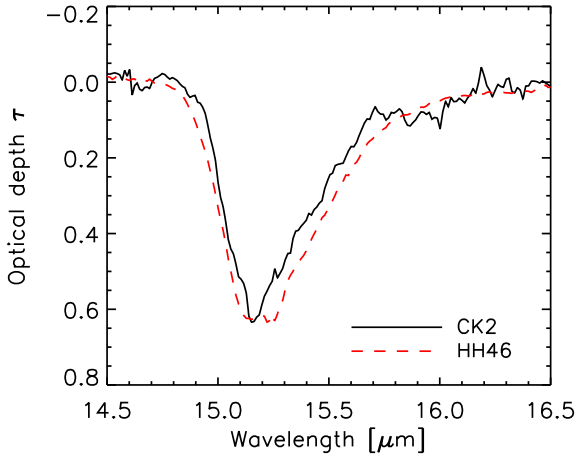

Figure 5.18 Comparison of the 15.2 μm CO_2-ice feature between the heavily extincted background object CK2 (Knez et al., 2005) and the embedded young source HH46 (Boogert et al., 2004). Due to higher temperatures in the vicinity of the embedded protostar crystallization occurs and and a double-peaked sub-structure appears characteristic of the pure CO_2 matrix (Ehrenfreund et al., 1998).

cloud, the spectrum of HH46 bears information about the immediate environment of the young star. Apart from being slightly broader, the spectrum of HH46 shows a double-peaked sub-structure which is caused by crystallization and effective segregation of the CO_2 and H_2O ice involved in the absorption. These processes take place when ice mixtures with concentrations of $CO_2/H_2O \geq 1$ are heated (Boogert et al., 2004). In space, this phase transition from amorphous to crystalline ice is expected to occur between 50-90 K and thus at higher temperatures than typically found in cold, dark molecular clouds. Thus, the 15.2 μm ice feature of HH46 shows that (at least) part of the ice must already have been heated by the embedded protostar. In fact, Boogert et al. (2004) fit the feature with a two-component ice model based on laboratory spectra with one component being highly processed polar ice with a laboratory temperature of $T_{lab} = 125$ K, and the

other component being an H_2O-rich, CH_3OH-deficient cold ice with $T_{lab} = 10$ K.[5] The spectrum of CK2 was fitted by Knez et al. (2005) solely with cold ice components. They used a polar mixture of H_2O:CO_2=1:1 and H_2O:CO_2=10:1 at 10 K with a ratio of 2:1 and an additional apolar component of CO:N_2:CO_2=100:50:20 at 30 K. The overall polar fraction was assumed to be 78 %.

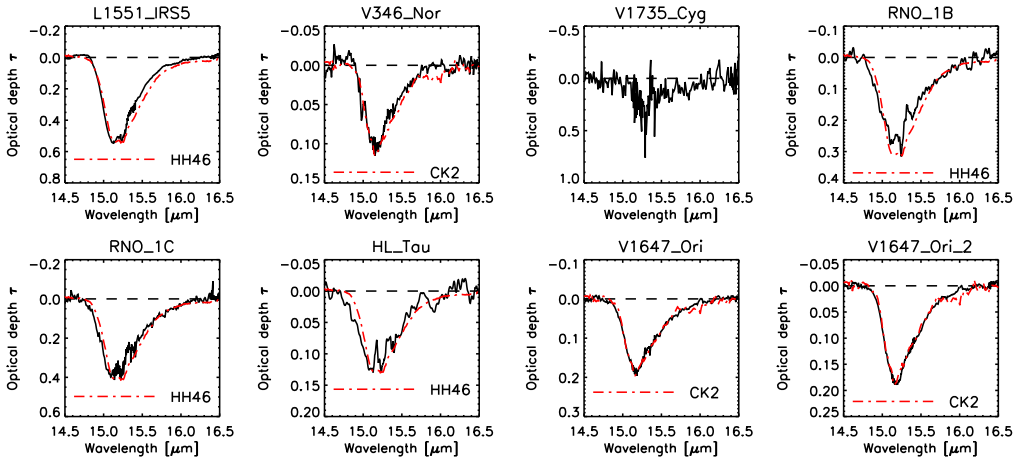

Figure 5.19 The 15.2 μm CO_2-ice feature observed toward some of our objects (black, solid lines). The spectra of HL Tau, RNO 1B and V1735 Cyg were smoothed by a factor of 20 to increase the signal to noise. Overplotted is either the scaled spectrum of HH46 or CK2 (red, dashed-dotted line; see Figure 5.18) depending on which profile fits better to the FUor data. Due to the remaining high noise level in the spectrum of V1735 Cyg no clear comparison to either reference object was possible. The absorption feature of V1647 Ori observed at the third epoch is not shown as these are only low-resolution data, while the data presented here (first and second epoch) were taken with the high-resolution spectrograph.

In Figure 5.19 we present the 15.2 μm features observed toward our FUor sample. For each object we overplot either the (scaled) spectrum of HH46 or CK2 depending on the shape of the profile. While the profiles of V1647 Ori and V346 Nor agree better with the profile of CK2 (the spectrum representing unprocessed ice), L1551 IRS 5, RNO 1B and 1C, and HL Tau show evidence for a double-peaked sub-structure and thus heating effects and processed ice. The comparatively bad quality of the V1735 Cyg spectrum does not allow a solid comparison to either reference spectrum. It is noteworthy that the spectrum of V1647 Ori is almost an exact copy of CK2 indicating that the ice composition is mostly identical. Based on the fitted reference spectrum we computed also the optical depth $\tau_{15.2\,\mu m}$ for each object and summarized the results in Table 5.6. The errors are based on the 1-σ uncertainties in the observed spectra.

The 6.0 and 6.8 μm ice features

The two well-known ice features at 6.0 and 6.8 μm are, although frequently observed toward high- and low-mass sources, quite complex and difficult to interpret. Certainly,

[5]The presence of CH_3OH in the ice feature can potentially be traced by the shape of the long-wavelength wing of the CO_2 profile showing additional absorption if CH_3OH is present in higher abundances.

Object	$\tau_{6.0\,\mu m}$	$\tau_{6.85\,\mu m}$	$\tau_{15.2\,\mu m}$
L1551 IRS 5	0.51±0.01	0.47±0.01	0.54±0.05
V346 Nor	0.05±0.01	0.06±0.01	0.12±0.02
V1735 Cyg	0.05±0.02	0.09±0.01	≈0.3
RNO 1B	0.20±0.01	0.18±0.01	0.32±0.04
RNO 1C	0.35±0.01	0.26±0.01	0.41±0.02
HL Tau	0.10±0.01	0.07±0.01	0.13±0.06
V1647 Ori	0.07±0.01	0.06±0.01	0.20±0.02
V1647 Ori 2	0.10±0.01	0.08±0.01	0.19±0.02
V1647 Ori 3	0.09±0.01	0.07±0.01	-[a]

Table 5.6 Optical depths of the main ice features at 6.0, 6.85 and 15.2 μm. [a] only low-resolution data.

a large fraction of the optical depth of the 6.0 μm band can be attributed to H_2O ice, but also other species might contribute to this absorption feature (Keane et al., 2001). For instance, slightly shortward, at roughly 5.85 μm, an additional absorption shoulder is sometimes superposed (e.g., Pontoppidan et al., 2005; Keane et al., 2001) for which formaldehyde (H_2CO) and formic acid (HCOOH) are theoretical candidates. Without any additional information (e.g., the 3.08 μm band of H_2O or the 3.47 μm band of H_2CO) it is thus difficult to determine the true water ice content in the 6.0 μm band. An additional absorption feature at 6.85 μm is often observed toward protostars (e.g., Keane et al., 2001), but also toward the extincted background star CK2 (Knez et al., 2005) and the edge-on disk CRBR 2422.8-3423 (Pontoppidan et al., 2005). Although a final identification of this band has yet to be provided, NH_4^+ seems to be one of the most promising candidates (Schutte & Khanna, 2003; Pontoppidan et al., 2005). However, van Dishoeck (2004) for example, mention also methanol (CH_3OH) as a potential carrier of this absorption band. Given all these uncertainties we restrict ourselves in this section to the computation of the optical depth of both of the above mentioned absorption bands. To do so we fitted a polynomial of fourth order to both absorption dips to eliminate the noise in the spectra. Figure 5.20 shows the observed spectra between 5.5 and 7.5 μm on an optical depth scale (black lines) with the resulting fits overplotted (red, dashed-dotted lines). The computed optical depth for each band and each object is given in Table 5.6. Like in the previous section the errors are based on the 1-σ uncertainties in the observed spectra.

5.3.4 Additional emission lines

For completeness we show in Figure 5.21 absorption and emission lines identified in the high-resolution regime of the SPITZER spectra, part of which are difficult to identify in Figures 5.7 and 5.8. Already Green et al. (2006) noted the S[III] emission lines at 18.7 and 33.4 μm in the spectrum of V1515 Cyg and argued that they originate from extended emission in the region and not from the object itself. The spectra of RNO 1B and RNO 1C show evidence for H_2 quadrupole emission around 17 μm and additional H_2 lines in the low-resolution part of the spectrum at shorter wavelengths. In chapter 4 we analyzed these emission lines in detail and concluded that they are related to shocks within a molecular outflow powered by the nearby embedded object IRAS 00338+6312. Fe[II] lines around

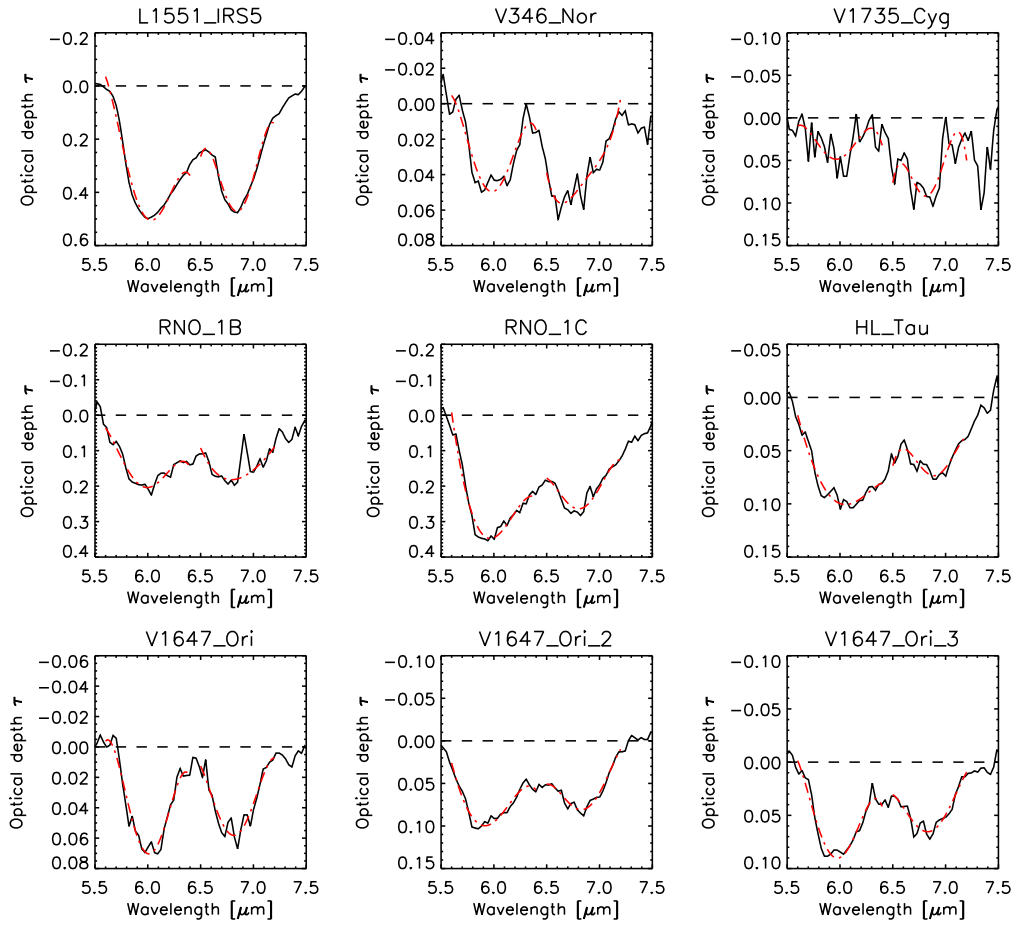

Figure 5.20 The 6.0 and 6.85 μm ice bands observed toward some of our objects (black lines). Overplotted are the polynomial fits of fourth order (red, dashed-dotted line) to determine the optical depths of the absorption bands.

17.9 μm are present in the spectra of L1551 IRS 5 and RNO 1B, and L1551 IRS 5 shows also the Fe[II] line near 26.0 μm. The Fe[II] lines of L1551 IRS 5 were already detected in the ISO/SWS spectrum of this source and attributed to hot and dense material located close to the root of the outflow (White et al., 2000). The line intensities did not fit the predictions from shock models. Concerning the Fe[II] line in the spectrum of RNO 1B, it seems likely that it arises in the outflow shocks that also excite the H_2 emission lines discussed in the previous chapter. Finally, V1057 Cyg shows gaseous CO_2 absorption slightly shortward of 15.0 μm.

5.4 Discussion

5.4.1 Two categories of FUors

The results presented here suggest that the sample of FUors can be divided into two categories based on the observational appearance of the 10 μm silicate feature. Therefore we decided to call the absorption feature objects ”Category 1”-FUors and the emission

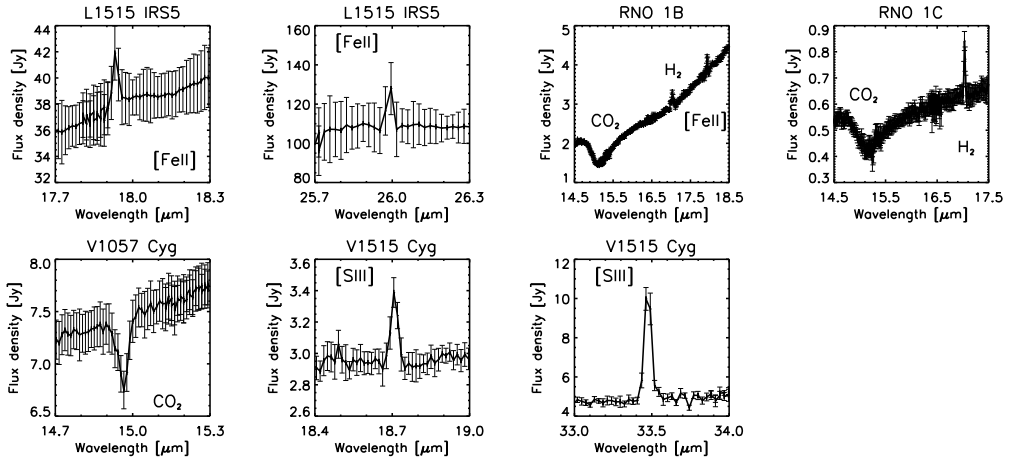

Figure 5.21 Zoom into emission lines, absorption lines and CO_2 ice bands detected in the high-resolution part of the spectra of some objects (see text).

feature objects "Category 2"-FUors. In the following we discuss the properties of the two categories in more detail.

Category 1 FUors: silicate and ice absorption features

In general it is possible to observe the silicate feature in absorption if the circumstellar disk surrounding a young object is seen close to edge-on (e.g., Men'shchikov & Henning, 1997). Given the amount of objects showing silicate absorption compared to the number of objects with silicate emission and assuming a random distribution of the orientation of the accretion disks, it is unlikely that all Category 1 FUors are seen edge-on. Rather, these objects are still more deeply embedded in their molecular envelopes covering a larger solid angle than the edge-on disk alone. These envelopes cause the ice and dust absorption features.

Figure 5.16 illustrates that all but one silicate absorption bands are fitted best either with the silicate composition observed toward the Galactic center by Kemper et al. (2004) or with the astronomical silicates from Weingartner & Draine (2001) and Draine (2003)[6]. Only the spectrum of RNO 1B is different in this respect, but, as already mentioned, there are strong hints that the absorption feature is altered by a superposed emission feature.

In Figure 5.22 we show the observed optical depths of the ices and the silicate feature in a scatter plot to look for any correlation. Although the range of optical depths we probe here is limited, it seems that at least for the ices there seem to be correlations (left and right plot in Figure 5.22). Fitting a straight line to the data we find:

$$\tau_{15.2\,\mu\mathrm{m}} = (0.349 \pm 0.037) \cdot \tau_{6.0\,\mu\mathrm{m}} + (0.040 \pm 0.009) \tag{5.4}$$

$$\tau_{6.8\,\mu\mathrm{m}} = (0.858 \pm 0.067) \cdot \tau_{6.0\,\mu\mathrm{m}} + (0.007 \pm 0.016) \tag{5.5}$$

This implies that the physical and chemical conditions within the envelopes and clouds causing the absorption is similar. For the silicates the situation is slightly different, since,

[6] L1551 IRS 5 requires a fraction of additional amorphous pyroxene grains.

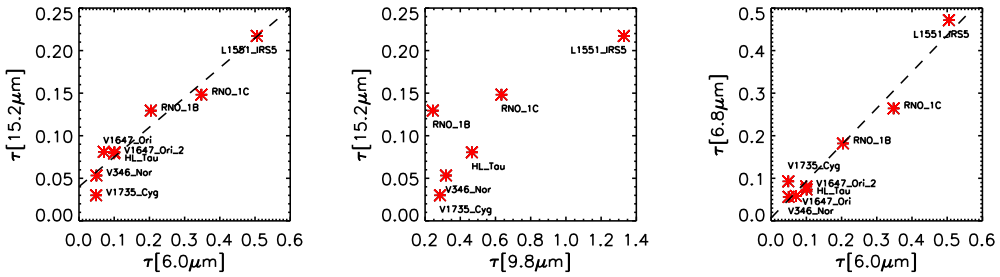

Figure 5.22 Correlation between the optical depths of ice features at 15.2 and 6.0 μm (left), ices and silicates at 15.2 and 9.8 μm (middle), and ice features at 6.8 and 6.0 μm (right). V1647 Ori is not shown in the middle plot as its silicate feature is seen in emission and not in absorption (see text).

as we have already pointed, their feature can be influenced by superposed emission. This shows nicely in the middle plot in Figure 5.22, where RNO 1B is shifted with respect to the other objects.

Finally, it is interesting to note that the objects showing evidence for ice processing in Figure 5.19 tend to show higher optical depths in the ice features than the other sources. This might suggest that the extinction for the latter objects (V346 Nor, V1735 Cyg) might be caused by ices somewhere in the line of sight to the source, rather than by material related to the young star. This might also explain, why V1647 Ori shows weak silicate emission, but ice absorption: the extinction is caused by cold foreground material, reflected also in the observed high value for A_V (see caption Figure 5.10). Only a small fraction of the intrinsically strong silicate emission feature of V1647 Ori can be detected with the sensitivity of SPITZER. Ground-based observations find the spectrum to be flat (Ábrahám et al., 2006).

Category 2 FUors: the silicate emission feature and its dust composition

As presented in Figure 5.10 and described in the related section, the emission profiles bear evidence for dust grain processing. Even after the correction for apparent interstellar extinction, the shape of the silicate profile differs from that of typical ISM dust. Like for TTauri stars and the slightly more massive HAeBes, the origin of the emission feature in the spectra of the FUors is the heated surface layer of the accretion disk. The apparent grain processing is believed to be only possible in circumstellar disks and not in less the dense circumstellar envelopes. While the emission layer for TTauri stars and HAeBes is mainly heated be the central stellar object, for FUors the hot inner parts of the accretion disk itself can act as the main illuminating source (e.g., Lachaume, 2004). Due to the high accretion rates of FUors those inner regions are extremely hot and account for a significant fraction of the total flux even at optical wavelengths (see, e.g., section 3.7). Furthermore, accretion disk models with a flared geometry were not only able to explain the SEDs of FU Ori and Bran 76 (Green et al., 2006), but they could also reproduce interferometric observations in the NIR (Malbet et al., 2005) and MIR (chapter 3). V1057 Cyg and V1515 Cyg show more emission at longer infrared wavelengths than the previous objects, which can be accounted for assuming a remnant infalling envelope in addition to the accretion

disks. This is supported by the results from K-band interferometry Millan-Gabet et al. (2006), where envelopes are required to explain the low NIR visibilities.

Concerning the dust composition it is interesting to note that, given the low peak-over-continuum ratio illustrated in Figure 5.11, grain growths must have already set in. This is supported by the results of our dust model fit. Furthermore, the spectra do not show evidence for crystalline dust particles. The mass fraction of crystalline particles in both dust models computed for the spectrum of FU Ori was negligible (see, Table 5.4). Since strength and shape of the silicate feature of FU Ori is comparable to those of Bran 76 and V1515 Cyg (Figure5.11), the dust composition in all objects is very similar. The spectrum of V1057 Ori is even broader and less pronounced than the other spectra, indicating even larger grains in the disk surface layer. The intrinsic feature of V1647 Ori is stronger than those of the other FUors, but no prominent signs of crystalline silicates are present either.[7]

As already mentioned in chapter 3, there are several reasons for which stronger crystalline features could have been expected to be detected. The high disk accretion rates should ease the detection of crystalline particles in two ways: (1) high accretion rates lead to high disk temperatures (Bell et al., 1997) which in turn should increase the amount of crystalline particles produced by annealing processes at T$\geq$800 K. (2) an increase in the accretion rate should also increase the radial and vertical mixing in the disk (Gail, 2001) transporting the crystalline particles farther out and to the disk surface, where they can be detected by means of MIR spectroscopy. However, neither in the innermost disk regions probed with MIR interferometry (chapter 3) nor in the SPITZER spectra presented here in Figure 5.10 or at longer wavelengths in Figure 5.7 we see any striking evidence for crystallinity. This means, that either those grains do not exist in large amount in these disks or they are somehow hidden.

The disks of FUor objects are different from those of TTauri or Herbig star disks in the sense that in the innermost regions of FUor disks the luminosity is accretion dominated (TTauri and Herbig star disks are irradiation dominated everywhere). At larger radii, also FUor disks are irradiation dominated, albeit the main heating source is not the central star, but rather the hot inner disk regions. Disk regions that are irradiation dominated have a surface layer that is warmer than the underlying disk interior; such an "inverted" temperature profile causes dust features to appear in emission. In the accretion dominated regions, the main heating source is the release of gravitational energy in the disk midplane. Here, the disk interior is at least as hot (and likely hotter) than the disk surface, causing dust features to be effectively hidden, or even to appear in absorption. Thus, it is conceivable that there are significant amounts of crystalline silicates present in the hot inner disk regions of our targets, even if they do not show up prominently in the spectra.

But what about crystalline silicates further from the central object, in irradiation dominated regions? Given the high accretion luminosity in our objects it seems unavoidable that large amounts of crystalline silicates are produced in the innermost disk regions. In addition to this, crystalline silicates may be produced *in situ* at large radii in shocks (Harker & Desch, 2002) or electric discharges (Pilipp et al., 1998; Desch & Cuzzi, 2000). If the disk is well mixed in the vertical direction, the crystalline silicates should be present in the surface layer of the disk at large ($\gtrsim$ few AU) radii, and show up in emission, which they evidently do *not* (at least, to a much lesser extent than in many TTauri and Herbig Ae/Be star disks, which are more evolved). This inevitably leads to the conclusion that

[7]The spectrum of Parsamian 21 does show a prominent feature at 11.3 μm but we attribute most of the related flux to PAH emission and not to crystalline silicates (see section 5.3.2).

crystalline silicates are *not* abundant in the surface layer of FUor disks at radii of more than a few AU from the central object, *contrary to expectations*.

At this point, we have no proper explanation for this observation. In order to animate the discussion, we will post the following idea, but stress that at this point this is mere speculation. The crystalline silicates are not present in the surface layer at larger radii, but may be present in the disk interior, where they are expected to be formed by virtue of the processes mentioned before. Thus, we need to explain why the crystalline silicates do not get mixed in the vertical direction all the way to the disk surface. One possibility is that the crystalline particles are somehow less well coupled to the gas, possibly because they are more compact (or less ”fluffy”) than the unprocessed dust particles. This may cause the selective settling of crystalline dust. A second possibility is the following. The accretion rate in FUor objects is high, suggesting that the disk is still being supplied with fresh material from the maternal envelope. This material, which is thought to contain exclusively small, amorphous dust particles, will in part ”rain” onto the disk surface at larger radii. If the rate at which this material falls onto the disk is higher than the rate at which it is mixed through the disk in the vertical direction, the disk may be covered by a ”blanket” of pristine material, effectively hiding the more processed material present in the disk interior. It is unclear whether this idea can be harmonized with the observation that the dust we see at the disk surface has undergone significant grain growth. This issue clearly calls for a much more detailed and quantitative investigation, which is beyond the scope of the present work.

5.4.2 Unifying the two categories of FUors: An evolutionary sequence

The spectral properties of the sample presented here draw a rather inhomogeneous picture of the group of FU Orionis objects. However, as most of them are convincingly classified as FUors, they do share some common observational and physical properties. In the following, we present an idea, how the apparent differences can be explained within a unified paradigm of FU Orionis objects.

Already 20 years ago Herbig (1977) and Hartmann & Kenyon (1985) suggested that each FUor might undergo several outbursts. More recent theoretical models show that gravitational instabilities in the accretion disk, driven by continuing infall from a remnant envelope, can account for intense bursts of high accretion rates which are intersecting more prolonged, quiescent periods of low accretion (Vorobyov & Basu, 2006; Boley et al., 2006). After several of these outbursts have occurred within a time span of several 10^5 years, the envelope, which is the trigger of the disk instabilities, vanishes, and the object enters finally a state of permanently low accretion. If one relates this final phase to the classical TTauri phase of low-mass YSOs, then FUors are younger than classical TTauri stars as already pointed out by Weintraub et al. (1991) and Sandell & Weintraub (2001).

Kessler-Silacci et al. (2005) analyzed the 10 μm silicate feature of 34 young stars and confirmed that the evolution of the feature of low-mass stars and the overall SEDs is similar to that of intermediate-mass stars: embedded objects, showing a pristine silicate band in absorption, evolve into objects showing a combination of silicate absorption and emission, and finally pure emission features appear, where dust processing leads to a broad range of shapes and strength. Since all these stages are represented in our sample, we believe that, indeed, the FUor-phase is the link between the embedded Class I objects and the more evolved Class II objects. In this context, the objects showing silicate absorption are younger and at the beginning of the period where subsequently numerous FUor

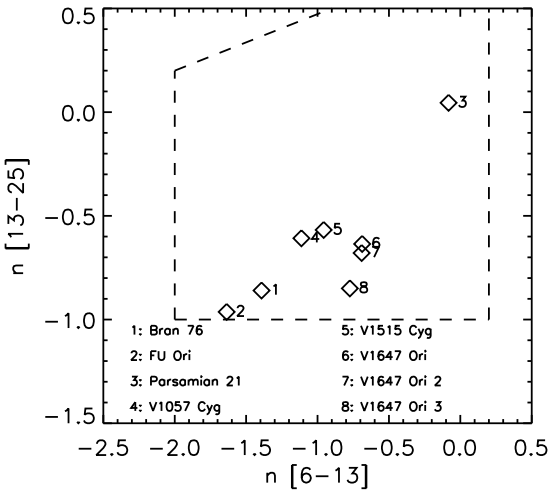

Figure 5.23 Spectral index n of the silicate emission objects evaluated between 13 and 25 μm vs. the spectral index between 6 and 13 μm. n is computed as $n \equiv d\log(\lambda F_\lambda)/d\log(\lambda)$. All objects populate the same area in the plot as the Class II objects in Taurus presented by Furlan et al. (2006) (dashed area). Due to the steep rise in its SED, Parsamian 21 lies slightly off from the other objects.

outbursts will occur, while the objects showing pure emission features are more evolved and possibly near the end of their FUor period. As illustrated in Figure 5.23 the spectral indices of the emission objects are indistinguishable from Class II objects in Taurus (Furlan et al., 2006). In particular, the objects FU Ori and Bran 76 appear to be the most evolved objects, because, as mentioned above, their SEDs do not require the presence of a large remnant envelope. A nice example of an intermediate object is RNO 1B, where the dominating absorption feature is altered by the underlying silicate emission from the accretion disk. Figure 5.24 illustrates with simple sketches the main features of the the two categories of FUors.

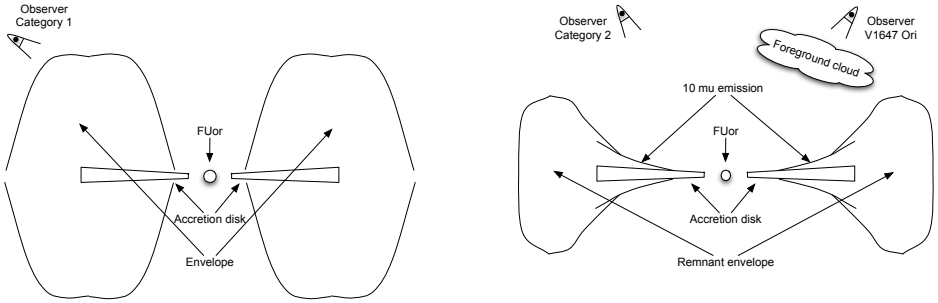

Figure 5.24 Simple graphical representation explaining the two categories of FUors (not to scale). Category 1 objects (left) show silicate absorption and are younger than than Category 2 objects (right) which show silicate emission. While Category 1 objects are still more deeply embedded in their envelopes and appear to be Class I sources, Category 2 FUors are similar to Class II sources. The spectrum of V1647 Ori can be explained assuming that extinction in the line of sight to this object creates the ice absorption features and reduces also the strength of the observed silicate emission. .

One question arises, though. If FUors are younger than classical TTauri stars but do already show clear evidence for dust coagulation, then why do some classical TTauri stars

show silicate emission features consisting purely of pristine and unprocessed dust? One possible explanation is linked to the high accretion rates of the FUors. It is believed that high disk accretion rates are related to a higher degree of turbulence and thus mixing in the disk. As a result, larger particles are coupled to the turbulent gas and mixed throughout the disk and to the disk surface, where they can be observed. Once the accretion rate, and hence the amount of mixing, drops, larger particles tend to settle to the disk midplane much faster than small particles, which remain in the disk surface layer. Thus, although large particles are present in the disk of a TTauri star, they might not reach the disk surface, and only the small grains produce a silicate emission feature. Again, as for the issue concerning the lack of crystalline grains, a more detailed theoretical modeling is certainly required to see to what extend this qualitative explanation is valid.

5.4.3 Parsamian 21 - intermediate mass FUor or Post-AGB star?

The strong PAH emission of Parsamian 21 is unique among the sample of FUors presented here, and the analysis rise serious doubts whether Parsamian 21 is indeed a member of this group. The initial classification was made by Staude & Neckel (1992) based on optical spectroscopy. These authors derived a spectral type of F5Iab, found a prominent P-Cygni profile in Hα and observed shock-induced emission in [O I], [N II] and [S II]. They also mention the detection of Li in their spectra, which is, however, not obvious from the data shown in the paper. New observations with higher spectral resolution would certainly be eligible. Although some of these features are commonly observed in FUors, they are not unique to this group of objects, as also HAeBes show, for instance, P-Cygni profiles in Hα. In addition, two of the main properties of FUors, an outburst in optical light and CO bandhead absorption profiles in the NIR (e.g., Hartmann & Kenyon, 1996), have not yet been observed for Parsamian 21.

To excite the PAH emission, sufficiently strong UV radiation is required. However, most FUors have a later spectral type than Parsamian 21 and lack, unlike TTauri stars, in general UV continuum excess emission (Hartmann & Kenyon, 1996). Furthermore, as mentioned above, the positions of the PAH emission bands are untypical for young stars and are comparable to those of two Post-AGB stars. In particular the band at 8.2 μm might represent freshly synthesized PAHs (Peeters et al., 2002). In addition, one of the Post-AGB stars from Peeters et al. (2002) and also HD 56126, a Post-AGB star with PAH and silicate emission (Hony et al., 2003), have the same spectral type as Parsamian 21. However, we should mention that Dibai (1969) and The et al. (1994) give a spectral type of A5Veα for Parsamian 21. This is too early for a typical FU Orionis object, but could also explain the PAH emission. Finally, the bipolar emission knots seen in Hα and [N II] in the optical spectrum of Parsamian 21 (Staude & Neckel, 1992), are also found in the bipolar outflows of evolved stars and ”pre-planetary” nebulae (e.g., in the ”Butterfly Nebula”, Solf, 2000). They are thus not only seen in young objects. Based on these findings, we believe that the FUor status of Parsamian 21 is at least very questionable. Either this object represents an intermediate mass FUor object, suggesting that also stars in this mass regime undergo phases of enhanced accretion, or, and this appears even more likely, Parsamian 21 is not even a young object but an evolved star, sharing typical properties with Post-AGB stars.

5.5 Conclusions and future prospects

Our conclusions can be summarized as follows:

- We presented the first space based spectroscopic MIR study of 14 FUors observed with the SPITZER SPACE TELESCOPE or the INFRARED SPACE OBSERVATORY.
- Based on the appearance of the 10 μm silicate feature, we divided the sample into two categories: Category 1 objects show the silicate feature in absorption, and the spectra show additional absorption bands at 6.0, 6.8 and 15.2 μm due to ices. Category 2 objects show silicate emission and (most of them also) indications for water vapor absorption at shorter wavelengths. Only one Category 2 object (V1647 Ori) shows ice absorption bands which we explain by foreground extinction and an intrinsically strong 10 μm emission feature.
- The silicate absorption is best explained with dusty and icy envelopes surrounding the Category 1 objects. Statistical reasons argue against all objects having accretion disks seen edge-on. The silicate emission of the Category 2 FUors arises from the surface layer of the surrounding accretion disks.
- The shape of the silicate band of the Category 1 objects is in agreement with typical dust compositions of the ISM. For one object (RNO 1B) the shape of the feature and the lack of optical depth longward of 10 μm can be explained with a superposed emission feature.
- Optical depths for the observed silicate and ice absorption bands were derived. We find an apparent correlation among the optical depths of the ices indicating similar environmental conditions for the objects. For the silicate feature, no correlation is expected.
- Using different interstellar models we computed the optical extinction toward the objects based on the depth of the silicate features. The results are in agreement with values found in the literature, given the uncertainties in the dust models and for the optical extinction values in the references. For RNO 1B the derived value for A_V is smaller than expected, indicating that on-top silicate emission might influence the optical depth at 10 μm.
- The emission profiles of the Category 2 objects show clear evidence for grain growth. Fitting a dust model to the spectrum of FU Ori reveals that, indeed, larger grains than typically observed in the ISM are required to explain the shape. As FUors are presumably younger than TTauri stars (see below), this indicates that grain growth sets in very early during disk evolution.
- Despite the high accretion rates of the FUor accretion disks and the resulting higher disk temperatures and mixing rates, we find hardly any evidence for crystalline grains. So far we lack a clear explanation for this observational results and leave it to further investigations.
- The two categories of FUors can be explained within a single paradigm, where Category 1 objects are younger and similar to Class I objects, while Category 2 FUors are more evolved and show already properties of Class II sources. This

explanation is in agreement with theoretical models which expect FUors to undergo several outbursts before they enter the more quiescent classical TTauri phase. Thus, the FUor-phase might indeed be the link between Class I and Class II objects and common to most young low-mass stars.

- Only one object (Parsamian 21) shows PAH emission similar to that observed in Post-AGB stars. We find that most other observational data for Parsamian 21 can also be explained with the object being an evolved star. In consequence, the FUor-status for this object is questioned.

Based on these findings, future investigations might include the following points:

- A complete MIR spectroscopic census of all known FUors would complement the data presented here and might help to derive conclusions concerning the duration of the FUor phase using statistical arguments.
- Multidimensional radiative transfer models have not yet been applied to FUor accretion disk, but they are required to derive a coherent picture of the disk structure, including the emission layer.
- Models for the dust evolution in accretion disks could try to explain quantitatively the observed large grain population and the apparent lack of crystalline silicates.
- Finally, if our conclusions are correct, then some of the known low-mass Class I objects might be FU Ori objects hidden in a quiescent phase between two consecutive outbursts. The observational properties of these objects might be revisited to search for any indication of FUor properties.

6. Young objects in the Taurus star-forming region

A deep near-infrared survey

Parts of this chapter are planned for publication in the Astrophysical Journal.
(Quanz, S. P., Henning, Th., Goldman, B. Brandner, W., et al., 2007, ApJ, in preparation)

THE FOLLOWING chapter presents the results of a large near-infrared (NIR) survey of the Taurus star-forming region. In the course of this survey the densest molecular cores were imaged in three NIR filters (J, H, and Ks). The images were used to search for new young objects surrounded by circumstellar disks, to analyze the properties and internal structure of the dense molecular cores, and to identify potential candidates for yet undiscovered young low-mass stars and Brown Dwarfs with masses down to the Jupiter mass regime. After a short introduction, the observations and the data reduction will be described before the main part of this chapter is dedicated to the above-mentioned scientific objectives.

6.1 Introduction

The Taurus star-forming region is certainly one of the best studied low-mass star-forming regions in the northern hemisphere. It lies at a distance of ~ 140 pc (Kenyon et al., 1994), has a mass of $\sim 10^4$ solar masses, an extension of ~ 20 pc (Ungerechts & Thaddeus, 1987), and is a relatively young star-forming region ($\tau \sim 1$ Myr, Briceño et al., 2003; Luhman et al., 2003). Taurus has been studied in all wavelengths regimes and large surveys helped tremendously to foster our understanding of the star formation process in the low-mass regime. Sub-millimeter and millimeter dust continuum observations of large samples of young objects allowed a statistical analysis of disk sizes, masses and the mass ratio between the disk and the central object (Beckwith et al., 1990; Andrews & Williams, 2005). Mid-infrared observations with the IRAC camera onboard the SPITZER SPACE TELESCOPE showed that some objects have cleared out inner gaps in their disks providing important information for the modeling of the disk structure and evolution (Hartmann et al., 2005). Large X-ray surveys, finally, provide insights into the magnetic activity of the young stars which in turn also influences the circumstellar disk, e.g, by ionizing the upper layers of the gaseous disk component (Guedel et al., 2006).

Partly based on these surveys and in combination with other observations, the initial mass function (IMF)[1] in Taurus has been studied intensively in the last years. It differs from the typical field IMF as no O- and B-stars are found in Taurus (e.g., Briceño et al., 2002). Additionally, it first seemed as if also at the low-mass end the number of Brown Dwarfs was too small compared to the typical IMF (Briceño et al., 2002). Recent studies, however, provided evidence that this might in fact not be the case (Luhman et al., 2006a; Guieu et al., 2006).

Due to its young age, the disk fraction in Taurus, i.e., the fraction of young stars surrounded by protoplanetary disks, is higher than in other low-mass star-forming regions as for instance IC 348 and Chameleon I. Luhman et al. (2006a) found that for stars (spectral type M6 and earlier) the disk fraction amounts to 61 ± 8% while the disk fraction of Brown Dwarfs (spectral type later than M6) is 40 ± 13%. Thanks to the small distance to Taurus it is possible to resolve (at least some of) the disks surrounding the TTauri stars. Knowing the disks' semi-major axes or for some objects the direction of a jet or an outflow perpendicular to the disk, it is possible to compare the orientation of the disks to each other and also to the ambient magnetic field. Such an analysis shows whether there is a preferred disk orientation in Taurus which might be related to the surrounding magnetic field lines. However, Ménard & Duchêne (2004) found for a sample of 37 classical TTauri stars no clear indication for a connection between the disk orientation and the local magnetic field.

6.2 Observations and data reduction

In a new deep near-infrared survey we observed 55 dense cores in Taurus between October 2004 and January 2006 (see Table 6.1). These cores were initially identified in the course of a large $H^{13}CO^+$-survey by Onishi et al. (2002). The observations were carried out with the wide-field near-infrared camera OMEGA2000 at the 3.5 meter telescope on Calar Alto (Spain)[2]. The prime focus camera is equipped with a 2048×2048 pixel HAWAII-2 detector, has a pixel scale of $0.45''$/pixel and an effective field-of-view of $\sim15'$. The 55 dense cores were covered with 24 telescope pointings. One additional field (tc50 in Table 6.1) harboring a newly discovered Proto-Brown Dwarf (Apai et al., 2005) was included in the survey. In total the observations covered an area of ~1.6 deg^2 on the sky. Figure 6.1 shows how the fields are distributed over the Taurus region. Each field was observed in the three NIR filters J, H, and Ks with central wavelengths at 1.21, 1.65, and 2.15 μm, respectively. Following a pre-defined dither pattern 30 frames were taken on each position having slightly different offsets from the specified center position. Each frame had an on-source integration time of one minute, so that after co-addition of the images the total integration time amounted to 30 minutes per filter and field. The limiting magnitude was ~ 19.5 mag in Ks. The data reduction was carried out with a dedicated pipeline developed at the MPIA by René Fassbender. The pipeline runs within the `MIDAS` environment and does flat-fielding, bad pixel and cosmic ray removal, sky subtraction and finally weighting and co-addition of the individual images to a combined final image for each field and filter. If one frame suffers substantially from bad quality, e.g., due to bad observing conditions in terms of seeing or transparency, this frame is rejected and not included in the final image. Table 6.1 lists the number of frames which could be combined for each field and

[1] The IMF describes the mass distribution of a newly formed stellar population.

[2] http://w3.caha.es/CAHA/Instruments/O2000/index2.html

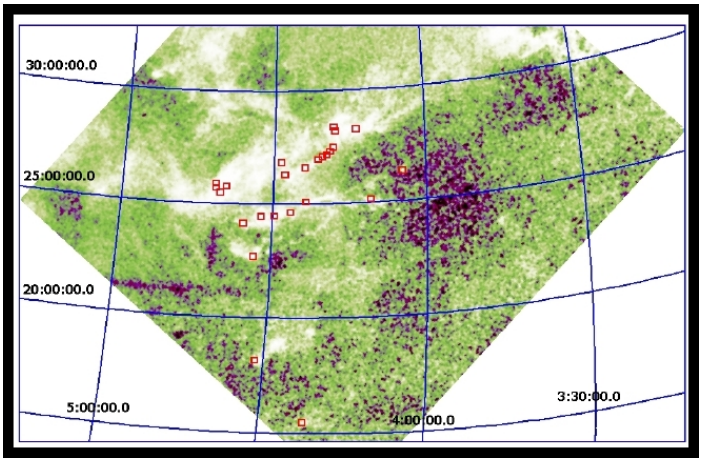

Figure 6.1 Distribution of the 25 OMEGA2000 pointings over the Taurus region. Each red square corresponds to one of the fields listed in Table 6.1. The background of the image is an extinction map based on Digitized Sky Survey I data with regions of higher extinction appearing brighter (Dobashi et al., 2005).

filter. A more detailed overview concerning the pipeline is provided in the OMEGA2000 Handbook[3].

Astrometry was applied to each field by comparing the positions of detected 2MASS point sources to those listed in the 2MASS Point Source Catalog (PSC) (Cutri et al., 2003). The overall accuracy of the astrometry is better than $2''$ with respect to the known 2MASS positions.

After visual inspection of the resulting final frames, photometry was carried out with the `daophot` package within the `IRAF`[4] environment. As the point spread function (PSF) does not vary tremendously over the chip, PSF-photometry was carried out instead of simple aperture photometry, in order to ensure reasonable flux measurements of close binaries and in more crowded regions. A reference PSF was created for each filter and field individually and then applied to all sources detected with a 3-σ confidence level. The resulting tables containing the fluxes for each field and filter were then cross-matched in order to identify sources that were detected in all three filters. For the cross-matching the coordinates of the measured flux peaks were required to match within 2 pixels.

Finally, the photometric calibration was achieved by comparing the measured instrumental magnitudes for selected reference stars to those listed in the 2MASS PSC. Here, only objects with the best ”quality flag” and ”read flag” in the 2MASS PSC were considered.Typically between 50 and 100 objects satisfying these criteria were detected in each field. By plotting the difference between the observed instrumental magnitudes and those measured in 2MASS against an observed color (i.e., J-H or H-Ks) and then fitting a straight line to the data points, it is possible to correct for existing color terms between the OMEGA2000 and 2MASS filter systems. However, before deriving a final fit and the final transformation parameters, a 3-σ clipping of a first fit was performed to exclude variable objects that would have altered the results significantly.

6.3 Scientific objectives and results

The major scientific objectives of the survey can be summarized as follows: (1) identifying new edge-on disk systems in Taurus, (2) investigating the near-infrared properties of

[3]http://w3.caha.es/CAHA/Instruments/O2000/OMEGA2000_manual.pdf
[4]http://iraf.noao.edu/

Field Name	RA (J2000)	DEC (J2000)	# of Exposures J / H / Ks	Seeing[″] J / H / Ks	Date
tc1a_1b	04h04m46.45s	26d19′27.7″	30 / 43 / 30	1.7 / 1.4 / 1.3	Dec. 05
tc2	04h10m53.64s	25d09′28.3″	28 / 28 / 30	1.3 / 1.0 / 1.0	Jan. 05
tc3_4	04h13m52.10s	28d15′45.8″	30 / 30 / 30	1.0 / 1.1 / 1.0	Jan. 05
tc5_6_7_8	04h18m00.87s	28d12′28.9″	30 / 28 / 30	1.0 / 1.0 / 1.5	Jan. 05
tc7_11	04h18m19.56s	28d23′59.2″	30 / 30 / 30	1.4 / 1.0 / 1.3	Oct. 04
tc9_10a_10b	04h18m25.60s	27d30′01.3″	30 / 30 / -	2.3 / 1.8 / -	Dec. 05
tc12a_12b	04h19m03.83s	27d19′27.4″	30 / 30 / 21	1.6 / 1.7 / 1.7	Oct. 04
tc13a_13b_14	04h19m44.22s	27d09′52.2″	30 / 27 / 29	1.2 / 1.0 / 1.2	Jan. 05
tc15_16a	04h20m35.70s	27d05′37.2″	30 / 30 / 30	1.4 / 1.3 / 1.3	Dec. 05
tc16a_16b_17	04h21m22.49s	26d59′08.0″	30 / 30 / 30	1.6 / 1.4 / 1.3	Dec. 05
tc18a_18b	04h21m58.98s	15d30′02.4″	30 / 29 / 28	1.1 / 1.2 / 1.3	Jan./Feb. 05
tc19	04h23m36.53s	25d05′55.3″	30 / 30 / 30	1.3 / 1.3 / 1.2	Dec. 05
tc20_21_22	04h23m55.75s	26d36′38.4″	30 / 30 / 30	1.8 / 1.7 / 1.2	Oct. 04
tc23_24	04h26m33.31s	24d38′47.4″	30 / 30 / 29	1.4 / 1.5 / 1.3	Oct. 04
tc25_26a_26b	04h27m53.53s	26d19′01.0″	30 / 30 / 30	1.2 / 1.6 / 1.2	Dec. 05
tc27	04h28m39.26s	26d51′39.2″	30 / 30 / 30	1.5 / 1.3 / 1.3	Dec. 05
tc28_29	04h29m40.00s	24d29′34.1″	30 / 30 / 28	1.9 / 2.4 / 2.4	Oct. 04
tc30	04h31m41.90s	18d09′50.7″	30 / 30 / 30	2.6 / 1.9 / 2.4	Oct. 04
tc31_32_33a_33b	04h32m19.18s	24d28′00.6″	30 / 30 / -	1.2 / 1.3 / -	Dec. 05
tc34	04h33m24.28s	22d42′15.9″	28 / 29 / 27	1.2 / 1.2 / 1.2	Jan./Feb. 05
tc35_36a_36b	04h35m44.37s	24d09′11.8″	29 / 30 / 30	1.2 / 1.1 / 1.0	Jan. 05
tc37_38_39_41	04h39m28.62s	25d47′29.6″	29 / 29 / 30	1.0 / 1.0 / 1.1	Jan. 05
tc42a_42b_42c	04h40m36.19s	25d29′53.4″	29 / 30 / 30	0.9 / 1.0 / 0.9	Jan. 05
tc43_44	04h41m28.61s	25d54′15.5″	30 / 29 / 30	1.0 / 1.1 / 1.0	Jan. 05
tc50	04h41m30.00s	25d42′30.0″	30 / 30 / 30	1.2 / 1.2 / 1.1	Dec. 05/Jan. 06

Table 6.1 Journal of the OMEGA2000 observations in Taurus. The seeing was measured in the respective NIR filters.

the dense molecular cores, and (3) identifying and selecting potential new low-mass stars and Brown Dwarfs with circum(sub)stellar disks. Each of these points and related results are discussed in the following sections.

6.3.1 Edge-on objects in Taurus

One of the initial scientific objectives of the survey aimed at the identification of new edge-on disk systems, either within the denser cores or nearby. By the time the survey was planned it was unclear whether the number of known edge-on objects corresponded to the number one would expect assuming a random distribution of the disk inclination of all known systems.

Are there ”enough” edge-on disks?

It was mentioned in the introduction of this chapter that Ménard & Duchêne (2004) did not find any preferred orientation of the disks. However, in their study the authors focused only on the orientation of the jet and/or disk semi-major axis and did neglect the third spatial dimension, i.e., the disk inclination. Based on near-infrared (and optical) images edge-on disk systems can be found directly, e.g., if they appear as a dark lane in front of the young star, or indirectly from a symmetrical object morphology, e.g., a bipolar reflection nebula. Several objects with an (almost) edge-on configuration were identified in our data (see, Figure 6.2), but all of them were already known from other observations and publications. To estimate whether the amount of edge-on systems is in agreement with the assumption of a random distribution of disk orientations, one has to be sure that *all* edge-on objects are detected in the survey. Knowing this number it is then possible to compute the ratio between those objects with an edge-on orientation and all detected Class I/II/III sources in the observed area. In case of a random distribution this ratio should be $\approx$ 10-15%, depending on which inclination angles are still considered as ”edge-on”.

The bottom right panel in Figure 6.2 shows that the data presented here were eventually not well suited to carry out this kind of analysis: The well-known edge-on object HH30 is not resolved and only a de-convolution of the image with the PSF reveals that this object is not a point-source. A second example for the lack of spatial resolution of the data is the edge-on object HK Tau B, which is a member of a close binary system. While the HST or ground based adaptive optics observations resolve the circumstellar disk (e.g., Stapelfeldt et al., 1998) our data do not even resolve the two components of the binary system. Thus, it seems as if high-spatial resolution observations are often pivotal to reveal an edge-on disk geometry at least for more evolved objects where the dusty envelope has vanished and does no longer create a rather large bipolar reflection nebula as those five seen in Figure 6.2.

However, a crude estimate of the amount of edge-on disks in Taurus can be made in the following way: Padgett et al. (1999) presented six edge-on objects based on HST observations out of which two are also shown in Figure 6.2. Taking furthermore into account HK Tau B, HV Tau C (Appenzeller et al., 2005) and IRAS 04301+2608 (Hartmann et al., 2005) one finds at least 13 objects that are known to be edge-on. Assuming that roughly 160 young stars are known in Taurus (Andrews & Williams, 2005) and knowing that some edge-on systems might have been missed so far due to the lack of high-resolution data, the number of edge-on disks can probably be reconciled with a distribution expected from a random orientation of the disk inclination.

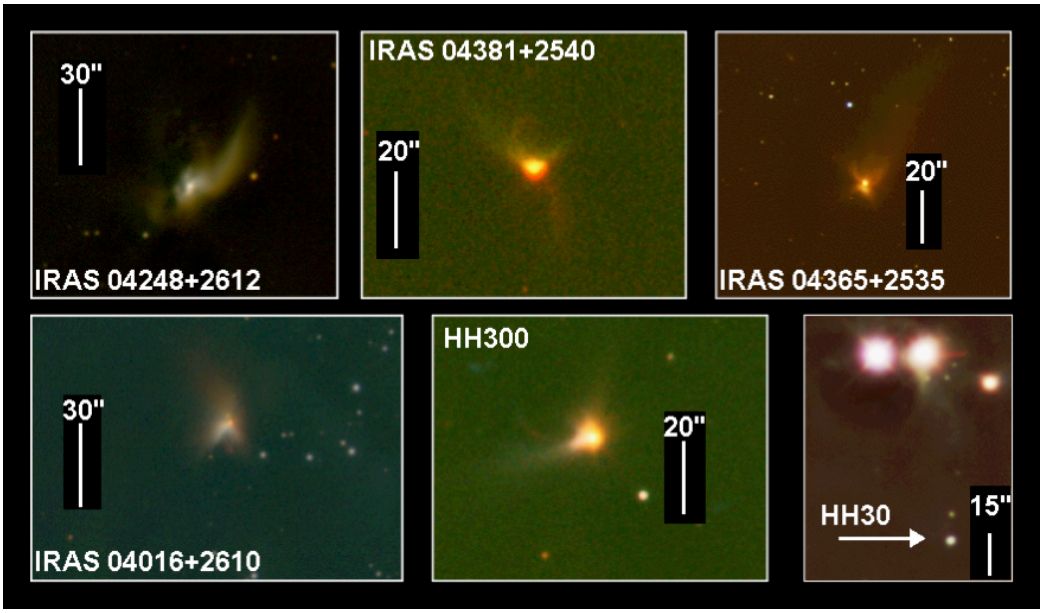

Figure 6.2 Sample of detected edge-on systems in Taurus. IRAS 04248+2612 and IRAS 04016+2610 were among a group of six edge-on objects observed with the HUBBLE SPACE TELESCOPE (HST) (Padgett et al., 1999). IRAS 04381+2540 (*top middle*) is believed to be a Proto-Binary Brown Dwarf system (Apai et al., 2005). The NIR image confirms this assumption as a faint, wiggled jet-like structure is seen in the Ks-band image. The wiggling of the jet can be caused by the presence of a companion. HH30 (*bottom right*), one of the best studied edge-on objects in Taurus, is not resolved and appears point-like. North is up and east is to the left in all images.

Colors of edge-on systems

To check whether there are any alternative ways based on low-resolution data to tell whether an object has an edge-on disk the (unresolved) NIR colors of the objects can be analyzed. One has to keep in mind, however, that at least some of these objects appear to be highly variable (e.g., HH30 shows variations in the NIR of up to several tenth of a magnitude; Wood et al., 2000). Furthermore, the NIR colors do not only depend on the disk inclination but also on a variety of other parameters such as inner disk radius, disk flaring angle, disk scale height, dust composition and grain sizes, only to name a few. Thus, it is no suprise that no clear trend shows up in Table 6.2 listing the unresolved NIR colors of some known edge-on objects. An additional check of the NIR properties

Object	J-H [mag]	H-K [mag]	Reference
IRAS 04302+2247	1.78	1.20	2MASS catalog
Coku Tau-Aur Star1	1.38	0.52	2MASS catalog
FS Tau B	1.73	1.60	2MASS catalog
HH30	0.94	0.87	2MASS catalog
HH30	1.00	0.24	OMEGA 2000

Table 6.2 Near-infrared colors of unresolved edge-on objects.

of edge-on disks was carried out using theoretical disk models. Based on the models of Dullemond & Dominik (2004) and implementing dust opacities from Min et al. (2005) we computed a grid of SEDs for different stellar masses, disk masses, disk radii and inclination angles. For the dust composition we used a mixture of amorphous Olivine (25%), Pyroxene (25%), and Carbon (50%) assuming a grain size of 0.1μm. The disk surface density was assumed to be proportional to 1/R and normalized to the given masses. The scattering was assumed to be isotropic. In Table 6.3 and Figure 6.3 we summarize the results of the models for a solar-mass star surrounded by disks with different disk masses (10^{-2} $M_\odot$ and 10^{-4} $M_\odot$), different outer radii (25 AU and 100 AU), and different inclination angles (80° and 90°). It shows that most modelled NIR colors are negative and thus

Disk Parameter	J-H [mag]	H-K [mag]
Inclination=80°		
M_{Disk}=10^{-2} $M_\odot$; R_{Disk}=25 AU	-0.48	-1.41
M_{Disk}=10^{-2} $M_\odot$; R_{Disk}=100 AU	-0.37	-1.33
M_{Disk}=10^{-4} $M_\odot$; R_{Disk}=25 AU	1.51	0.16
M_{Disk}=10^{-4} $M_\odot$; R_{Disk}=100 AU	1.42	0.12
Inclination=90°		
M_{Disk}=10^{-2} $M_\odot$; R_{Disk}=25 AU	-0.23	-1.33
M_{Disk}=10^{-2} $M_\odot$; R_{Disk}=100 AU	-0.48	-1.41
M_{Disk}=10^{-4} $M_\odot$; R_{Disk}=25 AU	-0.52	-1.48
M_{Disk}=10^{-4} $M_\odot$; R_{Disk}=100 AU	-0.51	-1.41

Table 6.3 Modeled near-infrared colors of edge-on objects.

blue and *not red*. This can be explained by the fact that the central source and also the inner regions of the disk, where most of the NIR excess of the disk is produced, are hidden due to the edge-on configuration (Figure 6.3). Thus, most NIR light that reaches the observer is scattered light from the outer disk regions and therefore rather blue in color. Only in the cases where the disk has an inclination of only 80° and is less massive the colors appear red.

It should be stressed that this modeling exercise did not aim at reproducing the colors of any specific object. The intention was to show that even with a quite simple disk model and very few parameters a broad range of NIR colors for edge-on disks can be created. This finding once more emphasizes that it is rather difficult to identify such objects based solely on NIR colors.

6.3.2 Properties of the dense cores

The second major scientific objective of the OMEGA2000 Taurus survey was to probe the dense molecular cores deeply in the near-infrared and to search for infrared counterparts embedded in the cores. However, none of the 44 cores that are believed to be starless based on observations with the INFRARED ASTRONOMICAL SATELLITE (IRAS) (Onishi et al., 2002) did show any unambiguous sign of an embedded near-infrared counterpart in the data presented here. The remaining 11 cores do have known IRAS and near-infrared counterparts and harbor relatively bright class 0/I objects.

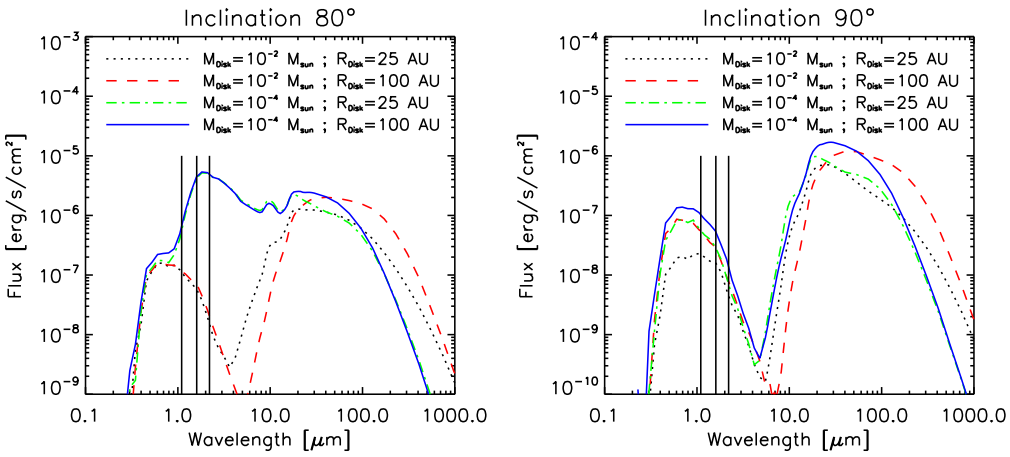

Figure 6.3 Model SEDs for a star-disk system with different disk parameters at an arbitrary distance of 1 pc. The central source has a mass of 1 $M_\odot$ and its photospheric emission was modeled using a Kurucz model. The disk mass is either 10^{-2} $M_\odot$ or 10^{-4} $M_\odot$ and the disk radius either 25 AU or 100 AU. The inclination was assumed to be 80° in the left panel and 90° in the right panel. The vertical black lines show the wavelengths of the NIR filters J, H, and Ks.

A Ks-band counterpart to IRAS 04166+2706

The only new detection was the Ks-band counterpart to the IRAS point source IRAS 04166+2706 (tc13b in Table 6.1) shown in Figure 6.4. So far, no NIR object was associated with this IRAS source. In the image a faint cone-shaped reflection nebula can be seen, which is most likely the outflow cavity of the known extremely high velocity outflow of IRAS 04166+2706 (Tafalla et al., 2004). Only the blue-shifted outflow cavity is visible as the red-shifted one is going deeper into the molecular cloud core where the higher extinction prevents its detection. Figure 6.4 also shows an example for a starless core (tc14) and a core with an embedded bright young stellar object (tc13a, IRAS 04169+2702).

Extinction within the cores

Some of the most interesting questions concerning the dense cores is certainly related to their 3-D structure. How dense are they really and how much extinction do they create? What is the internal structure of the cores and do they break up into several sub-cores? One possibility to address these questions is to map the dust column density through the cloud. Here, the dust is used as a robust tracer of the most abundant molecule H_2. Theoretical arguments as well as observational evidence show that this is a fair assumption (see, e.g., Alves et al., 1999, and references therein). Using the NICE Method (Near-Infrared Color Excess Method Lada et al., 1994; Alves et al., 1998) or the further developed NICER Method (NICE Revisited, Lombardi & Alves, 2001) which are both optimized multi-band maximum-likelihood techniques computing extinction values from the reddening of background objects, we started a project to see whether our data can potentially help to reveal the structure of the dense cores. First results are presented in Figure 6.5. We took four slightly overlapping fields (tc12a_12b, tc13a_13b_14, tc15_16a, tc16a_16b_17) and derived an extinction map of that region with a resolution of $1'$. For comparison

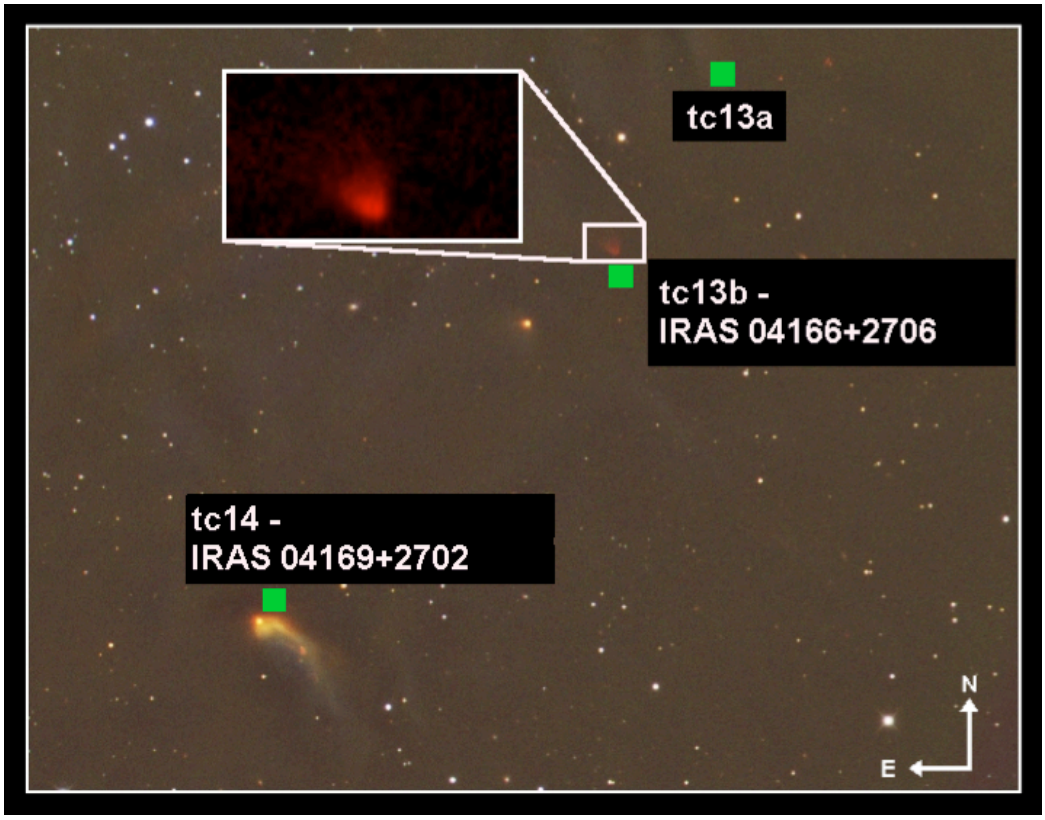

Figure 6.4 Near infrared color composite (J, H, Ks) of the central part of the tc13a_13b_14 field. The green squares denote the positions of the dense cores from Onishi et al. (2002). While the core tc14 is related to the bright young stellar object IRAS 04169+2702, tc13a is still starless. The core tc13b is related to a faint cone shaped reflection nebula which is only detected in the Ks-band. Shape and direction of this nebula fit very well to a cavity related to the outflow of the embedded low luminosity source IRAS04166+2706. North is up and east is to the left.

Figure 6.5 shows also an extinction map of the same region based on 2MASS data with a poorer resolution of $5'$. It is evident that yet unknown sub-structures appear and that the filament is way more inhomogeneous than previously thought. The extinction in this small map ranges from $A_V < 1$ mag to $A_V = 26$ mag.

These first results demonstrate that our data can possibly refine the structure of the dust and gas filaments in Taurus, and precious insights into the density fluctuations can be expected. A detailed analysis of the results and mapping of larger areas are beyond the scope of this work. At the time of writing this thesis, however, additional observing time was requested to map the yet missing areas along the main filaments.

6.3.3 Candidates for TTauri stars, Brown Dwarfs and Planetary Mass Objects

The Taurus data presented here are (1) unique in their deepness (more than 4 magnitudes deeper than the 2MASS survey), and (2) probing regions of relatively high extinction that were often avoided in other surveys (e.g., optical surveys for low-mass objects). Thus, they potentially include young objects which were not detected in previous observations.

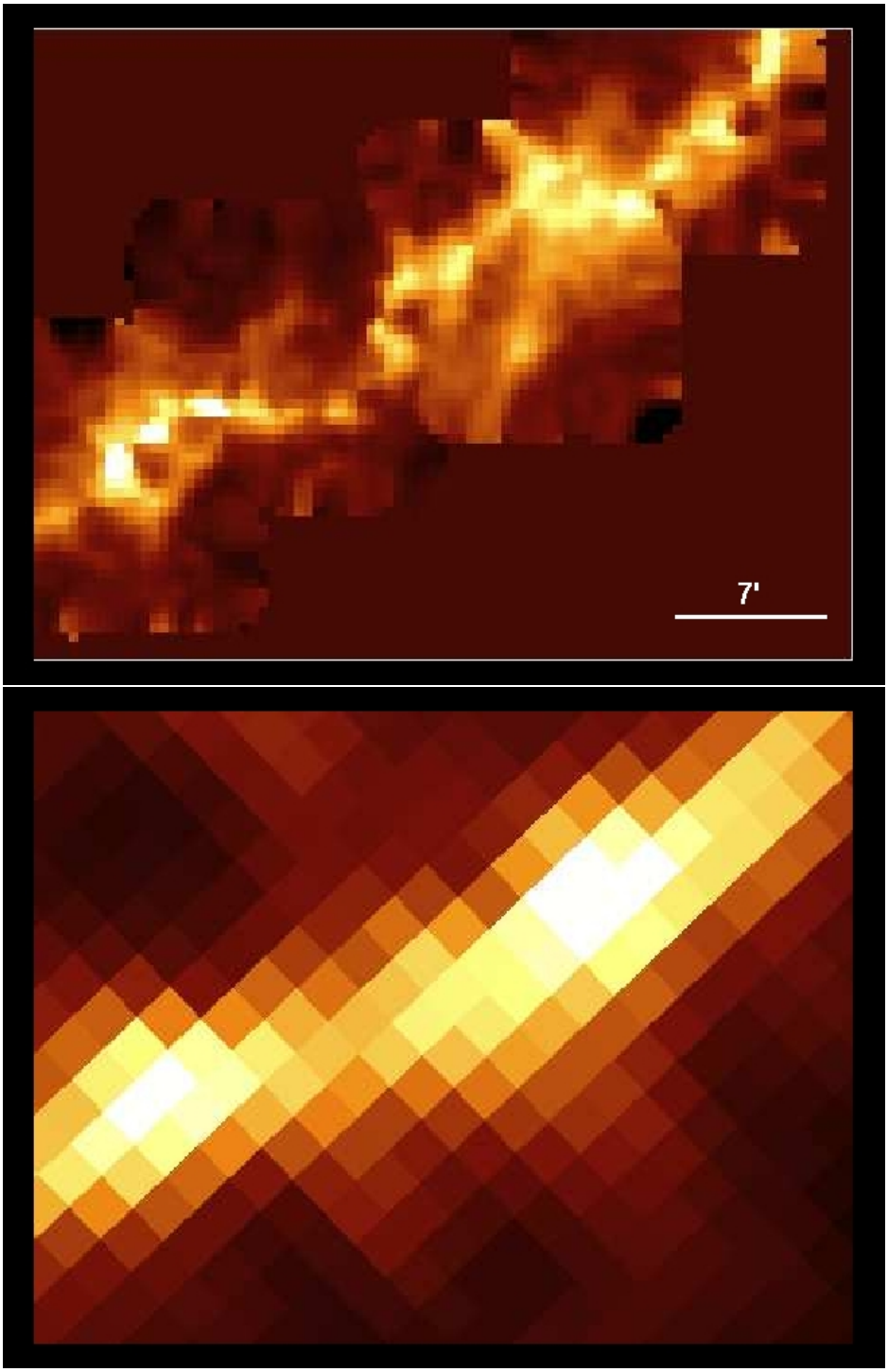

Figure 6.5 *Top:* Newly derived extinction map stretching along the Taurus main filament and covering four OMEGA2000 pointings. The resolution of the map is $1'$ corresponding to 0.04 pc at the distance of Taurus. *Bottom:* Extinction map of the same region based on 2MASS data. The unresolved filament in this map breaks up into an helical-like structure in the OMEGA2000 data.

Candidate selection based on J, H, K, and optical SDSS data

As the final object catalog of the survey contained more than 27800 objects being a large mix of foreground and background objects (stars and galaxies) and Taurus members one has to define certain selection criteria to identify candidates for young objects potentially surrounded by circumstellar disks. Figure 6.6 shows the distribution of the NIR magnitudes of the complete sample of detected objects. The steep rise at ≈15 mag results from

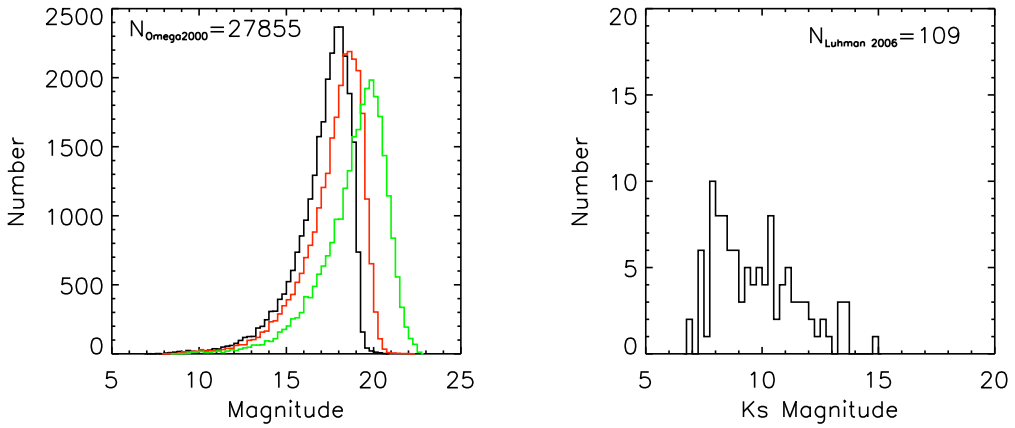

Figure 6.6 Histograms of objects in Taurus. *Left:* The 27855 objects detected in the survey presented here (Ks magnitudes in black, H magnitudes in red, and J magnitudes in green). *Right:* For comparison the Ks magnitude of 109 known young stars and Brown Dwarfs in Taurus from Luhman et al. (2006a).

faint background galaxies that are picked up: Metcalfe et al. (2006) found from galaxy counts in fields of low extinction outside the galactic plane that one might expect already more than 4000 galaxies per square degree on the sky only in the magnitude range between 18.0 and 19.0 mag. As one goes to even fainter magnitudes this number steeply rises as the probed volume of space increases drastically. The sharp drop at the faint end of the distribution in Figure 6.6 is defined by the sensitivity limit of the survey.

The right hand panel in Figure 6.6 also shows a histogram of known young stars and Brown Dwarfs in the Taurus region. It can be seen that most objects are relatively bright due to the short distance to the Taurus star-forming region. This implies that a lot of the fainter objects in our OMEGA2000 data are most likely not members of the star forming region but rather background stars or galaxies.

To differentiate between potential young members of Taurus in the survey and other objects it is useful not only to rely on the NIR data but to take into account also optical information. The Sloan Digital Sky Survey (SDSS) (e.g., Adelman-McCarthy et al., 2006) covered part of the observed Taurus area and offers up to five additional bands in the optical wavelength regime. Using these data, it is possible to make a first cut through the whole sample of objects by plotting K against I - J in a color-magnitude diagram (CMD). Knowing the distance to Taurus and having a reasonable assumption for its age, it is then possible to plot isochrones of young low-mass stars and Brown Dwarfs in the same diagram. While even distant galaxies have an I - J color typically between 0 and 2.5, faint, and thus low-mass, objects in the nearby Taurus region should be significantly redder. Appropriate isochrones can help to define the cut-off line.

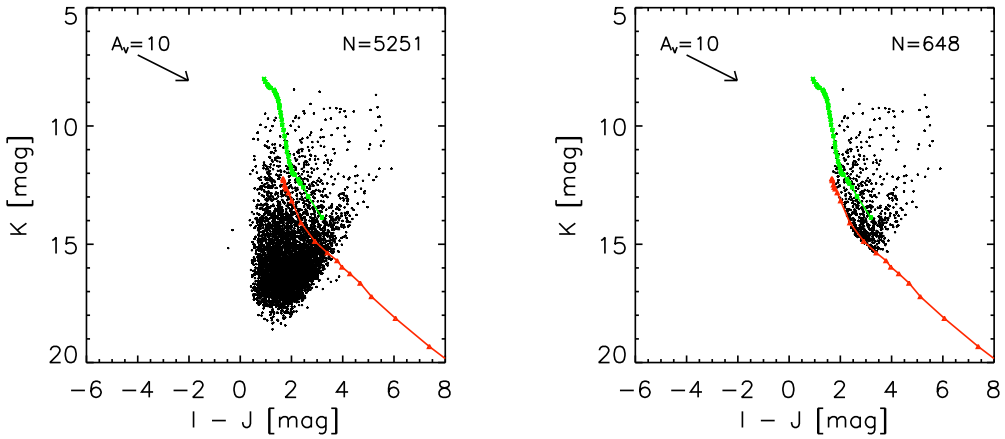

Figure 6.7 Color-magnitude diagrams based on optical (SDSS) and NIR (OMEGA2000) observations. The green and red line are 5 Myr isochrones based on the models of Baraffe et al. (2002) and Chabrier et al. (2000), respectively. The extinction vector is based on the interstellar extinction law of Mathis (1990) with R_V=3.1. *Left:* The initial sample of 5251 objects. *Right:* The remaining 648 objects fulfilling the selection criteria as described in the text.

Figure 6.7 shows such a CMD based on objects with a photometric error < 0.1 mag in the NIR and with a S/N > 5 in the SDSS i and z band. Out of more than 9000 objects that were commonly detected in the SDSS database and the NIR observations 5251 sources fulfilled both criteria. Theoretical isochrones computed by Baraffe et al. (2002) and Chabrier et al. (2000) are overplotted in the CMD.[5] The isochrones have an age of 5 Myr and cover the mass regimes between 0.02 $M_\odot$ and 1.4 $M_\odot$ (Baraffe et al., 2002), and 0.002 $M_\odot$ and 0.075$M_\odot$ (Chabrier et al., 2000). The assumed age is a rather conservative assumption because, as mentioned in the introduction of the chapter, Taurus seems to be significantly younger ($\tau \sim 1$ Myr). As younger objects tend to appear brighter (they have larger radii) and redder (e.g., due to circumstellar material), objects falling along the isochrones or lying above them are potential Taurus candidates and should be selected for further analyses. Figure 6.7 illustrates that, indeed, all faint objects with K > 15.2 mag appear to be too blue and are hence most likely background galaxies. Using the isochrones as a first selection criterium the number of objects is already reduced from 5251 down to 648. These objects are now, in a second step, plotted in a NIR color-color diagram (Figure 6.8). It can be seen that most of the candidates lie along the reddened main sequence or even along the reddened giant branch. Only very few sources populate the classical TTauri star locus (Meyer et al., 1997) or show otherwise any NIR excess emission. This indicates that the sample seems to be (at least partly) contaminated by background stars. To minimize the possibility of selecting mostly background giants the next selection step considers only objects lying on the right hand side of a reddened M3 main sequence star and showing positive NIR colors. The now remaining 22 objects are shown in Figure 6.9.

In a last step these objects are subject to individual examination. It turns out that the

[5] As the optical magnitudes of the isochrones are given in the Johnson-Cousins photometric system and the NIR magnitudes are computed in the CIT system, color transformations converting the observed 2MASS and SDSS fluxes are required. The transformation equations are given in Appendix A.

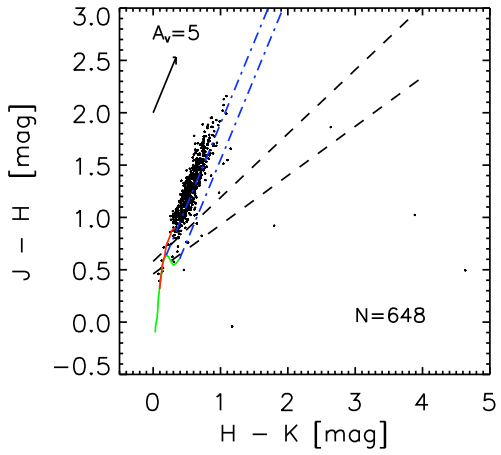

Figure 6.8 NIR color-color diagram of the 648 preliminarily selected candidates. The green solid line represents main sequence stars from B8 to M6, the red line class III giants from G0 to M7 (Bessell & Brett, 1988). The blue dash-dotted lines show the directions in which an M6 and an M3 dwarf would be moved due to extinction. The black dashed lines define the area of the classical TTauri star locus (Meyer et al., 1997), i.e., the region of the diagram TTauri stars tend to populate. The extinction law is the same as in Figure 6.7.

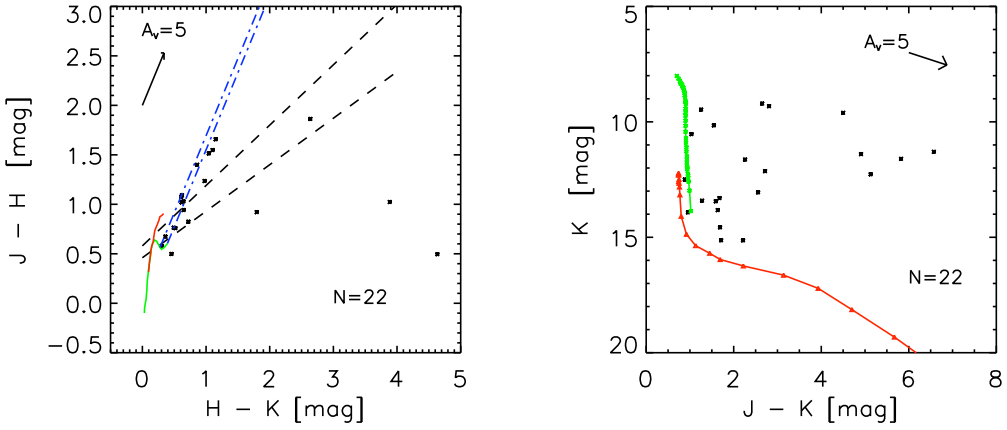

Figure 6.9 *Left:* NIR color-color diagram of the remaining 22 candidates. *Right:* NIR color-magnitude diagram of the same candidates. The green and red isochrones and the extinction law are the same as in Figure 6.7.

4 objects showing the most extreme H - K and J - K colors lie in the same OMEGA2000 field at the very edge of the detector in the Ks filter which probably altered the photometry in this filter. As these objects are in addition very faint and fuzzy in J and H band they are disregarded as potential candidates. As another object was observed and selected twice as it lies in a region where two telescope pointings overlapped we end up with a total number of 17 potential candidates for young low-mass objects with circumstellar disks.

Properties of the candidates

The above-mentioned 17 remaining objects appeared point-like in the NIR images and were cross-checked with the SIMBAD astronomical database[6]. 10 objects were already known as Taurus members and listed in the database. Their properties are summarized in Table 6.4.

Interestingly, these objects are without exception young low-mass objects and Brown

[6]http://simbad.u-strasbg.fr/simbad/

Name	RA [deg] (J2000.0)	DEC [deg] (J2000.0)	Spec. Type	Ref.
V410 X-ray 3	64.533226	28.434408	M6-M6.5	(d),(e),(f)
IRAS 04154+2823	64.633545	28.520967	-	(g)
2MASS J04242090+263051	66.087151	26.514154	M6.5	(a)
2MASS J04263055+2443558	66.627281	24.732157	M8.7	(b)
CFHT-BD-Tau 20	67.497971	24.552124	M5.5	(c)
ITG33	70.284416	25.935354	K7-M3	(h),(i)
CFHT-BD-Tau 19	65.283150	27.038923	M5.2	(c)
2MASS J04215450+2652315	65.477150	26.875559	M8.5	(b)
FU Tau	65.897499	25.050709	-	(g)
KPNO-Tau 4	66.866646	26.201296	M9.5	(j)

Name	R [mag]	I [mag]	J [mag]	H [mag]	K [mag]
V410 X-ray 3	16.66	13.99	11.57	10.90	10.53
IRAS 04154+2823	22.38	19.55	14.11	12.25	9.61
2MASS J04242090+263051	18.35	15.79	13.38	12.81	12.50
2MASS J04263055+2443558	21.28	17.95	14.69	13.93	13.41
CFHT-BD-Tau 20	17.45	14.86	11.70	10.88	10.15
ITG33	18.00	16.39	13.90	12.50	11.64
CFHT-BD-Tau 19	19.94	17.22	11.86	10.31	9.21
2MASS J04215450+2652315	23.81	18.95	15.46	14.44	13.82
FU Tau	16.48	13.60	10.73	9.96	9.47
KPNO-Tau 4	22.52	19.16	14.98	13.95	13.30

Table 6.4 Properties of selected but already known low-mass objects in Taurus. (a) Luhman et al. (2006a), (b) Luhman (2006), (c) Guieu et al. (2006), (d) White & Basri (2003), (e) Luhman et al. (1998), (f) Mohanty et al. (2005), (g) Harris et al. (1988), (h) Itoh et al. (1999), (i) Itoh et al. (2002), (j) Briceño et al. (2002)

Dwarfs in Taurus with spectral types as late as M9.5 which is up to now the latest spectral type known in this star forming region (Guieu et al., 2006). The unbiased selection and identification of these young low-mass objects hence confirms the validity of the selection criteria.

The remaining 7 objects were not listed in the SIMBAD database and are consequently regarded as potential new low-mass candidates of the Taurus star forming region. To collect more information about these objects mid-infrared images taken with the IRAC instrument onboard the SPITZER SPACE TELESCOPE were downloaded from the data archive[7]. The so-called "Post Basic Calibrated Data (PBCD)" were used to determine the flux of the objects in the first two IRAC filters at 3.6 and 4.5μm. Unfortunately, the sensitivity of SPITZER is insufficient to detect the objects also at 5.8 and 8.0μm, as

[7]These data are part of a large scale IRAC Taurus survey (PI: Deborah Padgett) and publically available.

only short exposure maps were obtained. As already described in section 4.3 the initial pixel values of the images were converted from MJy sr^{-1} to count rates DN s^{-1} (Data Numbers per second) and the corresponding magnitudes of the objects were obtained via $m = -2.5\log(x) + \Delta_{\rm ZP}$ with x denoting the flux measured in DN s^{-1} and $\Delta_{\rm ZP}$ being the zero point for each filter[8]. Afterwards, aperture photometry was carried out using the standard `atv.pro` routine in `IDL` with an aperture size of 2 pixel and a sky annulus from 10-20 pixel. Aperture corrections were carried out as described in the Data Handbook to obtain the final magnitudes.

Table 6.5 summarizes the observed properties of the 7 candidates. The objects for which IRAC data were available show an increase in brightness with increasing wavelength which means that they are unlikely background galaxies as otherwise a significant redshift would be required. This is, however, inconsistent with the NIR colors of the objects. Table 6.6 summarizes theoretically derived parameters for the objects based on the models of Chabrier et al. (2000).

Planetary mass objects with disks?

Particularly interesting objects are the candidates No. 1 - 3 in Table 6.6: their masses lie in the range between 5-20 Jupiter masses depending on the age of the assumed model. If the corresponding effective temperatures were spectroscopically confirmed then these objects would no longer be of spectral type M but rather L. This makes them very good candidates for being the lowest mass objects in Taurus known today as so far no object has been found with a spectral type later than M9.5 and with a corresponding effective temperature of $\sim$2500 K (Luhman, 2006; Guieu et al., 2006, and references therein). Also in other star-forming regions the detection of late M- or early L-type object is rather sparse up to now. So far there are three optically classified L dwarf candidates in the field showing some spectral signatures of youth (Kirkpatrick et al., 2001, 2006; Luhman et al., 2006b) and four additional objects in young star-forming regions (1-3 Myr) that are at the borderline between M and L-type objects. Especially the latter objects are subject to controversial discussions in the literature and their masses and spectral types are disputed: Jayawardhana & Ivanov (2006a,b) derived for four objects in Chameleon, Lupus and Ophiuchus spectral types of L0 and planetary masses while Luhman et al. (2007a) and Allers et al. (2007) derived at least for three of the objects significantly earlier spectral types (M7.25-M8.75) and higher masses. Based on photometry López Martí et al. (2004) selected 4 objects with spectral types between L0-L1.5 in the 3 Myr Chameleon I cloud, but spectroscopic confirmation of these objects is still pending. In the slightly older σ-Orionis cluster (3-5 Myr), Zapatero Osorio et al. (2000) spectroscopically confirmed the detection of 3 objects with a spectral type L0-L1.5 and 1 object with L4. It appears that this object has so far the latest spectral type convincingly measured in any well studied star-forming environment, as also in the IC 348 region (3 Myr) and the TW Hya association (5-10 Myr) only late M-type objects were found (Liu et al., 2003; Gizis, 2002). Depending on their age, the objects from Zapatero Osorio et al. (2000) can be considered as isolated planetary mass objects (i.e., M$<$13 M$_{\rm Jup}$). Lucas & Roche (2000) found additional 13 candidates for free-floating planets in Orion, but up to now no spectroscopic confirmation has been published.

[8]Zero points taken from Hartmann et al. (2005): 19.66 (3.6 μm), 18.94 (4.5 μm), 16.88 (5.8 μm), 17.39 (8 μm).

No.	RA [deg] (J2000.0)	DEC [deg] (J2000.0)	r[a] [mag]	i[a] [mag]	z[a] [mag]	R[b] [mag]	I[b] [mag]
1	69.037682	24.139215	23.42±0.41	21.09±0.08	19.34±0.07	22.89±0.38	20.00±0.35
2	69.946495	25.892265	22.65±0.22	20.17±0.04	18.66±0.04	21.92±0.22	19.16±0.17
3	70.163879	25.383886	23.60±0.48	21.47±0.11	19.73±0.12	23.16±0.57	20.47±0.47
4	70.238991	25.835516	23.41±0.41	20.74±0.07	18.81±0.05	22.78±0.41	19.63±0.31
5	70.381813	25.825609	20.17±0.03	18.68±0.01	17.47±0.02	19.82±0.05	17.87±0.04
6	67.549065	24.383184	19.90±0.02	17.90±0.02	16.86±0.02	18.79±0.08	17.18±0.08
7	65.898956	25.049837	22.25±0.14	20.19±0.05	17.80±0.05	22.16±0.22	19.11±0.20

No.	J[e] [mag]	H[e] [mag]	K[e] [mag]	3.6μm [mag]	4.5μm [mag]	5.8μm [mag]
1	16.84±0.01	15.75±0.03	15.13±0.03	14.62±0.08	14.43±0.09	-
2[c]	16.26±0.03	15.18±0.03	14.57±0.03	14.21±0.07	14.14±0.08	-
3	17.35±0.03	16.11±0.03	15.13±0.05	14.84±0.08	14.83±0.11	-
4	15.61±0.01	14.10±0.03	13.06±0.07	12.90±0.06	12.82±0.06	12.73±0.16
5	14.88±0.07	14.38±0.02	13.92±0.02	13.65±0.06	13.53±0.07	13.46±0.26
6	14.85±0.01	13.93±0.01	12.14±0.06	13.17±0.06	13.10±0.07	13.10±0.24
7[d]	15.03±0.02	14.09±0.01	13.44±0.02	-	-	-

Table 6.5 Fluxes of newly identified candidates for young low-mass objects in Taurus. [a]Magnitudes in SDSS photometric system. [b]Magnitudes in the Johnson-Cousin system. Transformation equations are given in Appendix A. [c]Object lies in so-called "pull-down" column from a bright star in the IRAC images. IRAC fluxes are probably underestimated. [d]Object is very close to another object ($< 3''$) and not resolved in the IRAC images. [e]Magnitudes in the CIT system. Transformation equations are given in Appendix A.

		1 Myr[a]			5 Myr[a]		
No.	M_J^b [mag]	Mass [M_{Jup}]	T_{eff} [K]	log g	Mass [M_{Jup}]	T_{eff} [K]	log g
1	9.98	7-8	2100-2150	3.5-3.6	15-20	2250-2500	3.9-4.0
2	9.40	10-12	2250-2350	3.6	15-20	2250-2500	3.9-4.0
3	10.49	5-6	1900-2000	3.5	12-15	2050-2250	3.9-4.0
4	8.75	20-30	2550-2700	3.7-3.8	20-30	2500-2700	3.8-3.9
5	8.02	20-30	2550-2700	3.7-3.8	30-40	2700-2800	3.8
6	7.99	30	2700	3.7	30-40	2700-2800	3.8
7	8.17	20-30	2550-2700	3.7-3.8	30-40	2700-2800	3.8

Table 6.6 Candidates for young low-mass objects in Taurus. Object properties based on theoretical models for 1 and 5 Myr. The mass is given in Jupiter masses and g denotes the surface gravity. [1]Magnitudes in CIT system. [a]Based on models of Chabrier et al. (2000). [b]Absolute J-band magnitude extinction corrected using Mathis (1990) and assuming A_V=4.0 and a distance modulus of 5.73 mag.

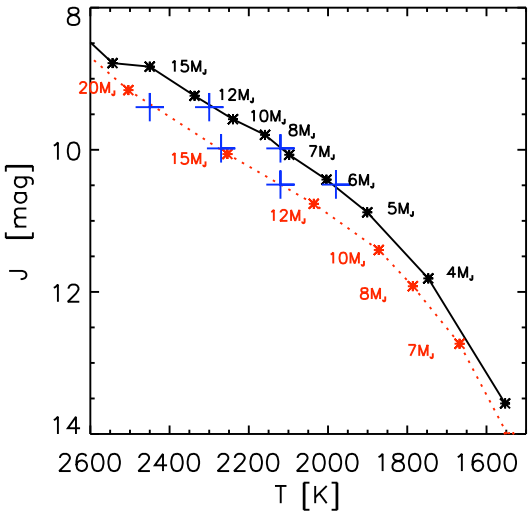

Figure 6.10 Hertzsprung-Russell diagram overplotting the first three candidates (blue crosses) from Table 6.6 on the 1 Myr (black solid line) and 5 Myr (red dotted line) isochrone from (Chabrier et al., 2000). The points along the isochrones show the positions of objects with 3-20 Jupiter masses for the 1 Myr isochrone and 7-20 Jupiter masses for the 5 Myr isochrone. For the 1 Myr isochrone all three objects are in the planetary mass regime, i.e., below 13 Jupiter masses.

Figure 6.10 shows the expected masses for the objects presented here again in a Hertzprung-Russel diagram for two different ages and a distance of 140 pc. Assuming that these objects are indeed very low-mass Taurus members it is possible to compare the observed photometric points with theoretical spectra for very low-mass objects. In Figure 6.11 the observed fluxes of the candidates are plotted together with synthetic spectra of low-mass cool dwarfs from Allard et al. (2003). Apparently all objects have an intrinsic NIR-excess. This is indicative of dusty circumstellar material implying that these objects are surrounded by ”circumplanetary” disks. However, as mentioned above, one has to be very careful with estimates for the masses of the objects based solely on photometric observations (see, e.g., results for Brown Dwarf masses in Allers et al., 2006, 2007). Only spectra can convincingly constrain the effective temperature and spectral type of an object. By the time of writing this thesis a DDT proposal for J-band spectroscopy with VLT/ISAAC for the three candidates was already accepted. However, the analysis of these

data is beyond the scope of this work, which had its main focus purely on the selection and identification of good candidates.

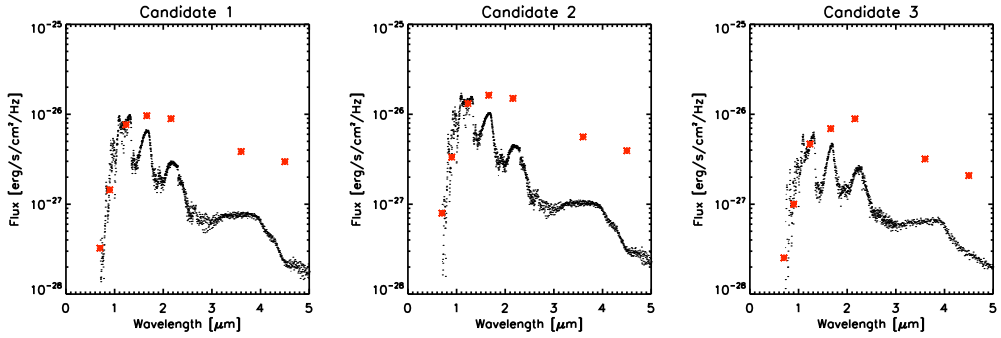

Figure 6.11 Photometric points (I, R, J, H, K, 3.6μm, and 4.5μm) of the first three candidates in Table 6.6 overplotted on synthetic spectra for cool dwarfs. The models (Allard et al., 2003) correspond to low surface gravity objects and effective temperatures of 2100 K, 2300 K, and 1900 K, respectively.

Candidate selection based only on J, H, K images

The candidate selection in the previous sections was based on the NIR images taken with the OMEGA2000 camera and complementary optical data from the SDSS. However, it was already mentioned that those data do not cover the complete Taurus area observed with OMEGA2000. To identify additional potential candidates for new TTauri stars and Brown Dwarfs we applied similar selection criteria to the NIR data only. In a first step we considered only those objects that (1) are brighter than 15.7 mag in K and (2) showed intrinsic photometric errors smaller than 0.1 mag in all three filters. Roughly 4400 sources fulfilled these criteria. From the previous section it is clear that the limitation on the brightness still enables the detection of objects with a few Jupiter masses. The thus selected objects were plotted in a NIR color-color diagram (Figure 6.12) and subject to further selection constraints. First, to avoid heavy contamination from background giants, the objects should lie on the right hand side of the line created by moving an M3 star along the reddening direction. Additionally, the objects should also lie on the right hand side of the 5 Myr isochrones in Figure 6.13. Similar criteria were already applied to the data in the previous section. After this selection process 148 objects remained in the sample. Since some of these sources were also detected in the optical SDSS data they had to be removed from the sample because they were either already selected in the previous section as candidates (see also Figure 6.13) or they did not fulfill the selection criteria applied there and were thus ruled out as good candidates. After this correction, 91 objects were left in the sample and cross-checked with the SIMBAD database for astronomical objects. Like in the previous section, some objects (in total 28) were already known. In the end, 63 objects were identified as potential candidates for new young, low-mass objects in Taurus. These objects as well as the known sources are listed in Appendix B (Tables B.1 and B.2). One has to keep in mind, though, that since thus far no optical data were analyzed for these objects the contamination, e.g., from background galaxies, is presumably relatively high.

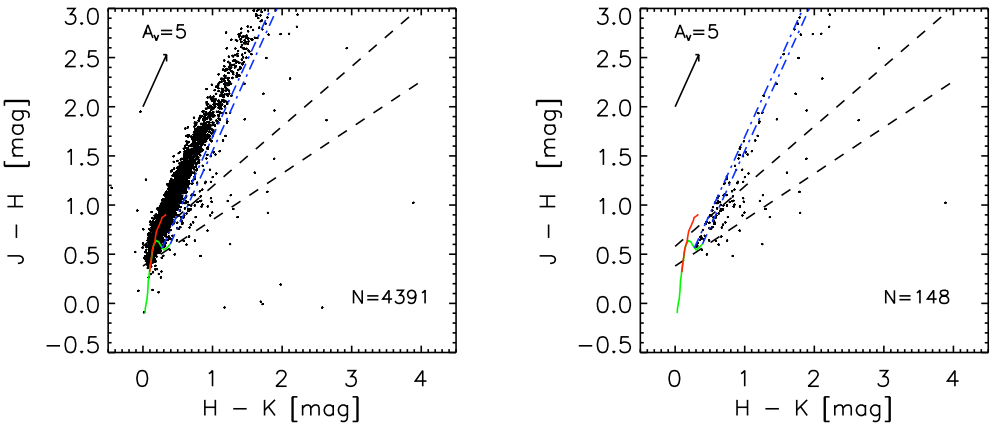

Figure 6.12 NIR color-color diagram of objects in Taurus. *Left:* Distribution of the 4391 objects with photometric errors smaller than 0.1 mag in all three filters. The green line shows the main-sequence, the red line the giant branch, and the area between the black dashed lines define the TTauri locus from Meyer et al. (1997). The dash-dotted blue lines represent the directions along which an M3 and an M6 star would be shifted due to extinction. The extinction vector is based on the result of Mathis (1990). *Right:* Same as plot on the left panel but now only for objects lying (1) on the right hand side of the line created by shifting an M3 star along the reddening direction and (2) on the right hand side of the 5 Myr isochrones shown in Figure 6.13.

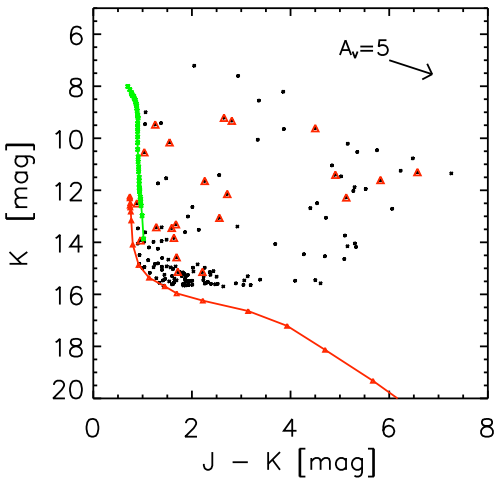

Figure 6.13 Color-magnitude diagram showing the 148 selected objects lying on the right hand side of a reddened M3 star in Figure 6.12 and simultaneously on the right hand side of the 5 Myr isochrones from Baraffe et al. (2002) (green) and Chabrier et al. (2000) (red). The red triangles denote the 22 objects that were already selected in the previous section where the NIR and optical data were combined.

Comparison to known young low-mass objects in Taurus

Finally, it is interesting to compare the NIR properties of the objects selected in the previous sections to those of known young TTauri stars and Brown Dwarfs. Therefore we took the list of objects from Luhman et al. (2006a) and plotted all data in a color-color and a color-magnitude diagram as illustrated in Figure 6.14. At least two things are worth mentioning: (1) most of the known objects lie in the color-color diagram in a region along the reddened main-sequence. In our selection, however, we required that the objects should lie on the right hand side of a line created by moving an M3 star along the reddening direction (green, dash-dotted line in left panel of Figure 6.14). The reason for this was to avoid

a large contamination by background giants and to focus first on objects with a relatively low probability of being such objects. On the other hand this means, however, that we might have sorted out potentially new low-mass objects. (2) the right panel in Figure 6.14 shows that most of our candidates are fainter than the objects from Luhman et al. (2006a). It should be kept in mind that, indeed, we were looking for potentially very low-mass objects. However, especially the NIR-based candidates suffer from contamination from background galaxies which are easier to eliminate if optical data are available.

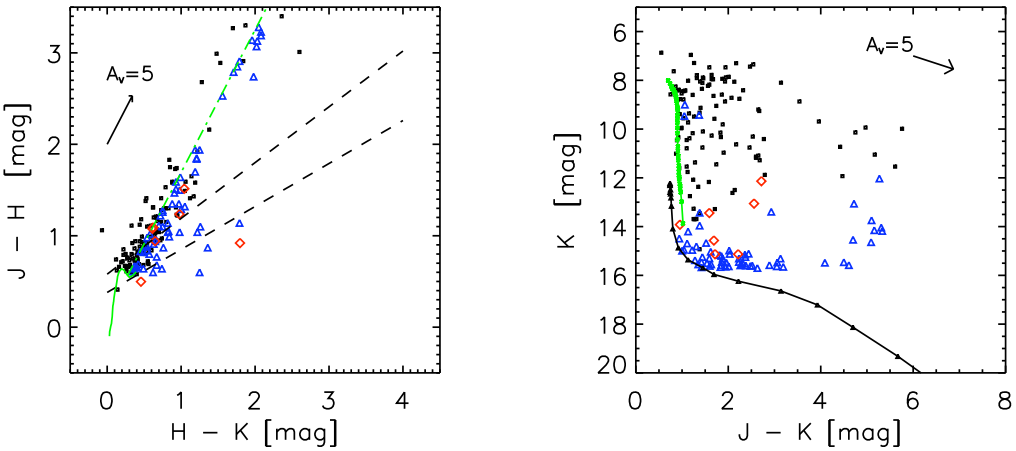

Figure 6.14 NIR color-color and color-magnitude diagrams similar to those shown in Figures 6.12 and 6.13 and comparing known young objects im Taurus from Luhman et al. (2006a) (black squares), our 7 objects selected based on NIR and optical data (red diamonds), and the 63 objects selected in the previous section based solely on NIR data (blue triangles). It is interesting that most of our candidates are fainter than the sample from Luhman et al. (2006a).

6.4 Conclusions and future prospects

To summarize the outcome of the new near-infrared survey in Taurus the following main conclusions can be drawn:

- In combination with optical and mid-infrared data it was possible to identify seven new candidates for young low-mass objects in the Taurus star-forming region. Three of these objects might be of spectral type L (to be confirmed) with masses between 5 - 20 Jupiter masses showing mid-infrared excess indicative of the presence of ”circumplanetary” disks. These objects are potentially the least massive objects in Taurus known today.

- Solely based on the near-infrared data 63 additional candidates for new low-mass members of Taurus were identified. Their nature is, however, not as well constrained as that of the candidates mentioned above due to the lack of optical data.

- One of the initial objectives of the survey, namely to identify new edge-on protoplanetary disks and to study their statistical appearance, could not be pursued as

initially planned. The spatial resolution of the OMEGA2000 camera was not sufficient to resolve known edge-on sources and high spatial resolution instruments (such as those onboard HST) are required.

- Also, from their near-infrared colors it is very difficult (if not impossible) to distinguish unambiguously edge-on systems from disks with other inclination angles. Edge-on objects show a high degree of intrinsic variability and there is a large variety of possible near-infrared colors for these systems resulting from different values for basic disk parameters.

- Apart from one exception (IRAS04166+2706, where a new Ks-band counterpart could be identified) all the observed dense molecular cores that had no near- or mid-infrared counterpart before still appear to harbor no deeply embedded central objects.

- With the data it is possible to derive extinction maps along the filaments with unprecedented resolution. First tests showed striking sub-structures in the filaments and revealed that their 3-D profile is much more complex than previously thought.

Based on the analyses of the data and the deep near-infrared images, several projects appear interesting to follow-up in the future:

- One of the first next steps is certainly the spectroscopic analysis of the selected low-mass candidates. If their assumed late spectral type is confirmed, additional follow-up observations have to be carried out to study the physical parameters of these free-floating planetary mass objects.

- Complementary optical data should be obtained for those new candidates where no such information is available yet. These data will help to further constrain the candidate selection and eliminate (at least) part of the contamination from background objects. The Canadian-French-Hawaiian Telescope (CFHT) recently published data from an optical Taurus survey which will serve as a good starting point. Eventually, for the remaining candidates additional spectra (optical or NIR) will help to clarify the spectral and object type.

- Not all circumstellar disks that were detected and resolved in our NIR images have been analyzed and modeled. Therefore one might want to consider the use of state-of-the-art radiative transfer codes to simulate the resulting images. When complemented with additional data (e.g., flux measurements at numerous wavelengths) the images and derived fluxes might constrain disk parameter such as the inclination, scale height and flaring angle.

- Finally, it seems interesting to search for variable objects and compare the photometry of all objects to the values listed in the 2MASS point source catalog. Young stars are known to be variable and some phenomena cause relatively strong changes (up to several magnitudes) in the observed fluxes (e.g., FU Ori outbursts, EX Lupi outbursts, UX Ori variabilities, etc.). In Appendix C (Table C.1) we provide a preliminary list of a couple of objects for which variations of at least one magnitude in one filter were observed.

7. General conclusions and outlook

Lessons learned and things to do

IN THIS LAST CHAPTER the main conclusions of this thesis and possible future studies related to this field of research are summarized. While at the end of each chapter particular summaries and conclusions were already provided, the following paragraphs emphasize the most relevant aspects in the broader context of star- and planet-formation research. The future projects suggested thereafter are mostly follow-up ideas linked directly to the results of the projects presented in this thesis.

7.1 Major conclusions

Accretion disks around FUors: Observations presented in this thesis clearly support the idea that FU Orionis objects are young stars surrounded by active circumstellar accretion disks. Although already commonly assumed, this picture was not fully accepted in the scientific community as some observations were also in agreement with rapidly rotating late-type stars with strong stellar winds (e.g., Herbig et al., 2003). The MIDI observations presented in chapter 3 resolve dusty structures several AU in size, which are difficult to explain without the presence of an accretion disk. Based on the observed visibilities, a simple model was derived, fitting most observations with a moderately inclined accretion disk, which is flat and accretion dominated in the inner AU, and flared and passively heated farther out. The silicate emission that some FUors show around 10 μm (chapters 3 and 5) is similar to that of TTauri stars ane Herbig Ae/Be stars and generally attributed to the heated surface layer of a protoplanetary disk. Thus, it is difficult to escape the conclusion that FUors are surrounded by accretion disks.

Dust processing in active accretion disks: In recent years, based on MIR spectroscopy, direct evidence for dust grain processing, e.g., grain growth and crystallization, has been found in the circumstellar disks around TTauri stars or Herbig Ae/Be stars. In chapter 3 the first dust composition study of an accretion disk surrounding a FUor was presented. As these observations included interferometric observations, it was possible to study the radial dependence of the dust composition within the accretion disk. The observed spectra showed clear indications of grain growth throughout the disk. Despite the high disk temperatures, no convincing evidence

for crystalline grains was found. In chapter 5 the sample of FUor accretion disks with silicate emission was increased to five objects,[1] and the results from chapter 3 were confirmed: All objects showed evidence for grain growths but hardly any signs of crystalline grains in their disks. As these objects are younger than classical TTauri stars (see below) and are partially still surrounded by a remnant envelope, these results imply, that grain growth sets in very early in the disk evolution. The non-detection of crystalline grains requires further investigations and modeling.

The link between Class I and II objects: The results in chapter 5 strongly support that FU Orionis objects are the bridge between Class I objects, which have a circumstellar disk but are still deeply embedded in their parent molecular envelope, and Class II objects, which are solely surrounded by a circumstellar disk having the envelope partly accreted and dispersed. Two categories of FUors were defined: Category I objects show silicate and ice absorption bands indicating a dense and embedded environment. Objects of this category are young objects and might just have entered the FUor-phase with several outbursts to be expected within the next 10^5 years. Category II objects show silicate emission features, often accompanied by water vapor bands in the NIR. These objects are more evolved and might be near the end of the FUor-phase close to entering the more quiescent TTauri-phase.

FUors in a cluster environment: So far, some FUors were known to be in a binary or multiple system. The results in chapter 4 indicate that FUors do also exist in cluster environments and may thus be more common than previously thought. This strengthens the idea that most young, low-mass stars possibly undergo this period of multiple accretion outbursts, regardless of their immediate stellar environment.

Circumstellar disks around very low-mass objects: Although the concept of circumstellar disks around young stars is observationally and theoretically well established, the existence of disks around sub-stellar objects has not been proven by observations until recently. Based on a NIR survey in the Taurus star forming region, new candidates for TTauri stars, Brown Dwarfs and free-floating planetary mass objects were presented in chapter 6. At least three sources are excellent candidates for being among the least massive free-floating objects with circum-sub-stellar disks known today. Although the masses of these objects are yet to be confirmed by means of spectroscopy, the findings argue in favor of a common formation mechanism for objects ranging from at least several solar masses down to a few Jupiter masses.

The classification of FUors: In chapter 2 and 5 it was shown that caution is advisable regarding the classification of FU Orionis objects in the literature. The sample and the observational evidence for the FUor-status of an object is highly inhomogeneous. Based on a detailed and thorough compilation and analysis of literature and new data, the objects V1331 Cyg and Parsamian 21 are presumably not in an active FUor-phase. V1331 Cyg might have undergone some outburst several thousand years ago, but nowadays it does not show evidence for active accretion. Parsamian 21 is probably not even a young object, but rather an evolved Post-AGB star.

[1] Parsamian 21 is not counted as its status as FUor is questionable.

7.2 Possible future projects

Photometric and spectroscopic confirmation of low-mass candidates: The deep NIR survey in Taurus, presented in chapter 6, revealed numerous objects that require further investigations. Highest priority is certainly given to the planetary mass object candidates and their circum-sub-stellar disks. Once the spectral type of these objects is determined, possibly confirming the planetary mass status, their observational properties should be studied across all wavelengths to learn more about their physical parameters. As mentioned above, they may be among the least massive free-floating objects with circum-sub-stellar disks known today, and their discovery would have direct impact on the initial mass function and the theory of star formation.

Radiative transfer simulations: The results derived from the simple analytical disk model in chapter 3 agree reasonably well with the observations. However, it would be beneficial to carry out multi-dimensional radiative transfer simulations to get better insights into the structure of the accretion disk. Such kind of simulations were already successfully applied to TTauri stars and Herbig Ae/Be stars, but disks with accretion rates as high as those of FUors were not yet modeled. It is certainly challenging to find a good description for the high accretion rates, leading to higher temperatures in the disk midplane compared to the surface layer at small disk radii. Also, the geometry of the innermost AU is uncertain (Is there a puffed-up inner rim as it is sometimes assumed for TTauri stars and Herbig Ae/Be stars? How far does the disk extend to the stellar photosphere?). However, especially for the prototype object of active accretion disks, FU Ori, a wealth of observational data can certainly help to constrain model parameters.

Modeling of dust evolution in accretion disks: As pointed out in chapter 3 and 5, the existence of large amorphous dust grains in accretion disks around FUors indicates that grain growth already takes place in the early phases of disk evolution. At the same time it is puzzling that no indications of crystalline grains are present in these comparatively hot and well-mixed disks. Models simulating the evolution of dust grains in an active accretion disk could attempt to address this issue and make predictions for observational quantities. In particular, it would be interesting to investigate how dust processing, accretion rate, turbulence, and mixing through the disk in vertical and radial direction are coupled.

High spatial resolution observations of accretion disks: From the observational side, it is certainly worth proposing further high spatial resolution observations of circumstellar disks. While a lot of data from MIDI/VLTI observations of bright Herbig Ae/Be stars have already been published, results for the low-mass regime are lagging behind. As illustrated in chapter 3, multi-baseline MIDI observations do not only help to derive geometrical properties of circumstellar disks, but they also allow us to get spatially resolved information about dust emitting regions and dust grain properties. Numerous publications on interferometric observations of TTauri stars are expected to appear in the near future, and additional data for FUors would certainly complement our understanding of accretion disks around low-mass stars. At the time of writing this thesis, observing proposals for the FUors Reipurth 50 and L1551 IRS 5 were submitted. Although both objects are Category 1 FUors,

MIDI observations will yield deeper insights in the envelope structure and might also reveal direct indications for the accretion disk. In addition, V883 Ori was already observed with MIDI at three baselines and clearly resolved. Yet a detailed analysis and modeling of the data has to be carried out. Finally, MIDI observations of Parsamian 21 were scheduled and the data can help to clarify the classification of this object.

Identification of new FUors: Based on the results presented in chapter 5, it would be worth searching for FUor-properties among Class I objects. Either these objects are in a quiescent phase of their evolution, or they do bear (e.g., spectroscopic) evidence for being a FUor. Already Reipurth & Aspin (1997) used infrared spectroscopy to identify potential FUor candidates among embedded Herbig-Haro energy sources based on the CO bandhead characteristics.

Bibliography

Ábrahám, P., Kóspál, Á., Csizmadia, S., Kun, M., Moór, A., & Prusti, T. (2004). Long-term evolution of FU Orionis objects at infrared wavelengths. *A&A*, **428**, 89–97.

Ábrahám, P., Mosoni, L., Henning, T., Kóspál, Á., Leinert, C., Quanz, S. P., & Ratzka, T. (2006). First AU-scale observations of V1647 Orionis with VLTI/MIDI. *A&A*, **449**, L13–L16.

Acke, B. & van den Ancker, M. E. (2004). ISO spectroscopy of disks around Herbig Ae/Be stars. *A&A*, **426**, 151–170.

Adams, F. C., Lada, C. J., & Shu, F. H. (1987). Spectral evolution of young stellar objects. *ApJ*, **312**, 788–806.

Adelman-McCarthy, J. K., Agüeros, M. A., Allam, S. S., Anderson, K. S. J., Anderson, S. F., Annis, J., Bahcall, N. A., Baldry, I. K., Barentine, J. C., Berlind, A., Bernardi, M., Blanton, M. R., Boroski, W. N., Brewington, H. J., Brinchmann, J., Brinkmann, J., Brunner, R. J., Budavári, T., Carey, L. N., Carr, M. A., Castander, F. J., Connolly, A. J., Csabai, I., Czarapata, P. C., Dalcanton, J. J., Doi, M., Dong, F., Eisenstein, D. J., Evans, M. L., Fan, X., Finkbeiner, D. P., Friedman, S. D., Frieman, J. A., Fukugita, M., Gillespie, B., Glazebrook, K., Gray, J., Grebel, E. K., Gunn, J. E., Gurbani, V. K., de Haas, E., Hall, P. B., Harris, F. H., Harvanek, M., Hawley, S. L., Hayes, J., Hendry, J. S., Hennessy, G. S., Hindsley, R. B., Hirata, C. M., Hogan, C. J., Hogg, D. W., Holmgren, D. J., Holtzman, J. A., Ichikawa, S.-i., Ivezić, Ž., Jester, S., Johnston, D. E., Jorgensen, A. M., Jurić, M., Kent, S. M., Kleinman, S. J., Knapp, G. R., Kniazev, A. Y., Kron, R. G., Krzesinski, J., Kuropatkin, N., Lamb, D. Q., Lampeitl, H., Lee, B. C., Leger, R. F., Lin, H., Long, D. C., Loveday, J., Lupton, R. H., Margon, B., Martínez-Delgado, D., Mandelbaum, R., Matsubara, T., McGehee, P. M., McKay, T. A., Meiksin, A., Munn, J. A., Nakajima, R., Nash, T., Neilsen, Jr., E. H., Newberg, H. J., Newman, P. R., Nichol, R. C., Nicinski, T., Nieto-Santisteban, M., Nitta, A., O'Mullane, W., Okamura, S., Owen, R., Padmanabhan, N., Pauls, G., Peoples, J. J., Pier, J. R., Pope, A. C., Pourbaix, D., Quinn, T. R., Richards, G. T., Richmond, M. W., Rockosi, C. M., Schlegel, D. J., Schneider, D. P., Schroeder, J., Scranton, R., Seljak, U., Sheldon, E., Shimasaku, K., Smith, J. A., Smolčić, V., Snedden, S. A., Stoughton, C., Strauss, M. A., SubbaRao, M., Szalay, A. S., Szapudi, I., Szkody, P., Tegmark, M., Thakar, A. R., Tucker, D. L., Uomoto, A., Vanden Berk, D. E., Vandenberg, J., Vogeley, M. S., Voges, W., Vogt, N. P., Walkowicz, L. M., Weinberg, D. H., West, A. A., White, S. D. M., Xu, Y., Yanny, B., Yocum, D. R., York, D. G., Zehavi, I., Zibetti, S., & Zucker, D. B. (2006). The Fourth Data Release of the Sloan Digital Sky Survey. *ApJS*, **162**, 38–48.

Allard, F., Baraffe, I., Chabrier, G., Barman, T. S., & Hauschildt, P. H. (2003). Brown Dwarfs and Extrasolar Planets. In D. Deming and S. Seager, editors, *ASP Conf. Ser. 294: Scientific Frontiers in Research on Extrasolar Planets*, pages 483–490.

Allers, K. N., Kessler-Silacci, J. E., Cieza, L. A., & Jaffe, D. T. (2006). Young, Low-Mass Brown Dwarfs with Mid-Infrared Excesses. *ApJ*, **644**, 364–377.

Allers, K. N., Jaffe, D. T., Luhman, K. L., Liu, M. C., Wilson, J. C., Skrutskie, M. F., Nelson, M., Peterson, D. E., Smith, J. D., & Cushing, M. C. (2007). Characterizing Young Brown Dwarfs Using Low-Resolution Near-Infrared Spectra. *ApJ*, **657**, 511–520.

Alves, J., Lada, C. J., Lada, E. A., Kenyon, S. J., & Phelps, R. (1998). Dust Extinction and Molecular Cloud Structure: L977. *ApJ*, **506**, 292–305.

Alves, J., Lada, C. J., & Lada, E. A. (1999). Correlation between Gas and Dust in Molecular Clouds: L977. *ApJ*, **515**, 265–274.

Andre, P., Ward-Thompson, D., & Barsony, M. (1993). Submillimeter continuum observations of Rho Ophiuchi A - The candidate protostar VLA 1623 and prestellar clumps. *ApJ*, **406**, 122–141.

Andrews, S. M. & Williams, J. P. (2005). Circumstellar Dust Disks in Taurus-Auriga: The Submillimeter Perspective. *ApJ*, **631**, 1134–1160.

Anglada, G., Rodriguez, L. F., Girart, J. M., Estalella, R., & Torrelles, J. M. (1994). A radio candidate for the exciting source of the L1287 bipolar outflow. *ApJ*, **420**, L91–L93.

Apai, D., Tóth, L. V., Henning, T., Vavrek, R., Kovács, Z., & Lemke, D. (2005). HST/NICMOS observations of a proto-brown dwarf candidate. *A&A*, **433**, L33–L36.

Appenzeller, I., Bertout, C., & Stahl, O. (2005). Edge-on T Tauri stars. *A&A*, **434**, 1005–1019.

Aspin, C. & Reipurth, B. (2003). Two Embedded Young Stellar Objects in NGC 2264 with FU Orionis Characteristics. *AJ*, **126**, 2936–2948.

Baraffe, I., Chabrier, G., Allard, F., & Hauschildt, P. H. (2002). Evolutionary models for low-mass stars and brown dwarfs: Uncertainties and limits at very young ages. *A&A*, **382**, 563–572.

Beckwith, S. V. W., Sargent, A. I., Chini, R. S., & Guesten, R. (1990). A survey for circumstellar disks around young stellar objects. *AJ*, **99**, 924–945.

Bell, K. R. & Lin, D. N. C. (1994). Using FU Orionis outbursts to constrain self-regulated protostellar disk models. *ApJ*, **427**, 987–1004.

Bell, K. R., Lin, D. N. C., Hartmann, L. W., & Kenyon, S. J. (1995). The FU Orionis outburst as a thermal accretion event: Observational constraints for protostellar disk models. *ApJ*, **444**, 376–395.

Bell, K. R., Cassen, P. M., Klahr, H. H., & Henning, T. (1997). The Structure and Appearance of Protostellar Accretion Disks: Limits on Disk Flaring. *ApJ*, **486**, 372.

Bergin, E. A., Melnick, G. J., Gerakines, P. A., Neufeld, D. A., & Whittet, D. C. B. (2005). Spitzer Observations of CO2 Ice toward Field Stars in the Taurus Molecular Cloud. *ApJ*, **627**, L33–L36.

Bessell, M. S. & Brett, J. M. (1988). JHKLM photometry - Standard systems, passbands, and intrinsic colors. *PASP*, **100**, 1134–1151.

Beuther, H., Churchwell, E. B., McKee, C. F., & Tan, J. C. (2007). The Formation of Massive Stars. In B. Reipurth, D. Jewitt, and K. Keil, editors, *Protostars and Planets V*, pages 165–180.

Biscaya, A. M., Rieke, G. H., Narayanan, G., Luhman, K. L., & Young, E. T. (1997). First-Overtone CO Variability in Young Stellar Objects. *ApJ*, **491**, 359.

Boley, A. C., Mejía, A. C., Durisen, R. H., Cai, K., Pickett, M. K., & D'Alessio, P. (2006). The Thermal Regulation of Gravitational Instabilities in Protoplanetary Disks. III. Simulations with Radiative Cooling and Realistic Opacities. *ApJ*, **651**, 517–534.

Bonnell, I. & Bastien, P. (1992). A binary origin for FU Orionis stars. *ApJ*, **401**, L31–L34.

Boogert, A. C. A., Pontoppidan, K. M., Lahuis, F., Jørgensen, J. K., Augereau, J.-C., Blake, G. A., Brooke, T. Y., Brown, J., Dullemond, C. P., Evans, II, N. J., Geers, V., Hogerheijde, M. R., Kessler-Silacci, J., Knez, C., Morris, P., Noriega-Crespo, A., Schöier, F. L., van Dishoeck, E. F., Allen, L. E., Harvey, P. M., Koerner, D. W., Mundy, L. G., Myers, P. C., Padgett, D. L., Sargent, A. I., & Stapelfeldt, K. R. (2004). Spitzer Space Telescope Spectroscopy of Ices toward Low-Mass Embedded Protostars. *ApJS*, **154**, 359–362.

Bouwman, J., Meeus, G., de Koter, A., Hony, S., Dominik, C., & Waters, L. B. F. M. (2001). Processing of silicate dust grains in Herbig Ae/Be systems. *A&A*, **375**, 950–962.

Briceño, C., Luhman, K. L., Hartmann, L., Stauffer, J. R., & Kirkpatrick, J. D. (2002). The Initial Mass Function in the Taurus Star-forming Region. *ApJ*, **580**, 317–335.

Briceño, C., Luhman, K. L., Hartmann, L., Stauffer, J. R., & Kirkpatrick, J. D. (2003). The Brown Dwarf Deficit in Taurus: Evidence for a Non-Universal IMF. In E. Martín, editor, *IAU Symposium*, page 81.

Briceño, C., Vivas, A. K., Hernández, J., Calvet, N., Hartmann, L., Megeath, T., Berlind, P., Calkins, M., & Hoyer, S. (2004). MCNeil's Nebula in Orion: The Outburst History. *ApJ*, **606**, L123–L126.

Burkert, A. & Hartmann, L. (2004). Collapse and Fragmentation in Finite Sheets. *ApJ*, **616**, 288–300.

Byun, D.-Y., Koo, B.-C., Tatematsu, K., & Sunada, K. (2006). Interaction between the Supernova Remnant HB 21 and Molecular Clouds. *ApJ*, **637**, 283–295.

Calvet, N., Hartmann, L., & Kenyon, S. J. (1991). On the near-infrared spectrum of FU Orionis. *ApJ*, **383**, 752–756.

Carr, J. S., Harvey, P. M., & Lester, D. F. (1987). The 2 micron spectrum of L1551 IRS 5. *ApJ*, **321**, L71–L74.

Casali, M. M. (1991). The Reipurth 50-north infrared source. *MNRAS*, **248**, 229–232.

Cesaroni, R., Galli, D., Lodato, G., Walmsley, C. M., & Zhang, Q. (2007). Disks Around Young O-B (Proto)Stars: Observations and Theory. In B. Reipurth, D. Jewitt, and K. Keil, editors, *Protostars and Planets V*, pages 197–212.

Chabrier, G., Baraffe, I., Allard, F., & Hauschildt, P. (2000). Evolutionary Models for Very Low-Mass Stars and Brown Dwarfs with Dusty Atmospheres. *ApJ*, **542**, 464–472.

Chavarria, C. (1981). A study of the peculiar T Tauri star V 1331 Cygni. *A&A*, **101**, 105–117.

Clarke, C., Lodato, G., Melnikov, S. Y., & Ibrahimov, M. A. (2005). The photometric evolution of FU Orionis objects: disc instability and wind-envelope interaction. *MNRAS*, **361**, 942–954.

Clarke, C. J. & Syer, D. (1996). Low-mass companions to T Tauri stars: a mechanism for rapid-rise FU Orionis outbursts. *MNRAS*, **278**, L23–L27.

Close, L. M., Roddier, F., Northcott, M. J., Roddier, C., & Graves, J. E. (1997). Adaptive Optics 0”-4.25pt.+1.25pt2 Resolution Infrared Images of HL Tauri: Direct Images of an Active Accretion Disk around a Protostar. *ApJ*, **478**, 766.

Coffey, D., Downes, T. P., & Ray, T. P. (2004). The evolution and simulation of the outburst from XZ Tauri - A possible EXor? *A&A*, **419**, 593–598.

Cohen, M. & Kuhi, L. V. (1979). Observational studies of pre-main-sequence evolution. *ApJS*, **41**, 743–843.

Cutri, R. M., Skrutskie, M. F., van Dyk, S., Beichman, C. A., Carpenter, J. M., Chester, T., Cambresy, L., Evans, T., Fowler, J., Gizis, J., Howard, E., Huchra, J., Jarrett, T., Kopan, E. L., Kirkpatrick, J. D., Light, R. M., Marsh, K. A., McCallon, H., Schneider, S., Stiening, R., Sykes, M., Weinberg, M., Wheaton, W. A., Wheelock, S., & Zacarias, N. (2003). *2MASS All Sky Catalog of point sources.* The IRSA 2MASS All-Sky Point Source Catalog, NASA/IPAC Infrared Science Archive. http://irsa.ipac.caltech.edu/applications/Gator/.

Desch, S. J. & Cuzzi, J. N. (2000). The Generation of Lightning in the Solar Nebula. *Icarus*, **143**, 87–105.

Dibai, E. A. (1969). Spectra of stars in cometary nebulas. *Astrophysics*, **5**, 115–124.

Dobashi, K., Uehara, H., Kandori, R., Sakurai, T., Kaiden, M., Umemoto, T., & Sato, F. (2005). Atlas and Catalog of Dark Clouds Based on Digitized Sky Survey I. *PASJ*, **57**, 1.

Donati, J.-F., Paletou, F., Bouvier, J., & Ferreira, J. (2005). Direct detection of a magnetic field in the innermost regions of an accretion disk. *Nature*, **438**, 466–469.

Dorschner, J., Begemann, B., Henning, T., Jaeger, C., & Mutschke, H. (1995). Steps toward interstellar silicate mineralogy. II. Study of Mg-Fe-silicate glasses of variable composition. *A&A*, **300**, 503.

Draine, B. T. (2003). Interstellar Dust Grains. *ARA&A*, **41**, 241–289.

Draine, B. T. & McKee, C. F. (1993). Theory of interstellar shocks. *ARA&A*, **31**, 373–432.

Dullemond, C. P. & Dominik, C. (2004). Flaring vs. self-shadowed disks: The SEDs of Herbig Ae/Be stars. *A&A*, **417**, 159–168.

Dullemond, C. P., Apai, D., & Walch, S. (2006). Crystalline Silicates as a Probe of Disk Formation History. *ApJ*, **640**, L67–L70.

Ehrenfreund, P., Dartois, E., Demyk, K., & D'Hendecourt, L. (1998). Ice segregation toward massive protostars. *A&A*, **339**, L17–L20.

Eisloeffel, J., Hessman, F. V., & Mundt, R. (1990). High resolution spectroscopy of the new FU Orionis object BBW 76. *A&A*, **232**, 70–74.

Elias, J. H. (1978). A study of the IC 5146 dark cloud complex. *ApJ*, **223**, 859–861.

Feigelson, E. D. & Kriss, G. A. (1983). A search for weak H-alpha emission line pre-main-sequence stars. *AJ*, **88**, 431–438.

Fiebig, D. (1995). Star formation in L1287. Main: the H_2_O maser. *A&A*, **298**, 207.

Forrest, W. J., Sargent, B., Furlan, E., D'Alessio, P., Calvet, N., Hartmann, L., Uchida, K. I., Green, J. D., Watson, D. M., Chen, C. H., Kemper, F., Keller, L. D., Sloan, G. C., Herter, T. L., Brandl, B. R., Houck, J. R., Barry, D. J., Hall, P., Morris, P. W., Najita, J., & Myers, P. C. (2004). Mid-infrared Spectroscopy of Disks around Classical T Tauri Stars. *ApJS*, **154**, 443–447.

Fridlund, C. V. M., Bergman, P., White, G. J., Pilbratt, G. L., & Tauber, J. A. (2002). The molecular disk surrounding the protostellar binary L1551 IRS5. *A&A*, **382**, 573–582.

Froebrich, D., Smith, M. D., & Eislöffel, J. (2002). Far-infrared spectroscopy across the asymmetric bipolar outflows from Cepheus A and L1448. *A&A*, **385**, 239–256.

Furlan, E., Hartmann, L., Calvet, N., D'Alessio, P., Franco-Hernández, R., Forrest, W. J., Watson, D. M., Uchida, K. I., Sargent, B., Green, J. D., Keller, L. D., & Herter, T. L. (2006). A Survey and Analysis of Spitzer Infrared Spectrograph Spectra of T Tauri Stars in Taurus. *ApJS*, **165**, 568–605.

Gail, H.-P. (2001). Radial mixing in protoplanetary accretion disks. I. Stationary disc models with annealing and carbon combustion. *A&A*, **378**, 192–213.

Gail, H.-P. (2004). Radial mixing in protoplanetary accretion disks. IV. Metamorphosis of the silicate dust complex. *A&A*, **413**, 571–591.

Geers, V. C., Augereau, J.-C., Pontoppidan, K. M., Dullemond, C. P., Visser, R., Kessler-Silacci, J. E., Evans, II, N. J., van Dishoeck, E. F., Blake, G. A., Boogert, A. C. A., Brown, J. M., Lahuis, F., & Merín, B. (2006). C2D Spitzer-IRS spectra of disks around T Tauri stars. II. PAH emission features. *A&A*, **459**, 545–556.

Gizis, J. E. (2002). Brown Dwarfs and the TW Hydrae Association. *ApJ*, **575**, 484–492.

Gonzaga, S. (2002). WFPC2 Data Analysis: A Tutorial, version 3.0, (Baltimore, STScI). In *"WFPC2 Data Analysis: A Tutorial", version 3.0, (Baltimore, STScI)*.

Goodrich, R. W. (1987). Spectral evolution of young stellar objects. *PASP*, **99**, 116–125.

Graham, J. A. & Frogel, J. A. (1985). An FU Orionis star associated with Herbig-Haro object 57. *ApJ*, **289**, 331–341.

Green, D. A. (1996). A Catalogue of Galactic Supernova Remnants (Green 1995). *VizieR Online Data Catalog*, **7187**, 0.

Green, J. D., Hartmann, L., Calvet, N., Watson, D. M., Ibrahimov, M., Furlan, E., Sargent, B., & Forrest, W. J. (2006). Spitzer IRS Observations of FU Orionis Objects. *ApJ*, **648**, 1099–1109.

Guedel, M., Briggs, K. R., Arzner, K., Audard, M., Bouvier, J., Feigelson, E. D., Franciosini, E., Glauser, A., Grosso, N., Micela, G., Monin, J. ., Montmerle, T., Padgett, D. L., Palla, F., Pillitteri, I., Rebull, L., Scelsi, L., Silva, B., Skinner, S. L., Stelzer, B., & Telleschi, A. (2006). The XMM-Newton Extended Survey of the Taurus Molecular Cloud (XEST). *ArXiv Astrophysics e-prints*.

Guieu, S., Dougados, C., Monin, J.-L., Magnier, E., & Martín, E. L. (2006). Seventeen new very low-mass members in Taurus. The brown dwarf deficit revisited. *A&A*, **446**, 485–500.

Gullbring, E., Hartmann, L., Briceno, C., & Calvet, N. (1998). Disk Accretion Rates for T Tauri Stars. *ApJ*, **492**, 323.

Hanner, M. S., Brooke, T. Y., & Tokunaga, A. T. (1998). 8-13 Micron Spectroscopy of Young Stars. *ApJ*, **502**, 871.

Harker, D. E. & Desch, S. J. (2002). Annealing of Silicate Dust by Nebular Shocks at 10 AU. *ApJ*, **565**, L109–L112.

Harris, S., Clegg, P., & Hughes, J. (1988). T Tauri stars in Taurus - The IRAS view. *MNRAS*, **235**, 441–456.

Hartmann, L. (2002). Flows, Fragmentation, and Star Formation. I. Low-Mass Stars in Taurus. *ApJ*, **578**, 914–924.

Hartmann, L. & Kenyon, S. J. (1985). On the nature of FU Orionis objects. *ApJ*, **299**, 462–478.

Hartmann, L. & Kenyon, S. J. (1996). The FU Orionis Phenomenon. *ARA&A*, **34**, 207–240.

Hartmann, L., Kenyon, S. J., Hewett, R., Edwards, S., Strom, K. M., Strom, S. E., & Stauffer, J. R. (1989). Pre-main-sequence disk accretion in Z Canis Majoris. *ApJ*, **338**, 1001–1010.

Hartmann, L., Megeath, S. T., Allen, L., Luhman, K., Calvet, N., D'Alessio, P., Franco-Hernandez, R., & Fazio, G. (2005). IRAC Observations of Taurus Pre-Main-Sequence Stars. *ApJ*, **629**, 881–896.

Henning, T., Burkert, A., Launhardt, R., Leinert, C., & Stecklum, B. (1998). Infrared imaging and millimetre continuum mapping of Herbig Ae/Be and FU Orionis stars. *A&A*, **336**, 565–586.

Henning, T., Mutschke, H., & Jäger, C. (2006). Astrochemistry: Recent Successes and Current Challenges, Proceedings IAU Symposium 231. In D. C. Lis, G. Blake, and E. Herbst, editors, *Astrochemistry: Recent Successes and Current Challenges (Proceedings IAU Symposium 231)*.

Herbig, G. H. (1960). The Spectra of Be- and Ae-TYPE Stars Associated with Nebulosity. *ApJS*, **4**, 337.

Herbig, G. H. (1966). Eruptive phenomena in early stellar evolution. *Vistas in Astronomy*, **8**, 109–115.

Herbig, G. H. (1977). Eruptive phenomena in early stellar evolution. *ApJ*, **217**, 693–715.

Herbig, G. H. (1989). Fu-Orionis Eruptions. In B. Reipurth, editor, *Low Mass Star Formation and Pre-main Sequence Objects*, page 233.

Herbig, G. H. & Dahm, S. E. (2006). The Pre-Main-Sequence Population of L988. *AJ*, **131**, 1530–1543.

Herbig, G. H., Petrov, P. P., & Duemmler, R. (2003). High-Resolution Spectroscopy of FU Orionis Stars. *ApJ*, **595**, 384–411.

Higdon, S. J. U., Devost, D., Higdon, J. L., Brandl, B. R., Houck, J. R., Hall, P., Barry, D., Charmandaris, V., Smith, J. D. T., Sloan, G. C., & Green, J. (2004). The SMART Data Analysis Package for the Infrared Spectrograph on the Spitzer Space Telescope. *PASP*, **116**, 975–984.

Hodapp, K.-W., Hora, J. L., Rayner, J. T., Pickles, A. J., & Ladd, E. F. (1996). An Outburst of a Deeply Embedded Star in Serpens. *ApJ*, **468**, 861.

Hony, S., Tielens, A. G. G. M., Waters, L. B. F. M., & de Koter, A. (2003). The circumstellar envelope of the C-rich post-AGB star HD 56126. *A&A*, **402**, 211–228.

Itoh, Y., Tamura, M., & Nakajima, T. (1999). A Near-Infrared Search for Companions around Very Low Luminosity Young Stellar Objects in Taurus. *AJ*, **117**, 1471–1484.

Itoh, Y., Tamura, M., & Tokunaga, A. T. (2002). Near-Infrared Spectroscopy of Very Low-Luminosity Young Stellar Objects in the Taurus Molecular Cloud. *PASJ*, **54**, 561–574.

Jaeger, C., Molster, F. J., Dorschner, J., Henning, T., Mutschke, H., & Waters, L. B. F. M. (1998). Steps toward interstellar silicate mineralogy. IV. The crystalline revolution. *A&A*, **339**, 904–916.

Jayawardhana, R. & Ivanov, V. D. (2006a). Discovery of a Young Planetary-Mass Binary. *Science*, **313**, 1279–1281.

Jayawardhana, R. & Ivanov, V. D. (2006b). Spectroscopy of Young Planetary Mass Candidates with Disks. *ApJ*, **647**, L167–L170.

Jennings, D. E., Weber, A., & Brault, J. W. (1987). FTS-Raman Flame Spectroscopy of High-J Lines in H2 and D2. *Journal of Molecular Spectroscopy*, **126**, 19–28.

Jordi, K., Grebel, E. K., & Ammon, K. (2006). Empirical color transformations between SDSS photometry and other photometric systems. *A&A*, **460**, 339–347.

Kant, I. (1755). *Allgemeine Naturgeschichte und Theorie des Himmels*. Zeitz, Bei W. Webel, 1798. Neue Auflage.

Keane, J. V., Tielens, A. G. G. M., Boogert, A. C. A., Schutte, W. A., & Whittet, D. C. B. (2001). Ice absorption features in the 5-8 μm region toward embedded protostars. *A&A*, **376**, 254–270.

Kemper, F., Vriend, W. J., & Tielens, A. G. G. M. (2004). The Absence of Crystalline Silicates in the Diffuse Interstellar Medium. *ApJ*, **609**, 826–837.

Kenyon, S. J. & Hartmann, L. (1987). Spectral energy distributions of T Tauri stars - Disk flaring and limits on accretion. *ApJ*, **323**, 714–733.

Kenyon, S. J., Hartmann, L., & Hewett, R. (1988). Accretion disk models for FU Orionis and V1057 Cygni - Detailed comparisons between observations and theory. *ApJ*, **325**, 231–251.

Kenyon, S. J., Hartmann, L., Gomez, M., Carr, J. S., & Tokunaga, A. (1993). RNO 1B/1C - A double FU Orionis system. *AJ*, **105**, 1505–1510.

Kenyon, S. J., Dobrzycka, D., & Hartmann, L. (1994). A new optical extinction law and distance estimate for the Taurus-Auriga molecular cloud. *AJ*, **108**, 1872–1880.

Kessler-Silacci, J., Augereau, J.-C., Dullemond, C. P., Geers, V., Lahuis, F., Evans, II, N. J., van Dishoeck, E. F., Blake, G. A., Boogert, A. C. A., Brown, J., Jørgensen, J. K., Knez, C., & Pontoppidan, K. M. (2006). c2d Spitzer IRS Spectra of Disks around T Tauri Stars. I. Silicate Emission and Grain Growth. *ApJ*, **639**, 275–291.

Kessler-Silacci, J. E., Hillenbrand, L. A., Blake, G. A., & Meyer, M. R. (2005). 8-13 μm Spectroscopy of Young Stellar Objects: Evolution of the Silicate Feature. *ApJ*, **622**, 404–429.

Khanzadyan, T., Smith, M. D., Gredel, R., Stanke, T., & Davis, C. J. (2002). Active star formation in the large Bok globule CB 34. *A&A*, **383**, 502–518.

Kirkpatrick, J. D., Dahn, C. C., Monet, D. G., Reid, I. N., Gizis, J. E., Liebert, J., & Burgasser, A. J. (2001). Brown Dwarf Companions to G-Type Stars. I. Gliese 417B and Gliese 584C. *AJ*, **121**, 3235–3253.

Kirkpatrick, J. D., Barman, T. S., Burgasser, A. J., McGovern, M. R., McLean, I. S., Tinney, C. G., & Lowrance, P. J. (2006). Discovery of a Very Young Field L Dwarf, 2MASS J01415823-4633574. *ApJ*, **639**, 1120–1128.

Knez, C., Boogert, A. C. A., Pontoppidan, K. M., Kessler-Silacci, J., van Dishoeck, E. F., Evans, II, N. J., Augereau, J.-C., Blake, G. A., & Lahuis, F. (2005). Spitzer Mid-Infrared Spectroscopy of Ices toward Extincted Background Stars. *ApJ*, **635**, L145–L148.

Kolotilov, E. A. & Petrov, P. P. (1983). Spectral evolution of young stellar objects. *Pis'ma Astr. Zh.*, **9**, 171–178.

Kolotilov, E. A. & Petrov, P. P. (1985). Spectral evolution of young stellar objects. *Pis'ma Astr. Zh.*, **11**, 846–890.

Konigl, A. & Pudritz, R. E. (2000). Disk Winds and the Accretion-Outflow Connection. *Protostars and Planets IV*, page 759.

Krist, J. (1993). Tiny Tim : an HST PSF Simulator. In R. J. Hanisch, R. J. V. Brissenden, and J. Barnes, editors, *ASP Conf. Ser. 52: Astronomical Data Analysis Software and Systems II*, page 536.

Kuhi, L. V. (1964). Mass Loss from T Tauri Stars. *ApJ*, **140**, 1409.

Lachaume, R. (2004). The vertical structure of T Tauri accretion discs. IV. Self-irradiation of the disc in the FU Orionis outburst phase. *A&A*, **422**, 171–176.

Lachaume, R., Malbet, F., & Monin, J.-L. (2003). The vertical structure of T Tauri accretion discs. III. Consistent interpretation of spectra and visibilities with a two-layer model. *A&A*, **400**, 185–202.

Lada, C. J. & Wilking, B. A. (1984). The nature of the embedded population in the Rho Ophiuchi dark cloud - Mid-infrared observations. *ApJ*, **287**, 610–621.

Lada, C. J., Lada, E. A., Clemens, D. P., & Bally, J. (1994). Dust extinction and molecular gas in the dark cloud IC 5146. *ApJ*, **429**, 694–709.

Laplace, P. S. (1795). *Exposition du Système du Monde*. Exposition du Système du Monde, by P.S. Laplace; new edition 1984; Editor: Fayard.

Larsson, B., Liseau, R., Men'shchikov, A. B., Olofsson, G., Caux, E., Ceccarelli, C., Lorenzetti, D., Molinari, S., Nisini, B., Nordh, L., Saraceno, P., Sibille, F., Spinoglio, L., & White, G. J. (2000). The ISO-LWS map of the Serpens cloud core. I. The SEDs of the IR/SMM sources. *A&A*, **363**, 253–268.

Lee, C. W., Myers, P. C., & Plume, R. (2004). A Survey for Infall Motions toward Starless Cores. III. CS (3-2) and DCO+ (2-1) Observations. *ApJS*, **153**, 523–543.

Leinert, C., van Boekel, R., Waters, L. B. F. M., Chesneau, O., Malbet, F., Köhler, R., Jaffe, W., Ratzka, T., Dutrey, A., Preibisch, T., Graser, U., Bakker, E., Chagnon, G., Cotton, W. D., Dominik, C., Dullemond, C. P., Glazenborg-Kluttig, A. W., Glindemann, A., Henning, T., Hofmann, K.-H., de Jong, J., Lenzen, R., Ligori, S., Lopez, B., Meisner, J., Morel, S., Paresce, F., Pel, J.-W., Percheron, I., Perrin, G., Przygodda, F., Richichi, A., Schöller, M., Schuller, P., Stecklum, B., van den Ancker, M. E., von der Lühe, O., & Weigelt, G. (2004). Mid-infrared sizes of circumstellar disks around Herbig Ae/Be stars measured with MIDI on the VLTI. *A&A*, **423**, 537–548.

Levreault, R. M. (1988a). A search for molecular outflows toward the pre-main-sequence objects. *ApJS*, **67**, 283–371.

Levreault, R. M. (1988b). PhD Thesis (University of Texas at Austin).

Liu, M. C., Najita, J., & Tokunaga, A. T. (2003). A Survey for Circumstellar Disks around Young Substellar Objects. *ApJ*, **585**, 372–391.

Lodato, G. & Clarke, C. J. (2004). Massive planets in FU Orionis discs: implications for thermal instability models. *MNRAS*, **353**, 841–852.

Lombardi, M. & Alves, J. (2001). Mapping the interstellar dust with near-infrared observations: An optimized multi-band technique. *A&A*, **377**, 1023–1034.

López Martí, B., Eislöffel, J., Scholz, A., & Mundt, R. (2004). The brown dwarf population in the Chamaeleon I cloud. *A&A*, **416**, 555–576.

Lorenzetti, D., Giannini, T., Nisini, B., Benedettini, M., Creech-Eakman, M., Blake, G. A., van Dishoeck, E. F., Cohen, M., Liseau, R., Molinari, S., Pezzuto, S., Saraceno, P., Smith, H. A., Spinoglio, L., & White, G. J. (2000). Far infrared spectroscopy of FU Ori objects. ISO-LWS observations. *A&A*, **357**, 1035–1044.

Lucas, P. W. & Roche, P. F. (2000). A population of very young brown dwarfs and free-floating planets in Orion. *MNRAS*, **314**, 858–864.

Luhman, K. L. (2006). The Spatial Distribution of Brown Dwarfs in Taurus. *ApJ*, **645**, 676–687.

Luhman, K. L., Briceno, C., Rieke, G. H., & Hartmann, L. (1998). A Young Star near the Hydrogen-burning Limit. *ApJ*, **493**, 909.

Luhman, K. L., Briceño, C., Stauffer, J. R., Hartmann, L., Barrado y Navascués, D., & Caldwell, N. (2003). New Low-Mass Members of the Taurus Star-forming Region. *ApJ*, **590**, 348–356.

Luhman, K. L., Whitney, B. A., Meade, M. R., Babler, B. L., Indebetouw, R., Bracker, S., & Churchwell, E. B. (2006a). A Survey for New Members of Taurus with the Spitzer Space Telescope. *ApJ*, **647**, 1180–1191.

Luhman, K. L., Wilson, J. C., Brandner, W., Skrutskie, M. F., Nelson, M. J., Smith, J. D., Peterson, D. E., Cushing, M. C., & Young, E. (2006b). Discovery of a Young Substellar Companion in Chamaeleon. *ApJ*, **649**, 894–899.

Luhman, K. L., Allers, K. N., Jaffe, D. T., Cushing, M. C., Williams, K. A., Slesnick, C. L., & Vacca, W. D. (2007a). Oph 1622-2405: Not a Planetary-Mass Binary. *ArXiv Astrophysics e-prints*.

Luhman, K. L., Joergens, V., Lada, C., Muzerolle, J., Pascucci, I., & White, R. (2007b). The Formation of Brown Dwarfs: Observations. In B. Reipurth, D. Jewitt, and K. Keil, editors, *Protostars and Planets V*, pages 443–457.

Lynds, B. T. (1962). Catalogue of Dark Nebulae. *ApJS*, **7**, 1.

Malbet, F., Lachaume, R., Berger, J.-P., Colavita, M. M., di Folco, E., Eisner, J. A., Lane, B. F., Millan-Gabet, R., Ségransan, D., & Traub, W. A. (2005). New insights on the AU-scale circumstellar structure of FU Orionis. *A&A*, **437**, 627–636.

Mathis, J. S. (1990). Interstellar dust and extinction. *ARA&A*, **28**, 37–70.

McMuldroch, S., Sargent, A. I., & Blake, G. A. (1993). The circumstellar environment of the FU Orionis pre-outburst candidate V1331 Cygni. *AJ*, **106**, 2477–2485.

McMuldroch, S., Blake, G. A., & Sargent, A. I. (1995). The FU Orionis Binary System RNO 1B/1C. *AJ*, **110**, 354.

Meeus, G., Waters, L. B. F. M., Bouwman, J., van den Ancker, M. E., Waelkens, C., & Malfait, K. (2001). ISO spectroscopy of circumstellar dust in 14 Herbig Ae/Be systems: Towards an understanding of dust processing. *A&A*, **365**, 476–490.

Ménard, F. & Duchêne, G. (2004). On the alignment of Classical T Tauri stars with the magnetic field in the Taurus-Auriga molecular cloud. *A&A*, **425**, 973–980.

Mennesson, B., Koresko, C., Creech-Eakman, M. J., Serabyn, E., Colavita, M. M., Akeson, R., Appleby, E., Bell, J., Booth, A., Crawford, S., Dahl, W., Fanson, J., Felizardo, C., Garcia, J., Gathright, J., Herstein, J., Hovland, E., Hrynevych, M., Johansson, E., Le Mignant, D., Ligon, R., Millan-Gabet, R., Moore, J., Neyman, C., Palmer, D., Panteleeva, T., Paine, C., Ragland, S., Reder, L., Rudeen, A., Saloga, T., Shao, M., Smythe, R., Summers, K., Swain, M., Tsubota, K., Tyau, C., Vasisht, G., Wizinowich, P., & Woillez, J. (2005). The Dusty AGB Star RS CrB: First Mid-Infrared Interferometric Observations with the Keck Telescopes. *ApJ*, **634**, L169–L172.

Men'shchikov, A. B. & Henning, T. (1997). Radiation transfer in circumstellar disks. *A&A*, **318**, 879–907.

Metcalfe, N., Shanks, T., Weilbacher, P. M., McCracken, H. J., Fong, R., & Thompson, D. (2006). Galaxy number counts - VI. An H-band survey of the Herschel Deep Field. *MNRAS*, **370**, 1257–1273.

Meyer, M. R., Calvet, N., & Hillenbrand, L. A. (1997). Intrinsic Near-Infrared Excesses of T Tauri Stars: Understanding the Classical T Tauri Star Locus. *AJ*, **114**, 288–300.

Millan-Gabet, R., Monnier, J. D., Akeson, R. L., Hartmann, L., Berger, J.-P., Tannirkulam, A., Melnikov, S., Billmeier, R., Calvet, N., D'Alessio, P., Hillenbrand, L. A., Kuchner, M., Traub, W. A., Tuthill, P. G., Beichman, C., Boden, A., Booth, A., Colavita,

M., Creech-Eakman, M., Gathright, J., Hrynevych, M., Koresko, C., Le Mignant, D., Ligon, R., Mennesson, B., Neyman, C., Sargent, A., Shao, M., Swain, M., Thompson, R., Unwin, S., van Belle, G., Vasisht, G., & Wizinowich, P. (2006). Keck Interferometer Observations of FU Orionis Objects. *ApJ*, **641**, 547–555.

Min, M., Hovenier, J. W., & de Koter, A. (2005). Modeling optical properties of cosmic dust grains using a distribution of hollow spheres. *A&A*, **432**, 909–920.

Mitchell, G. F., Johnstone, D., Moriarty-Schieven, G., Fich, M., & Tothill, N. F. H. (2001). A Submillimeter Dust and Gas Study of the Orion B Molecular Cloud. *ApJ*, **556**, 215–229.

Mohanty, S., Jayawardhana, R., & Basri, G. (2005). The T Tauri Phase Down to Nearly Planetary Masses: Echelle Spectra of 82 Very Low Mass Stars and Brown Dwarfs. *ApJ*, **626**, 498–522.

Molster, F. & Kemper, C. (2005). Crystalline Silicates. *Space Science Reviews*, **119**, 3–28.

Moro-Martín, A., Noriega-Crespo, A., Molinari, S., Testi, L., Cernicharo, J., & Sargent, A. (2001). Infrared and Millimetric Study of the Young Outflow Cepheus E. *ApJ*, **555**, 146–159.

Movsessian, T. A., Khanzadyan, T., Aspin, C., Magakian, T. Y., Beck, T., Moiseev, A., Smith, M. D., & Nikogossian, E. H. (2006). An outbursting protostar of the FU Orionis type in the Cygnus OB7 molecular cloud. *A&A*, **455**, 1001–1008.

Mundt, R. (1984). Mass loss in T Tauri stars - Observational studies of the cool parts of their stellar winds and expanding shells. *ApJ*, **280**, 749–770.

Mundt, R. & Eislöffel, J. (1998). T Tauri Stars Associated with Herbig-Haro Objects and Jets. *AJ*, **116**, 860–867.

Mundt, R., Appenzeller, I., Bertout, C., Krautter, J., & Chavarria, C. (1981). IUE observations of V 1331 CYG. *A&A*, **93**, 412–414.

Muzerolle, J., Megeath, S. T., Flaherty, K. M., Gordon, K. D., Rieke, G. H., Young, E. T., & Lada, C. J. (2005). The Outburst of V1647 Orionis Revealed by Spitzer. *ApJ*, **620**, L107–L110.

Neufeld, D. A., Melnick, G. J., & Harwit, M. (1998). Infrared Space Observatory Observations of Molecular Hydrogen in HH 54:Measurement of a Nonequilibrium Ratio of Ortho- to Para-H_2. *ApJ*, **506**, L75–L78.

Neufeld, D. A., Melnick, G. J., Sonnentrucker, P., Bergin, E. A., Green, J. D., Kim, K. H., Watson, D. M., Forrest, W. J., & Pipher, J. L. (2006). Spitzer Observations of HH 54 and HH 7-11: Mapping the H2 Ortho-to-Para Ratio in Shocked Molecular Gas. *ApJ*, **649**, 816–835.

Ochsenbein, F., Bauer, P., & Marcout, J. (2000). The VizieR database of astronomical catalogues. *A&AS*, **143**, 23–32.

Onishi, T., Mizuno, A., Kawamura, A., Tachihara, K., & Fukui, Y. (2002). A Complete Search for Dense Cloud Cores in Taurus. *ApJ*, **575**, 950–973.

Padgett, D. L., Brandner, W., Stapelfeldt, K. R., Strom, S. E., Terebey, S., & Koerner, D. (1999). HUBBLE SPACE TELESCOPE/NICMOS Imaging of Disks and Envelopes around Very Young Stars. *AJ*, **117**, 1490–1504.

Park, Y.-S., Lee, C. W., & Myers, P. C. (2004). A CO Survey toward Starless Cores. *ApJS*, **152**, 81–96.

Parmar, P. S., Lacy, J. H., & Achtermann, J. M. (1991). Detection of low-J pure-rotational emission from H2 in the Orion Bar region - Evidence for small-scale clumpiness. *ApJ*, **372**, L25–L28.

Peeters, E., Hony, S., Van Kerckhoven, C., Tielens, A. G. G. M., Allamandola, L. J., Hudgins, D. M., & Bauschlicher, C. W. (2002). The rich 6 to 9 vec mu m spectrum of interstellar PAHs. *A&A*, **390**, 1089–1113.

Perryman, M. A. C., Lindegren, L., Kovalevsky, J., Hoeg, E., Bastian, U., Bernacca, P. L., Crézé, M., Donati, F., Grenon, M., van Leeuwen, F., van der Marel, H., Mignard, F., Murray, C. A., Le Poole, R. S., Schrijver, H., Turon, C., Arenou, F., Froeschlé, M., & Petersen, C. S. (1997). The HIPPARCOS Catalogue. *A&A*, **323**, L49–L52.

Persi, P., Ferrari-Toniolo, M., Busso, M., Robberto, M., Scaltriti, F., & Silvestro, G. (1988). IRAS sources associated with nebulosities resembling Herbig-Haro objects. *AJ*, **95**, 1167–1172.

Pilipp, W., Hartquist, T. W., Morfill, G. E., & Levy, E. H. (1998). Chondrule formation by lightning in the Protosolar Nebula? *A&A*, **331**, 121–146.

Polomski, E. F., Woodward, C. E., Holmes, E. K., Butner, H. M., Lynch, D. K., Russell, R. W., Sitko, M. L., Wooden, D. H., Telesco, C. M., & Piña, R. (2005). Dust Morphology and Composition in FU Orionis Systems. *AJ*, **129**, 1035–1048.

Pontoppidan, K. M., Dullemond, C. P., van Dishoeck, E. F., Blake, G. A., Boogert, A. C. A., Evans, II, N. J., Kessler-Silacci, J. E., & Lahuis, F. (2005). Ices in the Edge-on Disk CRBR 2422.8-3423: Spitzer Spectroscopy and Monte Carlo Radiative Transfer Modeling. *ApJ*, **622**, 463–481.

Pringle, J. E. (1981). Accretion discs in astrophysics. *ARA&A*, **19**, 137–162.

Przygodda, F., van Boekel, R., Àbrahàm, P., Melnikov, S. Y., Waters, L. B. F. M., & Leinert, C. (2003). Evidence for grain growth in T Tauri disks. *A&A*, **412**, L43–L46.

Quanz, S. P., Henning, T., Bouwman, J., Ratzka, T., & Leinert, C. (2006). FU Orionis: The MIDI VLTI Perspective. *ApJ*, **648**, 472–483.

Quanz, S. P., Apai, D., & Henning, T. (2007). Dust Rings and Filaments around the Isolated Young Star V1331 Cygni. *ApJ*, **656**, 287–292.

Quanz, S. P., Henning, T., Bouwman, J., Linz, H., & Lahuis, F. (2007). Deeply Embedded Objects and Shocked Molecular Hydrogen: The Environment of the FU Orionis Stars RNO 1B/1C. *ApJ*, **658**, 487–497.

Quanz, S. P., Henning, T., Bouwman, J., van Boekel, R., Juhász, A., Linz, H., Pontoppidan, K. M., & Lahuis, F. (2007). Evolution of dust and ice features around FU Orionis objects. *ApJ*, to be submitted

Reipurth, B. (1985). Herbig-Haro objects and FU Orionis eruptions - The case of HH 57. *A&A*, **143**, 435–442.

Reipurth, B. & Aspin, C. (1997). Infrared Spectroscopy of Herbig-Haro Energy Sources. *AJ*, **114**, 2700.

Reipurth, B. & Aspin, C. (2004). The FU Orionis Binary System and the Formation of Close Binaries. *ApJ*, **608**, L65–L68.

Reipurth, B., Hartmann, L., Kenyon, S. J., Smette, A., & Bouchet, P. (2002). Evolution of the Fu Orionis Object BBW 76. *AJ*, **124**, 2194–2206.

Reipurth, B., Aspin, C., Beck, T., Brogan, C., Connelley, M. S., & Herbig, G. H. (2007). V733 Cep (Persson's Star): A New FU Orionis Object in Cepheus. *AJ*, **133**, 1000–1011.

Sandell, G. & Aspin, C. (1998). PP 13S, a young, low-mass FU Orionis-type pre-main sequence star. *A&A*, **333**, 1016–1024.

Sandell, G. & Weintraub, D. A. (2001). On the Similarity of FU Orionis Stars to Class I Protostars: Evidence from the Submillimeter. *ApJS*, **134**, 115–132.

Sargent, B., Forrest, W. J., D'Alessio, P., Li, A., Najita, J., Watson, D. M., Calvet, N., Furlan, E., Green, J. D., Kim, K. H., Sloan, G. C., Chen, C. H., Hartmann, L., & Houck, J. R. (2006). Dust Processing in Disks around T Tauri Stars. *ApJ*, **645**, 395–415.

Sato, S., Okita, K., Yamashita, T., Mizutani, K., Shiba, H., Kobayashi, Y., & Takami, H. (1992). Near-infrared spectrophotometry of FU Orionis variables. *ApJ*, **398**, 273–277.

Schneider, S. & Elmegreen, B. G. (1979). A catalog of dark globular filaments. *ApJS*, **41**, 87–95.

Schulz, N. S. (2005). *From Dust To Stars Studies of the Formation and Early Evolution of Stars*. From Dust To Stars Studies of the Formation and Early Evolution of Stars, by N.S. Schulz. Springer-Praxis books in astrophysics and astronomy. Praxis Publishing Ltd, 2005. ISBN 3-540-23711-9.

Schutte, W. A. & Khanna, R. K. (2003). Origin of the 6.85 μm band near young stellar objects: The ammonium ion (NH_4^+) revisited. *A&A*, **398**, 1049–1062.

Schütz, O., Meeus, G., & Sterzik, M. F. (2005). Mid-IR observations of circumstellar disks. I. Pre-main sequence objects. *A&A*, **431**, 165–174.

Servoin, J. L. & Piriou, B. (1973). First-Overtone CO Variability in Young Stellar Objects. *phys. stat. sol.*, **55**, 677.

Shevchenko, V., Yakubov, S. D., Ambaryan, V. V., & Garibdzhanyan, A. T. (1991). A Compact Star-Forming Region Associated with V1331-CYGNI. *Soviet Astronomy*, **35**, 135.

Shu, F., Najita, J., Ostriker, E., Wilkin, F., Ruden, S., & Lizano, S. (1994). Magnetocentrifugally driven flows from young stars and disks. 1: A generalized model. *ApJ*, **429**, 781–796.

Shu, F. H., Allen, A., Shang, H., Ostriker, E. C., & Li, Z.-Y. (1999). Low-Mass Star Formation: Theory. In C. J. Lada and N. D. Kylafis, editors, *NATO ASIC Proc. 540: The Origin of Stars and Planetary Systems*, page 193.

Skinner, S. L., Briggs, K. R., & Güdel, M. (2006). The Unusual X-Ray Spectrum of FU Orionis. *ApJ*, **643**, 995–1002.

Sloan, G. C., Keller, L. D., Forrest, W. J., Leibensperger, E., Sargent, B., Li, A., Najita, J., Watson, D. M., Brandl, B. R., Chen, C. H., Green, J. D., Markwick-Kemper, F., Herter, T. L., D'Alessio, P., Morris, P. W., Barry, D. J., Hall, P., Myers, P. C., & Houck, J. R. (2005). Mid-Infrared Spectra of Polycyclic Aromatic Hydrocarbon Emission in Herbig Ae/Be stars. *ApJ*, **632**, 956–963.

Smith, H. A., Fischer, J., Schwartz, P. R., & Geballe, T. R. (1987). Infrared line observations of low-luminosity outflow sources. *ApJ*, **316**, 265–274.

Snell, R. L. & Schloerb, F. P. (1985). Structure and physical properties of the bipolar outflow in L1551. *ApJ*, **295**, 490–500.

Snell, R. L., Dickman, R. L., & Huang, Y.-L. (1990). Molecular outflows associated with a flux-limited sample of bright far-infrared sources. *ApJ*, **352**, 139–148.

Solf, J. (2000). A high-resolution long-slit spectroscopic study of the various bipolar outflow components in M 2-9 ("Butterfly Nebula"). *A&A*, **354**, 674–690.

Spitzer, W. G. & Kleinman, D. A. (1960). Infrared lattice bands of quartz. *Physical Review*, **121**, 1324–1335.

Stahler, S. W. & Palla, F. (2005). *The Formation of Stars*. The Formation of Stars, by Steven W. Stahler, Francesco Palla, pp. 865. ISBN 3-527-40559-3. Wiley-VCH , January 2005.

Stapelfeldt, K. R., Krist, J. E., Menard, F., Bouvier, J., Padgett, D. L., & Burrows, C. J. (1998). An Edge-On Circumstellar Disk in the Young Binary System HK Tauri. *ApJ*, **502**, L65+.

Staude, H. J. & Neckel, T. (1991). RNO 1B - A new FUor in Cassiopeia. *A&A*, **244**, L13–L16.

Staude, H. J. & Neckel, T. (1992). The FU Orionis-type spectrum and bipolar outflow of Parsamyan 21. *ApJ*, **400**, 556–561.

Stecklum, B., Melnikov, S. Y., & Meusinger, H. (2007). The new nebula in LDN 1415 - A cry from the cradle of a low-luminosity source. *A&A*, **463**, 621–626.

Stocke, J. T., Hartigan, P. M., Strom, S. E., Strom, K. M., Anderson, E. R., Hartmann, L. W., & Kenyon, S. J. (1988). A detailed study of the LYNDS 1551 star formation region. *ApJS*, **68**, 229–255.

Strom, K. M. & Strom, S. E. (1993). The discovery of two FU Orionis objects in L1641. *ApJ*, **412**, L63–L66.

Tafalla, M., Santiago, J., Johnstone, D., & Bachiller, R. (2004). A highly collimated, extremely high velocity outflow in Taurus. *A&A*, **423**, L21–L24.

The, P. S., de Winter, D., & Perez, M. R. (1994). A new catalogue of members and candidate members of the Herbig Ae/Be (HAEBE) stellar group. *A&AS*, **104**, 315–339.

Timmermann, R. (1998). Ortho-H 2/Para-H 2 Ratio in Low-Velocity Shocks. *ApJ*, **498**, 246.

Tomisaka, K. (1998). Collapse-Driven Outflow in Star-Forming Molecular Cores. *ApJ*, **502**, L163+.

Ungerechts, H. & Thaddeus, P. (1987). A CO survey of the dark nebulae in Perseus, Taurus, and Auriga. *ApJS*, **63**, 645–660.

van Boekel, R., Waters, L. B. F. M., Dominik, C., Bouwman, J., de Koter, A., Dullemond, C. P., & Paresce, F. (2003). Grain growth in the inner regions of Herbig Ae/Be star disks. *A&A*, **400**, L21–L24.

van Boekel, R., Min, M., Leinert, C., Waters, L. B. F. M., Richichi, A., Chesneau, O., Dominik, C., Jaffe, W., Dutrey, A., Graser, U., Henning, T., de Jong, J., Köhler, R., de Koter, A., Lopez, B., Malbet, F., Morel, S., Paresce, F., Perrin, G., Preibisch, T., Przygodda, F., Schöller, M., & Wittkowski, M. (2004). The building blocks of planets within the 'terrestrial' region of protoplanetary disks. *Nature*, **432**, 479–482.

van Boekel, R., Min, M., Waters, L. B. F. M., de Koter, A., Dominik, C., van den Ancker, M. E., & Bouwman, J. (2005). A 10 μm spectroscopic survey of Herbig Ae star disks: Grain growth and crystallization. *A&A*, **437**, 189–208.

van Boekel, R., Ábrahám, P., Correia, S., de Koter, A., Dominik, C., Dutrey, A., Henning, T., Kóspál, Á., Lachaume, R., Leinert, C., Linz, H., Min, M., Mosoni, L., Preibisch, T., Quanz, S., Ratzka, T., Schegerer, A., Waters, R., Wolf, S., & Zinnecker, H. (2006). Disks around young stars with VLTI/MIDI. In *Advances in Stellar Interferometry. Edited by Monnier, John D.; Schöller, Markus; Danchi, William C.. Proceedings of the SPIE, Volume 6268, pp. 62680D (2006).*

van den Ancker, M. E., Bouwman, J., Wesselius, P. R., Waters, L. B. F. M., Dougherty, S. M., & van Dishoeck, E. F. (2000). ISO spectroscopy of circumstellar dust in the Herbig Ae systems AB Aur and HD 163296. *A&A*, **357**, 325–329.

van Diedenhoven, B., Peeters, E., Van Kerckhoven, C., Hony, S., Hudgins, D. M., Allamandola, L. J., & Tielens, A. G. G. M. (2004). The Profiles of the 3-12 Micron Polycyclic Aromatic Hydrocarbon Features. *ApJ*, **611**, 928–939.

van Dishoeck, E. F. (2004). ISO Spectroscopy of Gas and Dust: From Molecular Clouds to Protoplanetary Disks. *ARA&A*, **42**, 119–167.

Vorobyov, E. I. & Basu, S. (2006). The Burst Mode of Protostellar Accretion. *ApJ*, **650**, 956–969.

Voshchinnikov, N. V., Il'in, V. B., Henning, T., & Dubkova, D. N. (2006). Dust extinction and absorption: the challenge of porous grains. *A&A*, **445**, 167–177.

Wang, H., Apai, D., Henning, T., & Pascucci, I. (2004). FU Orionis: A Binary Star? *ApJ*, **601**, L83–L86.

Watson, D. M., Kemper, F., Calvet, N., Keller, L. D., Furlan, E., Hartmann, L., Forrest, W. J., Chen, C. H., Uchida, K. I., Green, J. D., Sargent, B., Sloan, G. C., Herter, T. L., Brandl, B. R., Houck, J. R., Najita, J., D'Alessio, P., Myers, P. C., Barry, D. J., Hall, P., & Morris, P. W. (2004). Mid-infrared Spectra of Class I Protostars in Taurus. *ApJS*, **154**, 391–395.

Weingartner, J. C. & Draine, B. T. (2001). Dust Grain-Size Distributions and Extinction in the Milky Way, Large Magellanic Cloud, and Small Magellanic Cloud. *ApJ*, **548**, 296–309.

Weintraub, D. A. & Kastner, J. (1993). The exciting young stellar object for the molecular outflow at the core of L1287. *ApJ*, **411**, 767–772.

Weintraub, D. A., Sandell, G., & Duncan, W. D. (1991). Are FU Orionis stars younger than T Tauri stars? Submillimeter constraints on circumstellar disks. *ApJ*, **382**, 270–289.

Weintraub, D. A., Kastner, J. H., Gatley, I., & Merrill, K. M. (1996). Diffraction-Limited 3.8 Micron Imaging of Protostellar Outflow Sources. *ApJ*, **468**, L45+.

Welin, G. (1976). Possible properties of pre-outburst FU ORI stars. *A&A*, **49**, 145–148.

White, G. J., Liseau, R., Men'shchikov, A. B., Justtanont, K., Nisini, B., Benedettini, M., Caux, E., Ceccarelli, C., Correia, J. C., Giannini, T., Kaufman, M., Lorenzetti, D., Molinari, S., Saraceno, P., Smith, H. A., Spinoglio, L., & Tommasi, E. (2000). An infrared study of the L1551 star formation region. *A&A*, **364**, 741–762.

White, R. J. & Basri, G. (2003). Very Low Mass Stars and Brown Dwarfs in Taurus-Auriga. *ApJ*, **582**, 1109–1122.

White, R. J. & Ghez, A. M. (2001). Observational Constraints on the Formation and Evolution of Binary Stars. *ApJ*, **556**, 265–295.

Wilgenbus, D., Cabrit, S., Pineau des Forêts, G., & Flower, D. R. (2000). The ortho:para-H_2 ratio in C- and J-type shocks. *A&A*, **356**, 1010–1022.

Wolniewicz, L., Simbotin, I., & Dalgarno, A. (1998). Quadrupole Transition Probabilities for the Excited Rovibrational States of H 2. *ApJS*, **115**, 293.

Wood, K., Wolk, S. J., Stanek, K. Z., Leussis, G., Stassun, K., Wolff, M., & Whitney, B. (2000). Optical Variability of the T Tauri Star HH 30 IRS. *ApJ*, **542**, L21–L24.

Xu, Y., Shen, Z.-Q., Yang, J., Zheng, X. W., Miyazaki, A., Sunada, K., Ma, H. J., Li, J. J., Sun, J. X., & Pei, C. C. (2006). Molecular Outflows around High-Mass Young Stellar Objects. *AJ*, **132**, 20–26.

Yang, J., Umemoto, T., Iwata, T., & Fukui, Y. (1991). A millimeter-wave line study of L1287 - A case of induced star formation by stellar wind compression? *ApJ*, **373**, 137–145.

Yang, J., Ohashi, N., & Fukui, Y. (1995). Interferometric Observations of the Circumstellar Molecular Structure around the Young Stellar Object in L1287. *ApJ*, **455**, 175.

Yun, J. L., Moreira, M. C., Alves, J. F., & Storm, J. (1997). Two new T Tauri stars and a candidate FU Orionis star associated with BOK globules. *A&A*, **320**, 167–171.

Zapatero Osorio, M. R., Béjar, V. J. S., Martín, E. L., Rebolo, R., Barrado y Navascués, D., Bailer-Jones, C. A. L., & Mundt, R. (2000). Discovery of Young, Isolated Planetary Mass Objects in the σ Orionis Star Cluster. *Science*, **290**, 103–107.

A. Color transformations

2MASS - CIT

(see, http://www.ipac.caltech.edu/2mass/releases/allsky/doc/sec6_4b.html)

$$
\begin{aligned}
(K_s)_{\rm 2MASS} &= K_{\rm CIT} - (0.019 \pm 0.004) + (0.001 \pm 0.005)(J-K)_{\rm CIT} \\
(J-H)_{\rm 2MASS} &= (1.087 \pm 0.013)(J-H)_{\rm CIT} - (0.047 \pm 0.007) \\
(J-K_s)_{\rm 2MASS} &= (1.068 \pm 0.009)(J-K)_{\rm CIT} - (0.020 \pm 0.007) \\
(H-K_s)_{\rm 2MASS} &= (1.000 \pm 0.023)(H-K)_{\rm CIT} + (0.034 \pm 0.006)
\end{aligned}
$$

2MASS - Bessel & Brett

(see, http://www.ipac.caltech.edu/2mass/releases/allsky/doc/sec6_4b.html)

$$
\begin{aligned}
(K_s)_{\rm 2MASS} &= K_{\rm BB} - (0.039 \pm 0.007) + (0.001 \pm 0.005)(J-K)_{\rm BB} \\
(J-H)_{\rm 2MASS} &= (0.990 \pm 0.012)(J-H)_{\rm BB} - (0.049 \pm 0.007) \\
(J-K_s)_{\rm 2MASS} &= (0.983 \pm 0.008)(J-K)_{\rm BB} - (0.018 \pm 0.007) \\
(H-K_s)_{\rm 2MASS} &= (0.971 \pm 0.022)(H-K)_{\rm BB} + (0.034 \pm 0.006)
\end{aligned}
$$

SDSS (*ugriz*) - Johnson-Cousins (*UBVRI*)

(see, Jordi et al., 2006)

$$
\begin{aligned}
r - z &= (1.584 \pm 0.008)(R-I) - (0.386 \pm 0.005) \\
i - I &= (0.247 \pm 0.003)(R-I) + (0.329 \pm 0.002)
\end{aligned}
$$

B. TTauri Stars and Brown Dwarfs in Taurus

	RA [deg] (J2000)	DEC [deg] (J2000)	J [mag]	H [mag]	K_S [mag]	Field name[a]
1	64.886215	27.340188	17.19 ± 0.06	16.14 ± 0.06	15.31± 0.06	2
2	64.943977	27.215307	17.30 ± 0.02	14.11 ± 0.02	12.03± 0.01	14
3	65.256958	27.012527	17.68 ± 0.08	16.33 ± 0.08	15.45± 0.05	18
4	65.078338	27.088125	17.86 ± 0.07	16.57 ± 0.07	15.57± 0.04	18
5	65.402618	15.433110	10.51 ± 0.01	9.85 ± 0.04	9.46± 0.03	15
6	65.387939	15.474070	15.99 ± 0.01	15.35 ± 0.03	14.99± 0.05	15
7	65.518745	15.605755	15.80 ± 0.01	15.11 ± 0.03	14.69± 0.03	15
8	61.130661	26.238998	16.89 ± 0.04	15.95 ± 0.05	15.30± 0.05	17
9	61.328166	26.249252	16.90 ± 0.05	16.22 ± 0.07	15.55± 0.06	17
10	61.126678	26.267478	16.69 ± 0.05	15.92 ± 0.06	15.25± 0.06	17
11	61.303279	26.268976	15.33 ± 0.05	14.69 ± 0.05	14.20 ± 0.06	17
12	61.298187	26.274993	15.99 ± 0.05	15.32 ± 0.06	14.95 ± 0.06	17
13	61.192993	26.457344	17.05 ± 0.07	15.95 ± 0.06	15.20± 0.06	17
14	67.054168	26.963323	17.18 ± 0.05	16.31 ± 0.07	15.55± 0.06	22
15	67.107688	26.736635	10.06 ± 0.01	9.41 ± 0.06	9.00 ± 0.04	22
16	67.294685	24.479398	18.12 ± 0.03	16.53 ± 0.02	15.60± 0.02	5
17	67.364715	24.492654	18.84 ± 0.04	16.90 ± 0.02	15.65± 0.02	5
18	67.383735	24.516534	17.78 ± 0.02	15.04 ± 0.01	13.06± 0.01	5
19	67.413261	24.528167	18.68 ± 0.04	16.84 ± 0.02	15.63± 0.02	5
20	67.292839	24.578271	18.33 ± 0.03	16.69 ± 0.02	15.70± 0.02	5
21	62.627567	25.100431	17.49 ± 0.06	16.50 ± 0.09	15.66± 0.09	11
22	62.608249	25.175519	16.66 ± 0.05	15.83 ± 0.07	15.38± 0.08	11
23	68.011146	18.075057	15.34 ± 0.03	14.50 ± 0.03	13.96± 0.03	6
24	67.993873	18.080976	17.09 ± 0.03	16.21 ± 0.04	15.67± 0.04	6
25	67.994049	18.052274	17.04 ± 0.02	16.13 ± 0.02	15.50± 0.03	6
26	67.814071	18.102607	17.51 ± 0.05	16.41 ± 0.04	15.15± 0.01	6

Table B.1 New Candidates for low-mass objects in Taurus identified in the Omega2000 survey. [a]The numbers correspond to the following fields listed on Table 6.1: 1 = tc7_11, 2 = tc12a_12b, 3 = tc20_21_22, 4 = tc23_24, 5 = tc28_29, 6 = tc30, 7 = tc35_36a_36b, 8 = tc37_38_39_41, 9 = tc42a_42b_42c, 10 = tc43_44, 11 = tc2, 12 = tc3_4, 13 = tc5_6_7_8, 14 = tc13a_13b_14, 15 = tc18a_18b, 16 = tc34, 17 = tc1a_1b, 18 = tc15_16a, 19 = tc16a_16b_17, 20 = tc19, 21 = tc25_26a_26b, 22 = tc27, 23 = tc50

	RA [deg] (J2000)	DEC [deg] (J2000)	J [mag]	H [mag]	K_S [mag]	Field name[a]
27	67.954978	18.184404	17.31 ± 0.03	16.27 ± 0.01	15.45± 0.02	6
28	67.873542	18.042375	14.81 ± 0.07	14.17 ± 0.09	13.43± 0.08	6
29	67.985939	18.149038	16.18 ± 0.06	15.58 ± 0.02	14.96± 0.05	6
30	67.819328	18.117515	17.62 ± 0.05	16.30 ± 0.02	15.25± 0.02	6
31	67.986145	18.148242	16.12 ± 0.01	15.30 ± 0.01	14.81± 0.02	6
32	67.953147	18.211380	16.88 ± 0.01	15.98 ± 0.01	15.46± 0.02	6
33	67.884368	18.272590	17.15 ± 0.01	15.87 ± 0.01	15.12± 0.01	6
34	68.006507	18.256341	16.97 ± 0.01	15.86 ± 0.01	15.16± 0.01	6
35	67.888183	18.130790	17.85 ± 0.05	16.81 ± 0.09	15.59± 0.07	6
36	67.889045	18.131265	17.54 ± 0.04	16.67 ± 0.07	15.31± 0.05	6
37	67.910217	18.228631	17.43 ± 0.05	16.83 ± 0.08	15.58± 0.06	6
38	67.909713	18.229507	17.00 ± 0.05	15.96 ± 0.07	14.98± 0.09	6
39	63.526397	28.170022	19.24 ± 0.05	16.33 ± 0.02	14.54± 0.02	12
40	63.587421	28.238855	18.44 ± 0.03	16.50 ± 0.02	15.31± 0.03	12
41	63.552448	28.198953	18.53 ± 0.09	16.68 ± 0.08	15.47± 0.08	12
42	68.394409	22.621589	16.65 ± 0.06	15.69 ± 0.06	15.03± 0.05	16
43	68.262573	22.712167	18.47 ± 0.10	16.77 ± 0.09	15.58± 0.08	16
44	68.252105	22.742073	17.55 ± 0.07	16.04 ± 0.07	15.11± 0.07	16
45	68.243980	22.747695	18.09 ± 0.08	16.59 ± 0.08	15.61± 0.09	16
46	68.400878	22.769601	17.84 ± 0.08	16.49 ± 0.08	15.52± 0.10	16
47	68.322807	22.815008	17.58 ± 0.02	16.36 ± 0.03	15.64± 0.08	16
48	68.824798	24.046152	10.79 ± 0.01	9.99 ± 0.07	9.42± 0.07	7
49	69.062736	24.049041	15.43 ± 0.01	14.82 ± 0.04	14.49± 0.03	7
50	68.813385	24.053022	17.64 ± 0.01	16.38 ± 0.04	15.63± 0.04	7
51	69.038475	24.068281	17.44 ± 0.06	16.30 ± 0.06	15.48± 0.08	7
52	68.925849	24.073820	17.21 ± 0.01	16.19 ± 0.02	15.61± 0.04	7
53	69.038627	24.061798	16.19 ± 0.02	15.21 ± 0.03	14.67± 0.04	7
54	69.864494	25.680349	19.35 ± 0.09	16.12 ± 0.02	14.04± 0.03	8
55	69.844268	25.817132	19.51 ± 0.07	16.23 ± 0.03	14.18± 0.03	8
56	69.906593	25.833139	17.98 ± 0.03	16.51 ± 0.02	15.60± 0.05	8
57	69.839302	25.874917	20.19 ± 0.10	17.34 ± 0.04	15.58± 0.04	8
58	69.784011	25.903610	19.96 ± 0.07	17.17 ± 0.04	15.46± 0.04	8
59	69.975837	25.709177	18.84 ± 0.07	15.70 ± 0.04	13.74± 0.03	8
60	69.818428	25.760335	16.32 ± 0.03	15.18 ± 0.03	13.39± 0.04	8
61	70.428535	25.662919	19.73 ± 0.09	16.66 ± 0.06	14.64± 0.04	23
62	70.320549	25.788238	19.31 ± 0.07	16.18 ± 0.04	14.15± 0.02	23
63	64.644599	28.498281	19.57 ± 0.08	17.04 ± 0.06	15.48± 0.04	1

Table B.1 - continued -

Name	RA [deg] (J2000)	DEC [deg] (J2000)	Field name[a]
IRAS 04169+2702	64.993469	27.165895	14
IRAS 04181+2654	65.297859	27.019241	19
IRAS 04191+1523	65.501838	15.505943	15
LEDA 3089400	61.333831	26.247327	17
HH 300	66.734474	24.726470	4
2MASS J04290498+2649073	67.270752	26.818678	22
GV Tau / Haro 6-10 IRC	67.350891	24.550421	5
[BFR2003]57	68.005173	18.083647	6
LDN 1551 NE	67.935143	18.142090	6
HL Tau	67.910164	18.232697	6
LDN 1551 IRS 5	67.892021	18.134666	6
XZ Tau	67.916977	18.232527	6
CoKu Tau 2	67.900566	18.238676	6
[GOK2004]89	68.016090	18.102152	6
HH 154	67.890480	18.1326437	6
IRAS 04108+2803	63.478016	28.192430	12
2MASS J04141188+2811535	63.549587	28.198212	12
[BBM92]42	68.329475	22.776136	16
2MASS J04930945+2246487	68.289429	22.780159	16
[HCA99]A/B	68.897453	24.138601	7
[HCA99]C	68.897073	24.140900	7
IRAS 04361+2547	69.807922	25.889257	8
[BBM92]50	69.896568	25.695715	8
IRAS 043817+2540 NIR B	70.302879	25.776575	23
[LR98]1	64.672211	28.456930	1

Table B.2 Names and coordinates of known objects in Taurus identified in the Omega2000 survey. [a]The field numbers are given in the caption of Table B.1.

Name	J [mag]	H [mag]	K_S [mag]
IRAS 04169+2702	17.48±0.03	13.77±0.02	11.25±0.01
IRAS 04181+2654	15.88±0.01	12.64±0.01	10.53±0.01
IRAS 04191+1523	17.09±0.08	14.80±0.05	12.69±0.02
LEDA 3089400	14.67±0.06	13.99±0.06	13.62±0.06
HH 300	16.21±0.06	13.02±0.02	10.46±0.01
2MASS J04290498+2649073	13.97±0.01	12.44±0.01	11.42±0.01
GV Tau / Haro 6-10 IRC	17.76±0.08	15.53±0.06	14.07±0.06
[BFR2003]57	16.87±0.02	15.99±0.03	15.41±0.03
LDN 1551 NE	16.49±0.03	13.68±0.03	11.47±0.02
HL Tau	10.54±0.02	9.21±0.03	7.61±0.01
LDN 1551 IRS 5	13.51±0.03	11.38±0.03	9.65±0.02
XZ Tau	9.26±0.01	8.19±0.04	7.21±0.02
CoKu Tau 2	13.39±0.01	11.52±0.01	10.06±0.01
[GOK2004]89	15.56±0.08	15.08±0.10	14.25±0.08
HH 154	17.24±0.05	16.28±0.08	14.98±0.06
IRAS 04108+2803	17.04±0.05	14.30±0.04	12.50±0.02
2MASS J04141188+2811535	13.05±0.01	12.27±0.01	11.73±0.02
[BBM92]42	12.06±0.01	10.10±0.01	8.21±0.05
2MASS J04930945+2246487	13.02±0.01	12.07±0.01	11.54±0.04
[HCA99]A/B	17.18±0.07	14.05±0.08	11.88±0.09
[HCA99]C	18.73±0.09	16.23±0.09	14.46±0.08
IRAS 04361+2547	15.37±0.06	12.43±0.07	10.21±0.04
[BBM92]50	17.25±0.06	13.88±0.05	10.78±0.02
IRAS 043817+2540 NIR B	17.47±0.10	14.88±0.08	11.95±0.03
[LR98]1	15.89±0.01	13.14±0.02	11.04±0.02

Table B.3 Near-infrared magnitudes of known objects in Taurus listed in Table B.2.

C. Highly variable objects in Omega2000 data

Comparison with 2MASS photometry

RA [deg] (J2000)	DEC [deg] (J2000)	J [mag]	H [mag]	Ks [mag]	ΔJ [mag]	ΔH [mag]	ΔKs [mag]	Field name[b]
70.489235	26.024530	14.95	13.75	12.37	-0.01	-0.27	-1.29	10
69.818428	25.760336	16.48	15.20	13.38	1.36	1.31	0.06	8
67.549065	24.383184	15.00	13.94	12.12	0.01	0.01	-1.37	5
61.069916	26.255867	14.13	15.02	14.81	-1.02	0.40	0.48	17
65.391533	27.099844	13.94	15.04	12.77	-1.65	-0.04	-1.96	19
64.895630	27.372574	15.56	14.89	12.17	0.09	-0.01	-2.55	2
67.061882	26.431496	14.80	12.61	13.60	-0.14	-1.33	-1.32	21
64.809349	27.044046	15.27	13.31	14.71	-0.78	-1.80	0.00	14
[a]65.283150	[a]27.038923	12.00	10.32	9.19	-1.85	-1.75	-1.35	18
		12.29	10.48	9.31	-1.57	-1.58	-1.24	19

Table C.1 The magnitudes listed in columns 3-5 are those observed with the OMEGA2000 camera. The offsets relative to the 2MASS observations are given in columns 6-8. [a]The last object is identical with 2MASS J04210795+2702204, an M5.2 Brown Dwarf discovered by Guieu et al. (2006), and was observed twice in an overlapping region of two OMEGA2000 fields in December 2005. It appears to be variable over short time scales and got significantly brighter over the last years. [b]The field numbers are given in the caption of Table B.1.

D. The non-detection of the 28.22 micron line in the RNO spectra

In the following, we analyze whether the non-detection of the 28.22 μm emission line in either spectrum is in agreement with the models. The two component models in Figures 4.9 and 4.11 can be used to predict the column densities of the S(0) emission line. One expects

$$\log \frac{\mathrm{N_{S(0)}}}{\mathrm{g_j g_s}} [\mathrm{cm^{-2}}] \approx 18.3\,\mathrm{cm^{-2}}$$

$$\log \frac{\mathrm{N_{S(0)}}}{\mathrm{g_j g_s}} [\mathrm{cm^{-2}}] \approx 18.8\,\mathrm{cm^{-2}}$$

for the spectra close to RNO 1B and RNO 1C, respectively. With g_s=1 and g_j=5 and applying Eq. (4.1), the following line intensities are derived:

$$\mathrm{I(2)_{1B}} \approx 1.64 \cdot 10^{-6}\,\mathrm{erg\,s^{-1}\,cm^{-2}\,sr^{-1}}$$

$$\mathrm{I(2)_{1C}} \approx 5.20 \cdot 10^{-6}\,\mathrm{erg\,s^{-1}\,cm^{-2}\,sr^{-1}}$$

The A-coefficient for the transition is $2.94 \cdot 10^{-11}\mathrm{s^{-1}}$ (Wolniewicz et al., 1998).

Taking into account the aperture size for the long-wavelength, high-resolution module of the spectrograph of 247.53 arcsec^2 ($\approx 5.82 \times 10^{-9}$ sr), the predicted integrated line fluxes amount to

$$\mathrm{F_{1B}} \approx 9.57 \cdot 10^{-22}\,\mathrm{W\,cm^{-2}}$$

$$\mathrm{F_{1C}} \approx 3.02 \cdot 10^{-21}\,\mathrm{W\,cm^{-2}}$$

To estimate the peak of the 28.22 μm line in janskys, we assume that the spectral resolution in the high-resolution modules is constant and that the FWHM of the S(0) line can be extrapolated from the FWHM of the S(1) line at 17.03 μm. Since we fitted a Gaussian profile to the emission lines and we want to derive the peak flux of this Gaussian, we also have to take into account the relation between the FWHM we measure for the line and the σ of the profile. This relation is FWHM=$\sqrt{8\ln 2} \cdot \sigma$. With the expected FWHMs of

$$\Delta\nu_{\mathrm{1B}} \approx 2.84 \cdot 10^{10}\,\mathrm{Hz}$$

$$\Delta\nu_{\mathrm{1C}} \approx 2.12 \cdot 10^{10}\,\mathrm{Hz}$$

we thus find corresponding peak fluxes of

$$\mathrm{F_{1B}^{peak}} \approx 0.034\,\mathrm{Jy}$$

$$\mathrm{F_{1B}^{peak}} \approx 0.152\,\mathrm{Jy}$$

These values have to be compared with the measured uncertainties in the spectra. The mean 1-σ level in the spectral range between 28.0 and 28.4 μm is, however,

$$\bar{\sigma}_{1\mathrm{B}} = 0.055$$

$$\bar{\sigma}_{1\mathrm{C}} = 0.082$$

so that even in the more favorable case of RNO 1C the emission line is not expected to be detected at a confidence level greater than $\approx$1.8 σ.

E. List of publications

Refereed journals

Quanz, S. P.; Henning, Th.; Bouwman, J.; van Boekel, R.; Juhász, A.; Linz, H.; Pontoppidan, K. M.; Lahuis, F. (2007). Evolution of dust and ice features around FU Orionis objects. *ApJ*, submitted

Gouliermis, D.; Quanz, S. P.; Henning, Th. (2007). Clustered Star Formation in the Small Magellanic Cloud. A Spitzer/IRAC View of the Star-Forming Region NGC 602/N 90. *ApJ*, in press

Quanz, S. P.; Henning, Th.; Bouwman, J.; Linz, H.; Lahuis, F. (2007). Deeply Embedded Objects and Shocked Molecular Hydrogen: The Environment of the FU Orionis Stars RNO 1B/1C. *ApJ*, **658**, 487

Quanz, S. P.; Apai, D.; Henning, Th. (2007). Dust Rings and Filaments around the Isolated Young Star V1331 Cygni. *ApJ*, **656**, 287

Ábrahám, P.; Mosoni, L.; Henning, Th.; Kóspál, Á.; Leinert, Ch.; Quanz, S. P.; Ratzka, Th. (2006). First AU-scale observations of V1647 Orionis with VLTI/MIDI. *A&A*, **449**, L13-L16

Quanz, S. P.; Henning, Th.; Bouwman, J.; Ratzka, Th.; Leinert, Ch. (2006). FU Orionis: The MIDI VLTI Perspective. *ApJ*, **648**, 472

Krause, O.; Rieke, G. H.; Birkmann, S. M.; Le Floc'h, E.; Gordon, K. D.; Egami, E.; Bieging, J.; Hughes, J. P.; Young, E. T.; Hinz, J. L.; Quanz, S. P.; Hines, D. C. (2005). Infrared Echoes near the Supernova Remnant Cassiopeia A. *Science*, **308**, 1604

Conference Proceedings

v. Boekel, R.; Ábrahám, P.; Correia, S.; de Koter, A.; Dominik, C.; Dutrey, A.; Henning, Th.; Kóspál, Á.; Lachaume, R.; Leinert, Ch.; Linz, H.; Min, M.; Mosoni, L.; Preibisch, T.; Quanz, S.; Ratzka, Th.; Schegerer, A.; Waters, R.; Wolf, S.; Zinnecker, H. (2006). Disks around young stars with VLTI/MIDI. Proceedings of the SPIE, Volume 6268, 626809

Quanz, S. P; Henning, Th.; Leinert, Ch.; Ratzka, Th.; Wolf, S. (2005). FU Orionis - The MIDI Perspective. Proceedings of the ESO Workshop on "The Power of Optical/IR Interferometry: Recent Scientific Results and 2nd Generation VLTI Instrumentation"

F. Acknowledgments

In retrospect it was definitely the right decision to do a PhD thesis at the Max Planck Institute for Astronomy in Heidelberg. The opportunities I was offered, in terms of scientific education and interaction with outstanding scientists and interesting people, are probably difficult to find in other places. Hence, in the last three years I met a lot of friendly and helpful people that I would like to thank.

First of all, I am very grateful to Prof. Thomas Henning for giving me the chance to do this PhD thesis under his supervision. I certainly benefitted a lot from his teaching and knowledge about the formation of stars and planets. Frequent scientific discussions helped to improve and push forward the different projects, part of which are summarized in this thesis.

Furthermore, I would like to thank Prof. Ralf S. Klessen for being the second referee of this thesis.

I am extremely grateful to numerous post-docs and scientists at the MPIA who always helped me out whenever I needed scientific advice or support. Some of them, however, were not only scientific mentors but became good friends. A lot of thanks to Hendrik Linz, Jeroen Bouwman, Henrik Beuther, Roy van Boekel, Wolfgang Brandner, Sebastian Wolf, Kees Dullemond, Bertrand Goldman, Daniel Apai, Hubert Klahr, Coryn Bailer-Jones, Oliver Krause, Jürgen Steinacker, Dimitrios Gouliermis, Cristina Afonso, Thorsten Ratzka, Rainer Köhler, Viki Jörgens, Ilaria Pascucci, Prof. Christoph Leinert, and Prof. Reinhard Mundt.

Numerous people read and corrected (at least part of) this thesis and provided a lot of useful suggestions how the style and content could be improved. For their precious help, I am deeply indebted to Hendrik Linz, Jutta Stegmaier, Henrik Beuther, Stephan M. Birkmann, Bertrand Goldman, Nadine Neumayer, Niels Rumpf and Boyke Rochau.

Unfortunately, there are just too many fellow PhD students at the MPIA that I have to thank for numerous reasons. Thus, it is pretty likely that I would forget somebody if I tried to name them all individually. Hence, a general thanks goes to all of the young folks at the MPIA! We spent are great deal of time together, shared some interesting years and, at least from my point of view, had some great fun during our workshops or other occasions!

I would like to mention a few student sub-groups, though, which I was lucky enough to be part of: (1) The breakfast and coffee-break crew with its long-time frequent members Boris Häußler, Stephan M. Birkmann, Jutta Stegmaier, Nadine Neumayer, Martin Hennemann, Micaela Stumpf, and Hendrik Linz. (2) The MPIA soccer and basketball teams and all its members that helped me to blow off some steam whenever required. (3) The MPIA student choir with its members Micaela Stumpf, Jutta Stegmaier, Boris Häußler, Alexander Schegerer, and Natascha Haas. (4) The two-guitars-that-yet-have-to-have-their-first-gig band ”Die Avocados aus Bebra” and their lead guitar player Hendrik

Linz. (5) The piano jazz crew with the superb musician Frithjof Brauer (I still do hope we get eventually a CD out!) Thanks to all of you for bringing fun to the past three years!

I am grateful to the support astronomers and staff at Calar Alto and VLT. I would also like to thank those people working hard to keep the marvelous space observatories HUBBLE SPACE TELESCOPE and SPITZER SPACE TELESCOPE running. Parts of this thesis would not have been possible without the efforts of those people.

Further thanks goes to Glenn Schneider, Murray Silverstone and Betty Stobie from Steward Observatory (Tuscon) for teaching me how to use and reduce HUBBLE/NICMOS data. Even if the interesting project we worked on had to be cancelled, I definitely benefitted from the two moths I stayed in Arizona.

It would also like to thank "my summer student" Lorne Hofstetter from Princeton who joined and supported me for two months in summer 2006 and worked hard on the OMEGA2000 data.

During the last three years I was happy to benefit from a full PhD-scholarship from the German *Friedrich-Ebert-Stiftung* and I am extremely grateful for the support. Special thanks to Frau Marianne Braun for her kind help as my contact person at the *Friedrich-Ebert-Stiftung*.

All this work would not have been possible without two people that I would like to thank deeply from my heart: my parents. During all I did and achieved thus far, it was very ensuring to know that they and their love were there whenever needed! My deepest thanks for supporting and believing in me!

Second but last, but certainly not least, a special thanks goes to Niels Rumpf. My years of studying in Heidelberg will always be strongly linked to my longtime roommate. Thanks for being the true friend everybody wishes to have!

Finally, it is my great pleasure to thank Silke Maria Zoller for making these times so precious and some years to remember. I wish for many more to follow.

Erklärung

Ich versichere, dass ich diese Arbeit selbständig verfasst und keine anderen als die angegebenen Quellen und Hilfsmittel benutzt habe.

Heidelberg, den _____ _____

(Sascha P. Quanz)